

Aerodynamic Sensing for
Autonomous Unmanned Aircraft Systems

by

Derrick W. Yeo

A dissertation submitted in partial fulfillment
of the requirements for the degree of
Doctor of Philosophy
(Aerospace Engineering)
in The University of Michigan
2013

Doctoral Committee:

Associate Professor Ella M. Atkins, Co-Chair
Professor Wei Shyy, Co-Chair
Associate Professor Luis P. Bernal
Professor Carlos E. Cesnik
Associate Professor Yin Lu (Julie) Young



To a young boy,
who was so busy playing with aeroplanes
that he forgot to grow up.

Acknowledgements



I have had a wonderful time at the University of Michigan and would like to mention the following people in particular, thereby letting everyone know how grateful I am for everything they have done for me.

Dr. Atkins: An entire chapter would be needed to adequately express my gratitude for your guidance, support and friendship throughout the years. Thank you for always providing me with a much-needed reality check every time I dropped by your office, in utter despair about some perceived research tragedy or new and exciting character flaw on my part. From midnight laundry madness to midday lawn mowing by way of epic battles with seasickness, our flight-test adventures have always been great fun. Working in your lab has been a wonderful journey and I am grateful for the memories.

Dr. Shyy: Thank you for all the encouragement and support you have provided me, in all the years since I first showed up at your office looking to start an aero-modeling club. Your confidence in me has always been inspiring even when I

inspired little confidence in anyone else. I have a long way to go as a researcher, and will always remember your advice.

Dr. Bernal: Thank you for the heroic levels of patience you have shown me over the years since my undergraduate days. In the context of this dissertation, thank you for not throwing me out of your office when I showed up one day waving a screwdriver with two tubes unceremoniously strapped to one end, proclaiming “My beta-probe works!”

To my friends and colleagues: Thank you, Ryan and Justin for always providing doses of sanity through the years along with much appreciated servings of humor. The A2Sys motorcycle gang did not last long and broke no laws, but I like to think we were Born to be Wild anyway. Thank you, Cat for always caring enough to provide feedback during practice presentations, even after everyone else had either fallen asleep or discovered the secret of the universe within their phones. Thank you, Roland for taking time off your own work to help me run the vacuum tests, and always being ready to visit a Mediterranean restaurant. Thank you, Dan for showing me the engineering behind the world of artistry and introducing me to the magical world of back-room Computer Aided Manufacturing. Thank you, Jerry for your capable assistance around the lab. To my other friends and loved ones who have supported me over the years, you know who you are: Thank you.

And finally, I would like to thank **my family**. Thank you, Mum and Pa for being my first research sponsors and buying me my first radio controlled aeroplane when I was six. Thank you for listening to the endless complaints from every school teacher I have ever had, and still sending me off to college anyway. Thank you, my dear sister, for having had to bear the brunt of my marvelous stupidity growing up. Thank you all for the patience and loving support you have provided me throughout my thirty one years of childhood. It has been a long time since that first RC flight, but I still always find myself standing about with an aeroplane in my hand and a big smile on my face.

Table of Contents

Dedication	ii
Acknowledgements	iii
List of Tables	ix
List of Figures.....	x
List of Appendices	xiv
Abstract	xv
Chapter 1 Introduction.....	1
1.1 Motivation	2
1.2 Basic challenges and requirements.....	3
1.3 Research objectives	4
1.4 Thesis overview.....	5
1.5 Contributions & innovations.....	8
Chapter 2 Background.....	11
2.1 Aerodynamic lift generation	11
2.2 Traditional approach to aerodynamic force measurements.....	14
2.3 A pressure-based aerodynamic data system	15
2.4 Flapping wing vehicle background.....	18
2.5 High angle of attack, fixed-wing UAS operations.....	21
Chapter 3 Pressure Based Aerodynamic Force Estimation for Flapping Wing Vehicles	26
3.1 Introduction.....	26
3.2 Experimental approach.....	27

3.3	Flapping wing experimental setup	28
3.3.i	Flap stand overview	28
3.3.ii	VICON testing instrumentation.....	31
3.3.iii	Vacuum chamber test setup and instrumentation.....	32
3.3.iv	Wind tunnel test setup and instrumentation	34
3.4	Flapping wing kinematics	37
3.4.i	Mechanical design and geometry	38
3.4.ii	VICON motion capture validation of mechanics.....	39
3.4.iii	3D Linkage solver and comparison to VICON data.....	42
3.5	Multi-phase experimental characterization of loads.....	44
3.5.i	Vacuum chamber measurements of inertial loads	44
3.5.ii	Wind tunnel vertical force and pressure measurements	45
3.6	Experimental data processing and analysis	46
3.6.i	Force-Torque sensor data – frequency domain analysis	47
3.6.ii	Pressure based aerodynamic force estimation	56
3.6.iii	Comparison of pressure based estimates and force sensor aerodynamic force measurements.....	60
3.7	Phase and magnitude shifts due to pressure lines	65
3.8	Forward flight cases	66
3.8.i	Forward flight test procedure	67
3.8.ii	Additional data processing for forward flight	68
3.8.iii	Forward flight test results.....	72
3.9	Summary of test results.....	74
3.9.i	Comparison of experimental methodologies.....	75
3.10	Flapping wing conclusions	77

Chapter 4 Aerodynamic Moment Estimation for Fixed Wing Vehicles in High Angle of Attack Maneuvering.....	80
4.1 Introduction.....	80
4.2 Steady level flight equations.....	81
4.3 Proposed linear model for high angle-of-attack flight.....	83
4.4 Embedded instrumentation.....	87
4.4.i Embedded pressure sensors on flight surfaces	89
4.4.ii Custom designed multi-hole probes.....	91
4.5 Aircraft configuration.....	92
4.6 Aerodynamic sensing - tail section	94
4.6.i Dedicated multi-hole probe for prop-wash estimation	95
4.6.ii Instrumented tail	97
4.7 Calibration of instrumentation	99
4.7.i Prop-wash probe calibration	99
4.7.ii Tail-surface pressure port and sensor calibration	104
4.8 Wind tunnel test procedure.....	105
4.9 Experimental data processing and analysis	107
4.9.i Pressure data processing	107
4.9.ii Frequency domain analysis of FT data	113
4.10 Propeller driven test cases	116
4.10.i Hover test results	116
4.10.ii Combined free-stream and prop-wash cases	122
4.10.iii Independence of pitch and yaw control surfaces.....	126
4.10.iv Summary of test results.....	128
4.11 Linear moment model development for hover	129

4.11.i	Moment coefficients for use with V_{pw} in hover.....	129
4.11.ii	Further investigation of the linear aerodynamics model.....	132
4.11.iii	Summary of the linear model analysis section.....	136
4.12	Direct aerodynamic sensing scheme	137
4.12.i	Calibration of pressure data integration using a low turbulence reference case	139
4.12.ii	Low turbulence free-stream calibration	140
4.12.iii	Calibration applied to hover data	142
4.12.iv	<i>Alpha25</i> and <i>5kCruise</i> Cases	145
4.13	Fixed-wing conclusions	148
4.14	Future work	149
Chapter 5 Conclusions and Future Work.....		152
5.1	Conclusions.....	152
5.2	Future work	154
Appendices		156
References		196

List of Tables

Table 3.1 Key physical dimensions of flapping wing test cases.....	35
Table 3.2 Key dimensionless parameters for flapping wing test cases.....	37
Table 3.3 Observed PSD peaks in vacuum Force-Torque data with flap-stand structural mode at 14Hz	51
Table 3.4 Cycle averaged and single-stroke aerodynamic force errors.....	55
Table 3.5: Peak force and phase comparison	64
Table 3.3.6: Peak-to-peak magnitude and phase comparison – single pressure measurement.....	66
Table 3.7 Summary of forward flight test cases.....	67
Table 3.8 Approximate no-wing flying baselines.....	69
Table 4.1 Funtana platform physical properties.....	92
Table 4.2 Prop-wash probe sensor configuration and port assignment.....	97
Table 4.3 Prop-wash probe calibration coefficients	103
Table 4.4 Summary of basic test cases.....	107
Table 4.5 Computed Number of SMA points for test cases.....	113
Table 4.6 Hover test prop-wash probe measurements for elevator sweeps.....	117
Table 4.7 Hover test conditions for elevator sweeps	118
Table 4.8: Hover test conditions for rudder sweeps.....	120
Table 4.9 Test conditions for the <i>5kCruise</i> case.....	123
Table 4.10: Test conditions for the <i>Alpha25</i> case.....	125
Table 4.11: Linear aerodynamic coefficients computed from hover data.....	132
Table 4.12. Estimated linear slopes from low-turbulence training case	142
Table C.0.1 Averaged Wing Rock Phase Information for Two Flights	186

List of Figures

Figure 2.1 Circulation around a backward rotating cylinder	13
Figure 2.2 NACA 8x6 supersonic wind tunnel Manometer boards in 1949. (www.space.com)	15
Figure 2.3 Overview of experimental configurations.....	16
Figure 2.4 Flapping wing test stand in vacuum chamber.....	17
Figure 2.5 Fixed wing test platform with internal force-torque transducer	17
Figure 3.1 Multiple phase experimental approach	27
Figure 3.2 Flapstand overview.....	29
Figure 3.3 Flap governor overview	30
Figure 3.4 Wing construction and embedded pressure port locations.....	31
Figure 3.5 Large VICON targets on rigid balsa wings.....	32
Figure 3.6 PEPL 'Junior' vacuum chamber.....	33
Figure 3.7 Vacuum chamber instrumentation schematic.....	34
Figure 3.8 Windtunnel test configuration	35
Figure 3.9 Custom designed flap mechanics.....	39
Figure 3.10 Wing marker YZ paths at different flap frequencies.....	40
Figure 3.11 Port wing tip-markerZ paths at different flap frequencies, with expanded view of maximum deviation during the stroke.	41
Figure 3.12 Port wing fore/aft marker phase difference remains constant between 1.3Hz and 4.3Hz.....	42
Figure 3.13 Sample linkage solver output with 17 crank steps for clarity showing crank positions with red dots and wing positions with black lines(Left). Corresponding computed wing flap angle output at given crank positions (Right).	43
Figure 3.14 VICON and 3D linkage solver stroke comparison.....	43
Figure 3.15 Vacuum Chamber Data Overview	45

Figure 3.16 Sample wind tunnel force and pressure measurements – Hover	46
Figure 3.17 Force-Torque sensor data processing for aerodynamic loads.....	47
Figure 3.18 Sample hover power spectrum - Simulated test run at 4.5Hz.....	48
Figure 3.19 Sample power spectrum comparison between flap frequencies in vacuum: 2.0Hz top, 4.5Hz bottom	50
Figure 3.20 Sample power spectrum comparison at 3.0Hz in Vavuum (top) and in air (bottom) - No additional modes in air.....	52
Figure 3.21 Ensemble Averaging Process for Force/Torque data and 95% CI - 3.5Hz in vacuum.....	53
Figure 3.22 Importance of correct encoder offset - 3.0Hz	54
Figure 3.23 Standard deviation intervals on subtracted aerodynamic load measurements - $f=3.0\text{Hz}$ and 3.5Hz	57
Figure 3.24 Examples of pressure measurements over left wing in hover : $f=3.5\text{Hz}$	58
Figure 3.25 Aerodynamic force estimates based on pressure measurements ...	59
Figure 3.26: Pressure based measurements of vertical aerodynamic force coefficients.....	60
Figure 3.27 Wing kinematics - Positive flap angles dennote wings above level .	61
Figure 3.28 First comparison of FT sensor measurements and pressure based force estimates	62
Figure 3.29 Comparison of vertical aerodynamic force measurements at hover	64
Figure 3.30: Pressure line length impact measurements – magnitude (left) and phase delay / lag (right)	65
Figure 3.31 Windtunnel testing subcases	68
Figure 3.32 Sample case with offset being accounted for using no-wing baseline	69
Figure 3.33 Sensitivity of force-torque histories to LP filter setting	70
Figure 3.34 PSD for 2.0Hz (Top) and 3.0Hz (Bottom) – Comparison between hover and forward flight cases.....	71
Figure 3.35 Frequency sweep at 2.3ms free stream. St. 0.14-0.24.....	72
Figure 3.36 Frequency sweep at 3.3ms free stream. St. 0.09-0.19.....	73

Figure 3.37 Sample quasi-steady panel method pressure solution - single lift peak.....	74
Figure 4.1 Pressure-Based Aerodynamic Instrumentation Concept	88
Figure 4.2 Distributed sensing and Wing Discretization for Pressure Based Lift	89
Figure 4.3: Mounting locations for Air-data and Prop-wash probes.....	91
Figure 4.4 Funtana RC aircraft platform	93
Figure 4.5: Wind tunnel test platform overview.....	94
Figure 4.6: Prop-Wash Probe Location and Geometry	96
Figure 4.7 Distributed sensing over tail surface and area discretization scheme	97
Figure 4.8. Embedded pressure ports and sensors, horizontal tail surfaces	98
Figure 4.9: Prop-Wash Probe Flow Angle Calibration Curves	100
Figure 4.10 Airspeed calibration with $\phi = 0$	101
Figure 4.11 Pressure differences at different airspeeds and horizontal-plane flow angles.....	102
Figure 4.12. Airspeed calibration for zero-flow-angle (left) and correction factor (right)	103
Figure 4.13 Sample calibration of an embedded tail surface sensor	104
Figure 4.14 Pressure calibration test setup for the left elevator.....	105
Figure 4.15: Basic test procedure overview – Tests performed at 25° , 0° and -25° α	106
Figure 4.16: Significant standard deviation intervals in raw pressure data	108
Figure 4.17 Variation of standard deviation intervals with increasing SMA period	110
Figure 4.18 Results of scaling of SMA period based on propeller RPM	111
Figure 4.19: Performance of a vortex-frequency-based SMA period scaling methodology.....	113
Figure 4.20: Structural response of the test stand near 5Hz.....	114
Figure 4.21 Flow excitations with multiples encountered at 4000 and 6000 RPM	115
Figure 4.22 Low turbulence free stream excitation of structural modes.....	116
Figure 4.23: Pitch moment measurements at hover	119

Figure 4.24: Yaw moment measurements at hover	121
Figure 4.25 Pitch and Yaw moment measurements at 12m/s and 5000rpm. ...	123
Figure 4.26: Pitch and yaw moments from the Alpha25 test case	125
Figure 4.27 Combined elevator and rudder deflection test cases showing negligible cross coupling between elevator and yaw moments	127
Figure 4.28 Combined rudder and elevator deflection test cases showing negligible cross coupling between rudder and pitch moments.....	128
Figure 4.29: Compiled FT data from hover cases and resulting linear fit.....	132
Figure 4.30: Comparison between linear model and compiled hover data	133
Figure 4.31: Linear model comparison with powered cruise test data	134
Figure 4.32: Linear model compared with <i>Alpha25</i> test case results.....	136
Figure 4.33 Low turbulence free stream training data set.....	141
Figure 4.34 Comparison between corrected pressure-based and FT measurements of hover pitch moments.....	143
Figure 4.35: Comparison between corrected pressure-based and FT yaw moment measurements for hover.....	144
Figure 4.36 Comparison of FT and pressure based coefficients at 3000RPM..	145
Figure 4.37: Corrected pressure based measurements at near-hover, <i>Alpha25</i> case.....	146
Figure 4.38 Corrected pressure based measurements at powered cruise	147

List of Appendices

Appendix A: Flight Funtana hardware and setup.....	156
Appendix B: Instrumentation details	171
Appendix C: Flight test results.....	173
Appendix D: Air data probe design.....	190

Abstract

Aerodynamic Sensing for Autonomous Unmanned Aircraft Systems

By Derrick W. Yeo

Autopilots currently rely on a single set of air data probe plus inertial measurements fed into linearized models to predict the aerodynamic forces and moments acting on a flight vehicle. While this approach is well suited to most aerospace applications, emerging flapping and fixed-wing unmanned aircraft systems (UAS) operated at post-stall conditions introduce aerodynamic forces that are complex and difficult to predict with such models and measurements. This research investigates the use of distributed pressure sensing for real-time aerodynamic force and moment characterization on flapping wing and small fixed wing UAS platforms.

Flapping flight is first considered. A flapping wing test platform has been built with pressure based instrumentation embedded in rigid wings along with an integrated force-torque sensor. Through a series of vacuum chamber and wind tunnel experiments, time-resolved aerodynamic loads generated by a rigid flapping wing at a Reynolds number of approximately 4500 have been measured using both sets of instrumentation. At hover, key parameters such as phase and peak magnitudes measured by force-torque and pressure sensors agreed to within 10%, providing cross-validation and showing that the embedded pressure sensing concept is suitable for future flight control applications.

Expanded aerodynamic data acquisition for a fixed wing UAS maneuvering in unsteady, post-stall flow conditions is also explored. This thesis introduces a reformulation of the steady fixed-wing flight equations for operations at high

thrust, low airspeed conditions. A wind tunnel test system was developed around an existing flight vehicle with a 1.8m wingspan. Measurements of the pitch and yaw moments due to the tail surfaces were collected directly through embedded pressure measurements and indirectly through a custom air data probe measuring propeller backwash near the tail. Test data was acquired to determine the in-flight aerodynamic pitch and yaw moments due primarily to propeller backwash when the UAS operates past stall. Through comparisons with torque-transducer measurements, both methods are shown to provide moment estimates within one standard deviation of transducer measurements at hover. Model coefficients or slopes in data trends also compared favorably over all other tests.

Chapter 1

Introduction

Unmanned aircraft systems (UAS) were initially developed as guided missiles after the turn of the 20th century. They first became distinguishable from projectiles in 1920 when Sperry gyroscopes and barometers were employed on the Kettering Aerial Torpedo in 1916[1]. By offering a form of on-board sensing, simple flight stabilization and guidance became possible though imprecise due to limitations in sensing and electronics.

During World War II, both Axis and Allied scientists developed remotely flown target drones and self-guided missiles, both of which are effectively classes of unmanned aircraft systems (UAS). The German *Vergeltungswaffe 1*, more commonly known as the infamous V-1 flying bomb, was a small aircraft powered by a pulsejet engine. It carried a barometer and a simple inertial guidance system based on pendulums, compasses and gyroscopic sensors mechanically linked to the control surfaces [2]. This rudimentary sensor scheme allowed the V-1 to maintain level flight, but was sensitive to external conditions such as weather or being perturbed into a spin by Allied aircraft.

The first role of the unmanned aircraft that did not involve being a missile or target drone was scientific. After the Second World War, a number of B-17s were converted into remotely-piloted QB-17s by the US Air Force to serve as remotely piloted drones collecting radioactive data over atomic mushroom clouds during Operation Crossroads [3]. During the Vietnam War, the UAS first adopted its now widespread reconnaissance and surveillance role when remotely-piloted Ryan Firebee drones were flown over Vietnam by the US Air Force [4].

While remotely piloted systems eventually took the Soviet Union to the moon in the 1970s with the Lunakhod rovers [5], the combination of a barometer and inertial sensors employed on the Kettering Aerial Torpedo and V-1 Flying Bomb remained fundamental both in manned and unmanned aircraft control applications. Combined with linearized aerodynamic force and moment models, these sensing strategies have adequately served the requirements of both manned and unmanned fixed-wing flight.

Since the Cold War however, shrinking electronic payloads have allowed for ever smaller unmanned aircraft. While representing numerous opportunities, flight operations at these small scales also present a range of aerodynamic challenges to the UAS designer. At the smallest scales, the use of flapping wings for both lift and propulsion promises an advantage over conventional fixed and rotary wing configurations [6]. Flapping flight mechanics bring new challenges due to the inherently complex and unsteady aerodynamics that are involved while fixed wing flight at small scales is subject to non-linear, low-Reynolds number effects [7]. The flow field encountered by a small aerial vehicle is more uncertain due to the exaggerated effects of atmospheric turbulence [8] and the radical flight profiles that are possible with small vehicles.

1.1 Motivation

As the mission profile of small UAS expands, they are beginning to operate in rapidly changing and complex flow environments either through flapping flight mechanics or through radical maneuvering. In addition to vertical take-off, aerobatic flight and transitions between different flight modes, small UAS with both conventional and novel configurations hold promise for able operation in urban canyons, under canopies, or indoors with constantly changing flow conditions that are challenging to predict [9].

Under these complex flow conditions, pre-determined aerodynamic coefficients and limited air measurements might not be able to adequately predict the aerodynamic forces acting on a flight vehicle. The current paradigm of inertial sensing coupled with linearized aerodynamic models is not capable of providing

accurate force and moment information or control surface authority due to the non-linear nature of the aerodynamics encountered. As a result of an inability to predict complex time-varying aerodynamic forces, the realm of unique flight mechanics and high performance aerobatic maneuvering has been mostly limited to either manned or remotely piloted vehicles.

When flow field measurements beyond basic wind vector information are directly acquired through expanded sensing, the principle of feedback control can be extended to the aerodynamics of the vehicle. This could allow for a wider range of uncertainties and unexpected perturbations to be handled by an onboard controller that can potentially expand the envelope of small UAS.

With the goal of expanding aerodynamic data beyond basic wind measurements, this thesis describes, implements, and models two platforms with a pressure based aerodynamic sensing scheme for small UAS operating in uncertain flow environments.

1.2 Basic challenges and requirements

To develop and validate the concept of comprehensive embedded aerodynamic sensing for small UAS

Achieving an accurate aerodynamic sensing capability on small UAS presents a number of challenges. First, a suitable flow measurement strategy must be devised that is inherently self-sufficient and portable while still providing sufficient flow information. While advanced flow measurement techniques available to fixed testing such as Particle Image Velocimetry (PIV) can capture a complete picture of the flow field, it is not practical to host onboard a flight vehicle. While a pressure measurement strategy is more limited in scope, it is more easily implemented on a flight vehicle.

Another challenge is in developing a suitable combination of sensor and data acquisition hardware and software. Measurements must be sufficiently accurate

and precise and must be acquired at sufficient rates to ensure adequate ability to capture unsteady flow characteristics and support filtering as needed. Hardware chosen must be capable of taking measurements of pertinent ambient flow conditions under all expected operating conditions. In addition to sensor selection, the configuration in which the sensors are deployed is also a fundamental component of an Aerodynamic Data System (ADS) as proposed. A suitable overall sensor strategy must employ the chosen hardware in such a way that measurements are taken at the locations that best allow estimation of the vehicle's aerodynamic state. Lastly, an expanded set of aerodynamic instrumentation also means an expanded set of aerodynamic data. A suitable methodology of converting sensor data to useful information such as estimates or predictions of aerodynamic forces and torques is required. A new, application-specific combination of hardware and data processing techniques must be developed to overcome the challenges inherent in measuring and characterizing flow conditions for small UAS operations.

Once implemented, any proposed instrumentation and data concept needs to be tested and validated. This represents its own series of challenges and requires an alternate and independent source of data. Suitable test hardware and test procedures must be developed, and experiments carried out. Appropriate techniques must also be used when processing and interpreting the data from these tests. Noise and bias must be considered and eliminated to the extent possible, and comparisons of independent data require careful study of similarities and discrepancies of datasets to yield the best models and best understanding of signal quality from each data source under each test and operating condition.

1.3 Research objectives

This research aims to provide two viable approaches to implementing and validating pressure based aerodynamic sensing for small UAS operating in uncertain flow conditions. Due to the hardware-intensive requirements of an

aerodynamic data system, an experimental approach to validating both approaches was adopted for this work.

Two UAS applications were examined: a flapping-wing test platform and a conventional fixed wing vehicle operating in post stall conditions. The objectives for each platform are listed below.

- 1) Develop test hardware that meets the requirements of each chosen application of the aerodynamic sensing concept. Each test setup must provide two independent forms of measurement for validation purposes.
- 2) Assemble an aerodynamic instrumentation package with sensors and data acquisition hardware based on the needs of each UAS platform.
- 3) Develop and carry out experiments that enable comparisons between pressure-based and alternate measurements of aerodynamic forces or moments.
- 4) Develop and utilize data processing methodologies suited to the specific flow conditions encountered by each platform.
- 5) Provide an analysis of the processed experimental data and draw conclusions on the proposed aerodynamic sensing concept and its implementation on small fixed-wing and flapping wing UAS.

1.4 Thesis overview

This thesis describes the development and validation of a pressure based aerodynamic sensing concept for UAS operating in uncertain flow conditions. Two test setups have been developed: one for flapping wing experiments and another based on a small aerobatic aircraft with a conventional propeller-driven configuration. Each is instrumented according to platform-specific requirements

and used in a series of ground-based tests. Independent force and torque measurements are taken to validate the sensing scheme and aid its development.

Chapter Two provides background information for both applications. It first describes the basic physical principles of aerodynamic force generation and describes the relationship between pressure and velocity which are the main flow parameters that can be easily measured with sensors. Current approaches to unsteady flow instrumentation are described followed by an overview of the proposed pressure based aerodynamic sensing concept used in this work. The chapter then describes the current state of the art as representative of engineered flapping wing vehicles, and provides a brief history of unmanned fixed wing operations at high angles of attack and hover.

Chapter Three documents the implementation of the aerodynamic sensing concept on flapping wing vehicles. On the flapping platform, a test stand was developed to serve primarily as a novel tool in studying flapping flight. It was configured to employ two experimental methods that independently measure the aerodynamic lift generated during the stroke of a rigid flapping wing. The first approach uses a force transducer to measure forces in air and vacuum and the second approach uses pressure measurements taken on the surfaces of the wing as a form of aerodynamic sensing. Results from both methods are used to validate each other and provide experimental data for a test case with easily simulated conditions. Specifically, Chapter Three first describes the design of the test hardware which includes a custom flap-stand, flap mechanics, and present instrumented wing construction techniques. A series of flap tests are described in which pressures are measured only in air and force/torque measurements are recorded both in air and in a vacuum. Note that vacuum testing is required to characterize inertial loads for the force-torque sensor. The methodology used to process the raw data is described. The processed data is then evaluated with respect to noise, repeatability and expected scaling trends. The chapter ends by

comparing the pressure sensor and force transducer measurement strategies based on their accuracy and flexibility.

Chapter Four describes the ground-based testing of a flight-capable aerodynamic data system for fixed wing vehicles operating at high angles of attack. A wind tunnel test setup has been developed from a flight test platform designed for high angle of attack flight. By integrating an internally mounted force-torque sensor, the test setup enables two approaches to implementing aerodynamic sensing to be explored. First a partial aerodynamic sensing scheme through an additional propeller backwash measurement is explored; this scheme is low-cost and non-invasive to the airframe. Second is a more complete direct moment measurement scheme which utilizes distributed sensing across the horizontal and vertical tail surfaces. The chapter begins by proposing a reformulation of the steady flight equations for propeller-driven, fixed-wing aircraft operations at post-stall angles of attack and in vertical hover. New terms are added to take advantage of expanded flow-field data that obtained through the proposed aerodynamic sensing scheme. The instrumentation design is presented along with a wind tunnel test setup adapted from an existing flight vehicle to house both pressure-based instrumentation and an integrated force-torque transducer. The chapter describes the experimental procedure and presents data processing techniques that allow both measurement approaches to be compared. Wind tunnel test data is used to evaluate and develop the aerodynamic sensing scheme and ends by summarizing key findings from this analysis.

Chapter Five summarizes the key findings from the research carried out for both platforms and ends with concluding remarks on the applicability of the aerodynamic sensing to UAS in general.

1.5 Contributions & innovations

The contributions of this research are summarized below with innovations highlighted.

- **Embedded aerodynamic sensing scheme for small UAS**

A pressure-based aerodynamic sensing concept has been developed and applied to flapping and fixed-wing UAS in this thesis. While the instrumentation hardware is based on existing technology, the combination and application of sensor configurations, data acquisition setup, and application-specific data processing methodology represents a new direction in small UAS embedded instrumentation. While this thesis focuses on results from ground-based testing, the deployment of the aerodynamic sensing concept for autonomous aerobatic flight operations is the next step with early efforts summarized in the appendices. The concept is made possible through innovations such as proposed reformulations of basic flight models, distributed sensing strategies, and actual flight instrumentation.

- **Independent force transducer and pressure-based measurements of the time resolved vertical forces generated by a pair of rigid flapping wings in air**

The time resolved vertical aerodynamic loads generated by a rigid flapping wing at $Re \sim 4500$ have been measured using a force-torque sensor and a distributed pressure sensing approach. A series of motion capture, vacuum chamber and wind tunnel tests were performed for both hover and forward-flight test conditions. This is made possible through innovative design of the flap mechanics and embedded electronics that allow for accurate and repeatable flap kinematics through all test phases.

- **Experimental validation of a direct, pressure-based approach to measurements of time resolved forces generated by a flapping wing**

With two independent measurements of the flap-resolved forces, a comparison between traditional force-transducer measurements and an embedded, distributed pressure sensing approach can be made.

A primary contribution in this research is to experimentally evaluate the potential of embedded pressure-based measurements to provide augmented feedback for future flight control systems. This was made possible through the innovative prototyping and manufacturing of instrumented flapping wings along with a suitable pressure sensing strategy.

- **Augmented steady flight equations and expanded aerodynamic sensing concept for fixed wing UAS**

The steady flight equations rely on airspeed, angle of attack and sideslip for the calculation of the aerodynamic forces generated by an aircraft. Two different reformulations are proposed that utilize additional air data measurements instead of a single wind vector for computing aerodynamic moments in flight. An accompanying fixed wing instrumentation concept that provides the necessary information is described.

While the aerodynamic model and aerodynamic instrumentation concept presented are elementary, the key contribution is the application of the two in tandem for a small UAS. By considering the actual instrumentation in the development of the flight model, this represents an innovative approach to aerodynamic modeling and sensing for small UAS that routinely operate past stall.

- **In-flight moment estimation for a fixed-wing UAS during high angle of attack flight**

Using the reformulated steady flight equations and a pressure based aerodynamic sensing system, two different methods of determining the pitch and yaw moments on a fixed wing aircraft are presented. One is applicable only in hover, and the other functions under all tested conditions.

Through innovations such as a dedicated propeller wash probe and propeller-scaled filtering technique, this research presents a methodology for computing a set of linear coefficients for the feedback control of pitch and yaw moments on a fixed wing aircraft in vertical hover. The significance of this relatively simple set of numbers is that it represents an extension of the basic and commonly-utilized linearized aerodynamic force and moment steady flight model valid only with small (pre-stall) angles of attack to the post-stall, slow to no free-stream velocity flight regime that cannot be handled by simple autopilots that rely on traditional linearized flow models. By combining the data from a multi-hole probe in a novel physical location with a new propeller wash velocity term, an augmented “steady flight” model for small UAS operating beyond stall, specifically in hover for this thesis, has been proposed, implemented, and validated.

Through a reformulation of the aerodynamic pitch and yaw moment equations, a system of distributed aerodynamic sensing for the vertical and horizontal tail surfaces are shown to enable in-flight measurements of pitch and yaw moments. These moments have been integrated into the corresponding steady flight equations. Through wind tunnel testing, this scheme is shown to be capable of providing additional aerodynamic data throughout two different flight regimes of a fixed wing UAS operating at high angles of attack. By documenting a process that has enabled a small UAS platform to measure aerodynamic pitch and yaw moments, this research has provided a methodology that can be employed on other small fixed wing UAS and ultimately for real-time moment characterization in flight.

Chapter 2 Background

This chapter describes the basic fluid dynamics principles that motivate and enable the aerodynamic sensing scheme developed in this thesis. It provides a brief description of the physical relationship between fluid velocity, pressure and resulting forces through the governing equations. A brief history of common flow sensing strategies is provided before the hardware and software supporting the pressure-based aerodynamic sensing system developed for this thesis is introduced and linked to implementations on the flapping-wing and fixed-wing platforms discussed in this thesis. A fourth section reviews state-of-the-art in designing, building, modeling and operating small unmanned flapping wing vehicles. The last section provides an overview of current unmanned fixed wing operations, with a focus on high angles of attack and hover applications.

2.1 Aerodynamic lift generation

When a body passes through a fluid such as air, its shape and motion cause the fluid to exert forces on the body. As a fluid deforms and changes in velocity occur, changes in the pressure exerted by the fluid on the body arise. This in turn causes changes in the forces exerted on the body. The relationship between the velocities, pressure and forces in a fluid are given by the Navier Stokes equation and the Continuity equation as described in [10]. These are reproduced here for two velocity components u, v in the x and y directions along with the incompressible continuity condition in Equations (2.1), (2.2) and (2.3). These relate pressure, mechanical pressure p , gravity, g and viscosity.

$$\frac{\partial u}{\partial t} + u \frac{\partial u}{\partial x} + v \frac{\partial u}{\partial y} = g_x - \frac{1}{\rho} \frac{\partial p}{\partial x} + \nu \left(\frac{\partial^2 u}{\partial x^2} + \frac{\partial^2 u}{\partial y^2} \right) \quad (2.1)$$

$$\frac{\partial v}{\partial t} + u \frac{\partial v}{\partial x} + v \frac{\partial v}{\partial y} = g_y - \frac{1}{\rho} \frac{\partial p}{\partial y} + \nu \left(\frac{\partial^2 v}{\partial x^2} + \frac{\partial^2 v}{\partial y^2} \right) \quad (2.2)$$

$$\frac{\partial u}{\partial x} + \frac{\partial v}{\partial y} = 0 \quad (2.3)$$

These governing equations follow from applying Newton's 2nd law and conservation of mass to a discrete volume within a fluid. Under steady, inviscid, incompressible flow simplifications, the relationship between fluid velocity and the pressure exerted by the fluid is given by Bernoulli's equation. When applied along a streamline with a stream-wise velocity V , it takes the well-known form shown in Eq. 2.4.

$$\left(p + \frac{1}{2} \rho V^2 + \rho g z \right)_1 \approx \left(p + \frac{1}{2} \rho V^2 + \rho g z \right)_2 \quad (2.4)$$

From Bernoulli's equation it can be noted that a fluid moving slowly exerts more pressure on its surroundings compared to a fluid moving quickly. This provides insight to the basic mechanism for aerodynamic force generation. It is the result of the relative motion in air caused by an object immersed in it, and is related to the velocities of the air particles in the volume that it imparts to a flow field. A more rigorous derivation can be found in [10]. Extending this concept of velocity being related to force, circulation is the line integral of velocity around a closed path enclosing the lifting body. The most common example is that of a backward rotating cylinder in a flow as shown in Figure 2.1.

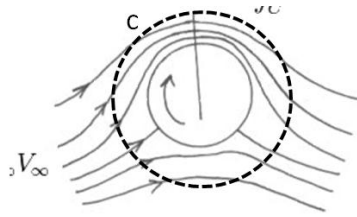


Figure 2.1 Circulation around a backward rotating cylinder

The Kutta-Joukowski theorem relates circulation, fluid speed and density directly to lift. The circulation around an object is given as

$$\Gamma = \oint_c V \cdot ds \quad (2.5)$$

where c is the integral path. Once the circulation is known, the sectional lift force L_{sect} can be computed as

$$L_{sect} = -\rho_{\infty} V_{\infty} \Gamma \quad (2.6)$$

This illustrates provides an intuitive, if simplified, view of how vortical structures in a flow are related to fluid forces. A more detailed presentation of potential flow theory can be found in [11]. A real-life fluid flow is viscous, leading to boundary layers near surfaces. These are layers of decelerated flow that are caused by the viscous interaction between the fluid and the solid interface. These layers can separate, causing the main flow around the body to deviate and assume a flow field that does not follow the contours of the body. In most conditions, this leads to vortical flow structures. Depending on the nature of the separation, this can lead to stable forces with stable vortices or unsteady forces as vortices are formed and shed.

On wings or other lifting surfaces, the linear relationship of lift versus inflow angle is valid up to this point of separation where the forces can begin to diminish and eventually turn unsteady, leading to non-linear and unsteady aerodynamic forces that are difficult to predict and model. This thesis proposes the concept of taking actual flow field measurements for UAS operating under these unsteady conditions as a means to quantify aerodynamic forces acting on aircraft surfaces that would be otherwise difficult to predict.

2.2 Traditional approach to aerodynamic force measurements

Since the Wright Brothers' 1901 wind tunnel, the most traditional approach to aerodynamic force and moment measurement has been to use a force balance and compare baseline measurements with no flow field to those obtained with a known free-stream flow. While scale models of manned aircraft were typically used, it is possible for full-scale small UAS to fit in moderate size tunnels such as the 5'x7' University of Michigan tunnel utilized for this work.

Since fluid velocity and pressure are related, flow speed sensing is also capable of giving estimates of aerodynamic forces. The earliest mechanical anemometer, a flat plate that deformed in the wind, can be traced back to 1450 [12]. Whisker-type flow speed sensors [13] represent a more recent incarnation of this oldest form of anemometry, operating based on the principle that a long whisker bends and vibrates in a moving fluid [14]. While these methods provide velocity information at a single point, velocimetry techniques such as Particle Image Velocimetry (PIV) and Laser Doppler Velocimetry (LDV) developed in the late 1970s [15] can provide entire velocity fields during an experiment but are limited to instants in time. As previously mentioned, the use of lasers and the requirement of flows to be seeded with tracers also limit such strategies to fixed testing.

As aerodynamic forces arise due to changes in pressure across the surface of a body, the most direct method of measuring these forces has been to embed ports in the surface of a body. Using banks of manometers such as those shown in Figure 2.2, the pressure differences at a series of points on a body or surface can be compared. Early pressure transducers and force sensors began using bonded strain gauges in the late 1930s, offering pressure or force differences in the form of electrical signals. Today, the same principles are implemented using piezo-resistive diaphragms that are batch fabricated thus reasonable in cost and offer high data rates in a compact form factor [16].



Figure 2.2 NACA 8x6 supersonic wind tunnel Manometer boards in 1949.
(www.space.com)

With high speed digital acquisition, pressure sensors have been used to capture unsteady flow phenomena. In purely lab-based experimental work, Hillaire and Carta [17] have taken pressure measurements over a range of oscillating wings with a symmetrical airfoil with different planforms. In more portable applications, Usherwood et al. have attached pressure transducers and accelerometers to the wings of Canadian geese [18] for pressure measurements.

As illustrated by these examples, the capabilities of high speed data acquisition and pressure sensor technology make pressure histories during unsteady flow phenomena possible using inherently portable instruments that continue to shrink in size [19].

2.3 A pressure-based aerodynamic data system

The overall aerodynamic instrumentation scheme presented in this thesis is based on high speed, spatially distributed pressure measurements. Precision sensors monitor the pressure at a number of locations across a lifting surface and these measurements are used to make estimates of the aerodynamic forces being generated. The data acquisition system used in this work is a PC/104 embedded computer that records the readings reported by the pressure

instrumentation at 1kHz. The advantages of the PC/104 system are that it is portable thus capable of either being affixed in proximity to a very small UAS such as the flapping platform described in Chapter 3 or fit inside a small UAS fuselage such as the fixed-wing Funtana described in Chapter 4. is that it fits inside The block diagram in Figure 2.3 gives an overview of the different test system configurations used for both fixed-wing and flapping-wing platforms.

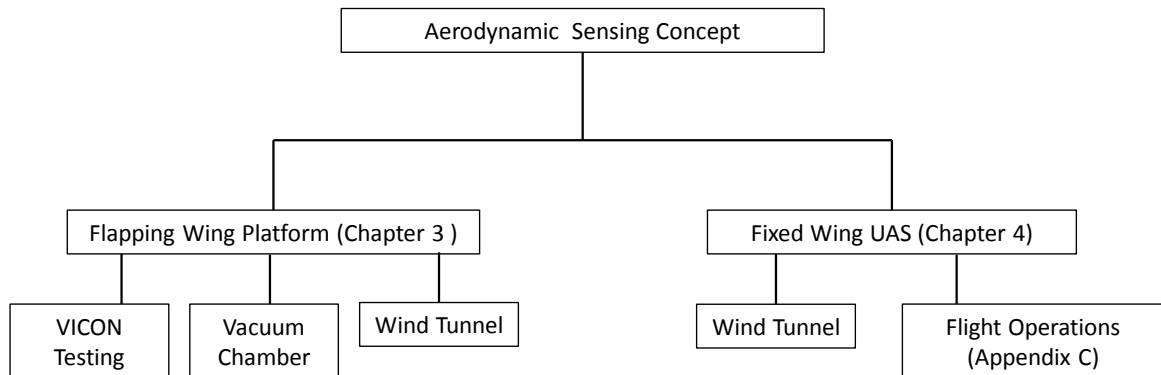


Figure 2.3 Overview of experimental configurations

In its flapping wing role, the aerodynamic data system is mounted to a custom-built test stand appropriate for testing in a wind tunnel and in a vacuum chamber. As part of a dedicated ground-test package, weight and portability are a secondary concern to accuracy so it is configured with larger, commercially available sensors that are more sensitive but are not practical for flight. The system includes a six degree-of-freedom (DOF) force-torque transducer for independent measurements of the aerodynamic forces. The test stand is shown in a vacuum chamber test section in Figure 2.4.



Figure 2.4 Flapping wing test stand in vacuum chamber

In its fixed wing application the aerodynamic data system has previously served as an integrated part of a small fixed wing UAS and is configured to be portable and lightweight. For the wind tunnel testing described in this thesis, the aerodynamic sensing package is expanded to include smaller-scale pressure sensors mounted in proximity to pressure ports while the complete flight platform itself has been adapted for wind tunnel testing with changes to accommodate an integrated force-torque transducer.



Figure 2.5 Fixed wing test platform with internal force-torque transducer

The process of locating these pressure ports and choosing the pressure sensors is described in more detail in the following sections for each application. Specifics

on the experimental configurations for each platform are discussed in their respective chapters.

2.4 Flapping wing vehicle background

Flapping wing platforms from micro [19,21] to small scale ~10cm [22,23,24] to larger scale vehicles [25,26,27] with ~1m wingspans have been developed and tested as an analogue to real bird flight. Autonomous ornithopters have been successfully flown by researchers utilizing extended fixed wing autopilot formulations. Krashanitsa [28] incorporated a Paparazzi autopilot unit on a Cybird P2 ornithopter and demonstrated autonomous, waypoint tracking flight. More recently, Lee et al [27] designed and built a flapping wing platform SF-2 which flew autonomously with a complete inertial measurement sensor suite.

While practical flapping wing vehicles have been successfully developed, their flight envelope and flight capabilities have not been precisely characterized. Most current flapping wing vehicles rely on moving surfaces adapted from traditional aircraft designs for attitude control. A single tail surface typically provides pitch and directional control and the main wings are not actuated beyond a fixed flapping stroke [25]. While such designs have successfully flown for both recreational and research applications, [22,23,26,27,28] they fail to afford ornithopters the agility of fixed or rotary wing vehicles. Even the Festo Seagull [29] which utilizes the most advanced wing actuation to date cannot mimic the full capabilities of its biological namesake. Incorporating attitude control actuation on the moving wings of an ornithopter presents even more challenges due to constantly changing forces and inherently non-linear aerodynamics, but offers the possibility of improved aerobatic performance.

Both experimental and numerical analyses play an important role in developing future control techniques and flap stroke kinematics. To simulate the aerodynamics of flapping wing flight, researchers have used Navier-Stokes Computational Fluid Dynamics (CFD) solvers as well as potential flow, discrete

vortex methods [30,31]. Flexible membrane wings and wing kinematics induce considerable coupling between fluid and structural dynamics during flapping. Therefore it is difficult to separate fluid-induced and structural loads.

Aerodynamic models must be coupled with structural solvers in order to describe the physics of a practical flapping wing. Researchers have coupled both CFD and discrete vortex methods with structural solvers [32,33,34] with results that can be validated against existing experimental data. The pressure-based instrumentation presented in this paper offers additional means of validating aerodynamic simulation results by providing an alternate source of force and pressure distribution data.

In terms of gathering aerodynamic data, force transducer-based experimental work has ranged from measurements of live biological flyers such as locusts [35] and dragonflies [36] and oil- and water- based studies of characteristic fluid flow fields [37,38,39] to tethered flight testing of existing flight vehicles of sizes ranging from insect-like scales [21,22,40,41] to those of bird-type scales [42]. One challenge in measuring aerodynamic forces with a force transducer is separating the aerodynamic forces from the inertial forces due to the moving wing structure. In order to do this, the inertial forces and torques due only to the wings' motion must be measured. Two possible approaches include the use of mass-tuned "inertial only" wings that have a negligible surface area, and running tests in a vacuum environment. Massey et al. [42] and Hubel and Tropea [43] built "inertial wings" from aluminum pipes and used those as an approximate structural load calibration to obtain aerodynamic forces. Singh and Wu [44,45] ran tests in a vacuum environment to obtain inertial loads generated by flexible flapping wings in order to extract the aerodynamic forces. Due to the absence of aerodynamic forces in a vacuum, flexible wings do not deflect exactly as they would in air.

In the work presented in this dissertation, a custom set of flap mechanics is configured to flap rigid wings in both air and vacuum. With rigid wings, the deflections in both vacuum and air are identical due to the absence of

aerodynamic coupling. This ensures that the measured structural loads in a vacuum match those encountered in air, allowing aerodynamic force results that can be used to verify the pressure based measurements. The rigidity of the instrumented flapping wings and repeatability of the flap stroke are verified using a Vicon motion capture system. Using the VICON system, passive markers are placed on the test wings to allow measurement of the surface and the wings flapped through a range of frequencies to vary wing loads.

In the above studies, measurements of the flow field are typically achieved using PIV instrumentation as in [37,39,41,43]. With PIV, the test fluid, either water or air, is seeded with tracer particles which allow the velocity of the fluid field to be measured. This provides flow visualization and the pressure field can be estimated by solving for the pressure distribution based on the velocity field. The current work evaluates the use of a pressure-based aerodynamic data system for flapping wing vehicles. Pressure ports across the wing allow a direct means of measurement that is portable and capable of being carried onboard. While such measurements cannot provide a complete picture of the flow field like PIV, they can be acquired and processed in real time. This allows for different flap strokes and wings to be quickly tested. Researchers have previously taken pressure measurements across the surface of actual micro flapping wing vehicles and large bird wings in flight, showing the potential for this approach to be easily implemented on practical flight vehicles. Usherwood et al attached pressure transducers and accelerometers to the wings of Canadian geese [18] and pigeons [46] while researchers from the University of Tokyo [19,47] have flight tested an insect-scale flyer with integrated, custom built pressure sensors in its flexible wing membranes. The distinction of this dissertation's approach and procedure is in its comprehensive instrumentation of a flapping wing with a known geometry, and its use in a controlled flow environment which can yield cleaner, more consistent datasets. Previous work by Usherwood and Ellington have used a similar pressure and FT measurement on biological wing designs [48,49] but in a revolving, propeller type situation that focuses on more traditional, steady state data. The test platform developed for this work operates

in a wind tunnel and possesses a simple but well-documented flap stroke. The well-characterized test conditions in this work enable measurement validation and comparison with force measurements not possible in free flight.

2.5 High angle of attack, fixed-wing UAS operations

In the last decade, UAS ranging from large to small sizes have been deployed for platform/payload validation, science, and surveillance roles traditionally associated with conventional fixed or rotary wing aircraft [50].

Small aerobatic UAS carrying modest payload weights are typically over-powered to the extent that even a single propeller-driven engine is capable of generating a thrust greater than total vehicle weight. This characteristic enables the small UAS to assume the advantages of a fixed wing platform with a rotary wing platform, specifically to fly with the efficiency of a fixed-wing aircraft but to also be capable of hovering over a site of interest and/or landing/perching without the need for a full landing strip. A small UAS with the ability to operate at high angles of attack and hover as well as perching can have applications across military and commercial sectors. Such a platform could move quickly and efficiently to new locations but still provide stationary close-range reconnaissance when required [51].

Wickenheiser [52] considered the large lift and drag coefficients at high angle of attack flight to be useful for the ARES-C Martian Exploration Vehicle, and employed a lifting-line-based analysis of the longitudinal aerodynamics of an ARES reconfigurable exploration craft. The closely-related concept of flapping wing vehicle perching has received some attention from the community [53,54,55,56,57,58,59]. Recent progress by Paranjape et al [58,59] has demonstrated the ability of a tail-less morphing wing glider to perch autonomously by actuating its dihedral angle. Desbiens et al [56] demonstrated the use of microspines landing gear for enabling a small vehicle to land and remain on vertical surfaces. The wing rock characteristics of a medium sized

Radio Control (RC) hobby aircraft flying at high angles of attack were studied by Lind and Johnson [60].

The aerodynamics of high angle of attack flight presents a number of challenges to fixed wing aircraft. Near stall, aircraft lift coefficients are nonlinear with respect to parameters such as angle of attack and airspeed. Lateral handling issues such as asymmetric wing stall and wing rock also pose challenges at high angles of attack [61,62] Early research focused on mitigating manned aircraft handling issues near stall and enhancing fighter jet maneuverability [62, 63,64,65]. This body of knowledge remains largely applicable to engineers exploiting high angle of attack flight on unmanned aircraft.

The current paradigm of small UAS instrumentation integrates inertial measurements supplemented by airspeed as a minimum or more capably a five-hole probe providing air-data measurements that include airspeed, angle of attack, and sideslip. Such systems have been successful in applications involving conventional fixed wing flight within the traditional flight envelope [66,67,68]. Such platforms have been provided the baseline capability for more advanced systems, with flight tests in cooperative control research [69] and even ocean-borne operations [70] demonstrating the flexibility and extensibility in UAS applications. Small autopilot systems such as the Kestrel Autopilot [71] and Micropilot are also capable of serving rotary wing vehicles [72].

High angle of attack aerodynamics challenges traditional UAS autopilot instrumentation and control laws which typically rely, for example, on a single linear relationship between angle of attack and coefficient of lift. Flight near or beyond the point of stall are subject to flow separation that results in aerodynamics that are unsteady, nonlinear, and sensitive to small changes in flight conditions. Aerodynamics that involve flow separation are therefore incapable of being handled by linear controllers [7,73] and the traditional instrumentation scheme.

Working within the limitations of the current small UAS instrumentation framework, a number of fixed wing UAS have been guided between cruise and hover in the last decade. Green and Oh developed indoor hobby aircraft that could autonomously transition from cruise to hover using inertial measurements and a linearized controller [74]. This impressive first autonomous fixed wing hovering work did not deal with the high angle of attack flight regime, using airframe properties such as low rotational inertia, high thrust/weight ratios and a control law that allowed it to “bully its way through stall”. A similar approach in avoiding the aerodynamic problems at high angles of attack using similar flight vehicles by Frank et al [75] also achieved successful autonomous transitions to hover and docking in a VICON motion capture environment. More recently, Cory and Tedrake [53] used the VICON system to provide valuable insight into the non-linear aerodynamic effects encountered during a perching maneuver. This was a step towards exploiting the aerodynamic phenomena at stall instead of avoiding it. Using VICON position data, instantaneous aerodynamic coefficients could be estimated. It was noted that while individual trials showed time-varying coefficients due to unsteady aerodynamic effects, the overall trend of averaged data over many trials agreed with simple flat plate theory. This allowed the formulation of an aerodynamic coefficient estimator based on angle of attack and elevator deflection given still indoor air and the kinematic data from the VICON environment.

Johnson et al [76] developed an adaptive controller that enabled autonomous transitions to and from hover. The guidance law used during the transition was similar in formulation to those used in previous work - the commanded inertial pitch angle was set to vertical to achieve the transition. A slow ramp approach and a faster step-change transition were tested and it was noted that both resulted significant altitude error during the transition. Johnson et al suggested that an airspeed-bleed strategy was a potential solution. In previous work [77], the use of pressure based aerodynamic sensing to support such a transition guidance phase was proposed. Processing pressure data over an instrumented wing chord, the autopilot was able to detect stall and could reliably bleed

airspeed up to the point it was detected before switching control modes. Flight tests [78] showed that expanded aerodynamic data could improve the ability of a simple, linear decoupled autopilot to operate under non-linear conditions. This work seeks to develop the concept of expanded aerodynamic data for small UAS operating at high angles of attack. It uses an expanded set of pressure measurements across the aircraft for additional flow information.

The concept of pressure-based estimation of the flow field above an airfoil has been a cornerstone of wind tunnel testing, but in stepping towards aerodynamics-based feedback, the most relevant efforts to our work have focused on enabling closed loop feedback in “onboard” active flow control schemes to alleviate flow separation or emulate control surfaces through the use of flow actuation. One successful example was implemented by Patel and Corke [79,80] who considered the time domain response from a high bandwidth pressure sensor to predict incipient flow separation at the wing leading-edge and trigger the activation of a plasma flow actuator.

Under attached flow conditions, Cox et al [81] used pressure based estimates of the lift curve above an airfoil as feedback for an automated a cruise flap. NASA has supported wind tunnel-based implementation and testing of a distributed actuation and sensing array for use on a blended wing body UAS, using a series of pressure measurements to study the effectiveness of a morphing wing control strategy. More information on these tests can be found in [82] and [83]. The AFOSR AVOCET project [84] aims to continuously tailor the pressure distribution and resulting forces and moments across the wing using advanced micro-tuft sensors and hybrid fluidic flow actuators.

The overall goals of the aerodynamic feedback concept proposed in this research bridges the two efforts described above. The existing active flow control framework developed by Patel et al [79,80] is suited to alleviate retreating blade stall in rotorcraft and expand their performance envelope. With the AVOCET project, flow measurement and actuation across the wing surfaces are closely coupled to vehicle control and the system aims to achieve a careful tailoring of

vorticity distributions in real time to also alleviate gusts and flow disturbances. While the intended purpose of the aerodynamic data presented in this work is to offer additional data for feedback control, our objectives are not to directly affect the flow structure but to provide improvements on how the conventional surfaces can be used.

The experimental approach presented in Chapter Four utilizes a full-scale UAS platform in a 5'x7' wind tunnel test section. Wind tunnel tests conducted previously on full-scale small UAS have characterized aerodynamic characteristics of an aircraft [85] for novel control strategies [86,87]. Using the actual flight vehicle as a test model allows for testing when the propulsion system is active. Landman et al investigated the longitudinal and lateral aerodynamic characteristics of a small UAS with and without power applied to the propeller [88]. Recent work by OI et al tested an aerobatic RC airframe in the presence of prop-wash using transducer based instrumentation and found that high thrust settings at low advance ratios serve to linearize control-surface response [89].

Chapter Four seeks a novel approach to fixed-wing UAS instrumentation that meets the challenges of high-alpha flight through expanded sensing. The presented experiments validate the hardware and concept as well as providing specific results for the UAS test platform, a Funtana commonly used by hobbyists for aerobatic flight.

Chapter 3

Pressure Based Aerodynamic Force Estimation for Flapping Wing Vehicles

3.1 Introduction

Using the Aerodynamic Data system, an experimental investigation of the aerodynamic forces acting on a flapping wing was carried out with the objective of validating pressure based measurements of the time-resolved forces generated by a flapping wing using a second set of independent measurements.

A test stand was developed to serve primarily as a novel tool in studying flapping flight. It was configured to employ two experimental methods to measure the aerodynamic lift generated during the stroke of a rigid flapping wing. The set of measurements are taken with a force transducer in both air and vacuum. The second approach uses pressure measurements taken on the surfaces of the wing as a form of aerodynamic sensing. Time-resolved stroke-plane forces from both methods are used to validate each other and provide experimental data for a test case with easily simulated conditions.

This chapter first presents the experimental procedure that were developed and the test hardware that was built, including a custom flap-stand, flap mechanics, and instrumented wings. It will describe a series of flap tests were conducted with pressures measured only in air and force measurements taken both in air and in a vacuum. It will present techniques used to process the raw data which is then evaluated with respect to noise, repeatability and expected scaling trends. Comparing the pressure sensor and force transducer measurement strategies are made based on their accuracy and flexibility and the chapter ends with a summary of key findings and a description of future work.

3.2 Experimental approach

Since our primary interest in this study is to assess the viability of using pressure measurements to estimate the aerodynamic forces generated by a flapping wing, it is critical that these loads be separated from the loads associated with the motion of the wings. To separate aerodynamic forces from inertial loads, multiple tests using the same wing kinematics had to be performed in both vacuum and in wind tunnel environments. Rigid wings that are not subject to aeroelastic deformations were chosen, allowing the flap stroke to be well documented in all relevant test conditions. This allowed the experiment to be run multiple times in different environments and the data from all the individual tests could be cycle averaged and merged. The three separate test phases which were used are depicted in Figure 3.1. The first phase involved testing in a vacuum chamber where the forces and torques due only to inertial loads can be measured. The second phase was to be conducted in the wind tunnel with the pressure lines disconnected to enable the full aerodynamic and inertial loads to be measured. The difference between the two readings will be the forces due to aerodynamic loads. The final phase involved taking only pressure measurements and was conducted in the wind tunnel as well but with one of the wings replaced the pressure wing that had the pressure ports connected.

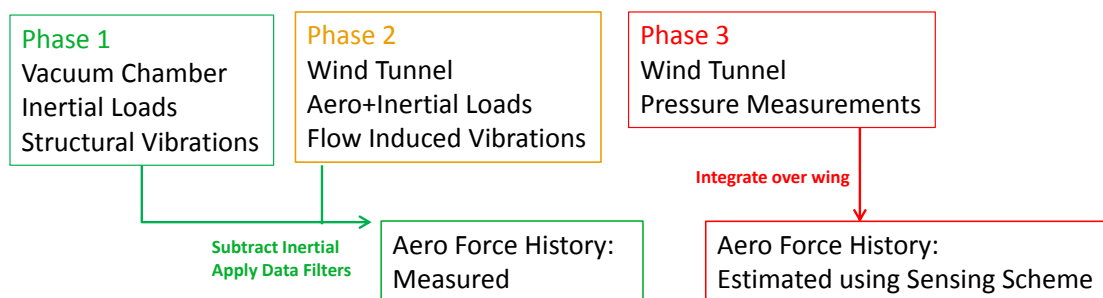


Figure 3.1 Multiple phase experimental approach

By splitting the experiment into these three separate test phases, three sets of data were combined to obtain an ensemble averaged cycle history of inertial

loads, aerodynamic loads, wing position and wing pressure histories. The design and verification of the rigid kinematics studied and the separate experimental phases are described in the following sections.

3.3 Flapping wing experimental setup

In order to run the multi-phase flap tests, a complete flapping wing system was developed. A stand was built to house both sets of instrumentation, a custom set of flap mechanics were developed and validated to provide consistent wing kinematics, and custom embedded electronics were built to run the tests under a variety of conditions. The following sections describe the components of the flapping wing test system and the facilities that were used during testing.

3.3.i Flap stand overview

The Flapping wing platform includes an integrated test stand and the actual instrumented wings. The flap stand was developed to house the instrumentation package during vacuum chamber and wind tunnel tests. Primary instrumentation includes a bank of low pressure MEMS pressure sensors and a six-axis force-torque (FT) sensor. The stand and instrumentation was conceived to enable a multi-phase experimental approach that combines results from three different tests. An overall schematic of the flap stand is shown in Figure 3.2. The test model, FT sensor, and a pitot probe are supported by an adjustable main arm to accommodate different test sections.

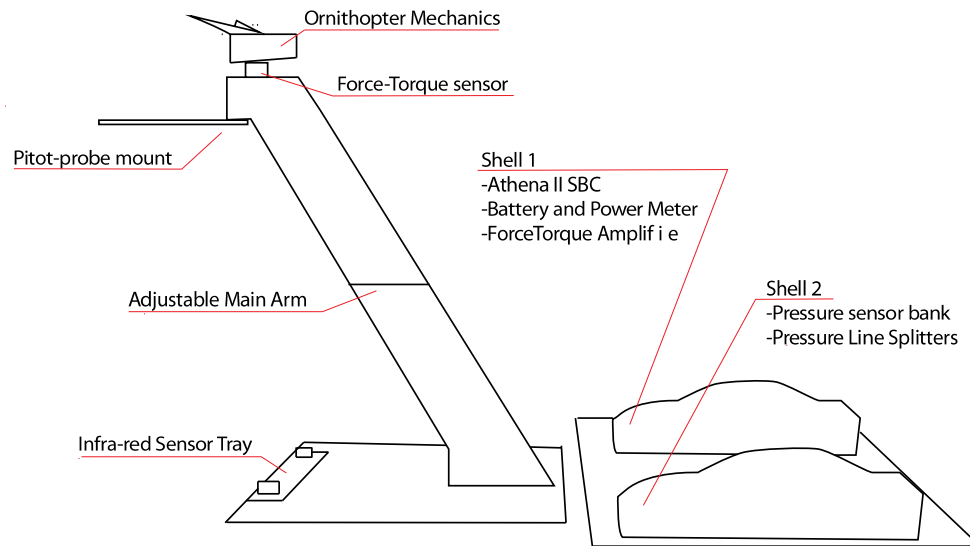


Figure 3.2 Flapstand overview

3.3.i.a Wing motion encoding and control

When using a beam balance to measure time-resolved flapping forces, Apker[90] found that using a brushed direct current (DC) motor with no feedback control resulted in unsteady flap frequencies during testing. Variation in flap frequency would present difficulties when attempting to recreate wing motion across experimental phases as wing loads vary between motion capture, wind tunnel, and vacuum tests. The design presented includes a custom-built magnetic encoder system and separate feedback controller to consistently regulate flap frequency using an integral-control algorithm developed for this experiment. A block diagram of the flap governor is presented in Figure 3.3. The closed loop integral controller and user interface is run on by a stand-alone set of microcontrollers. User commands are issued remotely using an infra-red remote control module using a Sony television IR protocol. This wireless remote control scheme is a versatile and straightforward method of controlling the flap experiment in different test environments, such as in a vacuum chamber. The controller module then alters the command signal to an RC brushless motor controller that drives the flap motor.

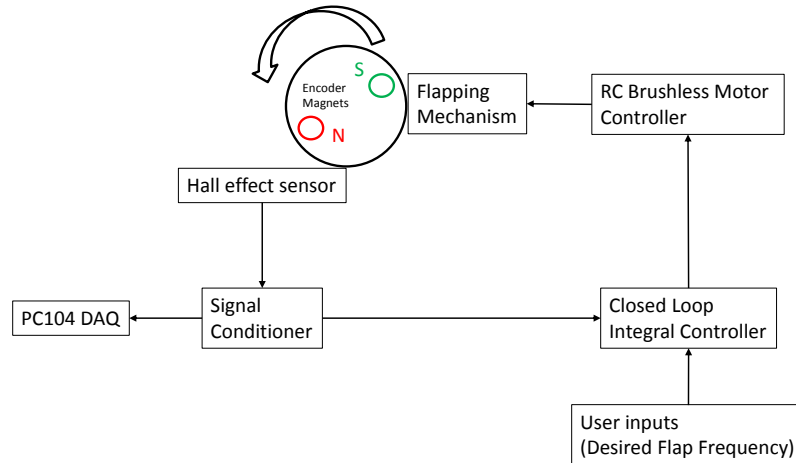


Figure 3.3 Flap governor overview

This arrangement makes it possible to use standard radio control drive components and motor controls which are readily available while allowing the ability to closely govern flap frequency.

3.3.i.b Pressure instrumentation and wing construction

The instrumented flapping wings were built by laminating sheets of thin balsa wood. Pressure readings are taken through ports located on the surface of the flapping wings. The pressure ports correspond to a coarse discretization of the wing surface as shown in Figure 3.4. Measurements at each port provide the differential pressure across the top and bottom surface of the wing at that point and can be simply multiplied by the area around its corresponding wing area and integrated over the wing to provide an estimate of the aerodynamic forces being generated through the flap stroke.

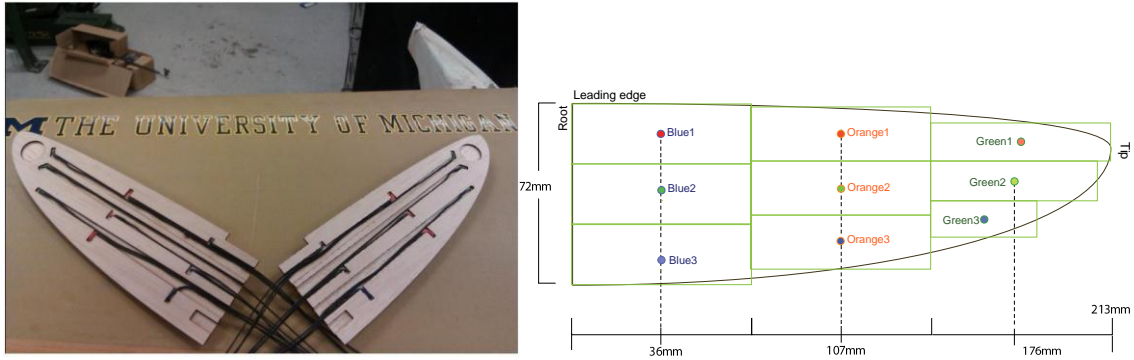


Figure 3.4 Wing construction and embedded pressure port locations

During wind tunnel tests, pressure lines and electrical wiring are routed to two aerodynamic shells located behind the stand which house the embedded computer, data acquisition hardware and pressure sensors. During vacuum chamber tests, the flap stand is mounted inside the chamber and electrical feedthroughs connect the test stand to the embedded computer outside. FT readings are taken using an ATI nano17 six-axis FT sensor to which the flapping mechanics are mounted. The sensor tip is connected to an ATI IFPS-1 interface/power supply unit and the voltages reported by the interface board are read by the AD converter on the embedded computer

3.3.ii VICON testing instrumentation

It is critical that the flap kinematics are tested for stroke accuracy and repeatability. The VICON motion capture system represents an alternate measurement of wing kinematics. By using an array of cameras operating in the near-infra-red spectrum and retro-reflective targets, the VICON system allows the tracking of targets in 3D space to a high degree of accuracy. By considering the drift of static targets, the measurement errors for the experimental set up used were less than 1mm in all axes.

The VICON phase was meant to test the mechanics for repeatability and adherence to their design kinematics. Preliminary testing was carried out in an eight VICON camera environment using large reflective targets available and a set of prototype balsa wings.



Figure 3.5 Large VICON targets on rigid balsa wings

During VICON testing, only the flap mechanics and embedded flap controller modules were used. This represents the simplest test stand configuration. All wing motion data was captured using the VICON system and the results of the validation are documented in a following section.

3.3.iii Vacuum chamber test setup and instrumentation.

For vacuum testing, a larger set of the test stands instrumentation package was necessary. The main data acquisition computer, wing position encoding system and force-torque sensor were used during vacuum tests in order to measure the flapping loads associated with only the motion of the wing structure.

Tests were conducted in the University of Michigan Plasma-dynamics and Electric Propulsion Laboratory (PEPL) 'Junior' vacuum chamber. The pressure was automatically maintained at 8.3torr which corresponds to ~11% of atmospheric pressure. Due to the lack of convection cooling available in a

vacuum, it was determined that the embedded PC104 computer system had to be left outside the vacuum chamber. It was positioned near the floor of the chamber and connected using electrical feedthroughs and specially built wiring harnesses. Through a series of harness tests, it was determined that the FT sensor, magnetic encoder and new infra-red wing position sensor were not adversely affected by the change in wiring scheme for the vacuum chamber set up. These remained available during vacuum chamber tests.

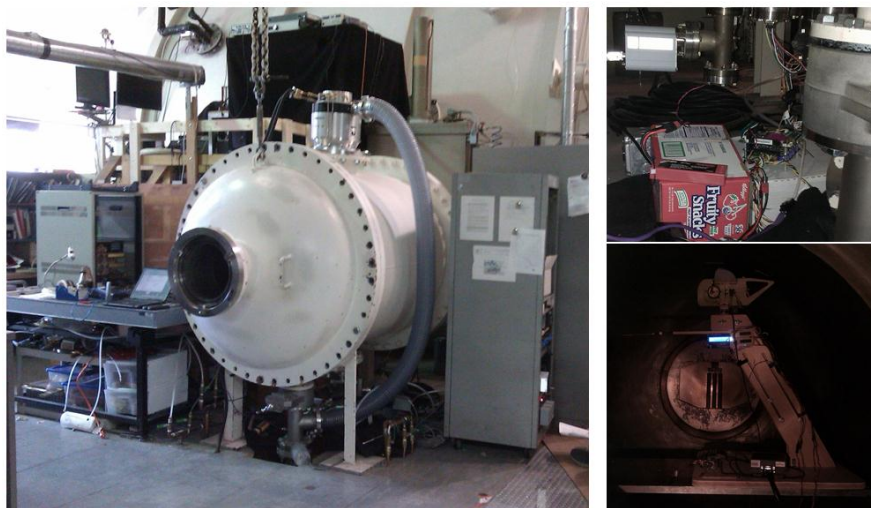


Figure 3.6 PEPL 'Junior' vacuum chamber

The micro-controller based flap-governor and remote interface operate at a lower voltage and it was determined they were in no danger of micro-arcing or overheating under a low vacuum. These components remained mounted on the stand when in the vacuum chamber and facilitated flap frequency control. A Sony TV remote control was used to transmit Infra-red command signals through a viewing port and to the microcontrollers on the flag-governor. This custom built and programmed infra-red remote control system is convenient in a wind tunnel environment but was critical for vacuum chamber testing. With a limited number of electrical feedthroughs, using an infra-red remote allowed changes in the

desired reference flap frequency and operational mode to be made from outside the vacuum chamber without requiring additional wiring. The back-lit LCD screen on the stand also remained in vacuum and provided a real-time display of flap frequency and the status of the closed loop controller which could be read through the viewing port. The schematic shown in Figure 3.7 summarizes the instrumentation configuration used in the vacuum chamber.

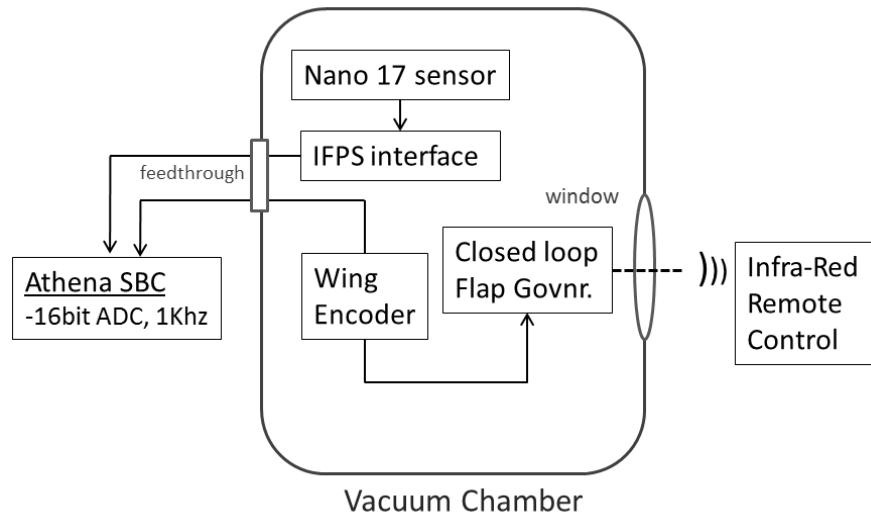


Figure 3.7 Vacuum chamber instrumentation schematic

3.3.iv Wind tunnel test setup and instrumentation

The full set of flap stand instrumentation was used when testing in air. In addition to the wind encoding and force measurements, the pressure measurement system was also operated. Wind tunnel testing was conducted in the UM 5 ft. x 7 ft. wind tunnel. The flapping stand mounted in the test section is shown in Figure 8. While the aerodynamic data system and overall sensing concept is intended for forward flight, tests were first run at hover in order to develop data processing methods before introducing a free stream. The test stand in the wind tunnel test section is pictured in Figure 3.8. In earlier testing, it was noted that the pressure lines exiting the instrumented wing caused significant noise in the force

measurements. As such, a second instrumented wing was built solely for the purpose of taking force measurements.



Figure 3.8 Windtunnel test configuration

Hover data was taken at 3.0Hz, 3.5Hz, 4.0Hz and 4.5Hz. Based on the plunge amplitude of 157mm and frequency, these cases correspond to Reynolds numbers between 3500 and 5500. Some key physical parameters of the flapping wing tests conducted are summarized in Table 3.1.

Table 3.1 Key physical dimensions of flapping wing test cases

Physical Length	Symbol	Value (mm)
Half Span	b	213
Root Chord	C	72
Mean Chord	C_m	61
Plunge Amplitude	h	157

Based on these physical characteristics, the area and mean chord of the wing is computed in the traditional manner for an elliptical planform but the half span is considered when calculating the aspect ratio in this study. In the absence of a free stream, the tip velocity of the flapping wing is used as the reference velocity

when considering the dimensionless numbers. In this paper, the average tip speeds are considered. At hover, the Reynolds number that compares of the ratio of inertial forces to viscous forces for the flow phenomena in question is defined as shown in Equation (3.1) and depends on the flapping frequency through V_{tip} .

$$Re = \frac{V_{tip} \cdot c_m}{\nu} \quad (3.1)$$

When considering unsteady flow phenomena, the reduced frequency offers an indication of how unsteady the flow field around the object is. When considering a flapping wing in forward flight, it can be thought of as a comparison between how quickly flow disturbances are convected by the free stream and the speed of the motion causing the disturbances. However at hover with no free stream, the mean half stroke tip speed of the wing is used as the reference velocity instead, as shown in Equation (3.2). In this situation, the reduced frequency can be thought of more as a comparison between the typical length scale of the flow disturbance and the characteristic length of the object causing it. Since this definition relates tip speed to the mean chord, only the geometry of the wing and stroke kinematics influence the reduced frequency at hover.

$$k = \frac{f \cdot \pi \cdot c_m}{V_{tip}} \quad (3.2)$$

The non-dimensional parameters that represent the flapping tests conducted are presented in Table 3.2. In the following sections, we summarize the current mechanical design, sensor hardware, experimental strategy, data processing methods and present a brief description of experimental results.

Table 3.2 Key dimensionless parameters for flapping wing test cases

Dimensionless Parameter	Symbol	Value
Aspect Ratio	AR	3.75
Thickness Ratio	h^*	0.05
Reynolds Number	Re	$3.5 - 5.5 \times 10^3$
Reduced Frequency	k	0.62

The force measurements in the vacuum chamber from Phase 1 were used in conjunction to those taken in the wind tunnel FT measurement phase (Phase2) to yield a measurement of the aerodynamic loads. By subtracting the inertial loads from the combined air and inertial loads, a history of the aerodynamic forces of the characteristic stroke are obtained. The measurements from pressure ports in Phase 3 allow the reconstruction of pressure history across the wings surface during the test.

3.4 Flapping wing kinematics

The geometry and kinematics of a flapping wing are a critical component of any flapping wing experiment. This section describes the geometry and kinematics of the flapping wings used in in this study. It provides details on the mechanical design and construction of the mechanics, describes a kinematics model and documents VICON motion capture tests that were carried out to validate the flap stroke.

3.4.i Mechanical design and geometry

The first generation flapping mechanism was taken from an actual Cybird flight vehicle [91] and suffered from a fair amount of mechanical free play in both the main wing hinges, as well as backlash in the transmission. This caused wing kinematics to be inconsistent between different test conditions, limiting the ability to compare test and analysis results. Furthermore, the axially oriented transmission and crank arm produced a small phase difference between left-right wing strokes. These observations were consistent with those previously made by Hong and Altman [92] who also used the Cybird mechanism to flap flexible in-house wings and quantify the lift generated by the simplest practical flapping kinematics.

As a commercial alternative was not available to the authors, a revised set of mechanics was designed and built to address both these issues using sturdier parts, and a more rigid triple deck chassis was built with fiberglass plates and steel spacers. A transverse crank configuration used successfully by the hobby industry was adopted. Two sets of main wing bearings are included to support the main root of the wing to avoid torsional deflection along the feathering axis during flapping.

The current stage of this research requires consistent and repeatable mechanics for experimental testing, but with an ultimate goal of creating a flying platform. To facilitate this future purpose, the authors studied wing kinematics that were practical for ornithopter flight. The four-bar crank configuration is sturdy, compact and already flight-proven in existing ornithopter designs. A flapping stroke similar to current ornithopters was realized in this work. It can be adjusted for amplitude and flap angle through the final linkage geometry. The transmission was designed to take advantage of high quality electric motor systems readily available for the hobby industry. The spur gear of the first reduction stage was chosen to mesh with Radio Control hobby helicopter 48-pitch pinion gears common for applications of this size. A six tooth 32-pitch pinion rod was interfaced with this spur gear and used to drive the final crank assembly that also

accommodates a pair of magnets for wing position feedback. The transmission and main chassis are shown in Figure 3.9

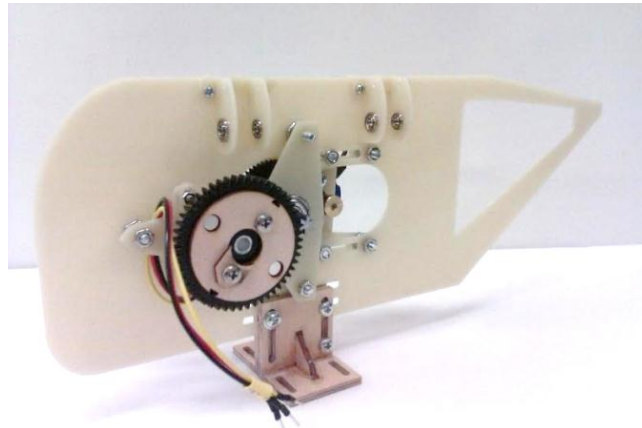


Figure 3.9 Custom designed flap mechanics

3.4.ii VICON motion capture validation of mechanics

The main objective of this test was to confirm that the flap kinematics did not change appreciably at test frequencies between 1Hz and 4Hz and that the rigid wings did not deform when placed under load. For a preliminary test set, seven markers were used and their trajectories in space during a flap stroke are compared across a range of flapping frequencies. The underlying reasoning is that if marker trajectories were the same at 4.3Hz as they were at 0.3Hz, this would indicate that the flap mechanics remained rigid and consistent throughout the anticipated test frequency range. From the results, the mechanics and wing configuration tested were estimated to be consistent within 2% (by flapping angle) across the range of required flapping frequencies. Testing between 0.0Hz and 1.3Hz was not possible with the current power configuration as the drive motor and motor controller combination loses commutation when the mechanics are operated below 1.3 Hz. However, it is unlikely that the mechanics will malfunction between 0.0Hz to 1.3Hz while being able to perform correctly between 1.3Hz and 4.3Hz which the targeted flapping frequency range.

3.4.ii.a Repeatability and consistency Under Load

Ornithopter flapping stroke repeatability and consistency was evaluated using the VICON motion capture system with multiple visual markers placed on each wing. These 'standard' VICON markers weighed approximately 3 grams each and resulted in wing weights of approximately 20 grams. This meant VICON wing weights of approximately 140% of the instrumented test wings. Figure 3.10 and Figure 3.11 show displacement trends over multiple flapping cycles for the two wings, where coordinate X represents fore-aft motion, Y represents lateral motion, and Z represents vertical motion. Collected data shows that marker paths do indeed match within the target frequency range. Overall YZ trajectories of the outboard wing markers are shown in Figure 3.10 for flap frequencies between 1.3Hz and 4.3Hz. Dots of different colors represent paths taken at different flap frequencies and units are in mm. These plots show raw data from complete flap stroke time histories, not averaged flap stroke histories to highlight any inconsistency in mechanism motion or measurement.

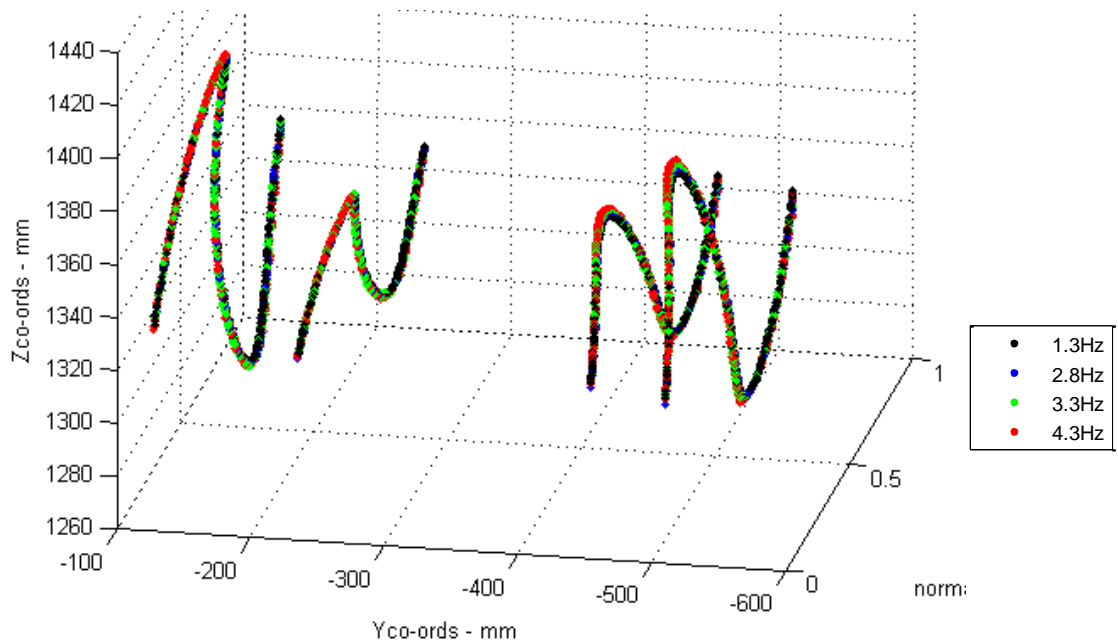


Figure 3.10 Wing marker YZ paths at different flap frequencies

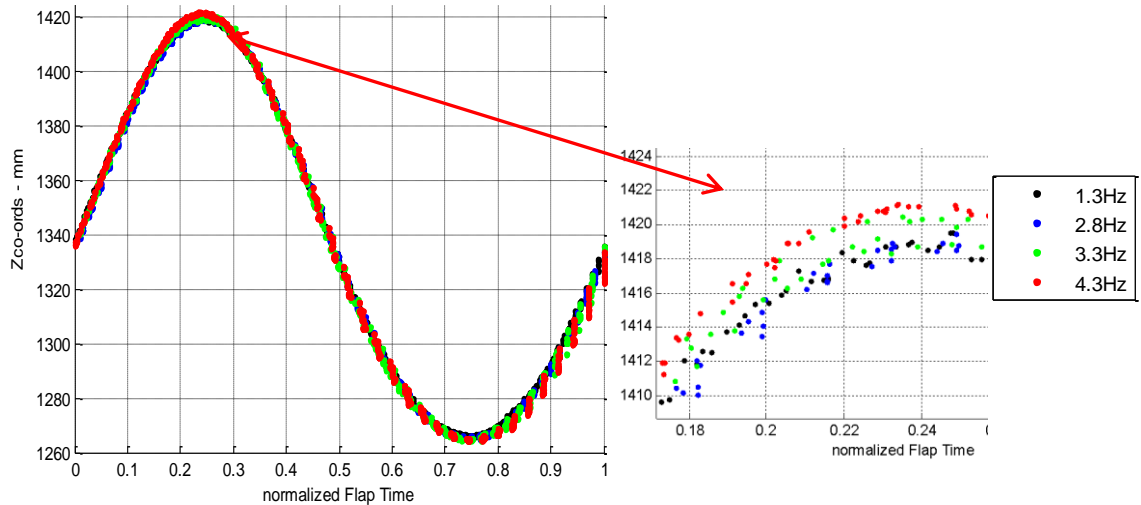


Figure 3.11 Port wing tip-marker Z paths at different flap frequencies, with expanded view of maximum deviation during the stroke.

3.4.ii.b Absence of unintended deformation along the feathering axis

Another concern was wing root deformation along the feathering axis introducing a pitch motion, as was encountered with previous mechanics. To estimate the severity of this kind of deformation in the current mechanics, the change in phase difference between leading 'fore' and 'aft' VICON markers on the wings were compared at multiple flapping frequencies. In a stroke where only the flapping angle changes, the phase difference between fore and aft markers should remain constant. These tests were run up to a higher frequency of 4.3Hz to check for deflection along this axis. In Figure 3.12, Z-axis paths for fore-aft markers do not deviate in phase with increasing frequency, suggesting that changes in phase difference is negligible going from 1.3 to 4.3Hz.

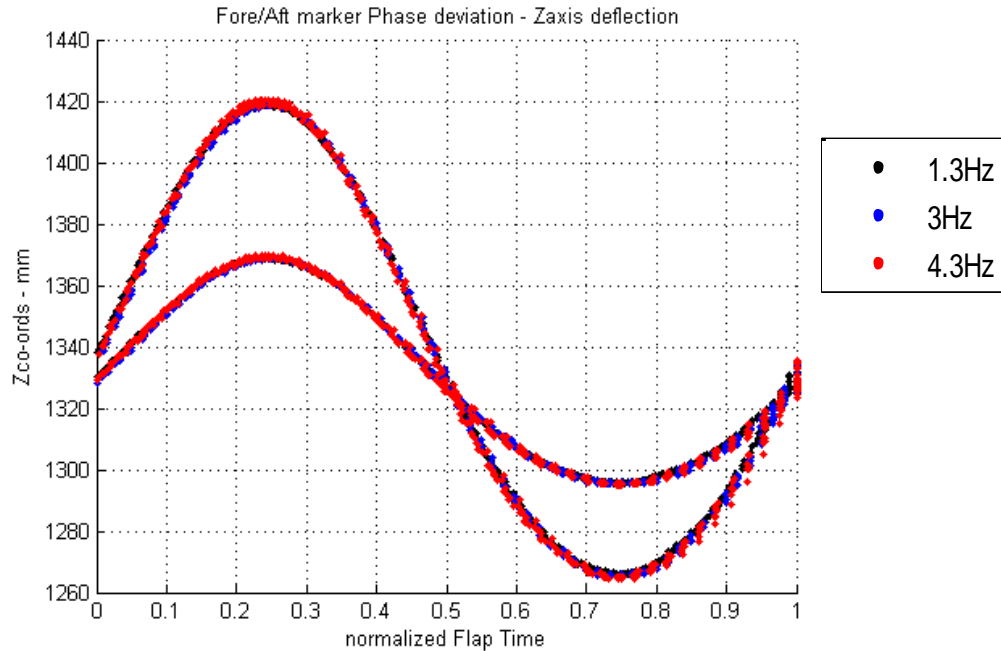


Figure 3.12 Port wing fore/aft marker phase difference remains constant between 1.3Hz and 4.3Hz

3.4.iii 3D Linkage solver and comparison to VICON data

During the mechanical design process, a 3D linkage code was written to provide wing flap angle as a function of crank position. This code was used for initial sizing of the components and during simulations it was used to predict actual wing kinematics produced by the final linkage geometry. A sample output of the 3D linkage solver is presented in Figure 3.14 shows a comparison of compiled flap angle histories calculated using VICON marker position data and the output from the linkage solver. This comparison experimentally validates the kinematics solver over a stroke, and the assumption that crank rotation rate is constant throughout the flap cycle. On the previous Cybird mechanics, the transmission could not produce sufficient torque, resulting in an upstroke that was significantly slower than the down-stroke due to the mechanics struggling to lift the wings.

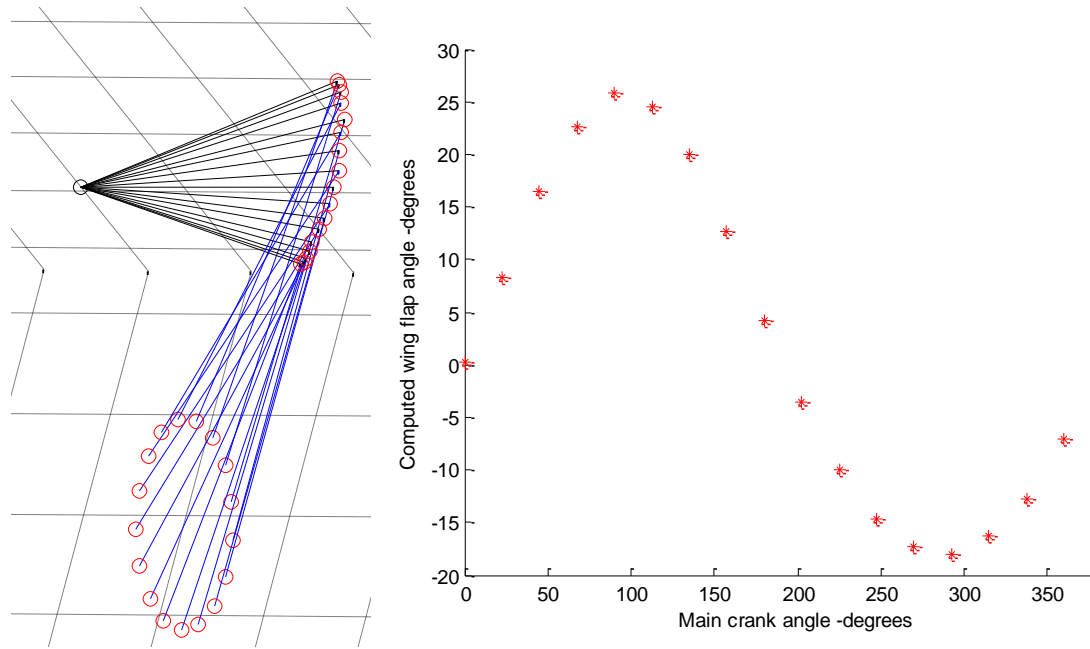


Figure 3.13 Sample linkage solver output with 17 crank steps for clarity showing crank positions with red dots and wing positions with black lines(Left). Corresponding computed wing flap angle output at given crank positions (Right).

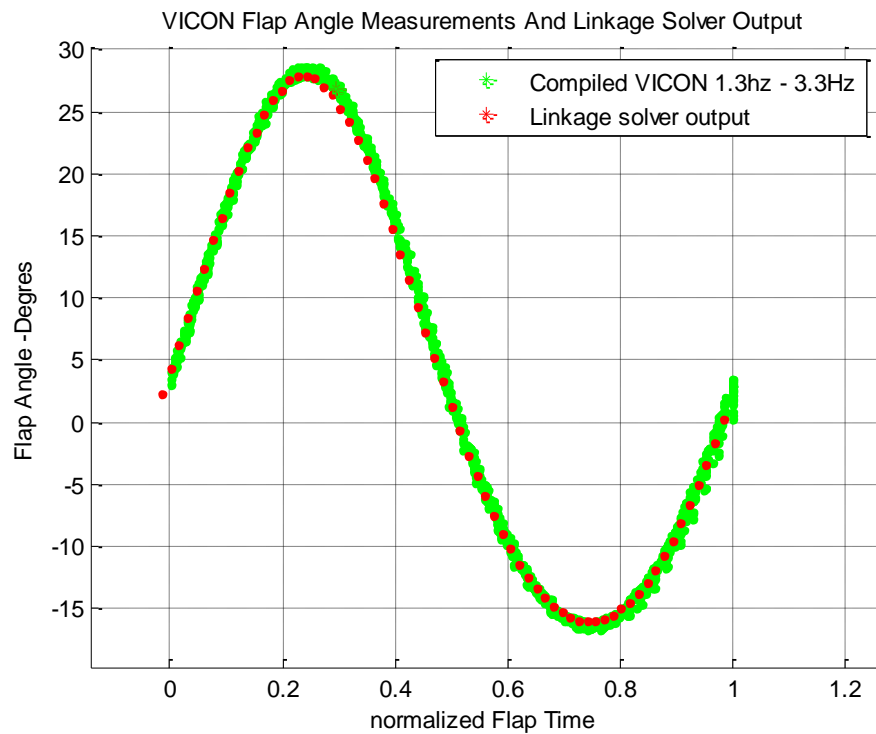


Figure 3.14 VICON and 3D linkage solver stroke comparison

As can be seen above in Figure 3.14, predictions and VICON measurements match. Again, the maximum error is considered. When compared to the baseline 1.3Hz VICON run, the maximum measured error encountered at the top was found to be ~ 0.3 degrees, or less than 1% of full angular deflection. This consistency in phase indicates there is no appreciable loss of actuation rate on the upstrokes and that the transmission in the current mechanism produces sufficient torque for the system.

3.5 Multi-phase experimental characterization of loads

3.5.i Vacuum chamber measurements of inertial loads

Two frequency sweeps were carried out before and immediately after the chamber had been vented to offer a first order check of the results. Due to the tight wall clearances between the vacuum chamber test section and the wing tip path, this set of hover results were not considered to be reliable and was only used as an immediate, first check of the Vacuum results. The plots in Figure 3.15 show averaged vertical force (F_z) histories from the 4 different flap frequencies when in vacuum and at 1 atmosphere. The convention used was for positive vertical forces to be in the direction that created lift in the body frame of the mounted vehicle. These were post-processed using a 6th order Butterworth Low Pass Filter implemented in Matlab with a cut off frequency of double the flap frequency. The selection of these filter settings are discussed in the following data analysis section. While the loads are very similar, there are distinct differences between the vacuum and air measurements at the ends of each half-stroke which showed that the chamber did indeed go into a vacuum and the tests provided a different set of results. With the chamber at 1atm, it was noted that the recorded loads showed slightly increased peak magnitudes and a slight change in phase due to aerodynamic effects. It can also be noted that due to the asymmetric flap stroke, the resulting inertial loads are not symmetric either, with a flatter upward force peak in the second half of the stroke.

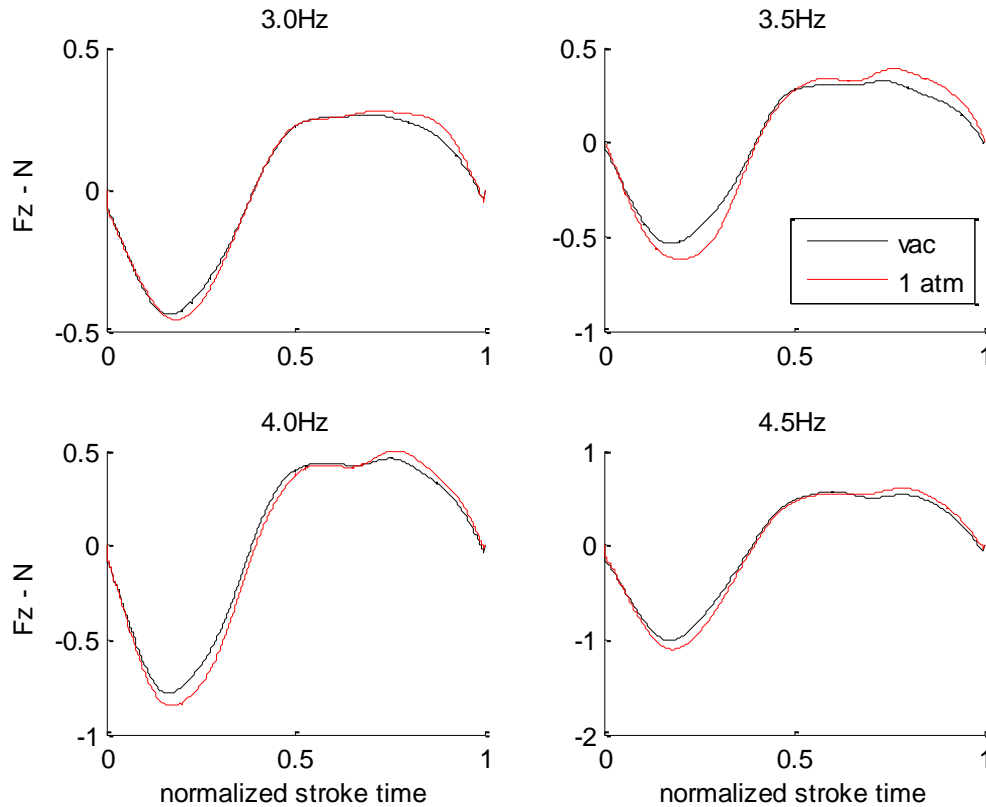


Figure 3.15 Vacuum chamber data overview

3.5.ii Wind tunnel vertical force and pressure measurements

Hover data was taken at 3.0Hz, 3.5Hz, 4.0Hz and 4.5Hz. Based on the plunge amplitude of 157mm and frequency, these cases correspond to Reynolds numbers between 3500 and 5500 as described earlier. A set of sample results at 4.0Hz are shown in Figure 3.16 where the vertical force measurements are compared against those taken in vacuum on the left. On the right hand side, the pressure port readings throughout the characteristic stroke are shown. The blue, orange and green ports represent pressures from the most inboard, mid-span and most outboard span-wise sections respectively. On each span-wise location, red, green and blue dots denote pressure from the leading edge, mid-chord and trail-edge pressure ports.

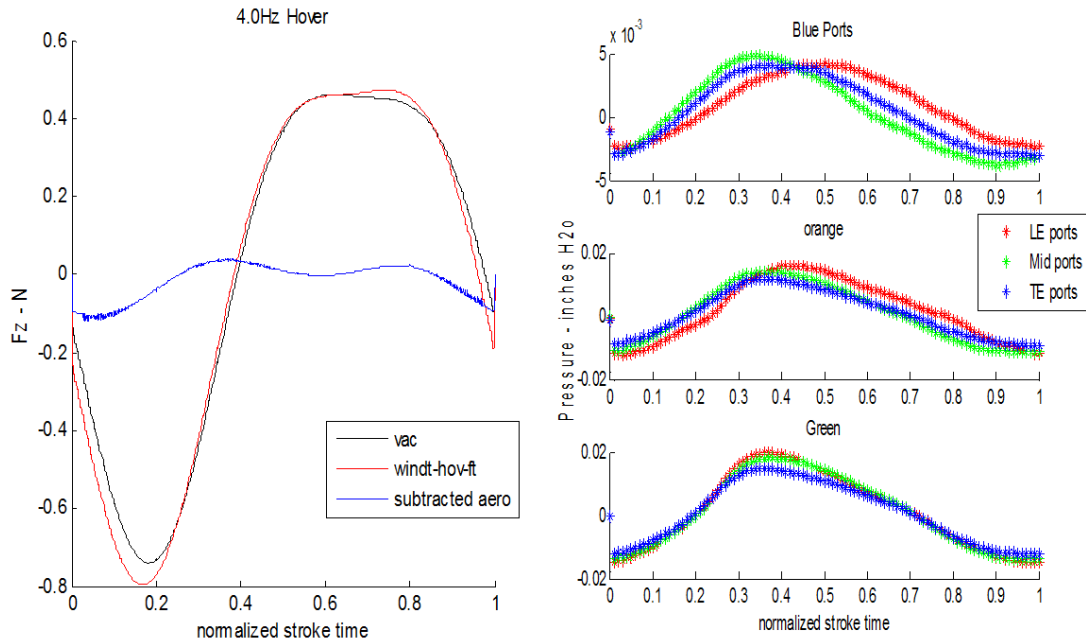


Figure 3.16 Sample wind tunnel force and pressure measurements – Hover

The force measurements in the vacuum chamber from Phase 1 were used in conjunction to those taken in the wind tunnel FT measurement phase (Phase2) to yield a measurement of the aerodynamic loads. By subtracting the inertial loads from the combined air and inertial loads, a history of the aerodynamic forces of the characteristic stroke are obtained. The measurements from pressure ports in Phase 3 allow the reconstruction of pressure history across the wings surface during the test based on the pressure port locations and a coarse discretization of the wing as described in Section III. These pressure measurements are integrated for a second estimate of the aerodynamic loads during a characteristic stroke. The data processing methods used are described in more detail in the following sections.

3.6 Experimental data processing and analysis

This section describes both the data processing techniques used to facilitate a comparison of the pressure based force histories to those recorded by the force-torque sensor. For the force torque sensor, the determination of filter settings and the ensemble averaging technique used to obtain single-flap histories from each part of the multiple phase test process is described. The processed single flap

histories from vacuum chamber and wind-tunnel tests are subtracted to provide aerodynamic force measurements. A schematic depicting how the force-torque data is processed is shown in Figure 3.17

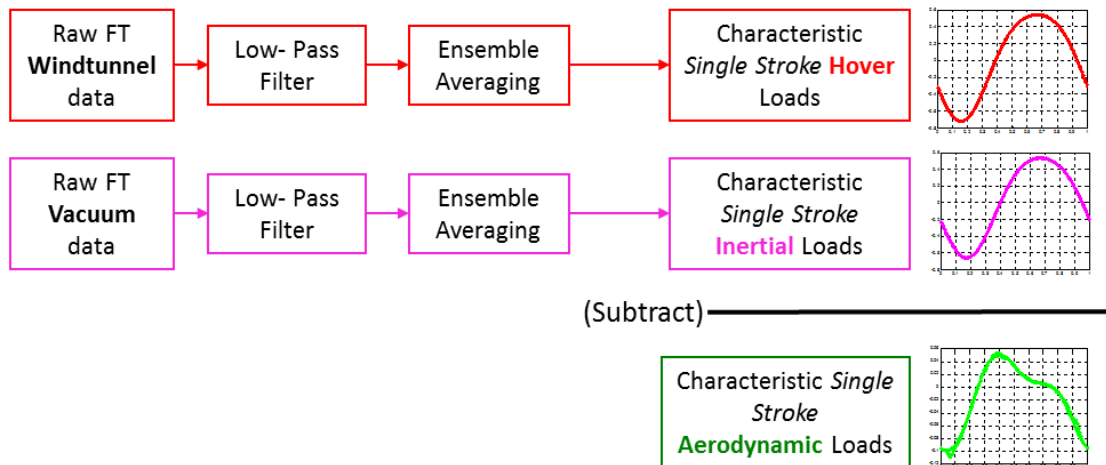


Figure 3.17 Force-Torque sensor data processing for aerodynamic loads

The ensemble averaging technique for raw pressure measurements is then described along with the method used to estimate aerodynamic loads from the pressure measurements. Finally, the two are compared in order to validate the pressure based approach to estimating aerodynamic loads.

3.6.i Force-Torque sensor data – frequency domain analysis

The measurements taken by the Force Torque sensors include contributions from the structure including structural modes of the flapping wing vehicle and the test stand itself. In order to take measurements of the aerodynamic forces alone, these structural contributions that arise from the test stands structural response need to be separated from the overall signal. With force data acquired from vacuum and air, a frequency domain analysis of measurement signals was carried out to document the various periodicities present in the data. By comparing the data between multiple cases in different test environment, the causes behind the different periodicities can be identified. The results of this analysis were used to establish the post processing filter parameters for the data. Once modes are determined to be the result of the flapping motion, test stand

structural response, or the aerodynamics, appropriate filter settings that exclude unwanted effects can be selected. As vertical forces are the primary measurement for this analysis, the power spectrum of the Z axis force component was considered in processing all data.

3.6.i.a Test stand structural response – vacuum data only

First, periodicities associated with the flap stands structural response were sought. To get a basic idea of what flapping related data could be expected to look like, an ‘analytical version’ of the test was run using the simulated kinematics from the 3-dimensional linkage solver written for the test mechanics. Since the flapping kinematics are accurately represented by a 4th order Fourier fit, 4 peaks are expected and this is shown in the spectrum (Figure 3.18) below for 4.5Hz. It was noted from the baseline power spectrum that the contribution from the 4th mode is relatively small compared to the first three.

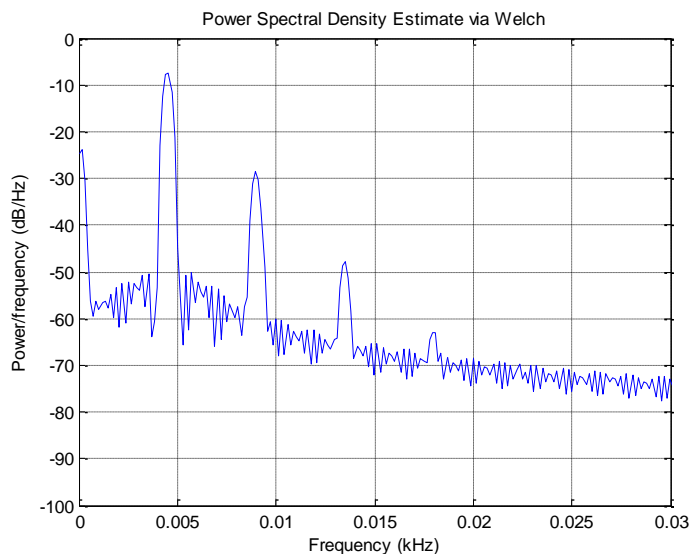


Figure 3.18 Sample hover power spectrum - Simulated test run at 4.5Hz

The power spectra of data taken in a vacuum at different frequencies were then generated using the pwelch function in Matlab which uses Welch’s method to compute the power spectral density of a given signal. These experimental spectra were compared to the simulated version and it was noted that the four

peaks at multiples of the flapping frequency seen in the analytical case were not generally encountered in the experimental data. Shown in Figure 3.19 are two sample power spectra of the vertical force component in vacuum. Only the first two were apparent in all test cases. From the data, it also appeared that a set of three periodicities at higher frequencies about 8 times the flap frequencies were present. However, these did not turn out to always be at frequencies that were multiples of the main flap frequency. Since no significant aerodynamic forces were present in vacuum, only periodicities up to 4 times the flap frequency are expected due to the kinematics. As such, these periodicities at high frequencies were determined to be due to the structural response of the flap stand and needed to be filtered.

More care was taken in considering a periodicity that was noted at approximately 14Hz. It appeared to be the result of the flap stands response but it was not always apparent. It was possible that it was a mode of the flapping forces. 14Hz and could have simply been the 4th harmonic from the flapping stroke when flapped at 3.5Hz or close to the third harmonic at 4.5Hz. However, from the analytical case the peak resulting from the 4th harmonic is small compared to the third harmonic and a 3rd flapping harmonic was never observed unless it coincided with the 14Hz mode in question. When operating at 2Hz, the peak at 14Hz was also observed even though 14Hz is too high to be related to the main flapping frequency. Based on these two observations, it was thus considered

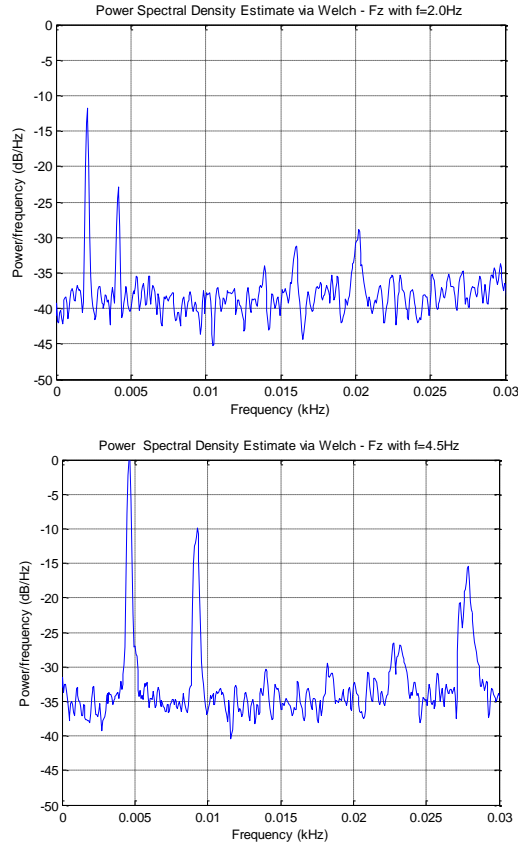


Figure 3.19 Sample power spectrum comparison between flap frequencies in vacuum: 2.0Hz top, 4.5Hz bottom

likely that the mode at 14Hz was due to the structural response of the test stand. The modes observed throughout a frequency sweep in vacuum are summarized in Table 3.3. Due to the non-flapping related mode at 14Hz, it was determined that a low pass filter with a cut off frequency that was lower than 12Hz would be needed in order to remove the contribution of test-stand structural response from the inertial force torque measurements. While a filter cut off frequency of 4 times the flap frequency was thought to be necessary to preserve all information, the contributions of the 3rd and 4th harmonic did not appear to be significant in practice, suggesting that no major flap force information was contained within the raw data at frequencies 3 and 4 times the flap frequency. A filter cut off that was 2 times the flap frequency was chosen for all the vacuum chamber cases.

3.6.i.b Identification of modes caused by aerodynamic forces – comparing air and vacuum data

It was anticipated that aerodynamics might contribute to periodicities at higher frequencies than the main flap frequency. It is necessary to identify these modes so filter settings that do not interfere with aerodynamic data can be chosen around them. In order to identify modes due to aerodynamics, power spectrums for air and vacuum data taken at the same flapping frequency are compared and additional modes in the air cases are sought. However, it was found when comparing the power spectrums of tests run in vacuum and in air that no additional peaks were discernible when aerodynamic forces were present. It was determined that no additional ‘aerodynamic modes’ were apparent and that filter settings for the vacuum and air data could be the same. For the data presented in this paper, a low pass filter with a cut off frequency of 2 times the main flap frequency was used for both in-air and vacuum cases. A sample comparison at 3.0Hz is shown in Figure 3.20.

Table 3.3 Observed PSD peaks in vacuum Force-Torque data with flap-stand structural mode at 14Hz

Flap Freq	Mode Freq						
2.0Hz	2.075	4.15	13.9	16.05	20.2		
2.5Hz	2.63	5.19			20.32	25.3	
3.0Hz	3.17	6.29			21.12	24.05	
3.5Hz	3.48	6.96	13.92			23.25	26.73
4.0Hz	4.08	8.3	12.39	16.48	20.81	24.96	
4.5Hz	4.58	9.27	13.98	18.19		23.19	27.83

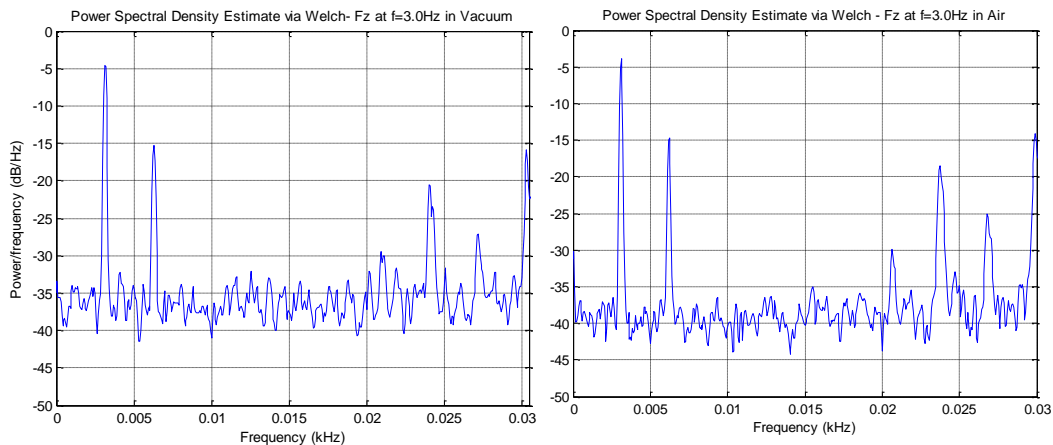


Figure 3.20 Sample power spectrum comparison at 3.0Hz in Vavuum (top) and in air (bottom) - No additional modes in air

3.6.i.c Ensemble averaging process for force measurements

For each test case, the mechanism was flapped for an interval of 30-40 seconds to allow multiple flap cycles to be captured. The force measurements are then filtered using a Butterworth filter implemented in Matlab with a low pass cut-off that is two times the flap frequency based on the analysis described in the preceding section. Data from the magnetic encoder was used to identify individual flap strokes and split the filtered force data set into multiple single-flap measurements. A time scale is then used to establish along a normalized period and the data from each trial is overlaid on this temporal grid. If test data was not available at a particular point in time along the normalized period, a linear interpolation between neighboring points was used in its place. The result of this is a normalized flap period with each point in time containing a number of measurements from the number of flap cycles captured. These sample populations are then used to determine the statistics at each point in the normalized period assuming a normal distribution. A sample result is shown in Figure 3.21 showing the differences in error as more flaps are used in the data. The blue dots denote the 95% CI around the ensemble averaged values. The plots along the bottom show the diminishing width of the 95% confidence interval

as the number of flaps considered is increased from 4 to 138. When generating the following plots, the normalized time scale is split into 100 intervals for clarity.

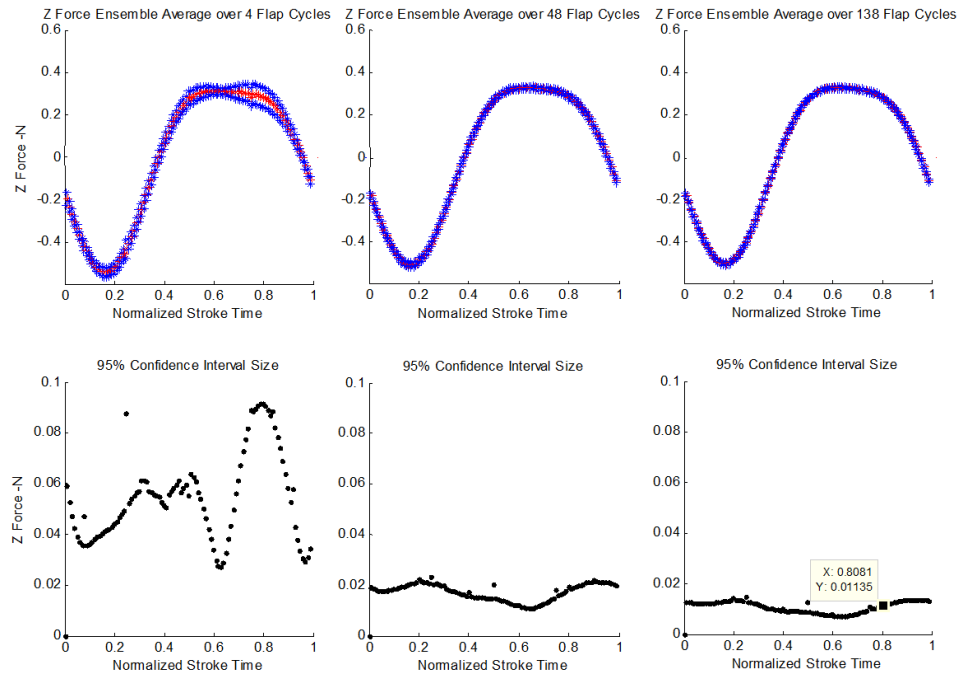


Figure 3.21 Ensemble Averaging Process for Force/Torque data and 95% CI - 3.5Hz in vacuum

3.6.i.d Verification of single-stroke aerodynamic force history using cycle averaged forces

In combining the data from three different tests, a number of challenges were encountered in obtaining the best measurement of aerodynamic forces. Most significantly, small errors in phase synchronization between the cases when subtracting loads between the vacuum loads from wind tunnel loads could lead to large errors in aero force estimates. For example, a 3% phase error could lead to complete reversal of aerodynamic force histories due to the nature of the load subtraction process. The plots in Figure 3.22 Importance of correct encoder offset - 3.0Hz depict the effect of a small change in encoder timing on the resulting aerodynamic estimates.

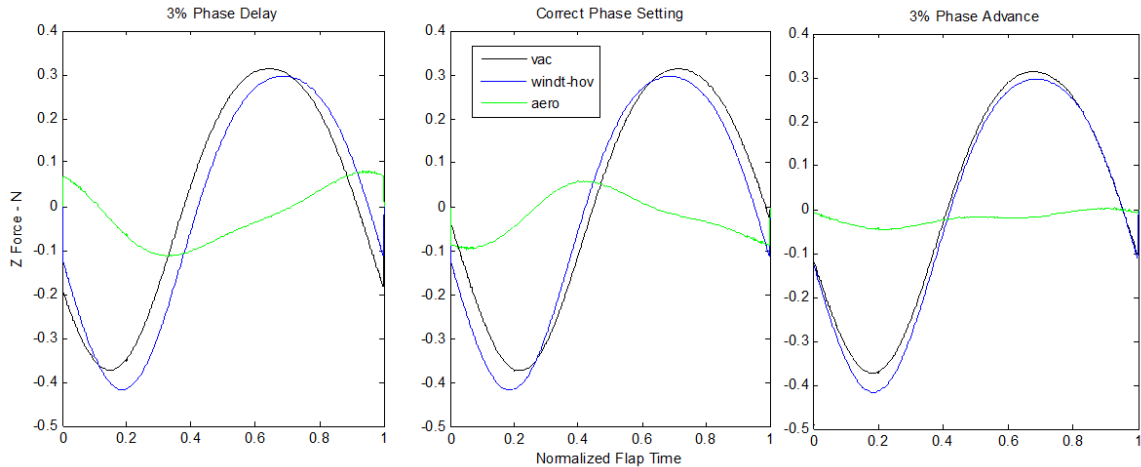


Figure 3.22 Importance of correct encoder offset - 3.0Hz

In order to provide a secondary means of verifying the subtracted aerodynamic force data is consistent with the forces measured in air and in vacuum, cycle averaged forces were considered. Since the cycle average force measurements of the raw data taken over a long period are less dependent on filter settings and potential encoder offsets, they offer a more reliable alternative measurement with which to evaluate the single-stroke results and to ensure that the force measurements are consistent with themselves.

The unfiltered data was first used to compute the average vertical force in either test case. The average force in a vacuum throughout the total number of flaps was subtracted from the average force in air to provide an estimate of the cycle averaged aerodynamic force for that flapping frequency. This was then used to verify that the subtracted single-cycle aerodynamic loads resulted in the same cycle averaged aerodynamic loads from the subtracted aerodynamic load histories. This technique verified that the flap cases run at the four frequencies provided an accurate estimate of single-cycle aerodynamic forces that were within 5% of the cycle averaged measurements. The resulting data from this comparison is compiled in Table 3.4 Cycle averaged and single-stroke aerodynamic force errors

Table 3.4 Cycle averaged and single-stroke aerodynamic force errors

	Fz Averages					
Freq	Windtunnel	Vac	Target air-vac	Offset	Single Flap Final	Error
	(N)	(N)	(N)	(ms)	(N)	
3.0Hz	1.411E-02	5.795E-03	1.991E-02	vac-0	2.07E-02	~4%
3.5Hz	-3.153E-04	-6.642E-03	6.327E-03	vac-0	6.47E-03	~2%
4.0Hz	2.660E-04	-1.553E-02	1.580E-02	vac-0	1.52E-02	~4%
4.5Hz	-2.112E-03	-8.646E-03	6.534E-03	vac-0	6.46E-03	~ 1%

3.6.i.e Confidence Intervals on subtracted aerodynamic loads

While an error analysis is important in any experiment, the challenging nature of obtaining a measurement of the aerodynamic force from two sets of data from two completely different environments made an investigation of the errors more critical. The test stand and pressure measurement system are intended for forward flight conditions such as those presented in previous work [91]. The aerodynamic loads encountered at hover are much smaller and approach the resolution of the ATI Nano 17 sensor. Further, the data from two different test runs are combined so the error of both individual test runs must also be combined. If the interval of uncertainty around the measured aerodynamic force estimates were too big relative to the data itself, the usefulness of the test setup would need to be reassessed. The statistics of each set of FT measurement results are computed at each point in the normalized characteristic stroke by considering the total number of data points available and assuming a standard distribution. In this manner, the standard deviation is computed for each point in the characteristic average stroke from wind tunnel test and vacuum chamber tests. When the inertial loads are subtracted, the standard deviations are added. The combined standard deviation can then be used to provide an estimate of the

confidence interval around the final data point. The two plots in Figure 3.23 present the standard deviation intervals encountered from different parts of a normalized flap stroke. The plots in Figure 3.23 present data from the two slower cases which have the two biggest relative standard deviation intervals. This is due to smaller overall measurements and sample sizes during test runs of fixed duration. Even so, the average trends and magnitudes are not obscured when surrounded by the standard deviation interval. This suggests that the hover data yielded reasonable error statistics despite previous concerns about sensor performance at the lower aerodynamic forces encountered at hover.

3.6.ii Pressure based aerodynamic force estimation

Pressure data was compiled in a manner described in previous work [93] by the authors. Due to the large volume of relatively consistent raw pressure data, a simple spatial and temporal averaging scheme was used to form the pressure history of a characteristic flap stroke. This technique accounts for slight phase time offsets between individual flap strokes and was amenable to an error characterization. More details on the process used can be found in [93]. A typical set of pressure histories is shown at $f=3.5\text{Hz}$ in Figure 3.24. As mentioned above, the blue, orange and green ports represent pressures from the most inboard, mid-span and most outboard span-wise sections respectively. On each span-wise location, red, green and blue dots denote pressure from the leading edge, mid-chord and trail-edge pressure ports.

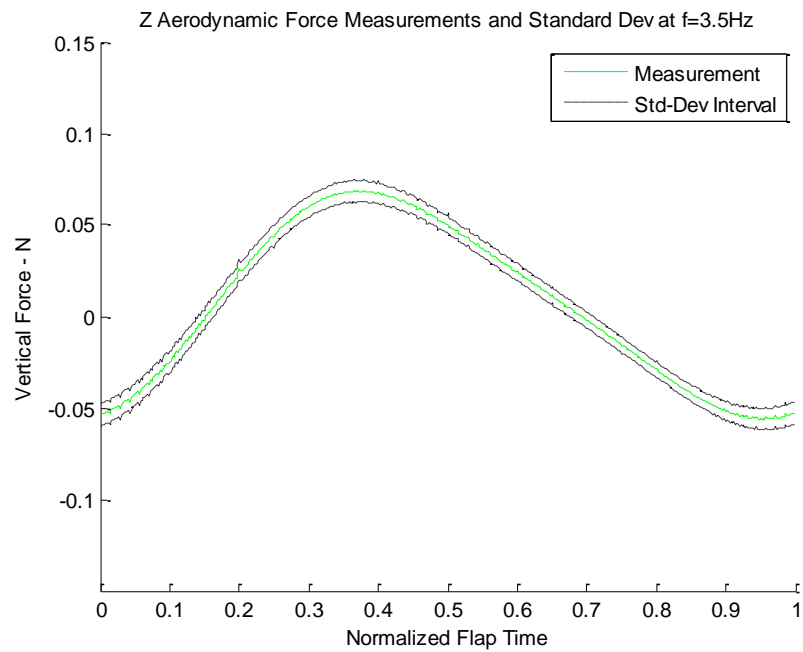
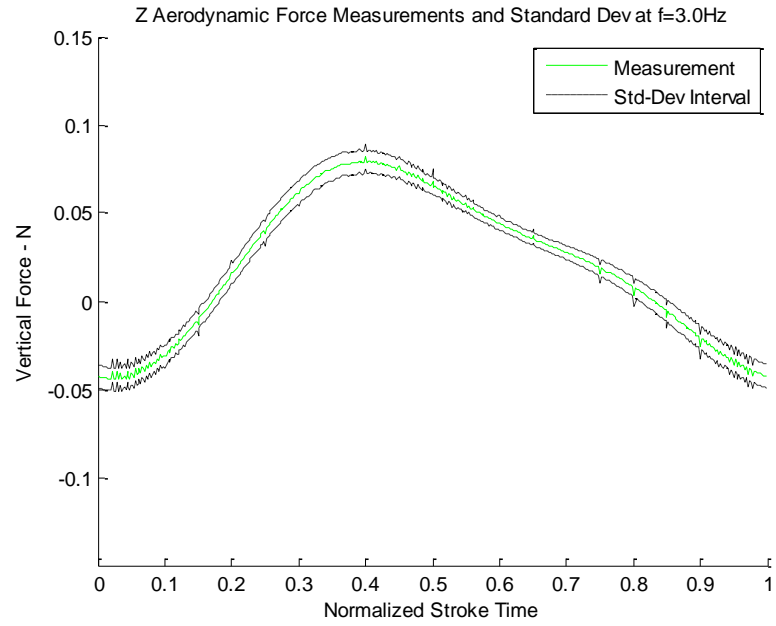


Figure 3.23 Standard deviation intervals on subtracted aerodynamic load measurements - $f=3.0\text{Hz}$ and 3.5Hz

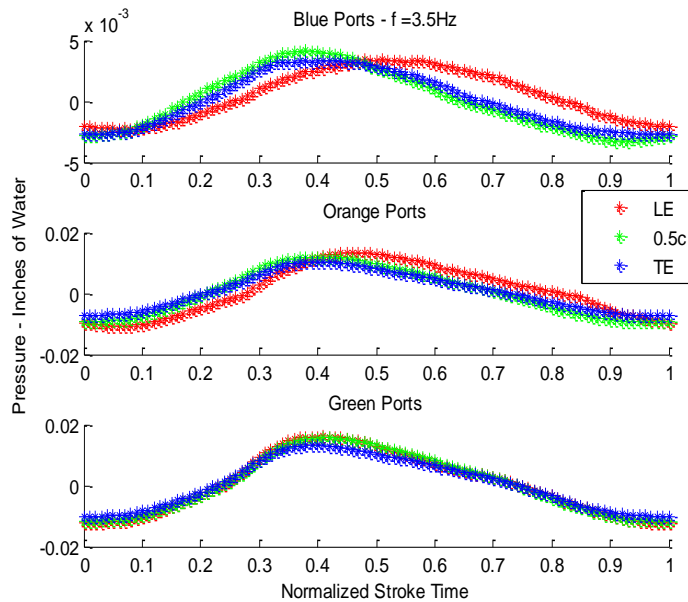


Figure 3.24 Examples of pressure measurements over left wing in hover :
 $f=3.5\text{Hz}$

It can be noted that the pressure distributions do not show appreciable variation between leading edge, mid-chord and trailing edge wing locations. This indicates the absence of leading edge suction. From previous sets of forward flight pressure results [93], leading edge suction is indicated by the red dots indicating data from the leading edge ports reporting larger pressure magnitudes throughout the stroke. This observation corresponds to our expectation of fully separated flow across the wing at hover and the current set of data is consistent with measurements taken during previous tests. Estimating aerodynamic loads using these pressure measurements is straightforward as the wings used are rigid and the stroke kinematics known. Since the motion is a pure flap, the orientation of the wing surfaces is also always known. As described in section III, the pressure ports give measurements of differential pressure across the surface of the wing these are easily integrated across the coarse grid and resolved based on the flap angle of the wing. A compilation of the aerodynamic force histories for the four test cases are shown in Figure 3.25. It can be seen that the magnitude of the pressure forces increase with frequency as expected. At each frequency, a

kink is observed at approximately $t=0.75$. This is due to the non-symmetrical flap stroke and is an expected trend.

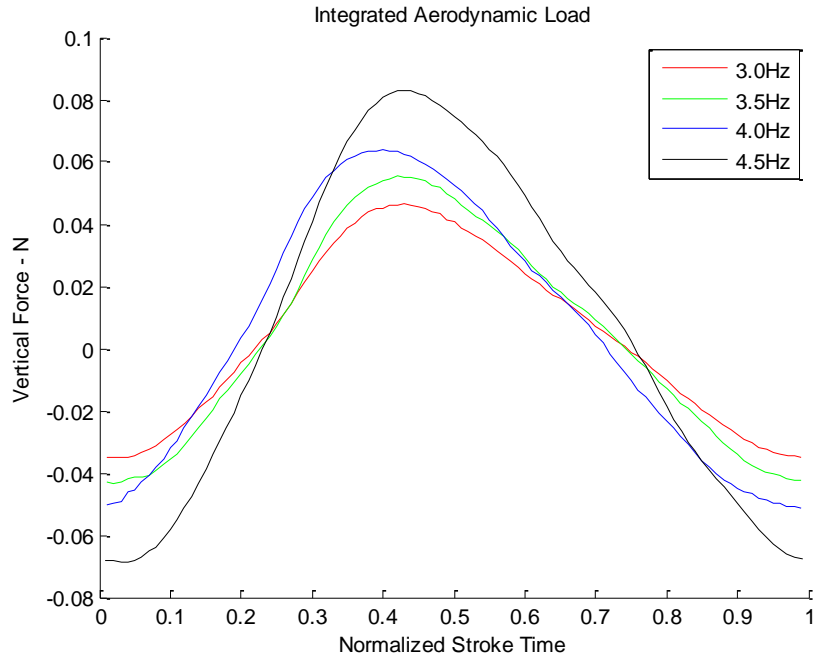


Figure 3.25 Aerodynamic force estimates based on pressure measurements

Aerodynamic force coefficients for the lowest and highest frequency cases are plotted in Figure 3.26. When normalized by averaged tip speed, the force coefficients become independent of flap frequency. This trend is expected as the forces due to dynamic pressure scale with tip velocity squared, which is in turn proportional to frequency. The experimental results demonstrate this independence, verifying that the pressure instrumentation is functioning consistently throughout the flapping frequency range.

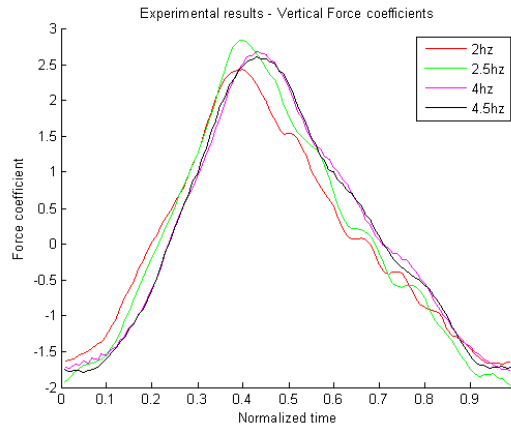


Figure 3.26: Pressure based measurements of vertical aerodynamic force coefficients

In order to experimentally verify the ability of the pressure based aerodynamic feedback system, measurements of the same vertical force taken using the ATI FT sensor need to be compared and checked for agreement to these pressure-based estimates. The techniques used to process the force measurement data from the vacuum chamber and wind tunnel tests are documented in the following sections.

3.6.iii Comparison of pressure based estimates and force sensor aerodynamic force measurements

One requirement of an aerodynamic feedback system is the ability to provide a real time estimate of the aerodynamic loads. In working towards this goal, it is first necessary to ensure that the pressure based estimates can provide results comparable to those obtained using a multiple phase test procedure involving the characterization of inertial loads in a vacuum. In order to assess the viability of the pressure based aerodynamic sensing system, single stroke Z force history measured using the FT sensor and estimated using the pressure measurements need to be compared. The data presented in the following comparisons are

generated with the wing phase shown in Figure 3.27. The normalized stroke begins with the wings crossing their midpoint flap angle while on their upstroke. At about $t=0.25$, the wings reach their top most position and begin their down stroke. Due to asymmetry in the stroke, the wing decelerates more slowly at the bottom of the down stroke and spends more time in its bottom position between $t=0.7$ and $t=0.8$ before finally beginning the upstroke again.

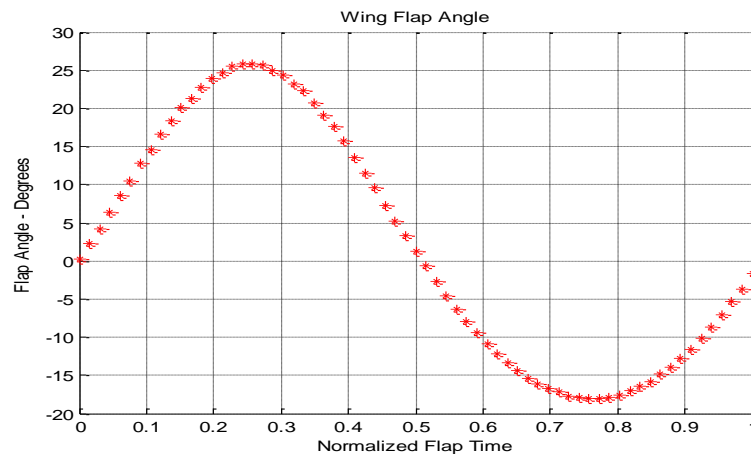


Figure 3.27 Wing kinematics - Positive flap angles denote wings above level

3.6.iii.a Long pressure line force comparison – hover

The first step in the process was to directly compare the best-guess results of force torque measurements to the filtered pressure measurements. Results from the first test set up are overlaid in the plots comprising Figure 3.28. From the comparison, it can be seen that the pressure based estimates exhibit similar trends and track the measured vertical forces. At $t=0.7$ a change in slope of aerodynamic loads are encountered in both sets of data. At the same time, distinct differences are apparent. The magnitudes estimated by the pressure based aerodynamic data system are smaller compared to those reported by the force measurements. There is an approximate 10-15% phase lag in the pressure estimates for the test cases. This suggests that a certain amount of information is indeed being lost by the pressure based estimates as only aerodynamic forces can explain the difference between the cycle-averaged forces in air and in

vacuum. Since the pressure instrumentation appears to correctly track the forces being generated, these results suggest that the pressure measurement system has the ability to provide a basic estimate of aerodynamic forces and is feasible but requires further investigation.

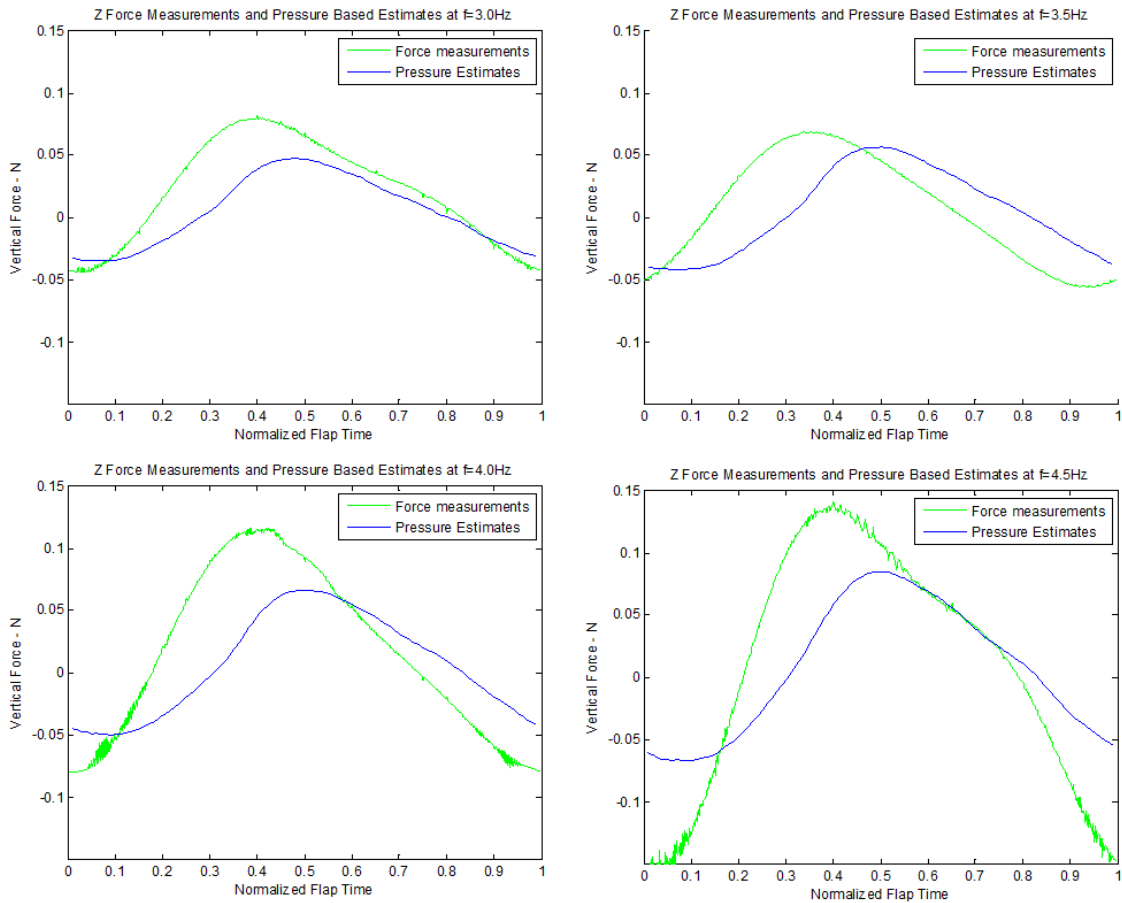


Figure 3.28 First comparison of FT sensor measurements and pressure based force estimates

As the calibration of the pressure and force instrumentation has been checked for agreement using a steady fixed NACA wing test case for reference, a calibration error is not expected to be the cause of the observed discrepancies.

The most probable cause is thought to be the length of the pressure lines used. Due to the large volume of air in them and the relatively small pressure port size on the wing, the pressure lines behave like a physical low-pass filter. It was

thought that this low-pass filter effect in the pressure lines would explain the differences in trend and the smaller predicted force magnitudes.

3.6.iii.b Second comparisons with shorter pressure line lengths

To explore this possibility further, a second set of hover data was taken with the pressure lines shortened from 1.3m to 0.3m as a pre-cursor to a short set of test runs with different pressure line lengths. In order to facilitate these new pressure line lengths, the pressure sensor tray had to be temporarily moved from its designed position behind the flap stand and attached on the back of the main arm. It was hypothesized that if the discrepancies were due to this physical mechanism, the dramatic reduction in pressure line length should allow the aerodynamic predictions to more closely match the modified force measurements. The results of this comparison are shown in Figure 3.29. When a short pressure line length is used a noticeable improvement in phase error is observed. This is accompanied by larger magnitudes predicted by the pressure based measurement system and a better overall match throughout the test cases.

The second comparison supports the hypothesis that the additional low-pass filter effects explained some of the main discrepancies observed when using the original flap stand setup. This result indicates that the current pressure measurement system is capable of estimating aerodynamic loads in a general manner and the approach is feasible. This second set of results is presented in Figure 3.29. Both sets of force histories are sinusoids with phase matching within 3% for all but the 3.5Hz case which showed agreement within 7%. Positive lift peaks matched within 8% for all except the 3.0Hz case, which showed a large deviation of 20%. Negative lift peaks agreed within 9% except for the 4.5Hz case which showed a significant 35% discrepancy that is most likely due to increased flap stand vibrations affecting the force measurements. These points of comparison are summarized in Table 3.5 with outliers highlighted in red.

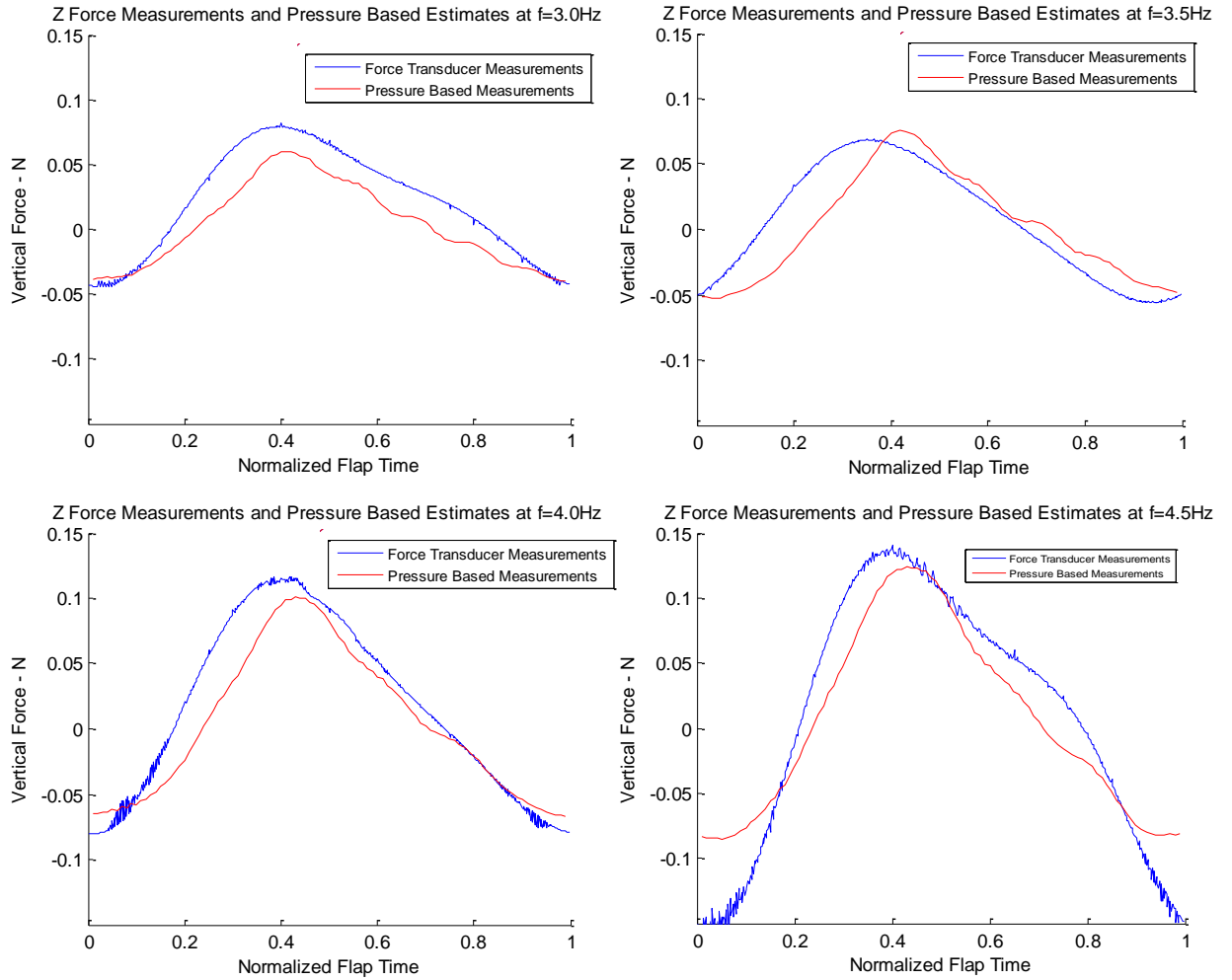


Figure 3.29 Comparison of vertical aerodynamic force measurements at hover

Table 3.5: Peak force and phase comparison

Flap Freq	Percentage Error		
	Pos Peak %	Neg Peak %	Phase %
3.0Hz	19.5	8.2	0.6
3.5Hz	5.2	2.3	6.8
4.0Hz	7.8	8.9	2.6
4.5Hz	7.6	35	3.0

Despite the challenge of measuring relatively small aerodynamic loads and comparing measurements between independent sets of data, these results indicate good agreement between both experimental data sets. The force histories show the same general trends and other than the outliers noted above, key quantities such as phase and peak magnitudes match to within 10%. Since the two sets of measurements show a good match in qualitative trends and key quantitative parameters such as peak magnitudes and phase, this analysis concludes that the pressure based measurement are sufficiently accurate for future feedback control.

3.7 Phase and magnitude shifts due to pressure lines

Since the pressure sensors are remotely located, lengths of pressure lines are needed to connect the wing ports to the pressure sensors. While the flap stand was reconfigured to accommodate shorter runs, a minimum length between 300mm and 400mm for each sensor is still required for the system to function, so the low pass filter effect cannot be completely removed.

To estimate the remaining effect of this minimum length run on the pressure measurements, a series of flap tests were carried out. At a given test frequency, the output of a single pressure port was studied as the pressure line length was increased from the minimum. The phase delay and magnitude reduction with increasing pressure line length was characterized at 3Hz and 4.5Hz which corresponds to the lowest and highest hover case flap frequencies.

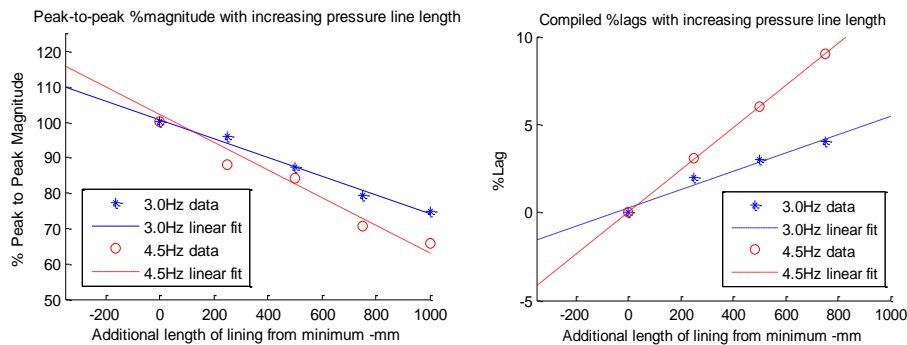


Figure 3.30: Pressure line length impact measurements – magnitude (left) and phase delay / lag (right)

Table 3.3.6: Peak-to-peak magnitude and phase comparison – single pressure measurement

Projected Improvements		
Flap Frequency	Peak-to-peak Mag%	Phase%
3.0Hz	9.80%	1.50%
4.5Hz	15.70%	4.20%

It was noted that the effects of long pressure lines were linear with increasing length up to 1 meter. For a simple estimate of maximum pressure line induced error, it was assumed that this relationship continues for 350mm beyond the minimum line length. A linear extrapolation was performed to estimate a range of maximum errors in magnitude and phase due to pressure-line-induced filtering. This is summarized in Table 3.3.6. At hover frequencies, the estimated errors in peak-to-peak magnitude range between 9.8% and 15.7%. The estimated errors in lag range between 1.5% and 4.2%. These estimates suggest that the pressure lines can account for the differences between FT and pressure sensor data described above.

3.8 Forward flight cases

Forward flight tests were performed in the UM 5x7 wind tunnel at two free streams. Both cases were run with a zero degree angle of incidence. The free stream velocities were chosen to provide an overlapping range of Strouhal numbers for comparison to previous windtunnel tests. In addition to the Reynolds number and reduced frequency introduced previously for hover conditions, the Strouhal number is direct a comparison of the average tip velocity of the wing tip and the incoming flow velocity.

$$St = \frac{2h \cdot f}{U_{\infty}} \quad (3.3)$$

The instrumentation on the flap stand was used to measure free stream velocity, allowing for a more complete description of the incoming flow. This includes an estimate of the incoming turbulence intensity which can be obtained by the rms velocity fluctuations (st-dev) by the mean velocity. Table 3.7 summarizes the forward flight cases that were run in the wind tunnel.

Table 3.7 Summary of forward flight test cases

FS	Mean V (m/s)	St. Dev (m/s)	Turb. Intensity (%)	Flap freq. range (hz)	St. range
Case 1	3.31	0.038	1.148	2.0-4.0	0.09 - 0.19
Case 2	2.31	0.011	0.476	2.0-3.5	0.14 - 0.24

3.8.i Forward flight test procedure

Due to the nature of the measurements required, a single set of forward flight results involve multiple test phases. As the pressure lines interfere with force-torque measurements, these two tests are conducted separately using different left wings. A flapping frequency sweep is performed twice, once with the pressure instrumented wing and once with the mass balanced set of wings used in vacuum chamber tests. As there is no pressure instrumentation on the mechanics, the loads generated by the center body and force transducer mounting will not be measured by the pressure instrumentation. These forces are characterized by taking a complementary set of wind tunnel tests at the two different free streams with the wings removed from the test model. A breakdown of the wind tunnel test procedure for each of the two free streams is shown in Figure 3.31 Windtunnel testing subcases.

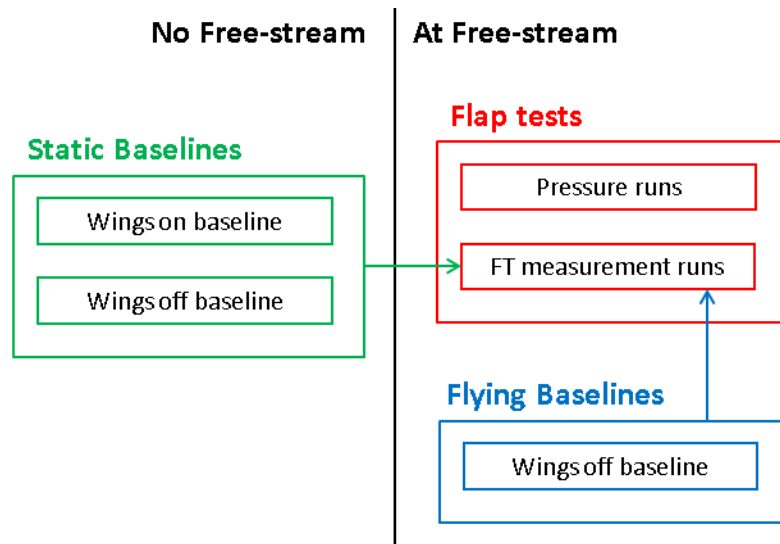


Figure 3.31 Windtunnel testing subcases

3.8.ii Additional data processing for forward flight

The data processing techniques described for the hover cases remain unchanged for the forward flight test results and only an additional consideration is needed in accommodating additional “flying baselines”, which are additional forces on the force-torque sensor due to the non-flapping components of the flap mechanism. A second analysis of the appropriate filter cut off frequency in the presence of a free-stream is also presented. These two issues are addressed in this section.

3.8.ii.a Flying-baselines for FT sensor

The wings-off baseline taken at each free stream allows the loads generated by the flapping mechanics to be estimated when comparing force transducer and pressure sensor measurements. While necessary, this process involves two additional force transducer measurements and the corresponding accumulation of error from each measurement. Table 3.8 summarizes the net forces generated by the mechanics and the corresponding standard deviation for each free stream. Integrating these measurements is a straightforward process; the mean values are added to all vertical force measurements taken by the force transducer at

that free stream and the standard deviation is added to the overall standard deviation interval of the corresponding measurement.

Table 3.8 Approximate no-wing flying baselines

	Mean Fz (N)	St.Dev (N)		
Tare	-0.3423	0.0019	net Fz (N)	St. Dev (N)
2.3ms	-0.543	0.0025	-0.2007	0.0044
3.3ms	-0.5658	0.0022	-0.2235	0.0041

The effect of considering the flying baseline on the comparison is illustrated by the sample plot in Figure 3.32. A 3.5Hz flapping case at 3.3ms is considered. The black set of lines represents the measured FT sensor and a standard deviation interval before the baseline correction is applied. The large offset in data due to the forces generated by the mechanics is accounted for by adding the results of the flying baseline run. The expansion of the error bars due to the additional measurement uncertainty is not significant.

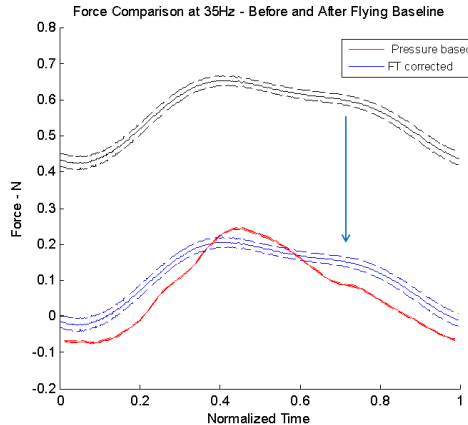


Figure 3.32 Sample case with offset being accounted for using no-wing baseline

3.8.ii.b Filter cut-off frequency for forward flight

The same strategy of low-pass filtering the force torque data before ensemble averaging described in the hover section was used again when processing forward flight data. As noted previously, the data is sensitive to changes in filter

cut off frequency. The best agreement with expected trends and pressure measurements is obtained when the cut-off is set at about twice the flapping frequency, f . However by increasing the cut-off frequency slightly to $2.5f$ and to $3.0f$, a significant change in the stroke histories can be seen. Most notably, a two-peak force history is generally obtained which is not expected for the single degree of freedom flapping motion realized by the mechanics. This is summarized in Figure 3.33 that presents mean FT measurements as reported using different LP filter cut off frequencies.

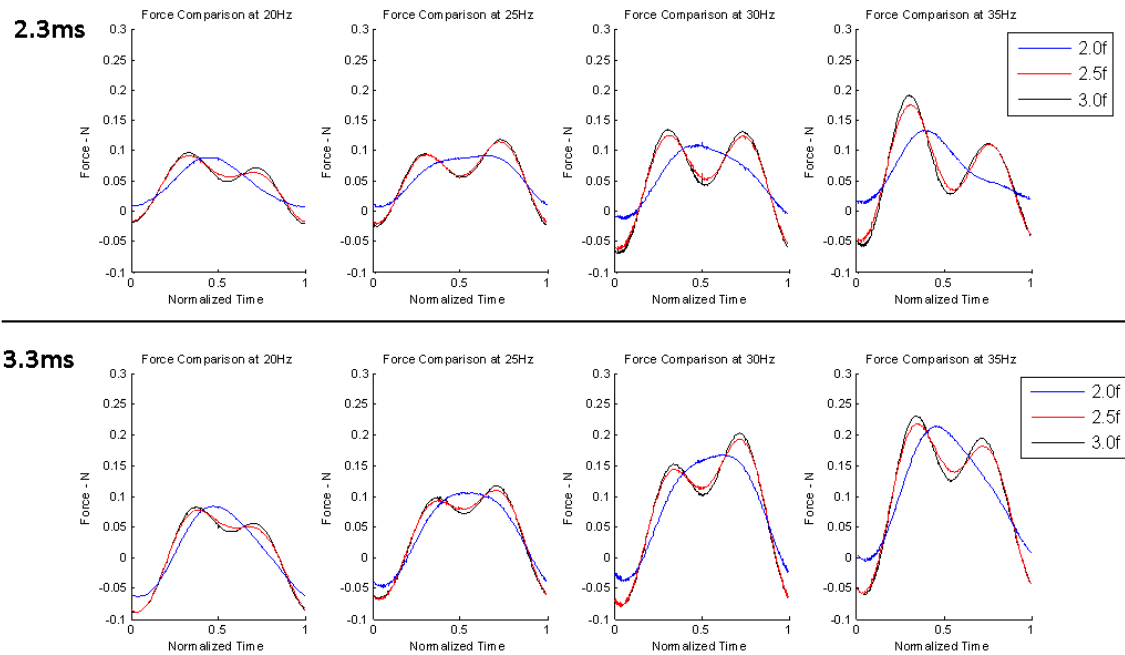


Figure 3.33 Sensitivity of force-torque histories to LP filter setting

As described before, this setting of $2.0f$ was chosen by analyzing the power spectrums of the raw data and determining that operating in air did not give rise to additional periodicities beyond $2.0f$ from operating in vacuum. Based on this, it was determined that additional information beyond $2.0f$ was not due to the aerodynamics at hover and most likely due to the structural response of the test setup. It was assumed that the same would hold true for the forward flight cases, but the sensitivity of the data to filter cutoff suggests that a third harmonic may be

present. As such the same process was used in analyzing two of the forward flight cases.

The power spectral densities of the vertical force signal for two flapping frequencies at hover and at the two different free streams were compared and are shown below. It can be noted that a third harmonic is not noticeable at hover but is more prominent when in a free stream. The comparisons for 2Hz and 3hz are shown in the sub-plots of Figure 3.34.

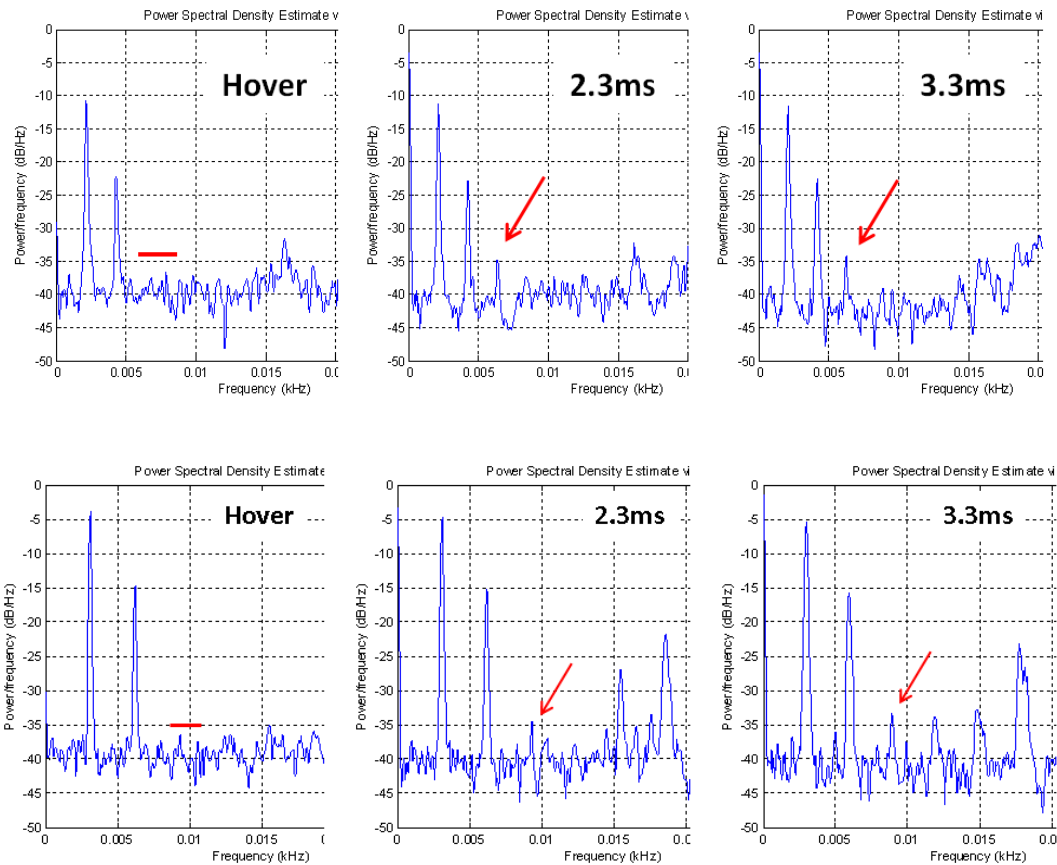


Figure 3.34 PSD for 2.0Hz (Top) and 3.0Hz (Bottom) – Comparison between hover and forward flight cases.

It can be noted from the brief analysis that a third harmonic is not apparent at hover, but is more noticeable with increasing free stream velocity. One possible explanation that the data supports is that the signals from aerodynamic loads at

hover are not large enough to have all modes fully captured by the instrumentation. As the signal to noise ratio is improved with larger loads in forward flight, this third mode might be more apparent and begin to manifest itself. However, this explanation assumes that the third harmonic is associated to the aerodynamic loads. This dual peak trend is not expected for these flap mechanics.

3.8.iii Forward flight test results

As with the hover cases, the main point of comparison between force transducer and pressure based estimates is that of vertical aerodynamic force histories. The following plots summarize the results of frequency sweeps at both free streams Figure 3.35 presents a frequency sweep at 2.3ms and Figure 3.36 depicts the same test cases at 3ms. At the 2.3ms free stream, the measurements both show larger magnitudes from hover and a slight bias towards generating positive lift. This is due to the incident free stream contributing to the instantaneous velocities achieved along the chord of the wing and the asymmetrical flap stroke.

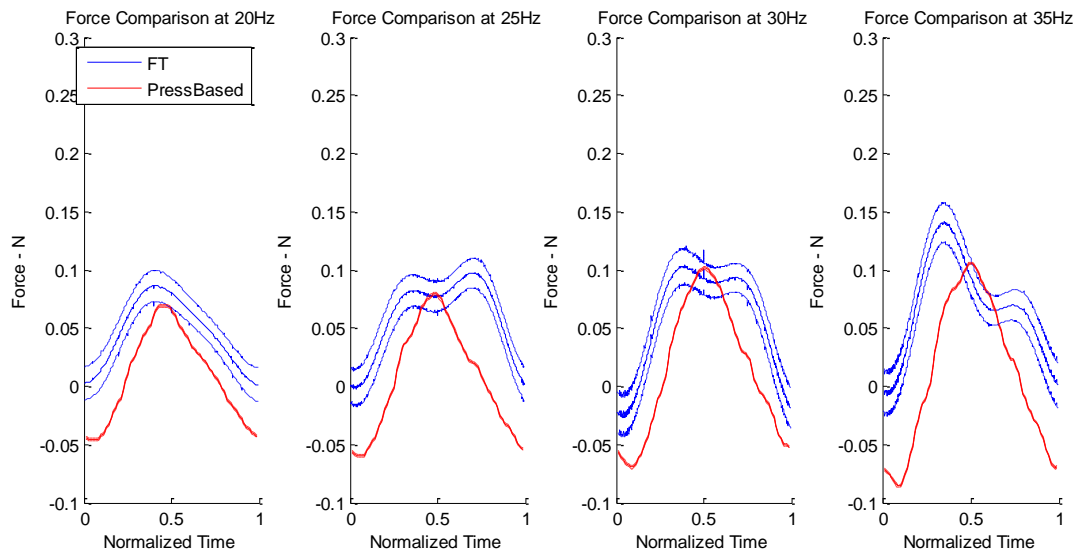


Figure 3.35 Frequency sweep at 2.3ms free stream. St. 0.14-0.24

These expected trends are present in both the force transducer and pressure based measurements, which show general agreement. The force sensor data

shows a constant offset at the slower 2.3m/s free stream that is less apparent at the faster 3.3m/s flight speed. By comparing the mean forces, the force transducer measurements at 2.3m/s show offsets between 25% and 38% while the results at 3.3m/s show offsets ranging from 5% to 21%. This suggests that the flying baseline measurement was a good approximation of the additional aerodynamic forces due to the supporting structure at the higher airspeed, but did not appear to be as successful at the slower wind tunnel setting. This highlights the additional difficulty of isolating the relatively small aerodynamic forces associated with flapping when using a measurement device that detects forces from every component to which it is attached. The pressure-based instrumentation can only measure aerodynamic forces and is not directly affected by the surrounding structure. While this characteristic makes pressure instrumentation ideally suited to taking aerodynamic measurements, it also means pressure instrumentation is incapable of providing measurements of any other phenomena that might be of interest when pursuing different experimental goals.

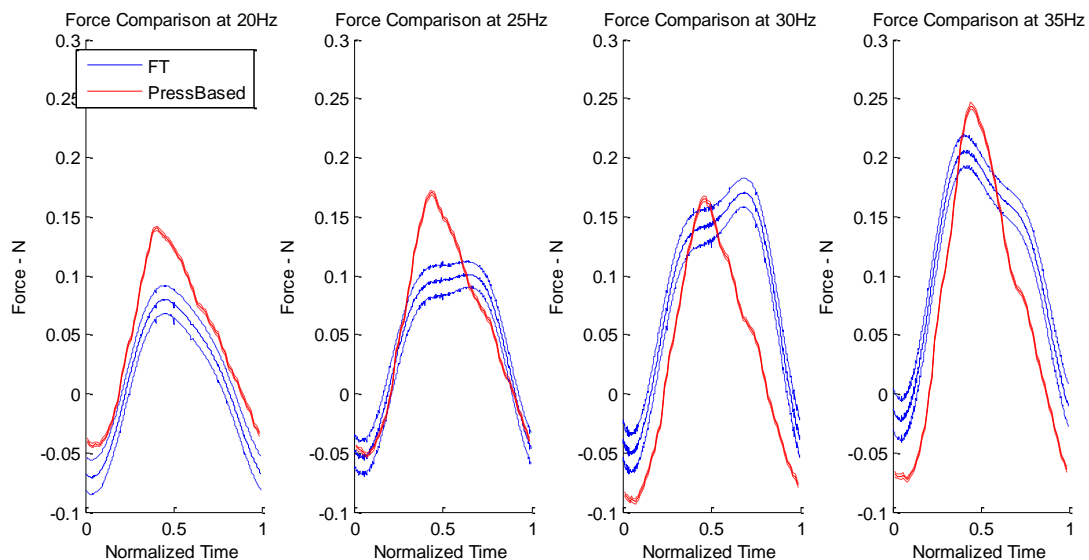


Figure 3.36 Frequency sweep at 3.3ms free stream. St. 0.09-0.19

3.8.iii.a Additional points of comparison - third mode

The source of the third mode is important in comparing force transducer measurements to pressure instrumentation estimates. When the third harmonic is considered, the force histories differ dramatically. The force measurements show two distinct peaks in the vertical aerodynamic forces during a flap stroke. The pressure based estimates do not show this same unexpected trend. Instead they report a single peak when the translational velocity of the wing is at its greatest, corresponding to the highest instantaneous velocities of the wing. Both simple panel method and available non-linear panel method predict this trend. Sample pressure calculations from a simple panel code for similar flap conditions are shown in Figure 3.37, showing a single peak in aerodynamic forces being generated at the midpoint of the down-stroke when instantaneous velocities are highest.

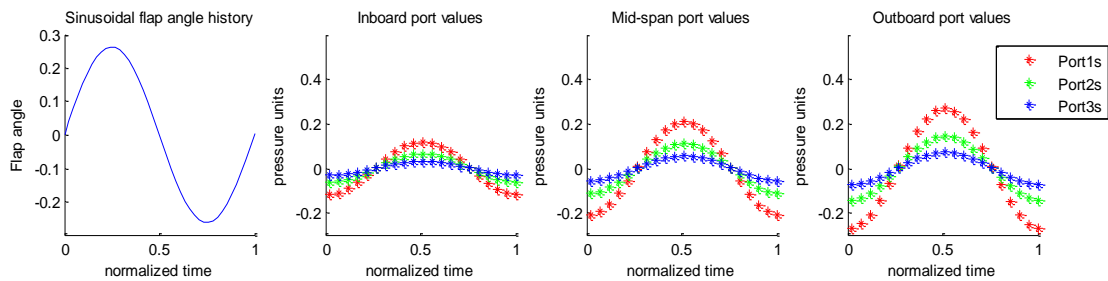


Figure 3.37 Sample quasi-steady panel method pressure solution - single lift peak

While potential flow computations are fundamentally simple, the results agree well with the pressure-based measurements. These suggest that a single lift peak is expected and the further justifies the 2f filter setting.

3.9 Summary of test results

The above test results show both methods were capable of adequately measuring the aerodynamic forces generated by a rigid flapping wing in air. The pressure based instrumentation provides aerodynamic force histories that demonstrate expected trends. The peak aerodynamic forces are encountered

when instantaneous wing velocities are at their highest and the peak-to-peak magnitudes of the measured vertical aerodynamic loads scale appropriately with flapping frequency. The pressure-based results are consistent throughout the frequency range, with the force coefficients from different cases seen to be independent of frequency. This suggests that the instrumentation is functioning correctly and is capable of qualitatively capturing the aerodynamic loads over the wings.

The accompanying set of force transducer measurements also show expected trends and scaling behavior. The peak to peak magnitudes of total loads in the vertical direction scale with the square of frequency, and the subtracted single-stroke vertical force averages are within 4% of the averaged aerodynamic force over multiple stroke histories.

When compared, both sets of independent measurements show general agreement. In the case of hover, the data showed peak forces to generally agree within 10% and phase to agree within 3%. This agreement suggests that both data sets are capable of quantitatively capturing the small aerodynamic loads generated by the rigid wing in air and allows both sets of measurements to be used in validating each other. In forward flight, additional measurements are needed to account for additional forces encountered in an incident free stream. A flying-baseline approximation was required that introduced additional error and uncertainty in the force transducer measurements. This was not necessary for the pressure instrumentation, which functioned equally well in both cases.

3.9.i Comparison of experimental methodologies

With two independent sets of aerodynamic force measurements, a comparison between both experimental methods can be made. When attempting to measure only the aerodynamic lift associated with flapping, the traditional force transducer based approach is disadvantaged. It is exposed to all the forces present during a test and is prone to data corruption from structural modes and disturbances. It is also indirect in that multiple measurements are needed to isolate the aerodynamic forces, resulting in added sources of uncertainty. When selecting

an appropriate sensor, additional factors such as test model mass and large inertial loads meant compromises in resolution had to be made for a larger measurement range. However, being able to measure loads in all three directions makes the force transducer approach more suited to other applications that involve taking total force measurements such as the thrust, drag and total lift from a complete vehicle or complete flapping wing design.

The pressure-based instrumentation can only detect aerodynamic forces, which is a distinct advantage when seeking to only measure aerodynamic forces. The direct nature of the pressure measurements meant no compromises in resolution were required and the pressure sensors could be chosen solely based on expected measurement ranges. Appropriately-selected and calibrated sensors allow for significantly less measurement uncertainty than with the force transducer approach. The pressure-based instrumentation also provides pressure distribution during a flap stroke. While not discussed in this paper, pressure distributions add an additional dimension to the available experimental results. Lift distribution data can provide insight to the flow conditions during an experiment, and can provide additional points of comparison to numerical results.

While more appropriate for this study, the use of pressure instrumentation is not without challenges. Due to the unsteady nature of flapping wing aerodynamics, the method is inherently sensitive to how the instrumentation is chosen and implemented. Long pressure lines between wing ports and remotely located sensors were observed to cause an artificial low pass filtering effect on the measurements as noted by the authors in earlier work [93], while pressure sensors mounted on the wings are subject to error due to the accelerations experienced during a flap stroke, as described by Usherwood et al. [18]. While the force transducer approach is overwhelmed by a wealth of unwanted data, the pressure instrumentation is limited in scope. For example, the pressure instrumentation used in this study is oriented in the vertical direction and can only provide force measurements normal to the surface of the wing. The approach is also inherently invasive as measurements must be taken on the flapping wings

themselves. The impact of adding instrumentation such as added weight and changes to wing deflection can be minimized through the use of micro-scale integrated sensors such as those used by Takahashi et al [19,47] provided these smaller sensors have sufficient resolution and accuracy.

3.10 Flapping wing conclusions

This chapter has presented an investigation of the aerodynamic forces generated by a rigid flapping wing in air through two experimental approaches. Using a force-torque sensor and distributed pressure sensing instrumentation embedded over the wing surface, two different measurements of the time-resolved vertical aerodynamic loads generated by a rigid flapping wing have been acquired. This has allowed a pressure-based approach to force measurement to be experimentally validated. Both sets of data show common trends and a high degree of quantitative agreement, demonstrating the ability of a pressure based system to provide sufficiently accurate measurements for future flight control applications. Our findings can be summarized in the following list.

- Experimental results indicate the pressure instrumentation is able to estimate aerodynamic forces over a rigid flapping wing. The pressure-based measurements are consistent across all test cases and scale appropriately with flap frequency. Force transducer measurements show peak-to-peak magnitudes of total loads in the vertical direction scale with the square of flap frequency, and the single-stroke vertical force averages are within 4% of the averaged force over multiple stroke histories.
- Force transducer measurements show agreement with the pressure-based results in terms of trends and key magnitudes. This agreement suggests both sets of instrumentation provide consistent and accurate results. These two independently-acquired datasets also enable a comparison of the two measurement methodologies.
- Pressure instrumentation allows direct measurements of aerodynamic forces enabling more straightforward data analysis and reduced measurement uncertainty than with force transducer data. In this study the

resolution of pressure forces was straightforward as the orientation of the rigid wing surfaces was always known. In a more general, flexible wing case, a method of measuring wing surface deflections will be needed.

- The force transducer approach requires baseline inertial data collection in a vacuum environment assuming wing deformations in both air and vacuum are identical. In forward flight supporting structure and mechanism aerodynamic loads introduce additional uncertainties in force transducer data.
- Pressure instrumentation is capable of measuring only aerodynamic forces, making the approach uniquely suitable for such measurements. Further, pressure instrumentation is capable of providing lift distribution information during an experiment that is not available with strictly force transducer measurements.
- While a force transducer approach can provide a complete picture of the overall forces at work in a flapping wing system, pressure instrumentation provides a simpler, more direct measure of flapping wing aerodynamic force. A force transducer detects contributions from all components to which it is physically connected during a test. This allows for a potentially more comprehensive overall picture of forces and torques but at the cost of being subject to data corruption due to noise and vibrations.
- A pressure based approach is inherently self-contained and has the potential to be used as embedded flight instrumentation. Actual implementation on future flight vehicles will depend on vehicle size and sensor technologies. While larger bird scale flapping wing vehicles might be able to accommodate commercially available pressure sensors [18], smaller insect scale flyers might require smaller-scale pressure sensors [19].Future work

Future work can exploit further use of pressure-based instrumentation for flapping wing vehicles. When coupled with a motion capture system such as

VICON to measure wing surface deformations in air, the pressure instrumentation can provide data for a large range of test cases with flexible as well as rigid wings. With a proven pressure based methodology, direct measurements of the aerodynamic forces can instead be used to determine actual inertial loads during a test without relying on a vacuum chamber test phase.

Chapter 4

Aerodynamic Moment Estimation for Fixed Wing Vehicles in High Angle of Attack Maneuvering

4.1 Introduction

An aerodynamic sensing system was developed for an aerobatic fixed wing platform to study the use of augmented aerodynamic data during small UAS operations outside conventional fixed wing flight envelopes. During high angle of attack flight, aerobatic maneuvering, or hover, flow conditions across the vehicle can differ greatly across the various flight surfaces. This challenges conventional small UAS autopilots that rely on inertial sensors and pitot tubes to provide airspeed, or at best airspeed, angle of attack, and sideslip, for models presuming coefficients valid only for pre-stall airspeeds and angles of attack. The proposed aerodynamic sensing concept aims to extend the current paradigm of small UAS autopilots through additional flow instrumentation. Our objective is to show that the proposed aerodynamic sensing system can provide means to extend the envelope of current small UAS autopilots through use of the proposed modeling scheme plus real-time pressure feedback.

This chapter describes a series of wind tunnel tests that examines the ability of the instrumentation package to provide real-time control surface aerodynamic moment estimates in a controlled test environment. Of particular interest for slow and hovering flight is the ability to directly measure and model pitch and yaw moments generated by the elevator and rudder in post-stall conditions when the aircraft wind vector is insufficient to produce significant flow across the tail surfaces, but where backwash from the propeller provides this flow. Below, the relevant steady level flight equations used in small UAS autopilots are first presented, and a new formulation for operations beyond stall is proposed. The experimental setup and process are then presented followed by an analysis of

test results. The chapter ends with a summary of key findings and describes future work.

4.2 Steady level flight equations

The steady flight equations represent the most basic principles of flight mechanics [94] and are used as the foundation for the development of small UAS autopilots. In this section, the aerodynamic force and moment equations for an aircraft in steady flight are described.

Under the steady flight assumptions, the forces generated by the main wing are used to characterize the lift and drag generated by the aircraft. These are given by the aerodynamic equations for lift and drag

$$L = \frac{1}{2} \rho V_{ac}^2 S C_L \quad (4.1)$$

$$D = \frac{1}{2} \rho V_{ac}^2 S C_D \quad (4.2)$$

where ρ is atmospheric density and V_{ac} is the free-stream airspeed of the aircraft. The lift and drag coefficients C_L and C_D depend linearly on the aircraft angle of attack α . This linear relationship is a good model up to the point of wing stall and flow detachment across the lifting surfaces.

$$C_L = C_{L_0} + C_{L\alpha} \alpha \quad (4.3)$$

$$C_D = C_{D_0} + \frac{C_L^2}{\pi e AR} \quad (4.4)$$

The lift coefficient is the combination of a constant offset C_{L_0} at zero angle of attack, and the linear lift coefficient associated with the wing, $C_{L\alpha}$. The drag coefficient similarly features a constant parasite drag constant C_{D_0} and a term that is dependent on lift, the aspect ratio (AR) of the wing and the Oswald efficiency factor e associated with its planform. Under steady flight assumptions, the pitch moment equation for an aircraft is

$$M = \frac{1}{2} \rho V_{ac}^2 S c C_M \quad (4.5)$$

where c is the root chord of the wing by convention, and S is the surface area of the wing.

The above steady flight equations inherently assume that the incoming wind vector can fully represent the longitudinal aerodynamic forces and moment of the entire aircraft. The non-dimensional pitch moment C_m combines the effects of all aerodynamic surfaces such as the wings, fuselage and horizontal stabilizer. It is a linear function of aircraft angle of attack α , and elevator deflection δ_e as given in

$$C_M = C_{M_0} + C_{M_\alpha}\alpha + C_{M_{\delta_e}}\delta_e \quad (4.6)$$

where the coefficients C_{M_0} , C_{M_α} , and $C_{M_{\delta_e}}$ are determined through theoretical models or through wind tunnel testing. Under steady flight conditions where neither the aircraft nor the horizontal tail is stalled, this linear relationship of predetermined coefficients and the aircraft wind vector are sufficient for the aerodynamic pitch moments to be closely approximated.

The lateral forces and moments, side force, yaw moment, and roll moment, must also be balanced for steady flight. For steady flight, aerodynamic side force application is typically not appreciable, although side slip can be used to reduce energy on approach, for example. In this work, focus is placed on use of the propeller backwash as a means of controlling the aircraft in post-stall conditions. Presuming sufficient flow over the tail, the vertical stabilizer and rudder can utilize the prop wash to control yaw, as will be explored in this chapter. As the horizontal and vertical tail sections are completely immersed in the propeller backwash, they are considered to be the more relevant to the current research. This chapter therefore focuses on longitudinal pitching moment and lateral yawing moment which can be controlled by the tail surfaces. Below the equations for yaw and roll moment are presented.

The equation for yaw moment N is

$$N = \frac{1}{2} \rho V_{ac}^2 S b C_N \quad (4.7)$$

where b is the wingspan. The yaw moment coefficient C_N is a linear function of the aircraft side slip angle, aileron deflection δ_a and rudder deflection, δ_r as given in

$$C_{N_{combined}} = C_{N\beta} \beta + C_{N\delta_a} \delta_a + C_{N\delta_r} \delta_r \quad (4.8)$$

where $C_{N\delta_a}$ is the yaw moment due to the differential drag caused by aileron deflection. The aerodynamic roll moment is given by

$$\mathcal{L} = \frac{1}{2} \rho V_{ac}^2 S b C_{\mathcal{L}} \quad (4.9)$$

where the roll coefficient depends linearly on slip angle β , aileron deflection δ_a and rudder deflection δ_r

$$C_{\mathcal{L}_{combined}} = C_{\mathcal{L}\beta} \beta + C_{\mathcal{L}\delta_a} \delta_a + C_{\mathcal{L}\delta_r} \delta_r \quad (4.10)$$

In summary, the steady flight force and moment equations based on relative wind velocity vector and a series of pre-determined coefficients enable a straightforward computation of aerodynamic forces and moments across the vehicle. While suitable for most forward flight conditions, this formulation is not applicable during operations beyond stall when the aircraft wind vector may not represent the local flow over the flight surfaces. A re-formulation of these aerodynamic moment equations is proposed below that includes additional components representing prop wash as well as free stream velocity terms.

4.3 Proposed linear model for high angle-of-attack flight

During operations outside the envelope of conventional forward flight such as at high angles of attack, effects such as flight surface stall and unsteady flow fields

across the vehicle mean that simple wind vector measurements and predetermined coefficients will be incapable of accurately modeling the aerodynamic forces and moments generated by an aircraft.

When the flow across the main wing separates at high angles of attack, aerodynamic forces can become unsteady and difficult to predict. A simplification of the basic lift and drag equations are proposed based on direct measurements taken over the surface of the wing, where the measured force normal to the chord line of left and right wings are L'_{Left} and L'_{Right} , respectively:

$$L = (L'_{Left} + L'_{Right}) \cos \alpha \quad (4.11)$$

$$D = \frac{1}{2} \rho V_{ac}^2 S C_{D_0} + (L'_{Left} + L'_{Right}) \sin \alpha \quad (4.12)$$

The aerodynamic lift is computed as the component of the combined pressure force from both wings that is normal to the wind vector. The drag is the combination of the parasitic drag coefficient C_{D_0} multiplied by dynamic pressure and the component of the main wing pressure force in the direction of the wind vector. The parasitic drag coefficient can be determined through wind tunnel testing.

Consider a propeller-driven, fixed wing aircraft with a conventional configuration but sufficient thrust to at least balance (lift) the full aircraft weight. Such an aircraft certainly can maintain altitude or potentially even climb without relying on wing-generated lift, but the wings and tail will still provide aerodynamic forces and moments that must be considered.

In order to sustain flight at high angles of attack beyond stall, the aircraft must rely more heavily on propeller thrust to balance its weight, resulting in high-speed prop wash causing local flow regions that differ greatly from the vehicle wind vector. Further, the interaction between the aircraft wind vector and the wind vector at high angles of attack make a mapping between throttle setting and the propeller backwash (prop-wash) challenging.

This work proposes the definition of a new prop-wash velocity variable V_{pw} and separation of the moment coefficient terms for the free-stream versus prop-wash velocities to better account for differing flow conditions at high alpha or hover. The equations presented in this section propose an expansion on the steady level flight equations to accommodate additional sensing and provide moment estimates that remain valid at high angles of attack and hover.

First consider the pitch moment equation. With additional prop-wash induced velocity V_{pw} over the tail surfaces, the equation can be re-written using separate aerodynamic coefficients for the horizontal tail $C_{M_{htail}}$ and the fuselage/wing combination $C_{M_{ac}}$ as

$$M = \frac{1}{2}\rho V_{ac}^2 S b C_{M_{ac}} + \frac{1}{2}\rho V_{pw}^2 S_{htail} C_{M_{htail}} \quad (4.13)$$

$$C_{M_{ac}} = C_{M_{ac_0}} + C_{M_{ac\alpha}} \alpha \quad (4.14)$$

$$C_{M_{htail}} = C_{M_{htail_0}} + C_{M_{htail\alpha}} \alpha_{tail} + C_{M_{htail\delta_e}} \delta_e \quad (4.15)$$

The coefficients $C_{M_{htail_0}}$, $C_{M_{htail\alpha}}$ and $C_{M_{htail\delta_e}}$ describe the pitch characteristics of the horizontal tail surfaces and can be determined through wind tunnel testing. Under steady flight conditions, both velocities will be comparable and this formulation approximates the conventional pitch moment equation. However, during low-speed-high-angle-of-attack flight when the velocity of the vehicle diminishes, the prop-wash induced velocity begins to dominate the flow field. The original formulation only considers V_{ac} and cannot account for the prop-wash while the proposed formulation includes a second term that better captures the aerodynamic state of the tail plane due to the prop wash. Near hover when the vehicle airspeed is negligible, forces and moments in the original formulation tend to zero thus is incapable of estimating the control moments from the elevator. By using additional information regarding flow over the tail, the proposed reformulation allows the pitch moments generated by the elevator to be estimated past free stream stall and even when in a hover. The entire second

term, $\frac{1}{2}\rho V_{pw}^2 S_{htail} C_{M_{htail}}$ can also be measured using distributed pressure sensing, or using additional inflow information across the tail section. The reformulation for the yaw moment equation follows in a similar manner for the vertical tail, as shown below.

$$N = \frac{1}{2}\rho V_{ac}^2 S C C_{N_{ac}} + \frac{1}{2}\rho V_{pw}^2 S_{vtail} C_{N_{vtail}} \quad (4.16)$$

$$C_{N_{ac}} = C_{N_{ac_0}} + C_{N_{ac\beta}}\beta \quad (4.17)$$

$$C_{N_{vtail}} = C_{N_{vtail_0}} + C_{N_{vtail\beta}}\beta_{tail} + C_{N_{vtail\delta_r}}\delta_r \quad (4.18)$$

As with the pitch moment equation, the entire second term can be estimated through direct aerodynamic measurements or through predetermined coefficients in conjunction with a velocity measurement as shown above. The coefficients $C_{N_{vtail_0}}$, $C_{N_{vtail\beta}}$, and $C_{N_{vtail\delta_r}}$ can be determined through wind tunnel testing. The moments associated with the tail surfaces are amenable to both a ‘partial’ and ‘complete’ sensing strategy. Since the prop-wash induced velocities are large and the tail surfaces may operate in an attached flow condition even when in a hover, it might be sufficient to utilize an additional velocity measurement in conjunction with a new set of coefficients. With a ‘complete’ distributed pressure sensing strategy, the entire moment contribution over the tail surfaces can be measured directly. If the prop-wash induced velocities are low or the control surface deflections too large to ensure attached flow over the tail surfaces, the distributed pressure measurement strategy over the tail can still provide estimates of yaw and pitch moments.

For roll, an approach that uses direct measurements is necessary. When the main wings operate in a post stall, separated flow regime, the aerodynamics are nonlinear and unsteady. The proposed roll moment equation presented below uses estimates of differential lift over the wings in conjunction with additional logic for aileron authority.

$$\mathcal{L} = \frac{1}{2}\rho V_{ac}^2 S b C_{L\beta} \beta + \frac{1}{2}\rho V_{pw}^2 S_{vtail} C_{L\delta_r} \delta_r + \mathcal{L}_{wings} \quad (4.19)$$

$$\mathcal{L}_{wings} = (L'_{Left} - L'_{Right}) b_{eff} \quad (4.20)$$

$$L'_{Left/Right} = f(\delta_{a_{Left/Right}}) \quad (4.21)$$

Here, L'_{Left} and L'_{Right} are direct measurements of the aerodynamic forces normal to the wing surface. The effective roll moment arm b_{eff} can either be determined based on the geometry of the wing or determined through wind tunnel testing depending on particular lift sensing scheme used.

The aerodynamic sensing concept suggested above was implemented for a small UAS to enable wind tunnel flight tests to determine coefficient values, followed by flight tests in which embedded sensors provide real-time feedback for the autopilot. Tests and results presented in the remainder of this chapter focus on the pitch and yaw sensing aspect of the proposed steady flight equation reformulation, which are the two values most directly influenced by propeller-induced flow.

4.4 Embedded instrumentation

A pressure-based aerodynamic sensing system was developed to augment traditional inertial sensing systems. This augmentation is particularly useful for operations in unsteady flow conditions such as past stall at high angles of attack where linearized aerodynamic models are less suitable. In these situations, the linearized relationship between control surface deflection and resultant aerodynamic forces is not directly applicable so external disturbances cannot be detected (by inertial sensors) until the vehicle is affected by them. Precision in feedback control therefore may benefit substantially in such conditions with direct aerodynamic moment information that would otherwise be difficult to predict.

The aerodynamic sensing package proposed in this work is based on a set of pressure measurements taken across the aircraft through pressure ports and

through multi-hole probes. An overview of the concept is shown in Figure 4.1. At each indicated location, a pair of pressure ports on the top and bottom surface is connected to a locally-mounted differential pressure sensor.

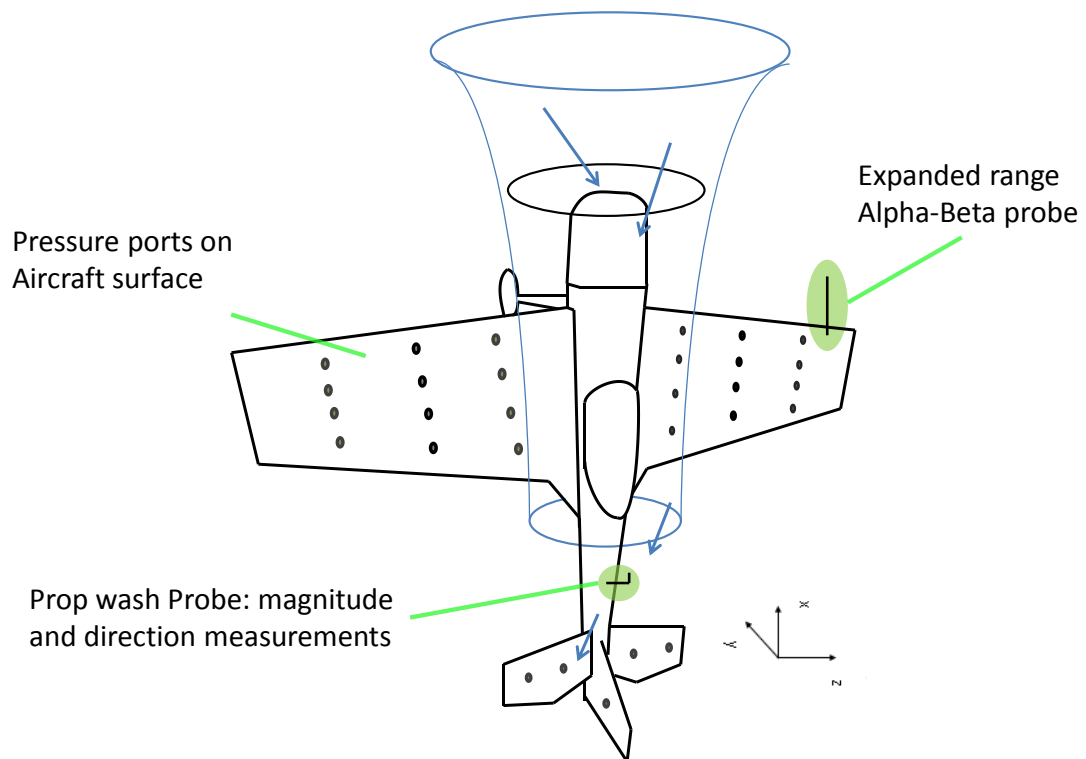


Figure 4.1 Pressure-Based Aerodynamic Instrumentation Concept

This section describes the key components of the sensing package and how each allows in-flight measurement of the proposed additional terms to the basic steady flight equations presented in the preceding section. The current configuration allows two different approaches to implementing aerodynamic sensing to be explored. First, a “Partial” approach through the use of predetermined coefficients and an additional prop-wash probe measurement, which is non-invasive to the structure and requires minimal additional instrumentation but requires careful modeling of the prop-wash flow. Second, a “Complete” approach to aerodynamic sensing is proposed that includes distributed pressure sensing across the tail surfaces. While the Figure 4.1

schematic also shows distributed sensing in the wing, this dissertation focuses on carefully establishing moments associated with prop-wash flow over the tail. Thus, while the instrumentation design is proposed for all surfaces, results focus on data acquired from tail surfaces only.

4.4.i Embedded pressure sensors on flight surfaces

Aerodynamic lift and drag forces are characterized primarily by understanding the variable distribution of pressure across the flight surface under different flight conditions. Using differential pressure measurements each comparing top versus bottom pressure at the same surface station, a coarse discretization, and area integration scheme, lift estimates from pressure sensor measurements in unsteady flow conditions can be calculated. The schematic in Figure 4.2 shows a rectangular panel approach to direct aerodynamic force measurement for the main wings.

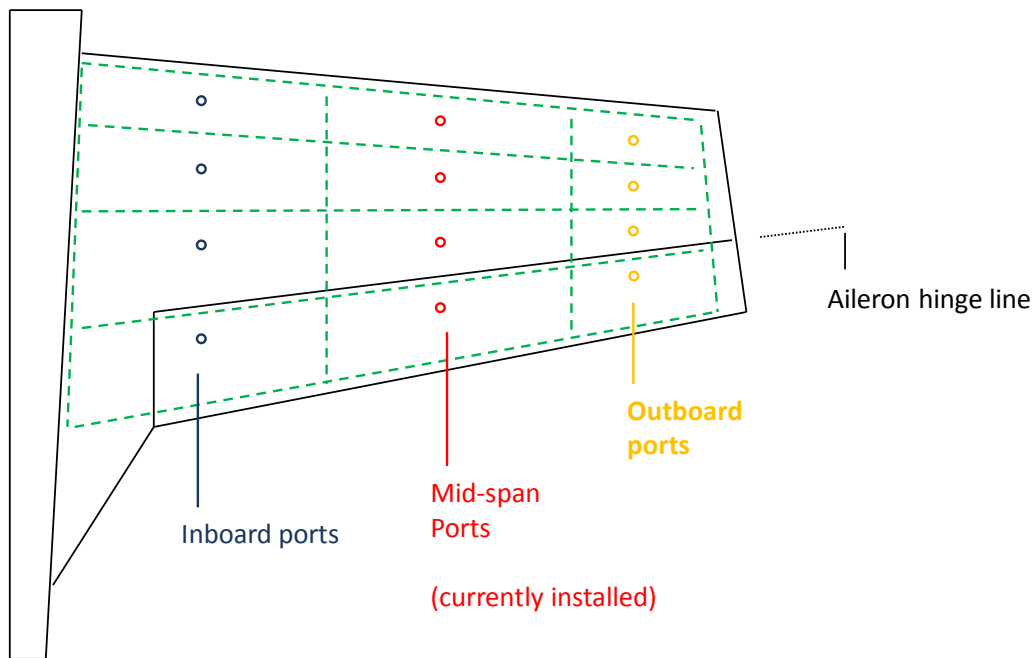


Figure 4.2 Distributed sensing and Wing Discretization for Pressure Based Lift Estimation

A Funtana wing design is shown; this platform was used for all fixed-wing tests presented in this dissertation. Each of the n rectangular panel with area S_i is accompanied by a differential pressure measurement $P_{\text{diff}-i}$. The normal pressure force term described in the preceding section can be calculated in flight by integrating the effect of all the panels as shown in Equation (4.22). Measured lift L'_{left} and L'_{right} can then be resolved into resultant wing lift and drag, provided sufficient free-stream flow to resolve a non-zero alpha as discussed above, then estimate roll moments in flight through direct measurement of L'_{left} and right L'_{right} .

$$L'_{\text{left}} = \sum_{i=1}^{n_{\text{left}}} P_{\text{diff}-i_{\text{left}}} \cdot S_{i_{\text{left}}} \quad (4.22a)$$

$$L'_{\text{right}} = \sum_{i=1}^{n_{\text{right}}} P_{\text{diff}-i_{\text{right}}} \cdot S_{i_{\text{right}}} \quad (4.22b)$$

The same approach is taken for aerodynamic force measurement over the tail surfaces and the resulting aerodynamic moments that are generated. As is done with the main wings, differential pressure $P_{\text{diff}-i}$ is measured across the horizontal tail, elevators, vertical tail and rudder at i locations. Each location corresponds to a panel of area S_{htail_i} that is l_i from the center of gravity and has a deflection angle of θ_i . This deflection angle is zero for panels on the stabilizers, and equal to the control surface deflection angle for panels on the rudder and elevator. As such, the terms relating to the control surfaces can be re-written as

$$\frac{1}{2} \rho V_{pw}^2 S_{\text{htail}} C_{M_{\text{htail}}} = \sum_{i=1}^{n_{\text{htail}}} \cos \theta_i \cdot P_{\text{diff}-i} \cdot S_{\text{htail}_i} \cdot l_i \quad (4.23)$$

$$\frac{1}{2} \rho V_{pw}^2 S_{\text{vtail}} C_{N_{\text{vtail}}} = \sum_{i=1}^{n_{\text{vtail}}} \cos \theta_i \cdot P_{\text{diff}-i} \cdot S_{\text{vtail}_i} \cdot l_i \quad (4.24)$$

4.4.ii Custom designed multi-hole probes

The proposed steady flight equation re-formulation is supported by additional multi-hole probes that provide flow vector measurements not commonly available on small fixed-wing UAS. An extended range angle of attack probe and a dedicated prop-wash probe are located on the aircraft as shown in Figure 4.3.

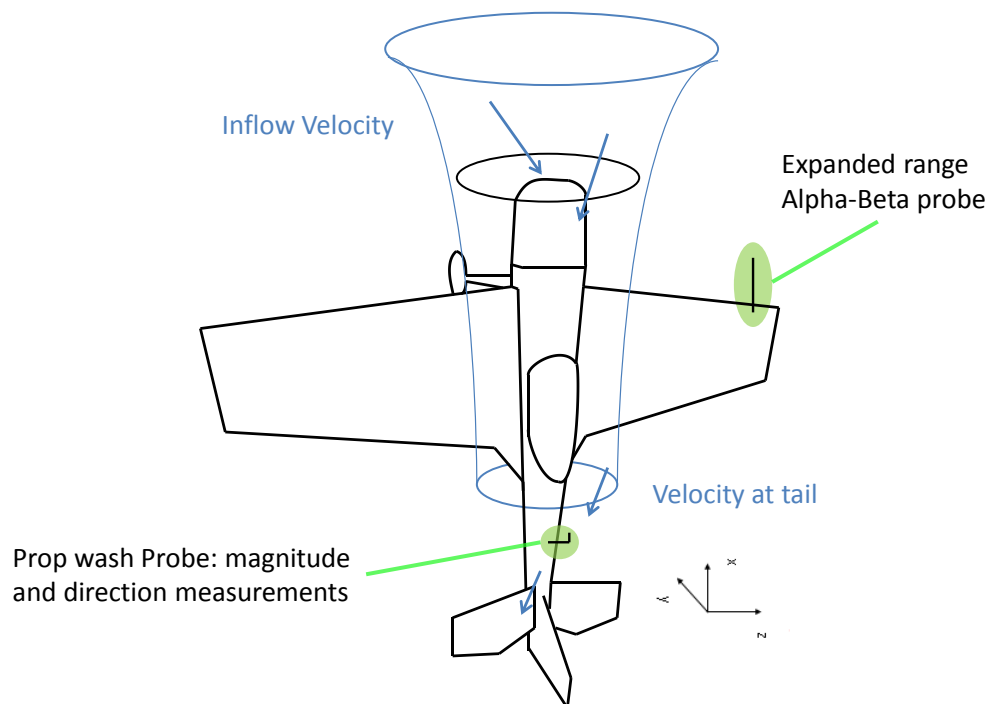


Figure 4.3 Mounting locations for Air-data and Prop-wash probes.

The extended range alpha-beta probe provides aircraft wind vector information V_{ac} , α , and β . The fuselage mounted prop-wash probe provides prop-wash induced velocity vector over the tail surfaces V_{pw} , α_{pw} and β_{pw} .

This dissertation focuses on static and wind tunnel calibration and validation of the instrumentation, along with a model of the yaw and pitching moments of the Funtana small UAS due to prop-wash. The instrumentation is in the process of being flight validated through remotely piloted and in the future autonomous flight testing. Current flight results and ongoing progress is described in Appendix C. This thesis chapter focuses on wind-tunnel based testing of the tail

instrumentation system to enable pitch and yaw moment estimation. Details on the sensing hardware are provided below.

4.5 Aircraft configuration

The Hangar-9 Funtana X100 is the commercial-off-the-shelf (COTS) small UAS chosen for both our flight tests and wind tunnel based experiments. In addition to being fully aerobatic, it also supports an appreciable avionics payload while maintaining sufficient thrust to stably hover, specifically a thrust to weight ratio larger than 1.5 when fully loaded with an avionics payload of 660 grams. The Funtana was also selected because of its structural strength and the large open volume inside the fuselage for installing and securing avionics components safely inside the aircraft. An electric motor propulsion system was chosen to minimize vibrations and exhaust with entrained fuel, which could affect the measured airflow and inertial state measurements. The motor is an E-flite Power 110 powered by two 4,150 mAH 14.8 V lithium Polymer batteries. Digital servos were used for all control surfaces. The ailerons use Hitech HS-5625MG servos, and the rudder and elevator used JR DS821 servos. The final flight configuration retains its aerobatic capability while providing an approximate flight endurance of fifteen minutes. Table 4.1 lists airframe specifications for the Funtana and a picture of the aircraft is shown in Figure 4.4.

Table 4.1 Funtana platform physical properties

Wing Span (cm)	176.5
Wing Surface Area (cm ²)	7,150
Weight with Payload (g)	5,000
Weight without Payload	3,800



Figure 4.4 Funtana RC aircraft platform

The focus of the ground based testing is on extending the ability of the Aerodynamic Sensing Concept to provide on-line estimates of control authority based on flow measurements over the tail, and then to evaluate and validate (if possible) the flow measurements with independent data. It will also allow conclusions to be drawn on the viability of the 'partial' aerodynamic sensing scheme for the tail surfaces where pre-determined coefficients are used in conjunction with prop-wash induced air flow data.

For the wind tunnel based experiments, a dedicated test platform based on the flight configuration was developed. It retains all the systems necessary for RC flight and includes additional internal structure for mounting a force-torque sensing system. The test setup is currently configured to operate in the University of Michigan 5x7 wind tunnel. An overview of the complete platform is shown in Figure 4.5. The key requirements of the test platform are a suitable propulsion system, a force-torque sensor, and the relevant components of the aerodynamic sensing system. For these tests, primary sensors include a fuselage mounted prop-wash (PW) probe and instrumented tail section, which are described in more detail below.

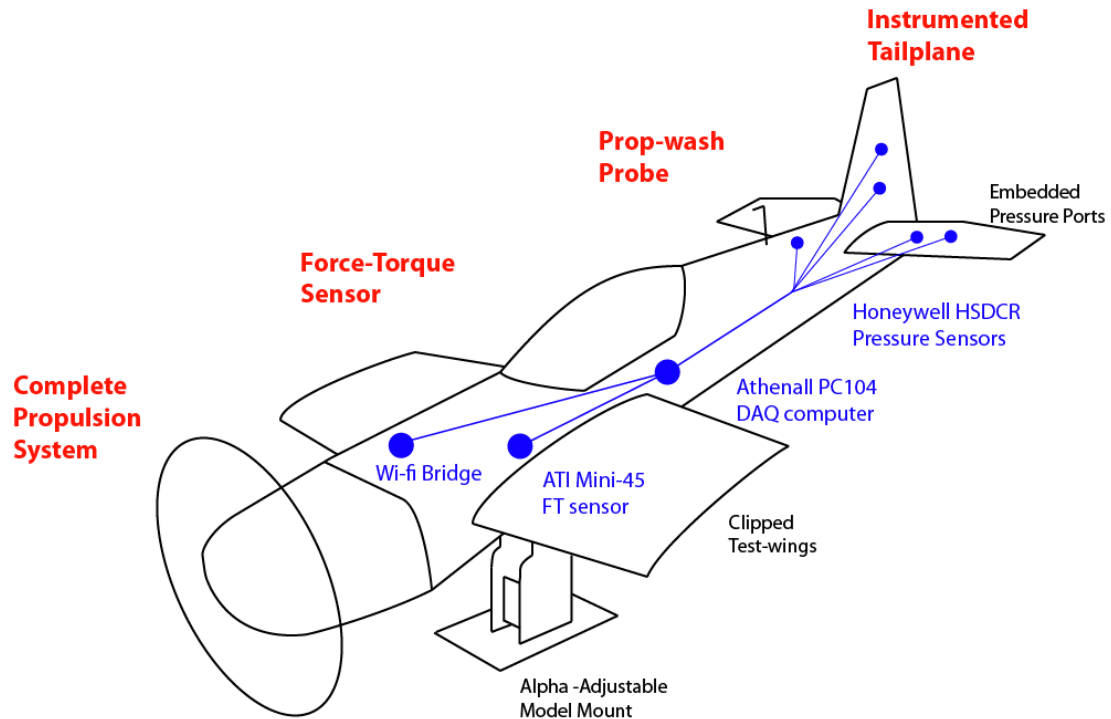


Figure 4.5 Wind tunnel test platform overview

A Diamond Systems (www.diamondsystems.com) Athena II PC104 computer is used for 16-bit analog data acquisition at 1000Hz (1kHz). The Athena is configured to communicate with an external laptop through a wireless access point. The ATI Industrial Automation (www.ati-ia.com) Mini-45 force-torque sensor has a maximum load capacity of 145N in the x and y directions and 290N in the Z direction. It is mounted internally with the tool-tip facing outwards. This allows the test model to be fully self-contained with no external wiring. The model is mounted on a custom-built, two-part stand that is adjustable for angle-of-attack and features a quick release bolt system to allow the model to be quickly repositioned.

4.6 Aerodynamic sensing - tail section

At high angles of attack, the flow across the tail surfaces can differ greatly from the flow conditions encountered by the aircraft in general. This is due to the incident flow caused by the high velocity propeller wash which is not typically considered by UAS autopilots. The aerodynamic sensing strategy for the

Funtana tail section was conceived to provide flow field information across the tail surface during uncertain flight conditions and allow real time estimates of control surface authority.

The tail instrumentation package is comprised of a prop-wash probe and embedded pressure ports distributed across the horizontal stabilizer, elevator, vertical stabilizer and rudder. The prop-wash probe is a custom designed multi-hole probe that provides flow magnitude and direction forward of the vertical stabilizer. The tail pressure ports allow for differential pressure measurements to be obtained across the tail surfaces and for aerodynamic forces to be calculated through an area integration scheme.

The prop-wash probe has been deployed on both the flight test and wind tunnel platforms while the instrumented tail surfaces have only been mounted on the wind tunnel test model. The following subsections describe the two main components of the aerodynamic sensing package implemented on the wind tunnel model.

4.6.i Dedicated multi-hole probe for prop-wash estimation

Key assumption of current fixed wing autopilot systems is that aerodynamic flight control authority is strictly a function of the free-stream wind vector. Since the flow speed over control surfaces typically scales according to flight speed ability to generate aerodynamic forces and moments using control strategies such as gain scheduling are commonly tied to free-stream airspeed and angle of attack. While this is reasonable for most fixed-wing forward flight regimes, it is not accurate during aggressive maneuvering or operations past stall.

For a fixed-wing aircraft with excess thrust such as the Funtana, during low speed flight and hover the thrust generated by the propeller plays a significant role in supporting the aircraft in flight. Further, the single-propeller puller configuration induces significant airflow across the tail control surfaces at moderate to high throttle settings. In hover, the effectiveness of the control

surfaces to generate aerodynamic moments and torque depend solely on the prop wash which itself creates moments of its own due to the swirl imparted by the blades. Being able to characterize how the stream of accelerated air evolves during aerobatic maneuvering can offer insight into how future control laws might be adapted to better enable autonomous aerobatic flight.

To this end, a custom designed multi-hole probe was built to measure prop-wash velocity and angle of incidence on the tail surfaces. It was designed to measure flow speed and inflow angles in two axes by using a set of prongs with each terminating in a small pressure port. Its operating principle is similar to a cobra-probe [95], but one key difference is it uses an aft facing pressure port for a local estimate of dynamic pressure as well as an ability to characterize reverse flow in aerobatic conditions such as “backsliding” at zero thrust that could be exploited. The probe is mounted in front of the tail section and located approximately one vertical stabilizer chord length upstream to avoid excessive interference with the flow over the vertical tail. The geometry of the probe and a picture of it mounted on the Funtana fuselage is shown in Figure 4.6.

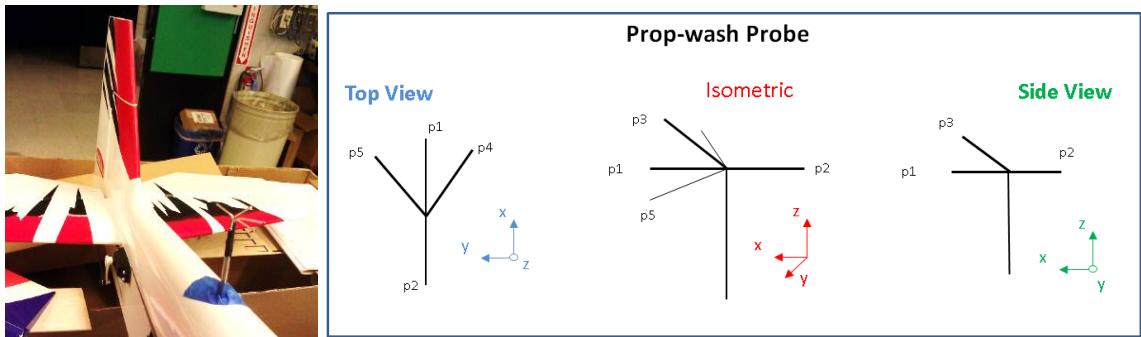


Figure 4.6 Prop-Wash probe location and geometry

The probe is built using aluminum tubing and provides flow angle and speed measurements by comparing the pressure measured across its prongs and is configured to use three differential pressure sensors. The current sensor configuration was chosen based on the expected pressure magnitudes encountered during wind tunnel and is summarized in Table 4.2. The procedure used to calibrate the prop-wash probe is described in Section 4.7.

Table 4.2 Prop-wash probe sensor configuration and port assignment

Probe Measurement	Pressure Sensor	Sensor Range (InH_2O)	Pressure Port Assignment
V_{pw} ,	HSCDR 2NGAA5	-0.3 to 2	P1 and P2
α_{pw}	HSCDR 1NDAA5	-1 to 1	P3 and P2
β_{pw}	HSCDR 4NDAA5	-4 to 4	P4 and P5

4.6.ii Instrumented tail

The tail surfaces on the wind tunnel model are instrumented with pressure sensors embedded within the structure. These provide real time measurements of the differential pressure across the tail surfaces that can be deployed during flight tests once verified by the FT measurements. The pressure ports are distributed across the horizontal stabilizer, elevator, vertical stabilizer and rudder as part of an area-discretization scheme. The schematic in

Figure 4.7 depicts the Funtana tail surfaces and provides an overview of the geometry used to discretize the tail surfaces.

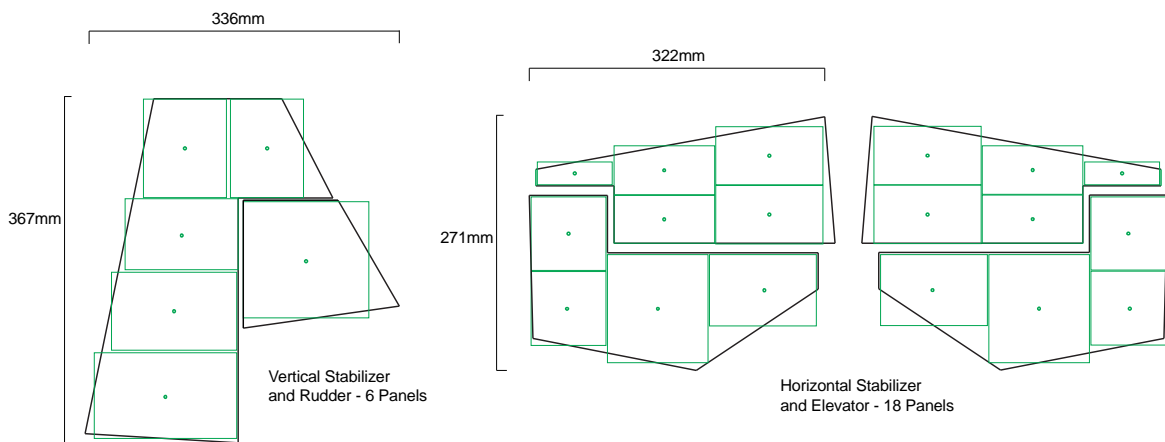


Figure 4.7 Distributed sensing over tail surface and area discretization scheme

The pressure ports are connected to Honeywell HSCDR 1NDAA5 pressure sensors with a $\pm 1InH_2O$ measurement range. These are the most sensitive sensors in the range HSCDR series that are small enough to be located within the surfaces. This allows for short and uniform pressure line lengths between

ports and sensors and reduces the low-pass filtering effect described in the flapping wing chapter. In order to accommodate the instrumentation, additional structure was fabricated and built into the tail surfaces. The horizontal stabilizer and elevators are shown in Figure 4.8.



Figure 4.8 Embedded pressure ports and sensors, horizontal tail surfaces
First, access panels were cut into the surfaces that were sheeted with balsa. The covering film over the rest of the sections were cut away and ironed along the exposed edges. Full size templates of the discretization scheme were laser-cut to locate each pressure port and each access panel. Where needed, additional balsa structure was fabricated and built into the elevators to accommodate the pressure ports. Holes were drilled and tygon tubing was used to connect the surface to each pressure sensor. The template designs are provided in Appendix B.

The ports and sensors are connected to provide differential pressure between top/bottom and left/right surfaces. This allows for a straightforward integration scheme such as the one used for the flapping wing force estimation. Once resultant aerodynamic forces are determined, the aerodynamic moments about the aircraft's center of gravity can be computed.

4.7 Calibration of instrumentation

The aerodynamic sensing system described in this chapter includes embedded pressure ports on the tail surfaces and a custom built multi-hole probe. The pressure ports in the tail were calibrated along with the pressure sensors, and the prop-wash probe was calibrated in a wind tunnel. The calibration procedures used for both are described in the following sub-sections.

4.7.i Prop-wash probe calibration

Calibration of the prop wash probe was performed in the University of Michigan 2'x2' instructional wind tunnel. The probe was mounted on a stand with adjustable orientation and data was taken at flow angles between -60 and 60 degrees at seven different airspeeds V_{air} between 3m/s and 21m/s. The first and second prongs were aligned with the wind tunnel flow by sighting down lengths of thread. Due to the use of forward/backward prongs, the reference dynamic pressure quantity changes slightly with inflow angle. This causes the calibration curves for α_{pw} and β_{pw} to be linear only for small flow angles. It was found that a 7th degree polynomial provided an adequate approximation. The data reduction and calibration scheme is described by Equations (4.25) through (4.27). The resulting calibration curves for prop-wash inflow angle are shown in Figure 4.9 for angles between -45 and 45 degrees.

$$\Delta q = p_1 - p_2 \quad \Delta \alpha = p_3 - p_1 \quad \Delta \beta = p_4 - p_5 \quad (4.25)$$

$$\alpha_{pw} = K_{\alpha 7} \left(\frac{\Delta \alpha}{\Delta q} \right)^7 + \dots K_{\alpha 3} \left(\frac{\Delta \alpha}{\Delta q} \right)^3 + K_{\alpha 2} \left(\frac{\Delta \alpha}{\Delta q} \right)^2 + K_{\alpha 1} \frac{\Delta \alpha}{\Delta q} + K_{\alpha 0} \quad (4.26)$$

$$\beta_{pw} = K_{\beta 7} \left(\frac{\Delta \beta}{\Delta q} \right)^7 + \dots K_{\beta 3} \left(\frac{\Delta \beta}{\Delta q} \right)^3 + K_{\beta 2} \left(\frac{\Delta \beta}{\Delta q} \right)^2 + K_{\beta 1} \frac{\Delta \beta}{\Delta q} + K_{\beta 0} \quad (4.27)$$

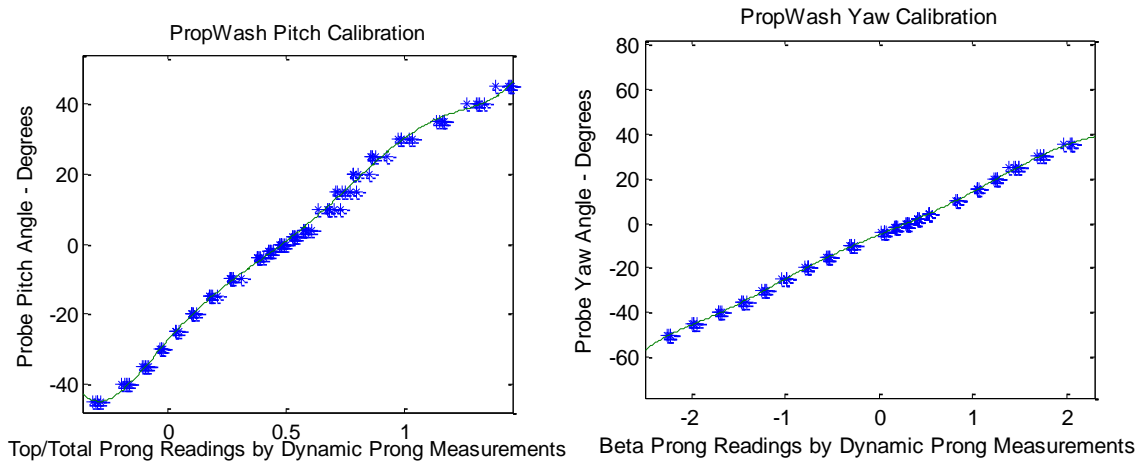


Figure 4.9 Prop-Wash probe flow angle calibration curves

For this dissertation, focus is placed on propeller backwash flow only so reverse-direction and larger-angle flows need not be considered in calibration. The normalized calibration data was consistent and general trends were as expected. While a 7th order polynomial was used for this calibration, the data is sufficiently linear that a simple linear fit would also be feasible in a situation with limited computing resources. When a linear fit is applied, the R^2 values for α_{pw} and β_{pw} are 0.9876 and 0.9934 respectively.

4.7.i.a Airspeed calibration

Due to the transverse mounting configuration of the prop wash probe, the estimate of dynamic pressure Δq is provided by a pair of fore-aft facing pressure ports instead of a traditional wing-mounted pitot probe. This configuration results in a scaled measurement of the dynamic pressure due to the rearward facing measurement and requires an additional calibration factor. This is experimentally determined by considering the airspeed calibration when the ports are aligned with the flow. In equation (4.28), the pitot-static airspeed formula with Δq given in Inches of water is scaled by the factor $K_{V_{pw}}$.

$$V_{pw_{\theta=0}} = K_{V_{pw}} \cdot \sqrt{\frac{2 \cdot 249.08 \cdot \Delta q}{\rho}} \quad (4.28)$$

Pressure data is taken with the probe lined up along the wind tunnel test section with flow angle $\phi = 0$. The airspeed is varied and a fit for $K_{V_{pw}}$ is obtained. The data and resulting calibration is presented in

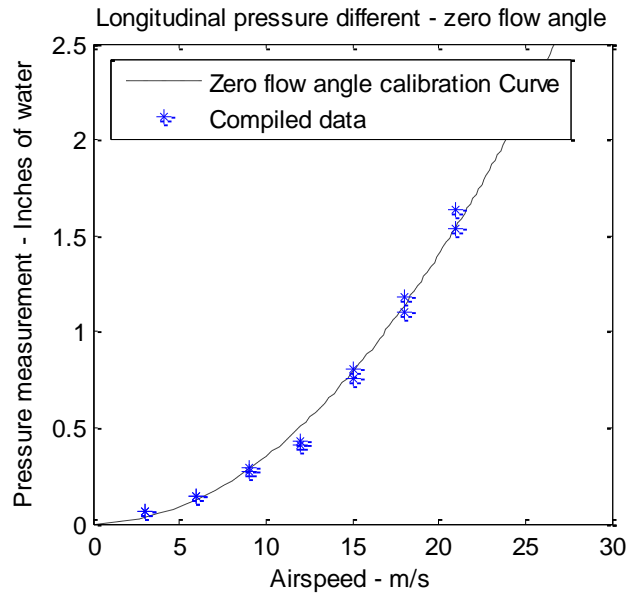


Figure 4.10 Airspeed calibration with $\phi = 0$

The fore-aft facing pressure port configuration is also sensitive to inflow angle and additional calibration steps are required to account for this effect. Figure 4.11 summarizes the variation of Δq at different flow speeds and different flow angles. In the data presented, the flow angle was varied with sideslip but the same misalignment applies if the flow was misaligned in alpha as well. Changing the flow angle at a given free stream velocity results in significant changes to Δq measurements taken with zero flow angle. At all velocities, it is observed to initially increase before decreasing at larger flow angles. As the geometry of the probe is constant, it is expected that this behavior is similar at all airspeeds within the test range. In order to verify this, the Δq values at the different free stream values are normalized based on the zero-angle measurement. These are also plotted in Figure 4.11, showing that the relationship between Δq and flow angle

are constant at all tested airspeeds. By normalizing the measurements, this deviation can be expressed in terms of flow angle ϕ .

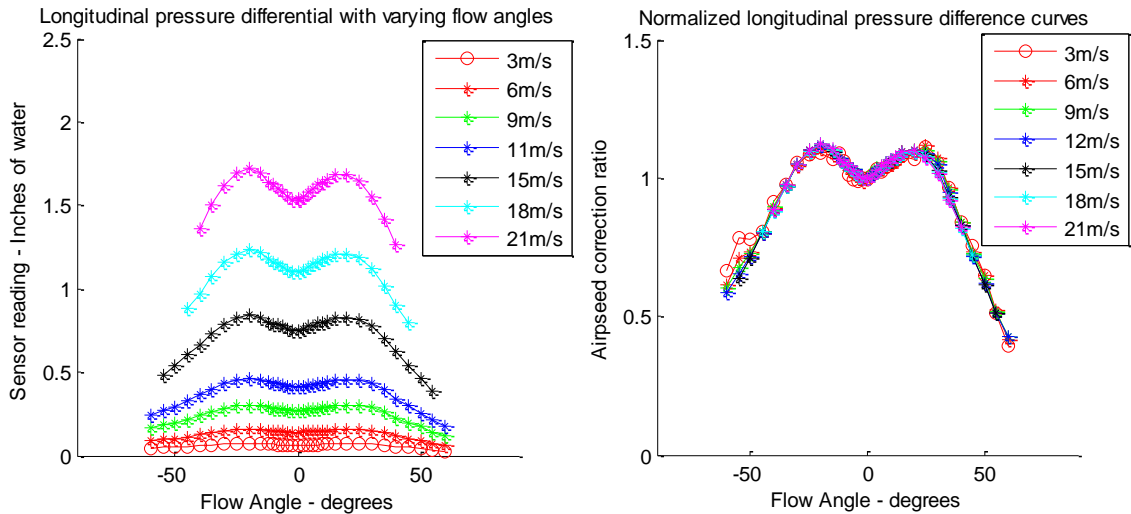


Figure 4.11 Pressure differences at different airspeeds and horizontal-plane flow angles.

Since flow angle is always known, an additional factor can be applied to correct for non-zero flow angles. This additional multiplier, cast as A_{ϕ} , relates Δq to indicated airspeed based on the current flow angle ϕ . When determining the value of A_{ϕ} , it is assumed that the relationship is symmetrical between positive and negative flow angles. This is reasonable as the effect of the miss-alignment between the fore-aft ports and the incoming flow depends only on the magnitude of ϕ . This is further supported by the symmetry observed in the data. Correction ratio data for flow angles greater than zero is compiled from the different free stream cases to form a calibration curve for A_{ϕ} . A third-order polynomial fit is then computed relating flow angle ϕ to A_{ϕ} . This is used in conjunction with the zero-flow-angle airspeed calibration given in Equation (4.28) and is shown in Equation (4.29) and Equation (4.30). The resulting calibrations are plotted

against experimental data in Figure 4.12 and the coefficients can be found in Table 4.3.

$$A_{\phi} = K_{\phi 3}\phi^3 + K_{\phi 2}\phi^2 + K_{\phi 1}\phi + K_{\phi 0} \quad (4.29)$$

$$V_{pw} = A_{\phi} \cdot K_{V_{pw}} \cdot \sqrt{\frac{2 \cdot 249.08 \cdot \Delta q}{\rho}} \quad (4.30)$$

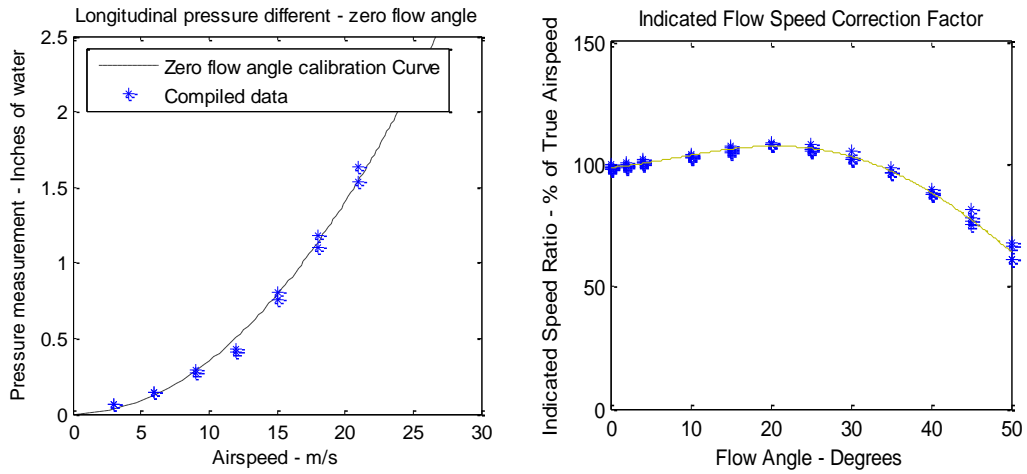


Figure 4.12 Airspeed calibration for zero-flow-angle (left) and correction factor (right)

Table 4.3 Prop-wash probe calibration coefficients

i	K_{α_i}	K_{β_i}	K_{ϕ_i}	$K_{V_{pw}}$
0	-27.269	-5.213	1.00	0.823
1	75.814	17.214	0.00055	
2	-34.57	-0.7229	-0.00066	
3	-142.85	-2.981	0.000019	
4	426.19	0.422		
5	-365.74	-0.828		
6	94.915	-0.0612		
7	3.6467	0.0658		

4.7.ii Tail-surface pressure port and sensor calibration

The Honeywell HSCDR 1NDAA5 pressure sensors pressure sensors embedded in the tail surfaces provide a measurement range of $\pm 1\text{inchH}_2\text{o}$ through a pre amplified analog signal that is linear over the 0-5V range. These were chosen as the HSCDR range were the smallest commercially available sensors available for this research that featured onboard amplifiers and could be embedded in the tail surfaces. A sample calibration of a HSCDR 1NDAA5 is shown in Figure 4.13.

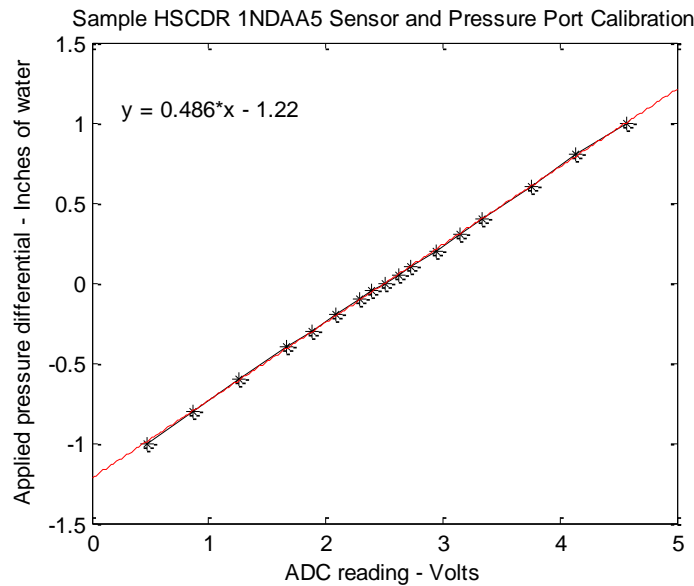


Figure 4.13 Sample calibration of an embedded tail surface sensor

All 24 sensors were calibrated during the embedding process. The pressure ports were connected to a harness splitting the pressure between a Dwyer inclined manometer and a syringe which was used to apply a pressure differential. The pressure calibration system for the left horizontal stabilizer/elevator is shown in Figure 4.14.

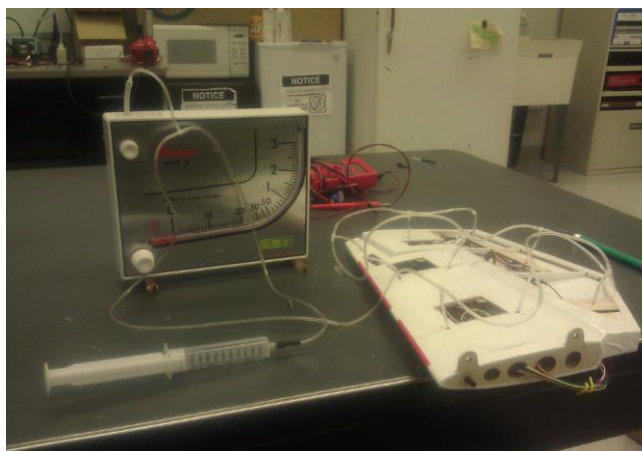


Figure 4.14 Pressure calibration test setup for the left elevator.

4.8 Wind tunnel test procedure

A series of wind tunnel tests were designed to evaluate the aerodynamic data system and to characterize prop-wash induced aerodynamic moments of the Funtana test platform under controlled and repeatable flow conditions.

The flow conditions across the tail surfaces were changed by varying wind tunnel free stream velocity, propeller revolutions per minute (RPM) and model mounting angle in the wind tunnel. A series of tail control surface deflection sweeps were carried out over a range of flow conditions. These include an elevator sweep with the rudder at zero deflection, a rudder sweep with the elevator at zero deflection, and a coarse combined rudder/elevator deflection sweep. The deflection ranges and step size were varied for each test condition depending on the maximum moments generated by the control surfaces to accommodate saturation limits of the embedded ATI force-torque sensor. An overview of this test series is shown in Figure 4.15.

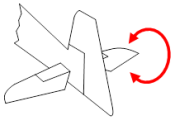
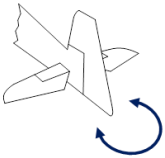
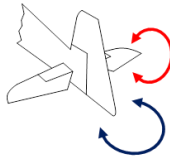
Throttle Setting	Pitch	Yaw	Coupled
			
45% ~12m/s Prop wash flow velocity	$\pm 40^\circ$ In 5° increments (20 data points)	$\pm 40^\circ$ In 5° increments (20 data points)	$\pm 40^\circ$ In ~15° increments
55% ~15m/s Prop wash flow velocity	$\pm 40^\circ$ In 5° increments (20 data points)	$\pm 40^\circ$ In 5° increments (20 data points)	$\pm 40^\circ$ In ~15° increments
75% ~18m/s Prop wash flow velocity	$\pm 35^\circ$ In 5° increments (18 data points)	$\pm 35^\circ$ In 5° increments (18 data points)	$\pm 25^\circ$ In ~10° increments

Figure 4.15 Basic test procedure overview – tests performed at 25° , 0° and -25° α .

An initial test series was run with the wind tunnel turned off and with all measured flow driven by the onboard propeller-driven thrust system. At a given propeller RPM, elevator and rudder deflection sweeps were carried out as described above. These were repeated for model mounting angles of positive 25° , 0° and negative 25° . When mounted at a non-zero angle of attack, a free stream in the test section is generated by the aircraft thrust system due to flow passage through the wind tunnel. The tunnel structure thus interacts with the prop-wash which results in different low-speed inflow conditions on the tail. A data set was also collected with the propeller fixed (no thrust) and a wind tunnel free stream of 12m/s. In this case, all flow is driven by the low turbulence free stream, allowing the instrumentation to be verified. The test conditions under which the basic test procedures were carried out are summarized in Table 4.4 where an 'X' indicates that the test case was run. A 5000RPM throttle setting was chosen for the

$\alpha = -25^\circ$ and $\alpha = 25^\circ$ cases to represent an approximation of a high-thrust low airspeed flight condition.

Table 4.4 Summary of basic test cases

	Free-Stream only	3000RPM	4000RPM	5000RPM	6000RPM
$\alpha = -25^\circ$				X	
$\alpha = 0^\circ$	X	X	X	X	X
$\alpha = 25^\circ$				X	

4.9 Experimental data processing and analysis

The wind tunnel experiments enable a comparison between aerodynamic pressure and ATI force-torque sensor (FT) measurements of tail section control moments. This allows verification of the two in-flight, aerodynamic data acquisition systems' ability to measure control surface moment application. To review, the full data acquisition DAQ package provides synchronized 1kHz data of unfiltered pressure measurements from the embedded sensors and resolved force and moment measurements from the ATI FT sensor. In order to compare both sets of measurements, the raw data from both sets of instrumentation must be pre-processed appropriately.

4.9.i Pressure data processing

The main objective of pressure data processing is to provide a reasonable estimate of the measurement noise that can be expected in actual flight conditions and to mitigate this noise through appropriate filter design and application. This will allow a more relevant comparison of pressure and transducer based instrumentation. Specifically, the filter must reduce or eliminate high-frequency fluctuations associated with the propeller while maintaining a high data update rate with minimal (acceptable) data lag.

Due to the turbulent nature of the flow behind a propeller, the raw pressure data is subject to significant noise that manifests itself as fluctuations about the average value that is representative of a given test condition. This can be quantified through the standard deviation of each data set. The plot in Figure

4.16 depicts a sample elevator sweep at 5000rpm with no free stream flow. The pressure measurements are integrated over the tail surfaces, allowing the aerodynamic moments to be computed and plotted. Each point represents the mean and standard deviation from 10 seconds of raw data.

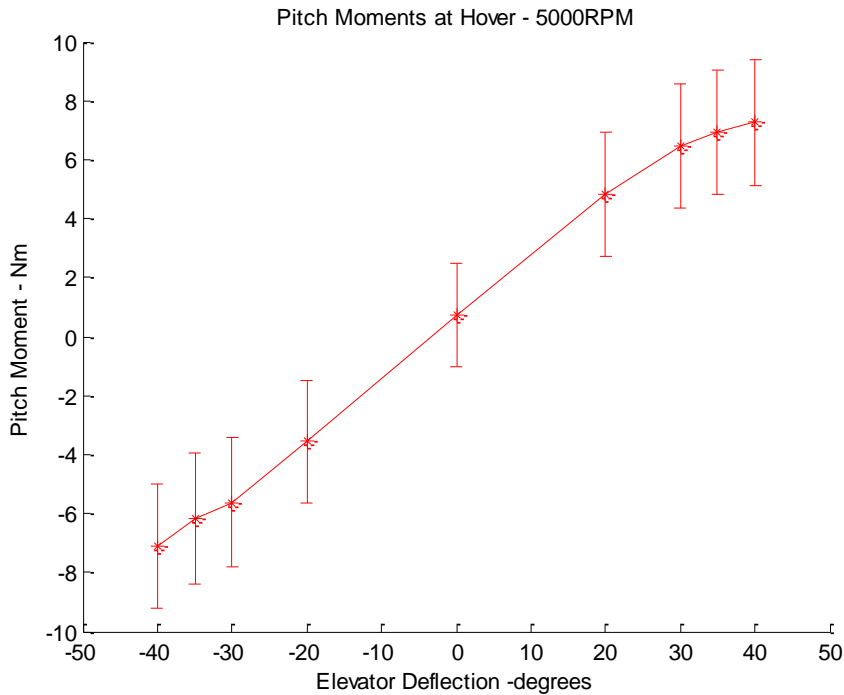


Figure 4.16 Significant standard deviation intervals in raw pressure data

The standard deviation intervals are observed to be large in comparison to the signal magnitude due to the highly turbulent flow field. While a post processing filter methodology such as the one taken for the FT data in Chapter 3 is suitable in an experimental scenario, a flight-ready filter algorithm will provide a more relevant estimate of how the aerodynamic instrumentation will perform when in the air. This section documents the approach taken to filtering raw pressure data collected during Funtana wind tunnel tests.

4.9.i.a Simple moving average filter

A filtering strategy that maintained a high data rate and but that could also be implemented for real-time data processing in flight was needed. For the purpose of this thesis, a Simple Moving Average filter (SMA) was chosen. An n point SMA is computed as the unweighted mean of the previous n measurements. For a series of n measurements $P_M, P_{M-1}, \dots, P_{M-(n-1)}$, the SMA is

$$SMA = \frac{P_M + P_{M-1} + \dots + P_{M-(n-1)}}{n} \quad (4.31)$$

where the period is the sampling rate multiplied by the number of averaged points and may be chosen based on the fluctuations present in the data. A period that is too short in comparison to the time scale of the main disturbance will result in excessive noise in the final signal, while a period that is too long will cause the aerodynamic data system to react too slowly to changing flight conditions. The following subsections describe the methodology used in determining a suitable period for the SMA filter.

4.9.i.b RPM-Scaled SMA period and filter performance

For operations within the wake of a propeller, it is assumed that the most important disturbance time scale will depend on propeller rotation rate. In order to verify this, a survey of SMA periods for different test cases was conducted. The standard deviation of each data set about an average value was chosen as a metric of filter performance. At each test RPM, a control surface sweep is performed and time averages at each elevator deflection are computed along with the standard deviation. The average width of the standard deviation for all deflection angles in the sweep is computed and normalized by the maximum pitch moment encountered. This normalized value represents the overall standard deviation for each RPM and is computed using a different number of

SMA points. In developing the filtering parameters, data from elevator sweeps is used. These are plotted in Figure 4.17 and show that the effect of SMA period on filter performance depends on propeller rotation.

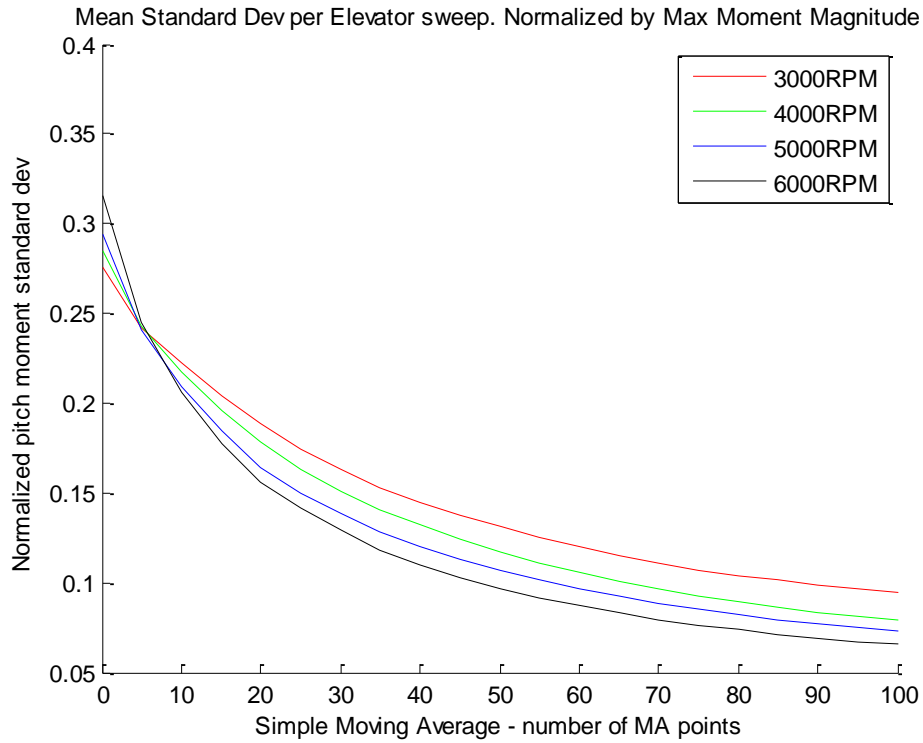


Figure 4.17 Variation of standard deviation intervals with increasing SMA period

Expanding this concept, a normalized SMA period was established based on the two per revolution flow excitation caused by each of the two propeller blades. This is based on the simplified assumption that the wake shed by each rotating blade is the main cause of pressure fluctuations in the data. This gives the SMA period for a particular test RPM as

$$T_{SMA} = \frac{1}{2} N_{wakes} \cdot \frac{60}{RPM} \quad (4.32)$$

where N_{wakes} refers to the time taken for approximately N wakes to be convected past the tail section. The variation of standard deviation based on SMA period is plotted on this “blade-wake” time scale in Figure 4.18. This time scale results in filter performance that is universal across the test RPM range.

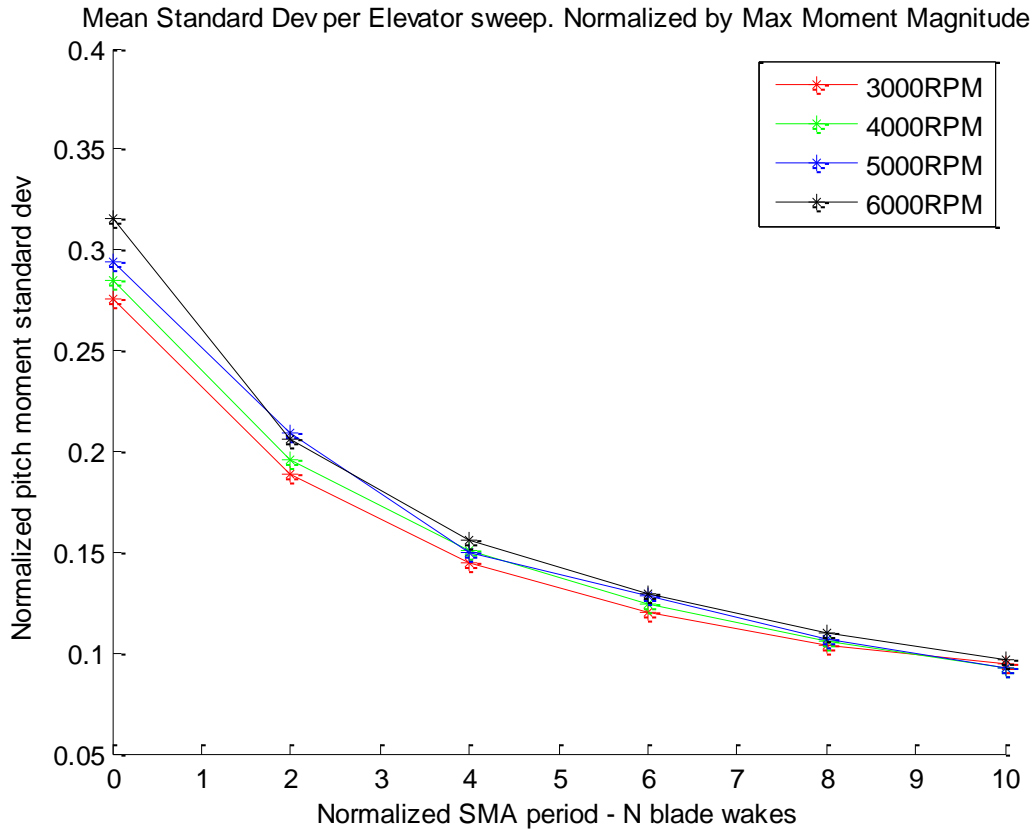


Figure 4.18 Results of scaling of SMA period based on propeller RPM

Note that with SMA periods that last as long as 2 propeller revolutions or 4 blade wakes, the standard deviation interval width throughout the test RPM range is approximately 15% of the maximum pitch moments encountered in a given thrust condition. If the SMA period is set to 5 propeller revolutions, standard deviation intervals are reduced to 10% of maximum deflection moments for all test cases.

Since RPM measurements may not always be available to the aerodynamic data system, this filtering strategy can be reformulated to utilize prop wash velocity

measurements and known characteristics of the propeller. Blade pitch is a unit of length defined as the distance advanced by the propeller over one full revolution if it turned in a solid medium with no slippage. It is customary to use the pitch angle of the blade at a radial point that is 70% of blade diameter [96]. As such, a frequency that is analogous to propeller RPM can be obtained by dividing the measured prop-wash velocity by the pitch of the propeller.

$$T_{SMA_{velocity}} = \frac{1}{2} N_{wakes} \cdot \frac{\text{Propellor Pitch}}{V_{pw}} \quad (4.33)$$

This version of the SMA period formula enables computing an appropriate SMA filter settings possible without RPM information. Figure 4.19 below shows that for N_{wake} greater than 6, or a filter period that lasts as long as three complete propeller revolutions, the standard deviation for all test cases falls within approximately 10% of the maximum measured pitch moment.

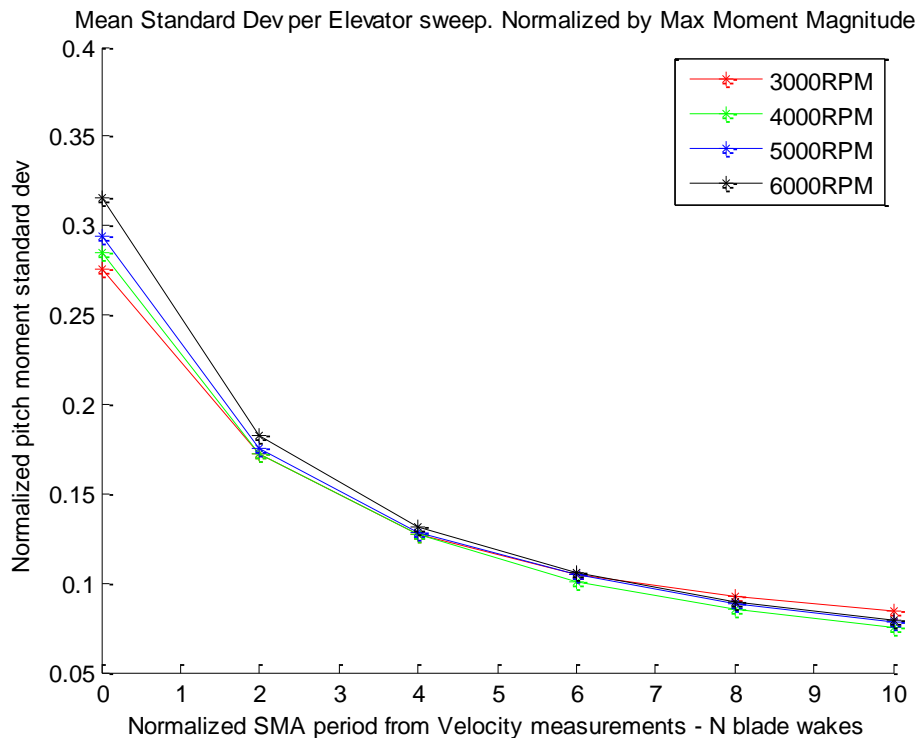


Figure 4.19 Performance of a vortex-frequency-based SMA period scaling methodology

For the purpose of comparing wind tunnel test results, an N_{wake} value of 4 was chosen. This corresponds to a SMA filter that averages data over the passage of four blade wakes or two complete propeller revolutions. It represents the most responsive filter setting that provides for consistent performance over the test range. By averaging over the period of two propeller revolutions, the filter is also sufficiently responsive for flight operations. This allows a comparison using data that is representative of the measurements that can be expected from the aerodynamic data system in flight.

Based on velocity measurements taken during tests and using a propeller pitch of 0.254m as specified by the engine manufacturer, the SMA filter settings for a 4 wake period with 1kHz sampling rate are summarized in Table 4.5..

Table 4.5 Computed Number of SMA points for test cases

Test Case RPM	Computed 2rev Period (s)	4-wake SMA filter points
3000	0.052916667	53
4000	0.043418803	43
5000	0.034794521	35
6000	0.028539326	29

These settings are used in generating the integrated pressure measurements for the prop-driven hover data presented in the following sections.

4.9.ii Frequency domain analysis of FT data

As only average forces and torques were required for this test, the frequency domain analysis of the FT data was limited to identifying anomalies and unexpected periodicities in the signals. Anomalies include modes associated with the structural response of the test stand and the unsteady aerodynamics. These can be differentiated by comparing the power spectral densities (PSDs) between

different propeller-only test cases, and also to a test case in which the structure is excited by a low-turbulence free stream.

When comparing different hover test cases, a common low frequency periodicity near 5Hz was observed along with its multiples. The plots in Figure 4.20 show the PSD for pitch moment measurements taken by the FT sensor between 0 and 50Hz. The two cases presented are a 4000RPM hover and a 6000RPM hover when mounted in the wind tunnel test section.

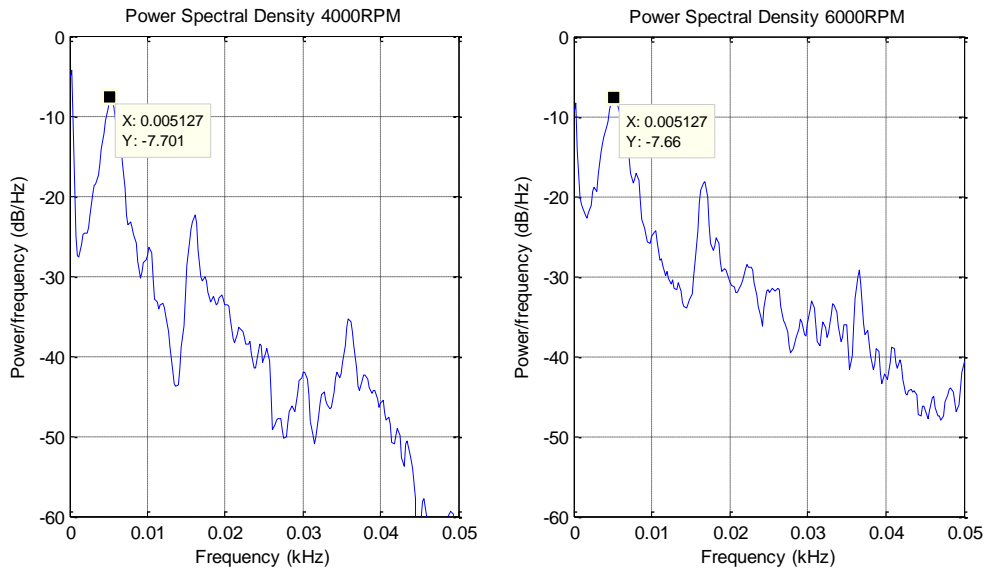


Figure 4.20 Structural response of the test stand near 5Hz

This periodicity at 5.1Hz is common across all propeller RPM settings, suggesting these peaks correspond to modes of the test structure. When considering higher periodicities at higher frequencies, it is observed that propeller RPM and its multiples are present. The 2nd multiple of propeller RPM is related to the tip vortex frequency from each of the two propeller blades and its contribution is noted to be approximately as significant as that of the the primary peak. This behavior is shown in Figure 4.21 for 4000 and 6000 RPM cases.

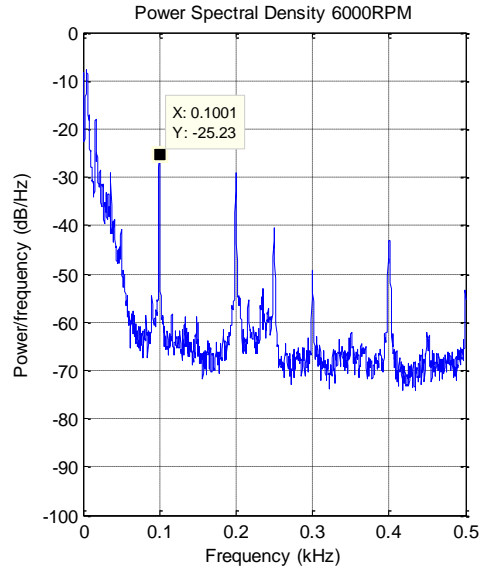
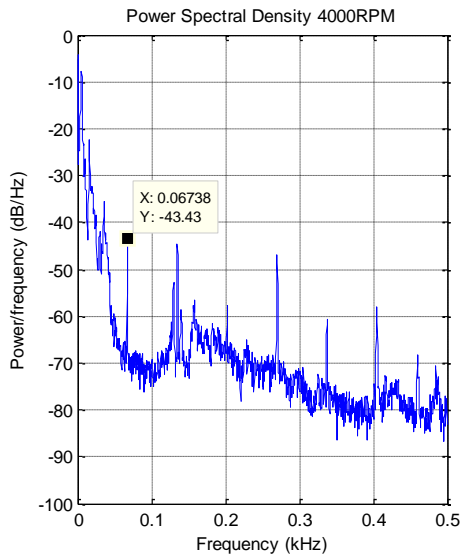


Figure 4.21 Flow excitations with multiples encountered at 4000 and 6000 RPM

An additional mode near 250Hz was also observed which is independent of propeller RPM. To examine this further, the PSD from a propeller-off test case where the structure is excited by an incident free stream of 12m/s is shown in Figure 4.22.

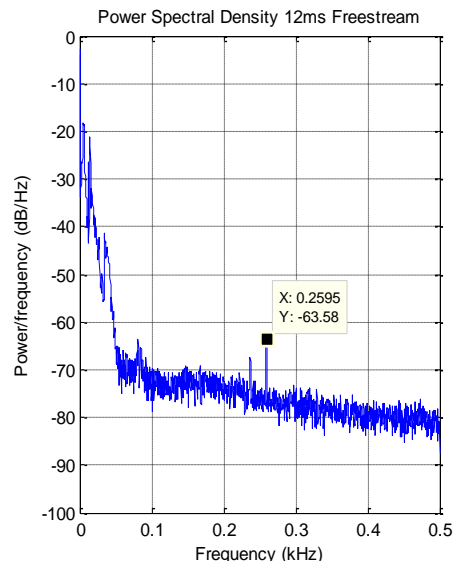
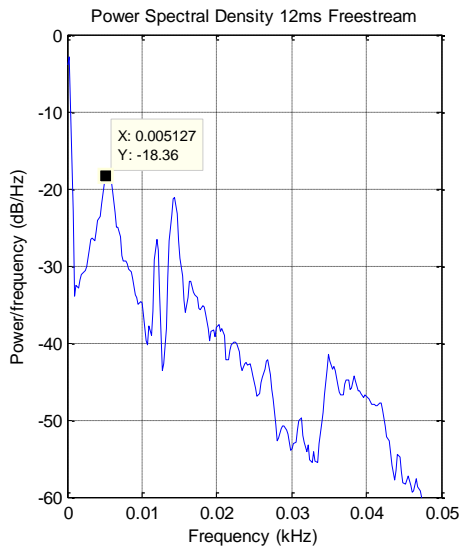


Figure 4.22 Low turbulence free stream excitation of structural modes

The same periodicity near 5Hz is encountered along with a diminished peak near 250Hz suggesting this is related to the test setup and unrelated to the unsteady aerodynamics. Based on this analysis, no unexpected periodicities associated with the aerodynamics were considered to be present in the FT data.

4.10 Propeller driven test cases

An objective of Funtana wind tunnel testing is to extend the ability of onboard aerodynamic sensing to provide real-time estimates of moments based on flow measurements over the tail as well as with the prop-wash probe. This section presents the data collected from the propeller-driven wind tunnel based tests that were performed.

In the following subsections, results from a set of hover tests are presented followed by a low-airspeed and a powered-cruise case. Test data will be summarized in a series of plots that describe the moments measured using both Aero and FT instrumentation with changing control-surface deflections. These results will be later used in developing two methodologies that extend the Aerodynamic Sensing Concept to high angle of attack and hover flight.

4.10.i Hover test results

High performance, propeller driven fixed wing aircraft such as the Funtana platform have the capability of steady hovering flight by using thrust to balance weight. A near-vertical attitude is then maintained through the use of large conventional control surfaces to control body-axis yaw and pitch with respect to vertical. Hover represents a challenge to traditional fixed-wing flight models and instrumentation because V_{ac} is zero and the wing is stalled. Researchers

[51,74,75] have successfully flown fixed-wing aircraft in hover with an augmented autopilot, but these autopilots have either experienced substantial tracking error (e.g., in altitude) or relied on high-speed external sensing (e.g., VICON motion capture). This section investigates the use of the distributed pressure sensing package to better capture and model yaw and pitching moments due to the propeller backwash enabling fixed-wing hover.

For this series of experiments, a simulated hover condition was established in the wind tunnel by mounting the vehicle level and leaving the wind tunnel motor off. All flow incident on the tail surfaces is due to the propeller wash. The propeller was run at 3000, 4000, 5000, and 6000 RPM. The test section access door was left open to minimize test section flow driven by the propeller. This allows the pressure and FT instrumentation to be compared in an approximately steady hover condition.

The flow direction measurements taken by the prop-wash probe during for the hover tests are summarized in Table 4.6. The flow angles appear to diminish slightly with increasing RPM but do not vary significantly. The proposed reformulation of the steady flight equations does not consider the swirl imparted by the propeller and these measurements are not used in the current analysis.

Table 4.6 Hover test prop-wash probe measurements for elevator sweeps

Prop RPM	α_{pw}	β_{pw}
3000RPM	-4.8	-11.6
4000RPM	-1.49	-12.44
5000RPM	-1.41	-10.29
6000RPM	-1.61	-9.44

4.10.i.a Hover pitch moment

Pitch control in a hover is achieved through the use of the conventional elevators operating in the high speed propeller wash. A series of elevator sweeps at were conducted at the four test RPMs. The conditions encountered for these tests are summarized in Table 4.7. Note that the wind tunnel is not climate-controlled thus

air temperature is influenced by ambient temperature in Michigan at the time of testing.

Table 4.7 Hover test conditions for elevator sweeps

Elevator Test Case	Average V_{pw} (m/s)	Air Temperature ($^{\circ}$ C)	Barometric Pressure (InHg)	Computed Air Density (kg/m^3)
3000 RPM	9.1	3	29.5	1.26
4000 RPM	11.7	8	29.4	1.23
5000 RPM	14.71	8	29.4	1.23
6000 RPM	17.81	3	29.5	1.26

The air density is calculated from temperature and barometric pressure measurements assuming dry air. Following convention, positive elevator deflections and pitching moments correspond to a nose up moment. Both sets of instrumentation show general agreement. As expected, pitch moments vary with increasing propeller RPM pressure. With increasing propeller RPM and flow unsteadiness, the standard deviations for both sets of measurements are larger. Pressure-based estimates are noted to be more susceptible to noise. The pitch moment data is summarized in Figure 4.23.

Both sets of instrumentation show that control moments are linear between a -25 and 25 degree elevator deflection range with a slight decrease in slope at larger deflections angles. The pressure based instrumentation consistently underestimates the measurements reported by the FT sensor, showing what appears to be a shallower slope. It is hypothesized that this is due to a consistent underestimation of the aerodynamic forces by the discretization scheme and this is explored in a later section.

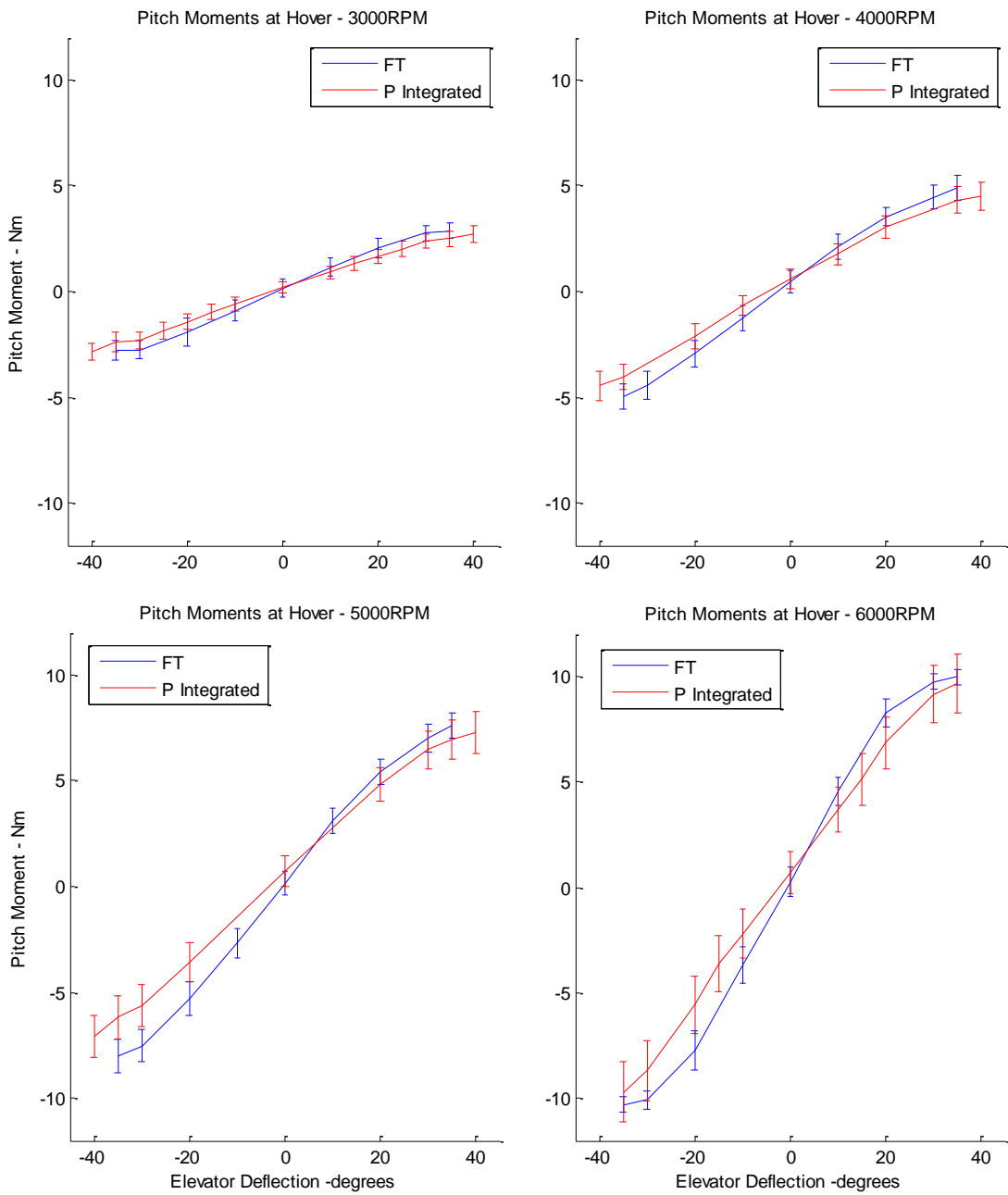


Figure 4.23 Pitch moment measurements at hover

4.10.i.b Yaw moment comparisons

As with the elevator, the rudder is used to command yaw moments when in a vertical hover. A series of yaw-only sweeps at the same propeller RPMs were carried out under conditions summarized in Table 4.8.

Table 4.8 Hover test conditions for rudder sweeps

Rudder Test Case	Average V_{pw} (m/s)	Air Temperature ($^{\circ}$ C)	Barometric Pressure (InHg)	Computed Air Density (kg/m ³)
3000 RPM	9.4	1	29.5	1.27
4000 RPM	11.93	11	29.4	1.22
5000 RPM	14.61	11	29.4	1.22
6000 RPM	17.81	1	29.5	1.27

As with the pitch moments and elevator deflections, convention is followed where positive rudder deflections result in positive yaw moments that point the nose of the aircraft to starboard. Both sets of instrumentation show general agreement. As expected, yaw moments scale with increasing propeller RPM. With increasing propeller RPM, the standard deviations for both sets of measurements are larger for yaw than for pitch. Pressure-based estimates are noted to be more susceptible to noise than FT data as with the pitch moment results but with fewer sensors and less cumulative measurement error, the standard deviation intervals of the aerodynamic yaw moment measurements were also noted to be smaller than for the pitch measurements. The yaw results are summarized in Figure 4.24.

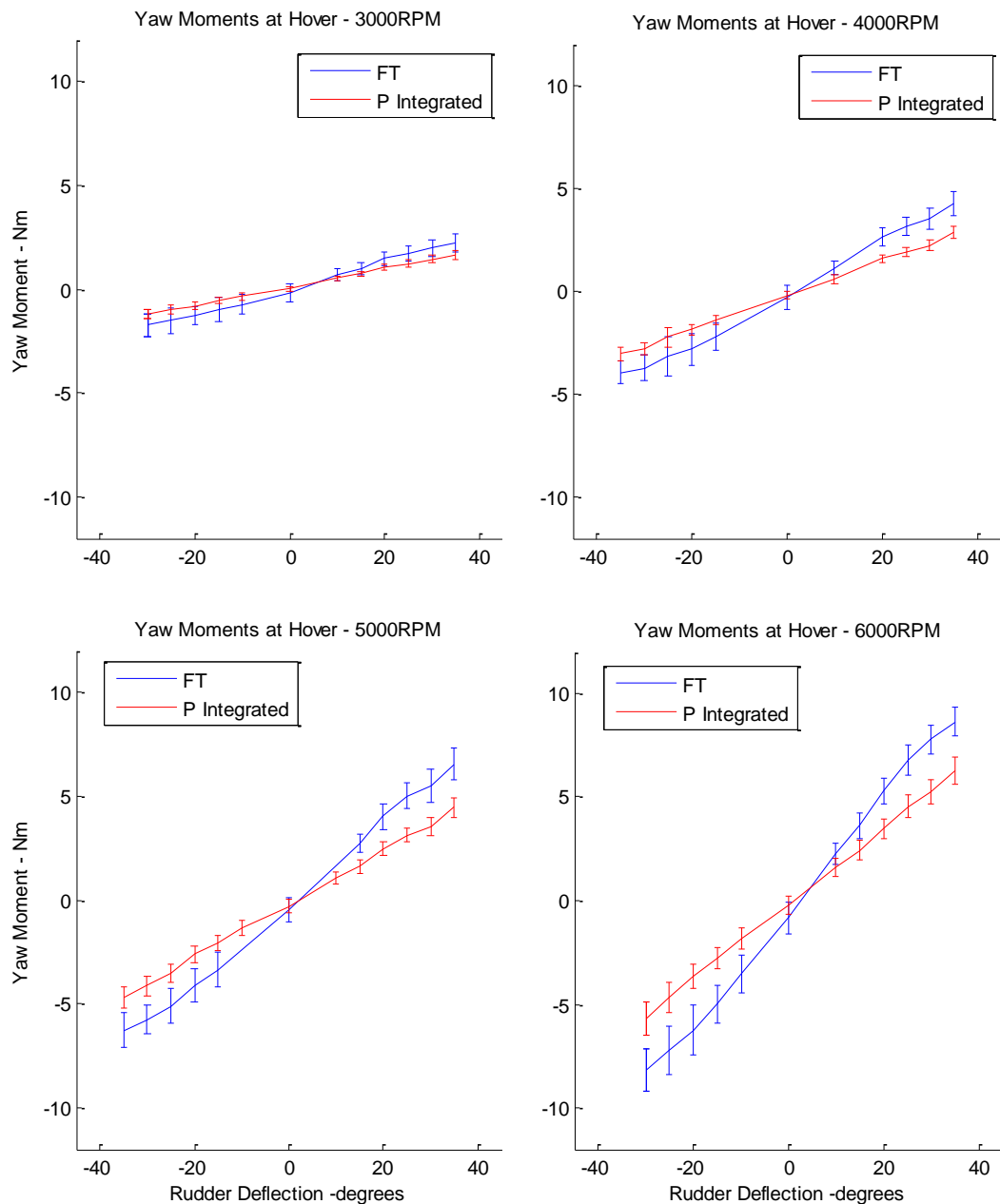


Figure 4.24 Yaw moment measurements at hover

Both sets of instrumentation show that control moments are mostly linear between a -25 and 25 deg range with a slight decrease in slope at larger deflections angles. As with the pitch moments, the pressure based instrumentation consistently underestimated the yaw moments measurements

reported by the FT sensor. The results show a larger discrepancy than that encountered with the pitch data which may be due to the yaw moment contributions from the un-instrumented vertical sides of the fuselage.

4.10.ii Combined free-stream and prop-wash cases

Hover is special case where the prop-wash is directed over the tail surfaces and is aligned with the fuselage. The flow conditions encountered during flight operations at high angles of attack are often more complex with an incident free-stream that can interact with the prop-wash. Two simple test cases were run to evaluate the aerodynamic sensing concept beyond hover.

The first is a simulated level cruise condition where the free-stream velocity vector is aligned with the thrust line. The second case represents a low-air-speed, post wing stall condition near hover. These two exploratory test cases were chosen to work within the constraints of the wind tunnel test section. The main focus of these experiments is providing data to evaluate the aerodynamic sensing scheme under mixed flow conditions. Plans for more comprehensive testing throughout the flight envelope of the aircraft are described in the future work section of this chapter.

4.10.ii.a Test case *5kCruise*: forward flight results

A 5000 rpm cruise flight test case approximates a flight condition where the incident free stream is substantial but still slower than the prop wash probe airspeed accounting for flow conditions aft of the propeller. This test provides a mixed flow environment across the tail surfaces where there is a significant degree of uniform flow over the airframe in addition to the incident propeller wash. The propeller is set to rotate at 5000 rpm with the aircraft mounted level in a free-stream of 12m/s. The conditions encountered during the *5kCruise* test case are summarized in Table 4.9.

Table 4.9 Test conditions for the *5kCruise* case

5kCruise Test Case	Average V_{ac} (m/s)	Average V_{pw} (m/s)	Air Temperature (°C)	Barometric Pressure (InHg)	Computed Air Density (kg/m ³)
Pitch	12.31	18.24	3	29.1	1.24
Yaw	12.35	19.32	3	29.1	1.24

With the addition of a low-turbulence free stream, both FT and pressure measurements show smaller standard deviation intervals. Note also that the control moments are significantly larger for the same surface deflections when at hover. This is due to the faster and more uniform velocity over the entire tail section driven by the free stream. The plots in Figure 4.25 summarize these results.

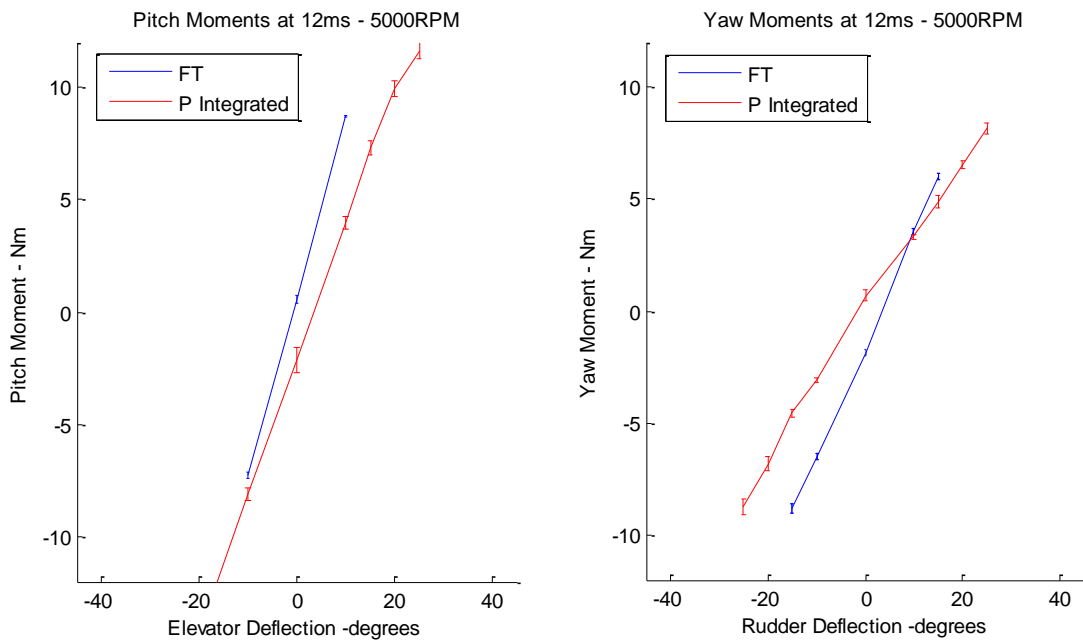


Figure 4.25 Pitch and Yaw moment measurements at 12m/s and 5000rpm.

While the velocities reported by the prop-wash probe are only slightly larger than those encountered at the 6000RPM hover case, it is clear that the resulting

moments are significantly larger. This indicates that prop-wash probe measurements alone are not sufficient in describing the flow conditions over the tail under all flight conditions. During flight operations that cross different flight regimes, the information from the prop-wash probe will still need to be augmented by conventional aircraft wind vector measurements, or else model coefficients will need to be scheduled by free-stream velocity conditions rather than strictly using prop-wash information. Further testing is planned and is described in the future work section at the end of this chapter.

Under these larger flow velocities, the distributed pressure sensing scheme still provides moment estimates that agree with those measured by the FT sensor. The moments remain linear with control surface deflection and the pressure-based slope is again seen to be shallower than the slope given by the FT data.

4.10.ii.b Test case *Alpha25*: low speed non-zero angle of attack case

In the cruise case, the incident free stream is aligned with the propeller wash resulting in relatively simple interaction. During operations at low free-stream airspeed, large angles of attack up to 50 degrees have been encountered that can dramatically change the local flow conditions across the tail surfaces. The conditions in this test case aim to represent some of these challenges, with the 25 degree angle of attack selected based on wind tunnel test section size constraints. For this test set, the aircraft is mounted at a 25 degree angle with respect to the test section and the door is shut. The propeller is driven at 5000RPM resulting in a small but measurable free stream through the test section. As an added complication, the tail surfaces are placed near the floor of the test section and are subject to wall interactions. The test conditions are presented in Table 4.9.

Table 4.10 Test conditions for the *Alpha25* case

Alpha25 Test Case	Average V_{ac} (m/s)	Average V_{pw} (m/s)	Air Temperature (°C)	Barometric Pressure (InHg)	Computed Air Density (kg/m ³)
Pitch	2.05	17.02	5	29.2	1.24
Yaw	2.01	16.9	1	29.5	1.27

With the propeller driven at 5000RPM, the measured prop-wash velocities are comparable to those encountered in the previous test case with a large free stream. This is likely due to the significant test section blockage causes by the model when mounted at 25 degrees causing a localized region of accelerated flow near the model. This does not affect the comparison since both sets of instrumentation are subject to the same flow conditions, making for a valid comparison. The results of the Alpha25 test case are plotted in Figure 4.26.

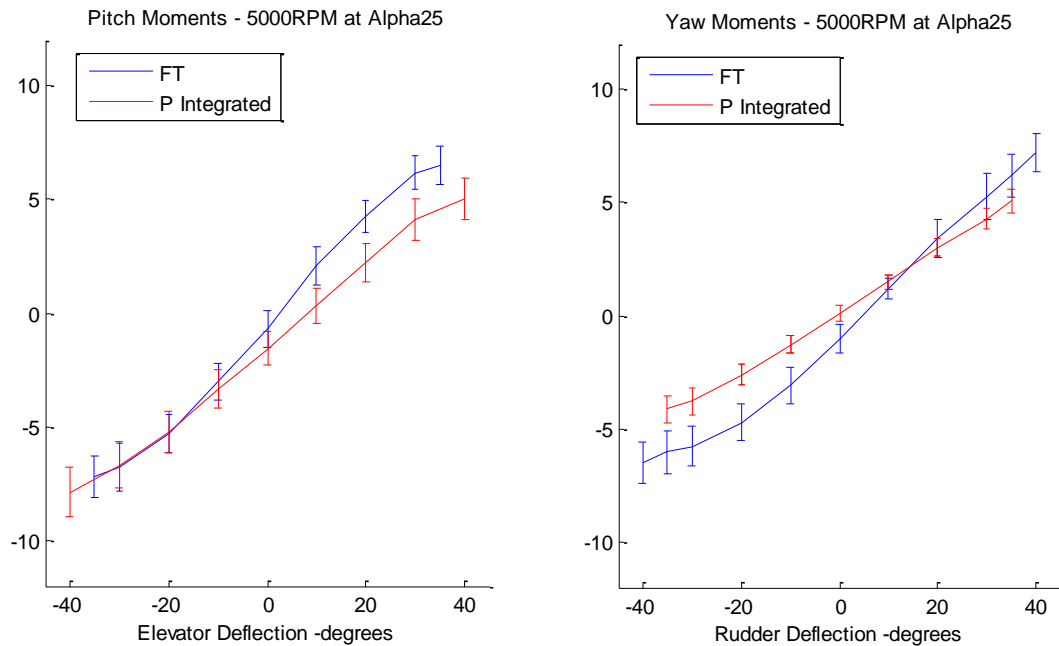


Figure 4.26 Pitch and yaw moments from the Alpha25 test case

The effect of wall interaction can be more clearly observed in the yaw moment data. At rudder deflections between -40 and -15 degrees, a change in slope is observed. This is likely due to the clockwise swirl caused by the propeller interacting with the test section floor thus affecting the flow angle of attack on the rudder. As with all the previous cases, the aerodynamic instrumentation is seen to consistently underestimate the resulting moments generated.

4.10.iii Independence of pitch and yaw control surfaces

In the steady flight equations, it is assumed that elevator and rudder commands are independent of each other such that elevator deflections do not affect yaw moments, and rudder deflections do not impact pitch moments. A series of tests were run to estimate the effect of elevator commands on the yaw moments when in a hover condition. This would determine if the reformulated flight equations for steady hover and high-angle of attack flight will require additional terms that account for this effect.

A rudder sweep was performed at a number of elevator deflections angles for each of the thrust settings and the yaw moments measured by the FT sensor are compared. These are plotted in Figure 4.27.

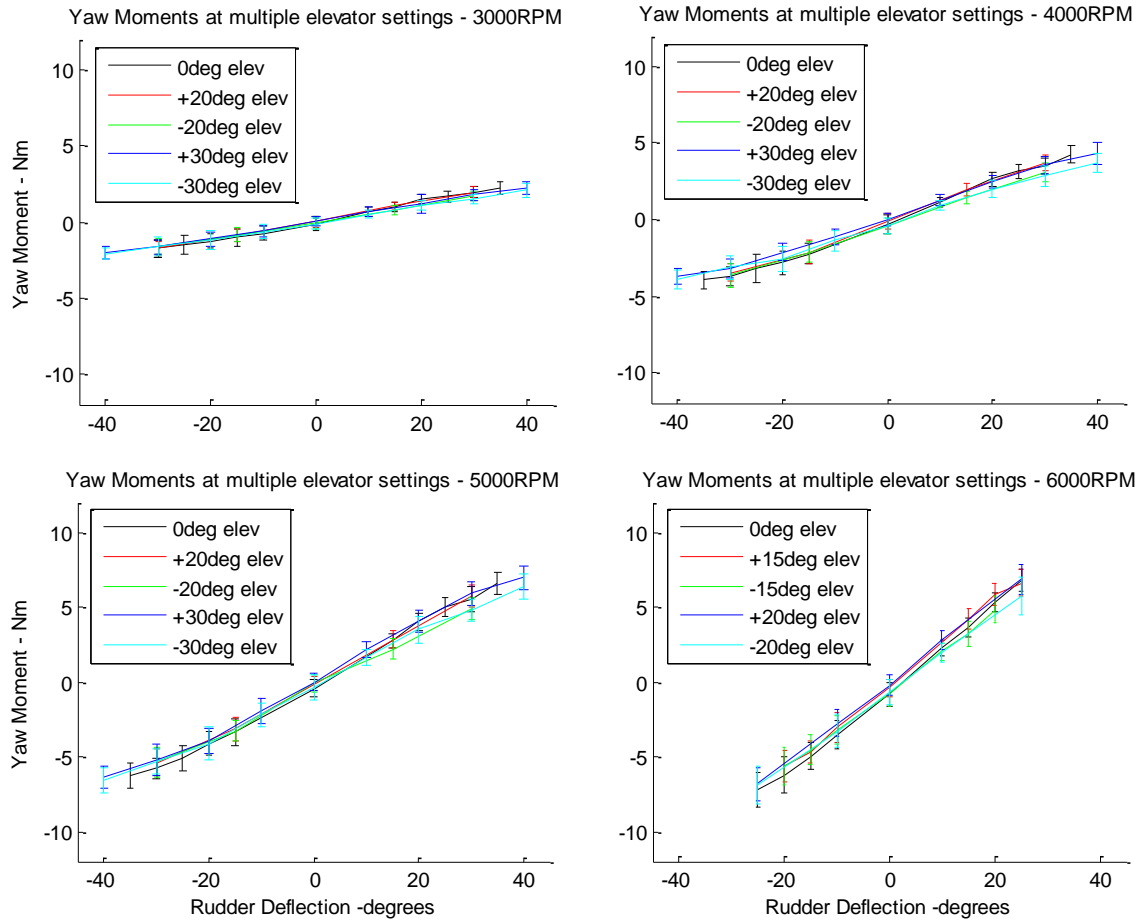


Figure 4.27 Combined elevator and rudder deflection test cases showing negligible cross coupling between elevator and yaw moments

Throughout the linear range of elevator deflection between -30 and 30 degrees, the yaw moments resulting from rudder commands do not vary appreciably. This shows the elevator does not affect the yaw moments across the test range. The data from these tests allow a limited characterization of the reverse relationship. Two sample plots at 3000RPM and 6000RPM are shown in Figure 4.28 depicting elevator sweeps with changing rudder. It can be observed that throughout the range of 30 and 30 degrees of rudder deflection, the relationship between elevator commands and pitch moments remains the same. This validates the assumption of decoupled pitch and yaw moment control in a hover.

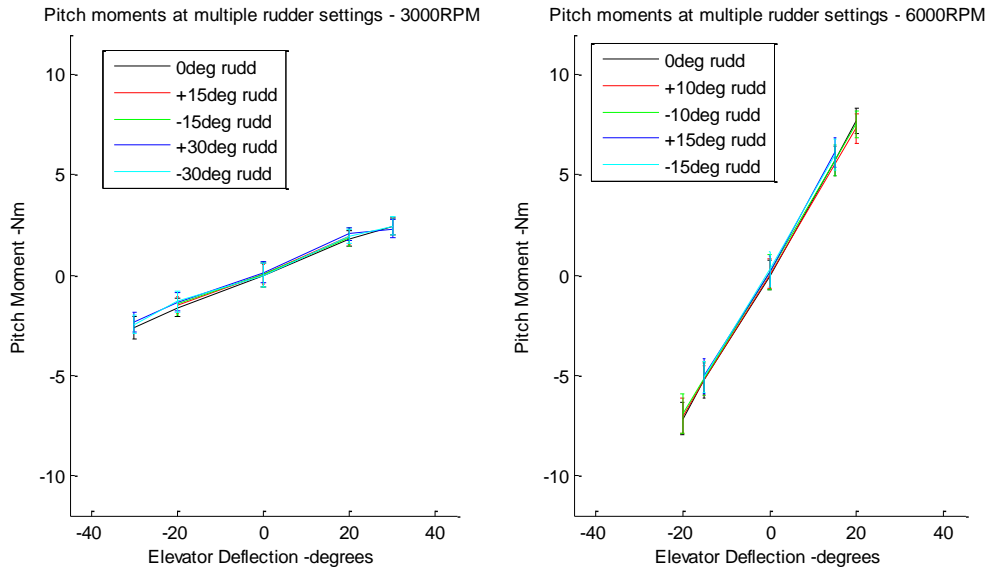


Figure 4.28 Combined rudder and elevator deflection test cases showing negligible cross coupling between rudder and pitch moments

4.10.iv Summary of test results

Pitch and yaw measurements from a series of wind tunnel based tests have been presented. Measurements from the aerodynamic sensing system were filtered using a simple moving average filter with a period equal to two propeller revolutions. This is representative of the quality of data that is available in flight. The FT measurements were time averaged.

Data from all the test cases indicate linear relationships between control surface deflections and the aerodynamic moments associated with them. This is in agreement with expected trends. A baseline comparison between independent FT and pressure based measurements indicate that the aerodynamic data system slightly underestimates the moments measured by the FT sensor. This discrepancy is discussed further below.

Airspeeds measured by the prop-wash probe increase with increasing propeller RPM as expected suggesting that the concept is valid and provides data that can be used for real-time flow characterization over the tail, potentially in conjunction

with free-stream flow measurements from the traditional wing-mounted air-data probe given mixed flow conditions

4.11 Linear moment model development for hover

While the post-stall flight regime is non-linear with respect to lift, drag and angle of attack, it was observed from the data that the pitch and yaw moment response to changing elevator and rudder deflections are largely linear when in a hover. This allows a linear moment model to be established based on experimental results.

The focus of the wind tunnel test series is to extend the ability of the aerodynamic sensing to provide enhanced estimates of control authority based on flow measurements over the tail. One approach is to simply extend the steady flight equations to hover by using the additional prop-wash probe measurements. This is only possible if the relationship between control surface deflections and aerodynamic moments are approximately linear in hover as they are in steady forward flight. From wind tunnel testing, it can be seen that the linear trends implied by the steady flight equations are indeed present in hover. This suggests that coefficients can be developed around additional wind vector measurements (from the prop-wash probe) even at zero vehicle airspeed.

This section presents pitch and yaw moment coefficients extracted from Funtana hover test data. This forms a linear aerodynamic moment model for hover that is analogous to the steady flight equations. The resulting model is compared against flight data and the limitations of the linear approximation are discussed, also motivating the additional use of distributed pressure sensing.

4.11.i Moment coefficients for use with V_{pw} in hover

Recall the proposed pitch and yaw moment equations from Equations (4.13) and (4.16):

$$M = \frac{1}{2}\rho V_{ac}^2 S b C_{M_{ac}} + \frac{1}{2}\rho V_{pw}^2 S_{htail} C_{M_{htail}}$$

$$N = \frac{1}{2}\rho V_{ac}^2 S c C_{N_{ac}} + \frac{1}{2}\rho V_{pw}^2 S_{vtail} C_{N_{vtail}}$$

With the additional prop-wash airspeed measurement and the moment measurements from the FT sensor, the new pitch and yaw coefficients for the reformulated steady flight equations can be determined. When in a hover, aircraft airspeed V_{ac} will approach 0. This allows the above equations to be simplified as

$$M_{hover} = \frac{1}{2}\rho V_{pw}^2 S_{htail} C_{M_{htail}} \quad (4.34)$$

$$N_{hover} = \frac{1}{2}\rho V_{pw}^2 S_{vtail} C_{N_{vtail}} \quad (4.35)$$

Since basic air data systems are only capable of measuring V_{ac} , this formulation represents the ability for feedback that is not available without additional instrumentation developed in this work. Through estimates of dynamic pressure $\frac{1}{2}\rho V_{pw}^2$ over the tail surfaces, the additional prop-wash probe measurement V_{pw} allows determination of the moments in hover. The moment coefficients were given previously by Equations (4.15) and (4.18) as:

$$C_{M_{htail}} = C_{M_{htail_0}} + C_{M_{htail_\alpha}} \alpha_{tail} + C_{M_{htail_{\delta_e}}} \delta_e$$

$$C_{N_{vtail}} = C_{N_{vtail_0}} + C_{N_{vtail_\beta}} \beta_{tail} + C_{N_{vtail_{\delta_r}}} \delta_r$$

In a fixed flight condition such as hover, the incident flow angles due to the propeller wash is approximately constant. This allows both terms to be treated as a single coefficient in hover as in

$$C_{M_{htail}} = C_{M_{htail_0_{hover}}} + C_{M_{htail_{\delta_e}}} \delta_e \quad (4.15a)$$

$$C_{N_{vtail}} = C_{N_{vtail_0_{hover}}} + C_{N_{vtail_{\delta_r}}} \delta_r \quad (4.18a)$$

where the coefficients are determined from the hover test series by normalizing the pitch or yaw moment data by tail surface area and by measured local dynamic pressure. Once the data has been normalized, a linear fit across the linear range of the data for the hover coefficients is obtained. The plots in Figure 4.29 show normalized pitch and yaw moment data and the resulting linear fit for each axis. The trend lines for the cases collapse when normalized and show strong linear trends. The resulting coefficients and R^2 correlation values are summarized in Table 4.11.

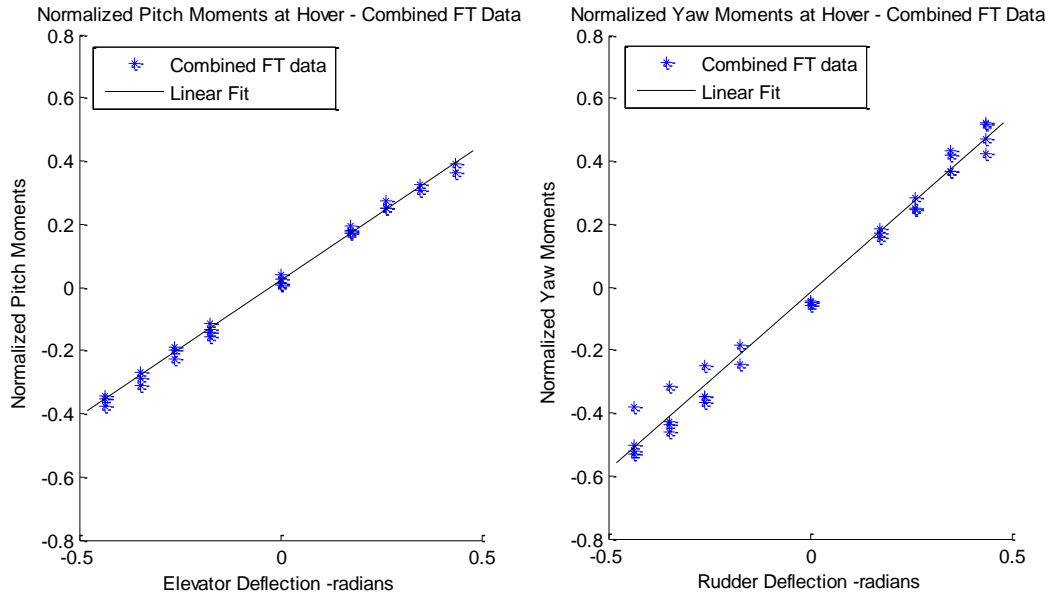


Figure 4.29 Compiled FT data from hover cases and resulting linear fit

Table 4.11 Linear aerodynamic coefficients computed from hover data

Axis	$C_{moment_0_{hover}}$	C_{moment_δ}	R^2
Pitch	0.0196	0.8689	0.996
Yaw	-0.0190	1.139	0.983

Through the described methodology, the coefficients in the proposed equations for hover, (34) and (35) can be determined. These represent a linear aerodynamic model similar to the basic steady flight equations that is made possible through an additional velocity measurement. Note that these coefficients are valid only for a range of operating conditions where aircraft airspeed is negligible and the prop-wash is approximately aligned with the fuselage.

4.11.ii Further investigation of the linear aerodynamics model

As with the original steady flight equations, the model described above is only valid in conditions for which a linear model is sufficient. Key coefficients are determined by only considering data within the ranges of control surface

deflections for which linear curve fits adequately approximate resulting moments. This section compares the output of the linear model against actual test data and discusses its performance under the different test conditions encountered.

4.11.ii.a Validation of the linear model for hover

Estimates of the linear model are compared against the normalized pitch and yaw FT data encountered in hover across all test conditions. Results are shown in Figure 4.30. Based this comparison, the pitch and yaw moment linear models are valid throughout a large range of the hover data. The linear models tend to overestimate moments due to deflections larger than 20degrees. All predictions are accurate for 4000, 5000, and 6000 RPM cases so long as the control surface deflection is 20 degrees or less. Pitch estimates are also consistently accurate for the 3000 RPM case.

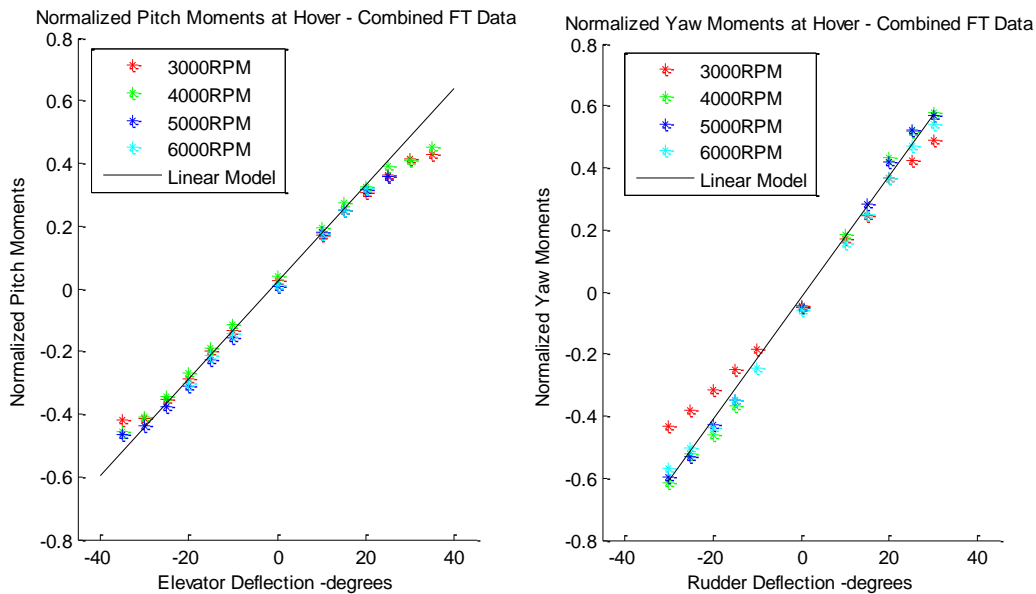


Figure 4.30 Comparison between linear model and compiled hover data

It can be noted that in a 3000RPM hover case, the test data shows a noticeable asymmetry in control authority for left-rudder commands. This is likely due to the relatively more pronounced clockwise flow structure at prop-wash velocities. Since the linear model is a compilation of all hover data, this asymmetry is not

reflected in its output. To summarize, when in a hover, the coefficient-based formulation of the reformulated steady flight equations generally work well in reproducing the pitch and yaw relationships that were used to determine its coefficients when an additional prop-wash velocity measurement is available.

4.11.ii.b Combined propeller and free-stream flow

The *5kCruise* test case combines an incident free stream at zero angles of attack and sideslip with propeller backwash. This data set allows the linear model to be evaluated under forward flight conditions, testing the hypothesis that the prop-wash probe will provide useful flow information over the tail section throughout the flight envelope. The comparison is presented in Figure 4.31 for both pitch and yaw.

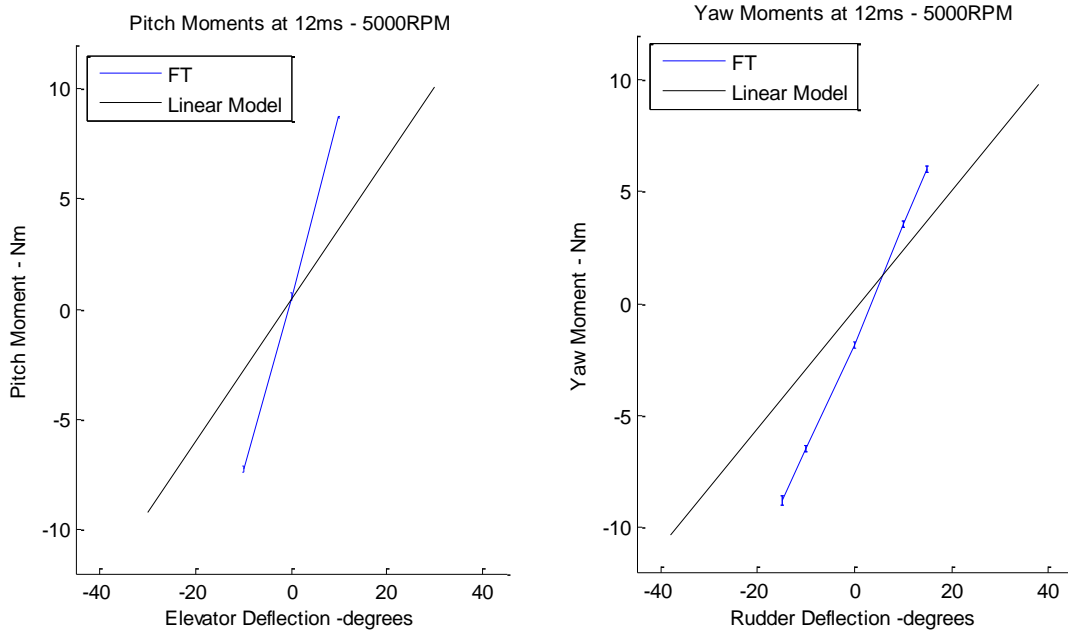


Figure 4.31 Linear model comparison with powered cruise test data

When in a forward flight condition, V_{ac} will be significant. Recall the steady flight equations for pitch and yaw moments from (4.13) and (4.16):

$$M = \frac{1}{2}\rho V_{ac}^2 S b C_{M_{ac}} + \frac{1}{2}\rho V_{pw}^2 S_{htail} C_{M_{htail}}$$

$$N = \frac{1}{2}\rho V_{ac}^2 S c C_{N_{ac}} + \frac{1}{2}\rho V_{pw}^2 S_{vtail} C_{N_{vtail}}$$

Since the coefficients $C_{M_{ac}}$ and $C_{N_{ac}}$ are still being determined as part of ongoing work, this comparison will focus only on the slope predicted by the linear model and prop-wash probe velocity measurement, V_{pw} . Using this model, the predicted slopes are significantly different from the actual measurements and the control moments are underestimated. This result shows that prop-wash probe measurements of velocity are not sufficient to fully describe the flow field across the tail surfaces and additional testing is needed to investigate the possibility of utilizing a linear aerodynamics model across different free stream conditions. We hypothesize that prop-wash plus traditional air-data probe measurements can enable such envelope-wide flow characterization but such tests are reserved for future work. The following section describes a comparison with the *Alpha25* test case that is similar to hover and examines the suitability of the linear model just outside its intended range of flow conditions.

4.11.ii.c Linear Model Applicability Near Hover

The linearized moment model developed at hover is further investigated at the slower free-stream conditions (2 m/s) established for the high-alpha wind tunnel test series discussed previously. By comparing the output of the linear model to the *Alpha25* case, the linear model can be assessed outside of the data that was used in its formulation, representing a “high-angle, slow flight” condition that might be quite useful for small UAS flight operations. In *Alpha25* configuration, the test section flow that is incident on the aircraft at a non-zero angle introduces a degree of free-stream interaction with the prop-wash. While the mounting angle of the aircraft is large, the incident free stream is small thus simulates an aircraft that is maneuvering near hover. Wall effects due to the test section represent unknown flow conditions outside of the original test series but cannot be avoided with the full-scale Funtana model and limited test section size. The comparison between acquired FT data for *Alpha25* and estimates from the models linearized from hover are shown in Figure 4.32 for both pitch and yaw.

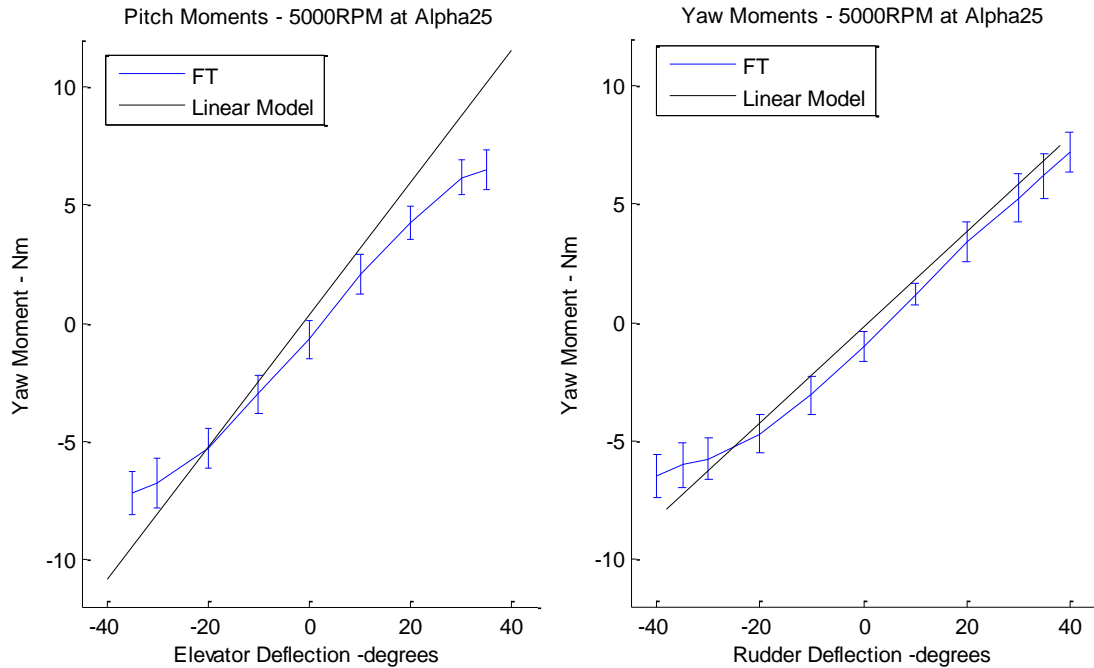


Figure 4.32: Linear model compared with *Alpha25* test case results

The linear model is capable of predicting the general trends but does not precisely align, particularly in pitch. The difference at small elevator deflections, on the order of 1.5Nm, is likely still adequate for use in a feedback control model. The linear model predicts yaw moments adequately until non-linear effects are encountered at large rudder deflections. However, the slope of the pitch data is noticeably different from the slope encountered in hover, suggesting that a new set of coefficients will be required even for small free-stream flow velocities.

4.11.iii Summary of the linear model analysis section

A linear aerodynamic moment model for hover has been proposed and formulated using data from wind tunnel based testing. A set of coefficients for hover were computed and verified capable of reproduce experimental data across multiple prop-wash flow conditions.

From a comparison with the *5kCruise* case, the prop-wash probe and hover model are determined to be incapable of fully describing the flow conditions over the tail when in an appreciable free-stream flow field. New linear coefficients will be required for different free stream flow conditions to enable the prop-wash and

traditional air-data probes to collectively represent moments accurately. Based on comparisons with the *Alpha25* case, even relatively small deviations from hover will require incorporation of free-stream flow terms into the moment equations.

Even if a full characterization of the aircraft is practical, a linear model will still be unable to deal with unexpected flow conditions or environments outside of the data used to create it. The embedded pressure sensing system outlines a more direct approach to determining the aerodynamic moments encountered in flight as discussed below.

4.12 Direct aerodynamic sensing scheme

A direct measurement scheme offers potential improvement over the linear modeling approach presented above. In the current configuration, distributed sensing across the tail section allows pressures to be measured across the stabilizer and control surfaces. This allows the actual aerodynamic moments induced by the tail to be measured in flight. By taking measurements instead of relying on models, information about a complex flow environment can be more accurately gathered for the future purpose of flight control.

As described in the background section, a reformulation of the steady flight equations is proposed as part of the overall sensing strategy. Recall the steady flight equations for pitch and yaw moments from (4.13) and (4.16):

$$M = \frac{1}{2}\rho V_{ac}^2 S b C_{Mac} + \frac{1}{2}\rho V_{pw}^2 S_{htail} C_{M_{htail}}$$

$$N = \frac{1}{2}\rho V_{ac}^2 S c C_{Nac} + \frac{1}{2}\rho V_{pw}^2 S_{vtail} C_{N_{vtail}}$$

Under the direct measurement scheme, the differential pressure $P_{\text{diff}-i}$ is measured across the horizontal tail, elevators, vertical tail and rudder at i locations. Each location corresponds to a panel of area S_{htail_i} that is l_i from the center of gravity and has a deflection angle of θ_i . This deflection angle is approximately zero for panels on the stabilizers, and equal to the control surface deflection angle for panels on the rudder and elevator. As previously described in (4.23) and (4.24), the terms relating to the control surfaces can be re-written as

$$\frac{1}{2}\rho V_{pw}^2 S_{\text{htail}} C_{M_{\text{htail}}} = \sum_{i=1}^{n_{\text{htail}}} \cos \theta_i \cdot P_{\text{diff}-i} \cdot S_{\text{htail}_i} \cdot l_i$$

$$\frac{1}{2}\rho V_{pw}^2 S_{\text{vtail}} C_{N_{\text{vtail}}} = \sum_{i=1}^{n_{\text{vtail}}} \cos \theta_i \cdot P_{\text{diff}-i} \cdot S_{\text{vtail}_i} \cdot l_i$$

Through direct measurements of aerodynamic moments and knowledge of control surface deflection, control authority can always be determined under uncertain conditions instead of relying on models and offline calibrations. This represents the ability ‘close the loop’ with regard to the aerodynamics in complex flow conditions in a manner not possible with simple air data systems. In order to support direct measurements, additional hardware must be embedded on the aircraft for distributed sensing. The test system includes 24 sensors in the tail each requiring its own data acquisition channel. While this configuration supports comprehensive data acquisition it may not be practical for smaller vehicles in its current form. However, our Funtana was of sufficient size to incorporate this DAQ system, particularly given that the Funtana carries no appreciable payload beyond its aerodynamic and FT sensing systems. Initial comparisons have shown that the raw data shows general agreement but additional calibration is required. The following sub-sections propose a calibration and correction methodology to enable the embedded pressure- measurements to be used to better characterize the moments. The calibration process is first described and the performance of the corrected aerodynamic sensing system is then evaluated.

4.12.i Calibration of pressure data integration using a low turbulence reference case

The objective of the calibration scheme described in this section is to realize the aerodynamic sensing frame work described in the reformulated steady flight equations. The current instrumentation has been shown to underestimate measured moments throughout the test range. In order to account for this, the nature of the discrepancies must first be characterized and then an appropriate method of quantifying identified discrepancies must be developed and tested.

From the test data, the discrepancy between FT and the pressure-based measurements appears consistent within each test case. The aerodynamic integration scheme predicts the same trends but with diminished magnitudes. The discrepancy increases with higher flow velocities and the pressure instrumentation consistently under-estimates the measured moments. Based on these observations, the error appears to be a scaling in the linear slope of the predicted aerodynamic moments. Observations that the pressure-based estimates show the same general trends and the discrepancies increase with larger dynamic pressures support this hypothesis. Such issues may be due to the coarse area discretization or pressure sensing location on each of the panels thus can be eliminated via more careful calibration.

A calibration methodology using a low turbulence free-stream test case is described below. By comparing the offsets in slope, a calibration for the aerodynamic instrumentation is computed from the single free-stream test case. This factor is then applied to the pressure-based measurements across all test cases and the corrected results are compared to FT instrumentation measurements.

4.12.ii Low turbulence free-stream calibration

A low turbulence test case can provide a uniform flow field without the predominant swirl and unsteady effects of the propeller wash. A reference test case was run by using the free-stream generated by the wind tunnel with the propeller fixed (zero thrust). The chosen airspeed of 12m/s (fluctuating up to 13m/s) represents a low speed cruise condition for the Funtana. The applicable equations are

$$M = \frac{1}{2} \rho V_{ac}^2 S b C_{M_{ac}} + A_M \sum_{i=1}^{n_{htail}} \cos \theta_i \cdot P_{diff-i} \cdot S_{htail_i} \cdot l_i \quad (4.36)$$

$$N = \frac{1}{2} \rho V_{ac}^2 S c C_{N_{ac}} + A_N \sum_{i=1}^{n_{vtail}} \cos \theta_i \cdot P_{diff-i} \cdot S_{vtail_i} \cdot l_i \quad (4.37)$$

where the coefficients A_M and A_N are sought to improve pressure-based estimation of pitch and yaw moments. Basic rudder and elevator sweeps are completed and measurements from both sets of instrumentation are compared under low turbulence flow conditions. No additional filtering is performed for the pressure measurements since the propeller is not rotating. These results are shown in Figure 4.33; note that the FT data for pitching moment is truncated once the sensor saturates between 15-20 degrees elevator deflection. The comparison for the low turbulence test case shows the same trends as in the other conditions, indicating observed discrepancies are due to issues in calibration rather than unsteady flow generated by the propeller. The pressure instrumentation gives moment measurements that follow the same trend but are smaller than those measured by the FT sensor. An offset with the control surfaces centered can also be observed. This is most likely due to the moments contributed by the aircraft fuselage and wing and described by coefficients $C_{M_{ac}}$ and $C_{N_{ac}}$ in the reformulated equations. Further testing to quantify these coefficients to form a complete aerodynamic model is described in the future work section.

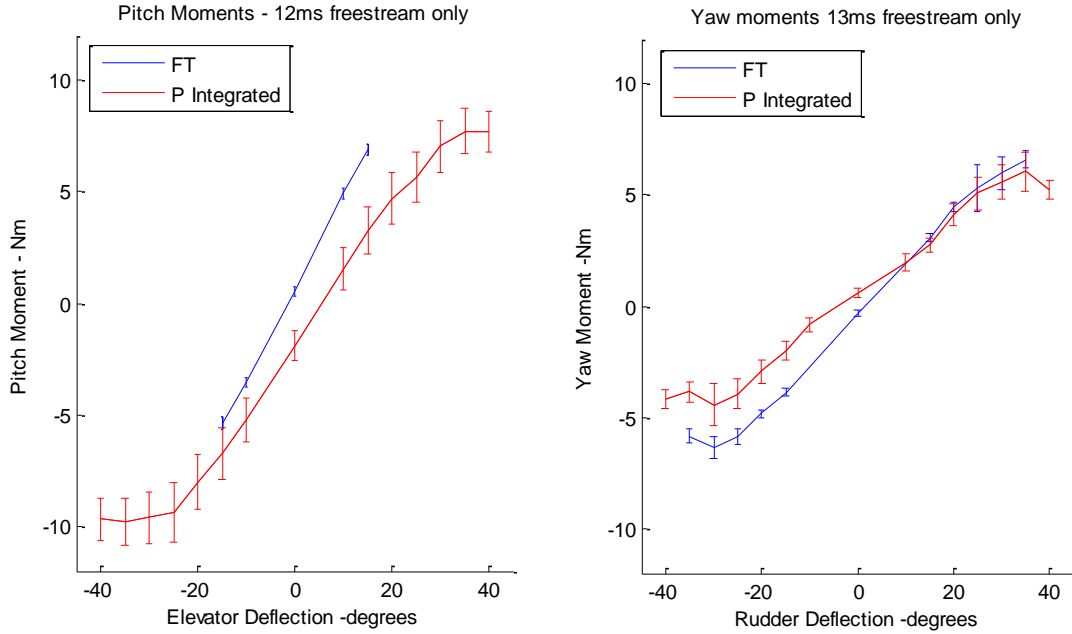


Figure 4.33 Low turbulence free stream training data set

Using these results as a training case, the coefficients A_M and A_N are computed by comparing the linear slopes of the pressure-integrated and FT sensor measurements. The linear slopes for each axis is computed by first choosing two control surface deflection angles, θ_1 and θ_2 on either side of a neutral setting that correspond to moments that are within the linear range of the data. Each θ_i will have two corresponding moment measurements from the aerodynamic sensing system and the FT sensor, denoted as $Mom_{Aero,i}$ and $Mom_{FT,i}$ respectively. The computation is given in equations (4.38) to (4.40)

$$Slope_{Aero_{M,N}} = \frac{Mom_{Aero,2M,N} - Mom_{Aero,1M,N}}{\theta_{2M,N} - \theta_{1M,N}} \quad (4.38)$$

$$Slope_{FT_{M,N}} = \frac{Mom_{FT,2M,N} - Mom_{FT,1M,N}}{\theta_{2M,N} - \theta_{1M,N}} \quad (4.39)$$

$$A_{M,N} = \frac{Slope_{FT_{M,N}}}{Slope_{Aero_{M,N}}} \quad (4.40)$$

Estimates of the linear slopes and the coefficients for pitch and yaw are summarized in Table 4.12.

Table 4.12 Estimated linear slopes from low-turbulence training case

Axis	$Slope_{Aero_{M,N}}$	$Slope_{FT_{M,N}}$	$A_{M,N}$
Pitch, M	19.589	24.549	1.253
Yaw, N	9.183	13.459	1.466

The computed coefficients determined from this ‘training set’ are used to scale the moments reported by the aerodynamic sensing system in the test cases. If the corrected aerodynamic moment measurements agree well with the FT measurements in the other cases, it shows that the same calibration is valid throughout the range of test conditions.

4.12.iii Calibration applied to hover data

The calibration terms calculated using the equations and parameters from the previous was applied to the propeller-driven test cases. As shown in Figures 4.30 and 4.31, the updated pressure-based moment measurements show good agreement with the FT measurements with overlapping standard deviation intervals at all data points. Corrected pitch moments at hover are plotted in Figure 4.34 followed by corrected yaw moments at hover in Figure 4.35. Based on these results, it can be concluded that the calibration factors factor computed in the low-turbulence test case applies to steady hover flight conditions. In contrast to the linear coefficients computed previously, the calibration is applicable throughout significantly different flight regimes.

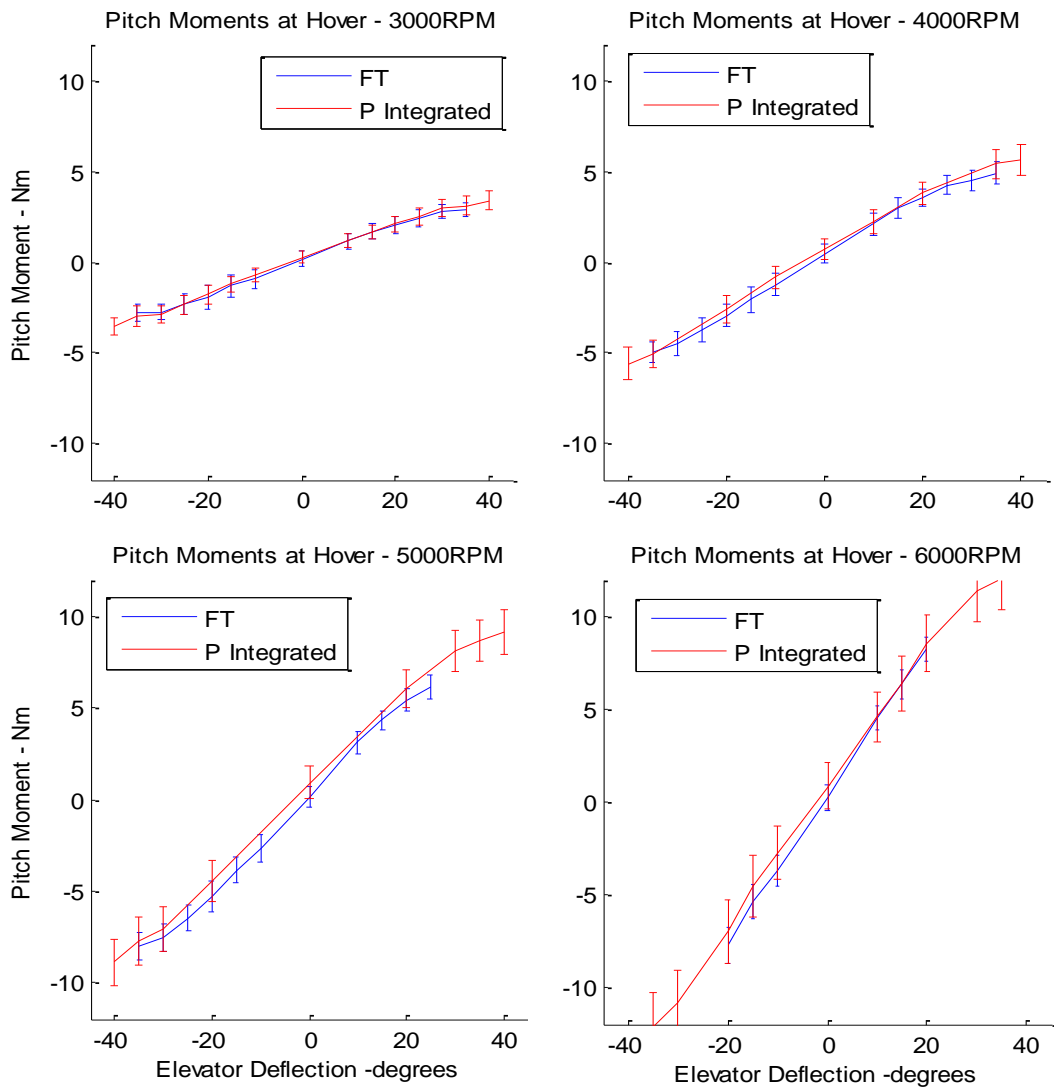


Figure 4.34 Comparison between corrected pressure-based and FT measurements of hover pitch moments

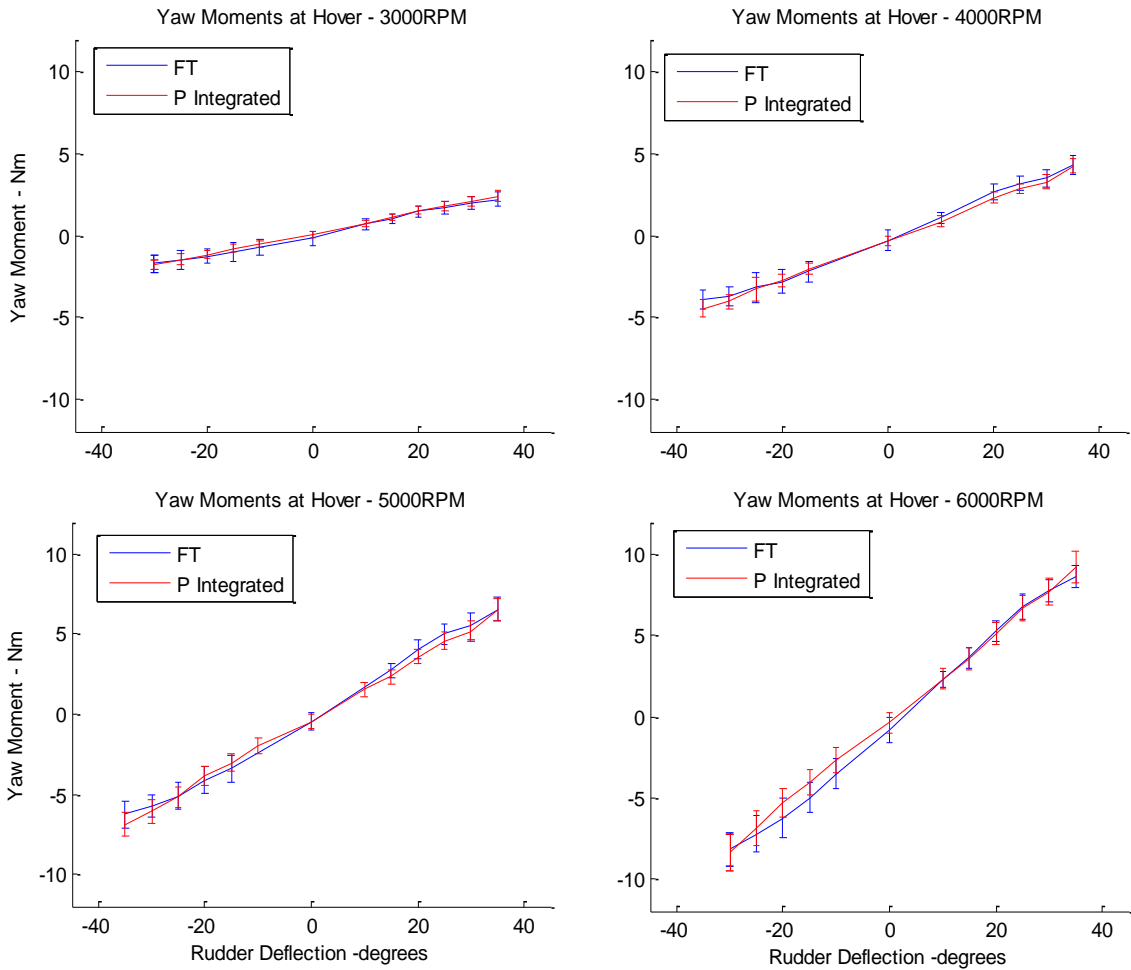


Figure 4.35 Comparison between corrected pressure-based and FT yaw moment measurements for hover

Further, the discrepancy in yaw coefficient at 3000RPM shown in the FT data is reflected in the corrected pressure data as shown in Figure 4.36. By comparing yaw moment coefficients computed from pressure and FT measurements, it can be concluded that the aerodynamic instrumentation is capable of accounting for asymmetries due to the non-linear aerodynamic effects encountered at low propeller rotation rates. Such characterization was previously shown to not be possible with the single prop-wash probe measurement system.

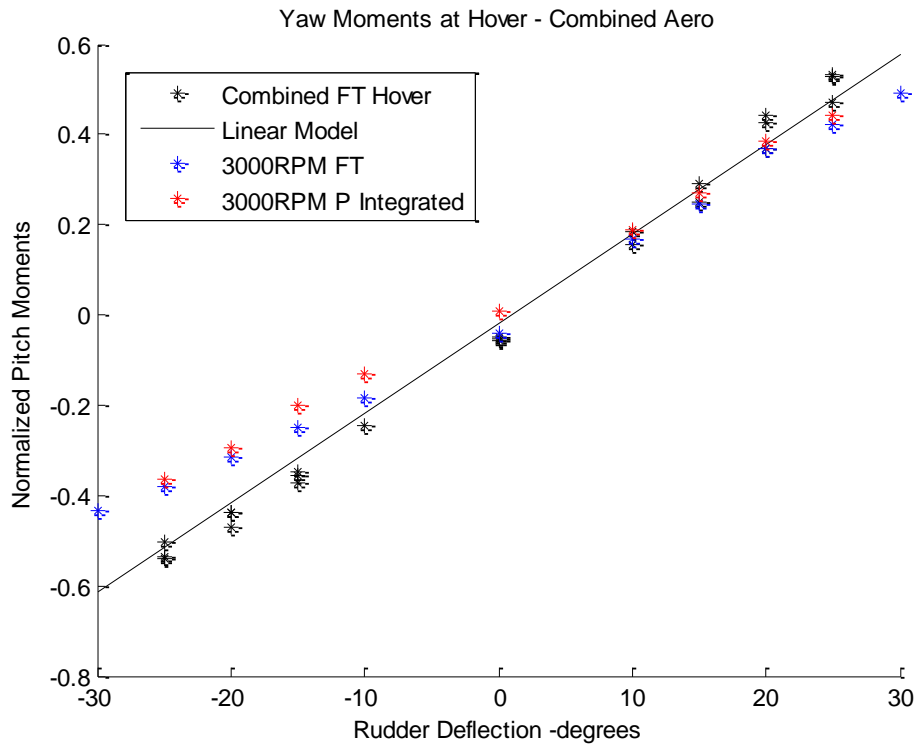


Figure 4.36 Comparison of FT and pressure based coefficients at 3000RPM

From the above comparisons, the distributed sensing scheme is shown to correctly measure both pitch and yaw moments when in a steady hover once the calibration is applied. Through embedded pressure measurements over the tail surfaces, the pressure-based sensing scheme is also capable of accounting for the non-linear aerodynamic effects encountered in test cases with the propeller driven at 3000RPM.

4.12.iv *Alpha25* and *5kCruise* Cases

The calibration was applied to data from the *Alpha25* and *5kCruise* cases then compared to FT measurements. The corrected slopes of the pressure based measurements for pitch and yaw are observed to accurately match FT data slopes. While the data point locations agree to within a standard deviation, a distinct offset is also apparent. The results are plotted in Figure 4.37 below.

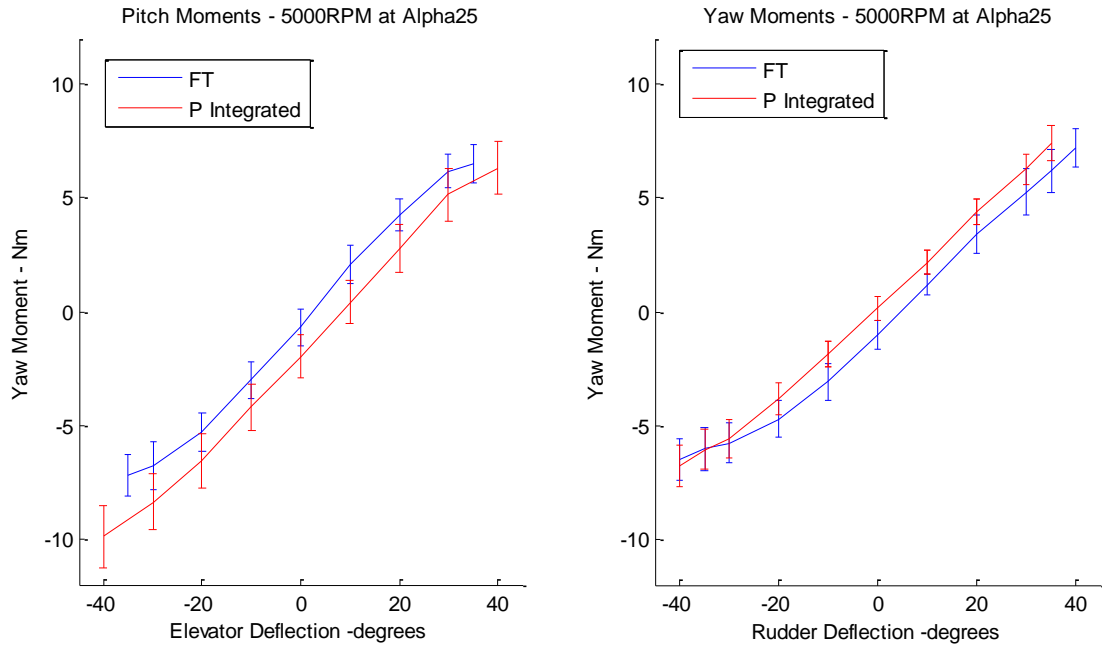


Figure 4.37: Corrected pressure based measurements at near-hover, *Alpha25* case

This offset is most likely due to moment contributions from the wing at a large angle of attack in a non-zero free-stream. This offset can be characterized through either a direct sensing scheme or through an experimentally-derived offset coefficient model. This augmentation is described in the future work section below. The need for such an offset is also apparent in the comparison to the powered cruise case. Both pressure based and FT sensor measurements show the same agreement in slope but with a distinct offset due to contributions from the wing and fuselage. This is shown in Figure 4.38. Note again that FT data is truncated once saturation is present.

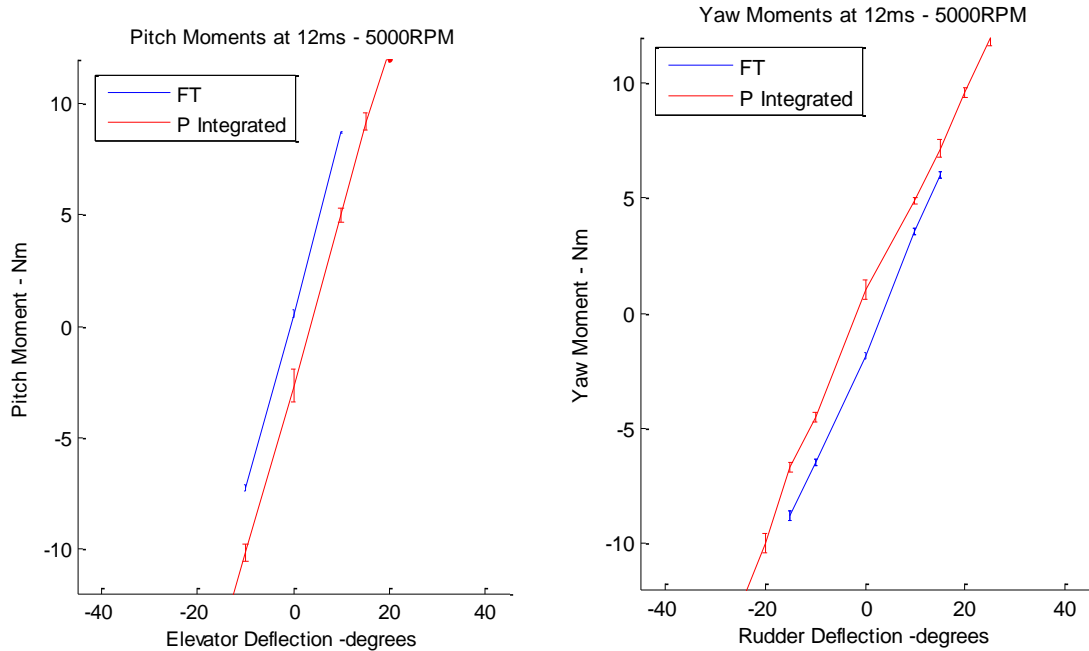


Figure 4.38 Corrected pressure based measurements at powered cruise

The powered cruise test case also demonstrates the ability of the pressure based sensing scheme to account for varying flow regimes. The control authority available in a forward flight situation is far greater than those induced by propeller flow alone as can be noted through much steeper slopes relating control surface deflection and resulting moments. Despite the significant change in flow conditions, the embedded pressure system reports results that are also valid in forward flight. Based on these results, the calibration factors formulated at a low turbulence cruise training data set is observed to be valid at all other test cases. Therefore, it can be concluded that with the distributed pressure instrumentation and a reference case, direct measurements of the aerodynamic moments generated by the tail surfaces can be taken.

This direct measurement scheme therefore offers a significant improvement over the linear model previously described. While a linear model requires multiple tests to determine coefficients for tail control authority under different flight conditions, calibrating the pressure based aerodynamic sensing system only

requires a single reference case since the calibration is the same for all flight regimes. A direct measurement scheme also means control authority can be accurately estimated under uncertain flow conditions. This scheme therefore provides the ability to 'close the loop' with regard to the pitch and yaw moment aerodynamics in complex flow fields in a manner not possible with more basic air data systems.

4.13 Fixed-wing conclusions

In this chapter, a reformulation of the steady flight equations for fixed-wing aircraft is proposed for operations at high angle of attack and hover, and an accompanying instrumentation concept is described. A wind tunnel test setup has been developed that enables two approaches to implementing aerodynamic sensing to be explored: a partial aerodynamic sensing scheme based on an innovative prop-wash probe measurement system, and a direct measurement scheme which utilizes distributed pressure sensing across the tail surfaces. An experimental procedure was described that allows both these approaches to be evaluated, and wind tunnel test data from the experimental series has been presented.

The following list summarizes key conclusions from this chapter:

- 1) Wind tunnel tests using integrated force-torque (FT), prop-wash probe, and direct pressure measurements show that both the prop-wash and embedded pressure measurement schemes are capable of accurately characterizing moments during hover flight.
- 2) A simple moving average (SMA) filtering scheme designed by scaling the filter period to passing wakes shed by the propeller blades produces a significant reduction in measurement uncertainty while maintaining a minimal response delay on the order of propeller revolution time.

3) A partial aerodynamic sensing scheme using a novel prop-wash velocity measurement has been designed, implemented, and evaluated. The coefficients of a linear aerodynamics model for hover have been determined. Using additional aerodynamic feedback, the steady flight equations for pitch and yaw moments have been extended to a steady hover flight condition, showing good agreement with direct FT sensor data in all hover test cases.

4) A comprehensive direct pressure measurement approach to aerodynamic sensing has been proposed and experimentally evaluated for estimating moments induced by the aircraft tail. A further reformulation of the steady flight equations allows the integration of distributed sensing across the tail surfaces for in-flight measurements of pitch and yaw moments. A calibration scheme is proposed and implemented, showing that the current instrumentation configuration with one calibration is indeed capable of providing accurate moment feedback for fixed wing UAS operating across the all evaluated wind tunnel conditions including flight at cruise, high angle of attack, and hover.

4.14 Future work

The work presented in this chapter is part of an ongoing effort to realize flight control enhanced with more comprehensive aerodynamic feedback than has been previously utilized to support small over-powered UAS flight outside the traditional fixed-wing envelope. This chapter has focused on quantifying the aerodynamic moments generated by the tail surfaces using two novel pressure sensing schemes capable of measuring flow generated by the propeller as well as free-stream flow.

While the distributed sensing scheme is capable of measuring moments under a wide variety of flight conditions, the large number of pressure measurements required to support it makes it challenging to implement and prone to failure. The partial sensing scheme is limited in its capability but requires no additional embedded pressure ports and is less prone to failure in harsh conditions. A

compromise between both extremes is sought as part of ongoing work, potentially combining both to provide the best feedback possible for flight control. In ongoing work, a full set of Funtana airframe stability coefficients is being obtained. As described above, discrepancies in the measured moments due to contributions beyond flow over the tail, including moments induced by the fuselage, wing and geometry of the motor mount, have not yet been addressed. Further wind tunnel and flight testing across the flight envelope is ongoing to quantify the other coefficients and provide a more complete ‘full envelope’ model for the Funtana small UAS platform and allow for development of in-flight sensing schemes. The objectives of these and future tests are summarized below.

1) A wind-vector fusion scheme is under development to combine traditional aircraft free-stream wind vector and prop-wash vector data to provide information on mixed-flow flight conditions. The aerodynamic moment coefficient for pitch moment from Equation (4.13), recalled below, will extend the two-probe sensing scheme in a manner we anticipate can support at least steady flight aerodynamic moment characterization in mixed flow fields as a counterpart to the distributed pressure sensing scheme.

$$M = \frac{1}{2}\rho V_{ac}^2 S b C_{M_{ac}} + \frac{1}{2}\rho V_{pw}^2 S_{htail} C_{M_{htail}}$$

The most basic logic that can be used to merge both airspeed measurements is to consider the differences between aircraft airspeed and the measured prop-wash velocity. For example, if V_{pw} much larger than V_{ac} , it is likely that the flow encountered by the tail surfaces is predominantly due to the propeller wash and will feature a linear response similar to those determined at hover. When V_{pw} and V_{ac} are comparable, the response of the tail surfaces will feature a steeper slope as observed in a cruise condition. Characterization of how the coefficients change as the two velocity measurements differ will allow the linear moment model to be extended to cover the full flight regime between cruise and hover.

2) Wind tunnel tests with the vehicle mounted at various attitudes in a variety of free stream conditions with the control surfaces at neutral will be carried out to determine the relevant coefficients. Using information gathered through the two wind-vector measurements, a methodology for switching between coefficients can be developed.

3) A direct sensing approach to aerodynamic force and moment measurement with instrumented flight-test wings as well as tail will also be explored. Pressure ports embedded in the wings will allow for direct measurement of the aerodynamic forces through a larger range of out-of-envelope flight conditions to supplement in-envelope estimates provided by linear equations and the free-stream air-data probe. A series of calibration and model validation experiments will be run to ultimately develop a full 6-DOF in and out-of-envelope model and real-time force and moment estimation capability for small UAS.

Chapter 5

Conclusions and Future Work

This thesis has sought to develop and validate the concept of comprehensive embedded aerodynamic sensing for small UAS operating in challenging flow conditions. This chapter provides a summary of the key findings and describes future work.

5.1 Conclusions

Two test setups have been developed and tested according to platform-specific requirements. These paragraphs summarize conclusions from this effort.

- **Embedded aerodynamic sensing scheme for small UAS**

A pressure based aerodynamic sensing concept has been successfully implemented on two different small UAS platforms. Both systems have been validated through secondary force and torque measurements taken with an independent transducer system. In both applications, the complete instrumentation package consisted of sensors, data acquisition hardware and data processing methodologies that serve each set of platform-specific goals. This framework contributes to the small UAS community as pressure sensing technology advances, available hardware shrinks, and vehicles are asked to perform in regimes not adequately characterized by traditional air-data probe plus inertial navigation systems.

- **Independent force transducer and pressure based measurements of the time resolved vertical forces generated by a pair of rigid flapping wings in air**

A pressure-based aerodynamic sensing concept has been successfully implemented for the measurement of aerodynamic force over rigid flapping wings at $Re \sim 4500$. Experimental results indicate the pressure instrumentation is able to estimate aerodynamic forces over a rigid flapping wing. The pressure-based measurements are consistent across all test cases and scale appropriately with flap frequency. Force transducer measurements show peak-to-peak magnitudes of total loads in the vertical direction scale with the square of flap frequency, and the single-stroke vertical force averages are within 4% of the averaged force over multiple stroke histories.

- **Experimental validation of a direct, pressure-based approach to measurements of time resolved forces generated by a flapping wing.**

A pressure-based aerodynamic sensing concept has been successfully implemented for the measurement of aerodynamic force over rigid flapping wings. The pressure-based and force-torque sensor results show agreement in qualitative trends, while key quantitative parameters such as peak magnitudes and phase agree to within 10%. Based on these comparisons, the approach is concluded to be suitable for flight control. Future ground based testing in flapping wing flight can also exploit the use of pressure-based instrumentation for force measurements. When coupled with a motion capture system such as VICON to measure wing surface deformations in air, the pressure instrumentation can provide data for a large range of test cases with flexible as well as rigid wings. With a proven pressure based methodology, an experimental procedure that is the mirror of the current approach can be applied. Aerodynamic loads could then be subtracted from total loads for estimates of the inertial loads

instead of requiring a separate set of vacuum chamber experiments and their attendant challenges.

- **Aerodynamic sensing for fixed wing UAS operating at large angles of attack and hover**

A flight-capable sensing system and platform has been adapted for ground based testing. An expanded aerodynamic data concept that includes comprehensive instrumentation and reformulated linear aerodynamic model has been validated through a set of wind tunnel tests.

The data has motivated a methodology for computing a set of linear coefficients for the feedback control of pitch and yaw moments on a fixed wing vehicle in a vertical hover. This more comprehensive approach to aerodynamic sensing has allowed the integration of distributed sensing across the tail surfaces for in-flight measurements of pitch and yaw moments. Through wind tunnel testing, this scheme is shown to be capable of providing additional aerodynamic data throughout two different flight regimes of a fixed wing UAS operating at high angles of attack and hover.

5.2 Future work

For the two small UAS applications featured in this thesis, further development of the flapping-wing and fixed-wing sensing systems have been described in detail at the ends of chapters three and four respectively. However, the future development of the proposed aerodynamic sensing concept and its applicability to UAS in general has yet to be addressed.

While the aerodynamic sensing concept proposed in this thesis has been formally presented as a collection of hardware and techniques, the main idea it represents is simple; add more air-data sensors to flight vehicles since they depend directly on the flow-field they operate in. For the majority of current UAS that operate within the realm of linear aerodynamics, additional flow sensing

would be redundant. However, it would be also be unreasonable to assume the current generation of flight vehicles will be the last. Perhaps the next generation of UAS will operate in urban canyons, defy hurricanes [100] and fly routinely in a state of post-stall super-maneuverability. Perhaps it is the next generation of UAS that will pose questions that have not yet been asked; questions to which an expansion of the aerodynamic sensing strategies proposed in this dissertation might be the answer.

Appendix A: Flight Funtana hardware and setup

This appendix describes key features of the flight test configuration for the aerodynamic sensing concept for fixed wing aircraft.

Appendix A.1 Avionics package and autopilot configuration

The Diamond Systems Athena II was selected as the onboard computer and runs all flight control and data acquisition. The Athena II includes multiple serial ports, an Ethernet port, flash disk, and a data acquisition package. The data acquisition system includes a high speed 16-bit analog to digital converter. The Midg-II inertial navigation system, built by Microbotics Inc., was installed to provide filtered measurements of aircraft inertial state, including GPS-based position and velocity, attitude, and body axis angular velocities. The Midg-II measures these values using GPS, a 3-axis magnetometer, 3-axis rate gyro, and a 3-axis accelerometer. The Midg-II provides state and position measurement updates at a rate of 50 Hz communicated to our flight computer via RS-232 serial port connection. A servo switch controller (SSC) built by Microbotics Inc., was used to record the servo commands sent by the pilot to the servos during flight. The SSC also provides the capability for the flight computer to command servo positions when in Autopilot mode and an override switch for the remote pilot to reposition the aircraft. Figure A.1 shows the overall system block diagram.

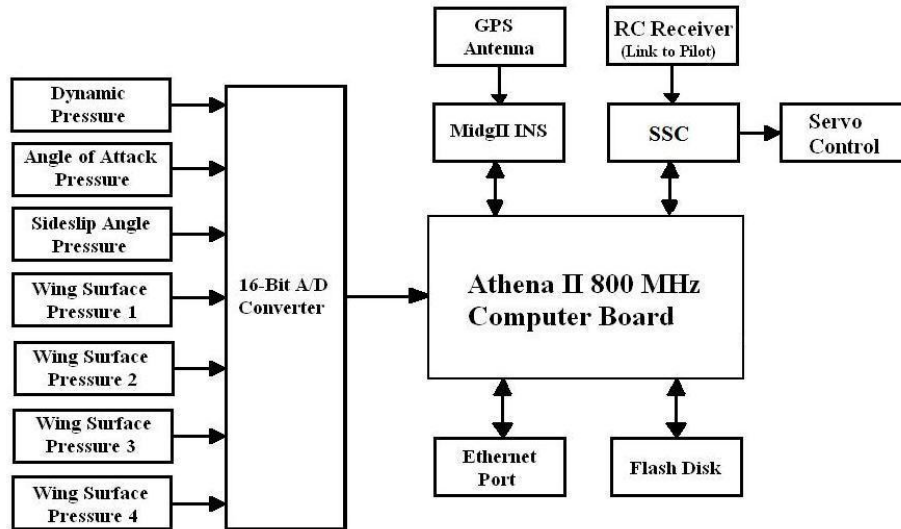


Figure A.1 Avionics overview

The payload capabilities of a small fixed wing vehicle allowed for actual flight testing of the aerodynamic sensing system to be carried out. Four Funtana airframes were built and instrumented. Versions dedicated to remotely piloted flight operations do not carry an IMU or SSC.

5.3 Appendix A.2 Expanded range α - β probe and calibration

An α - β probe was designed to be easily manufactured and to provide wind magnitude and direction measurements. Four thin aluminum tube probes were each aligned and attached to a standard pitot probe, as illustrated in A.2 . The probe was calibrated in the University of Michigan’s 2’X2’ wind tunnel. A calibration was developed to accommodate a larger range of flow angles, allowing angles of attack up to 75 degrees to be effectively measured. The calibration technique is similar to that described by Ostowari et al [97] in which a change in reference port is effected to correctly characterize wind at high flow angles. Within a moderate range of flow angles, the differential pressures measured by the α and β tubes are normalized by the pitot probe measurements. Past 45 degrees, the inverse relationship is utilized based on the reasoning that

at high flow angles, the α and β tubes are better oriented to measure total pressure. Combining both sets of calibrations give rise to linear calibration curves within their respective ranges, as described in following sections. As will be shown, this system reliably measures airspeeds higher than 2.5m/s, angles of attack up to 75 degrees and sideslip angles up to 45 degrees.

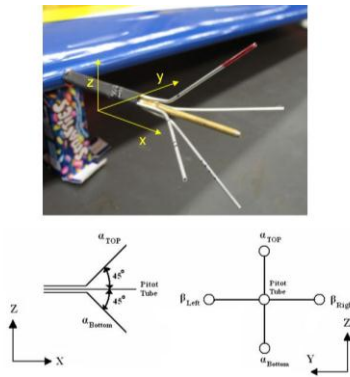


Figure A.2 Custom built expanded range Alpha-Beta probe

The calibration of the angle of attack, sideslip angle, and pitot (α - β) probe was performed in the University of Michigan's subsonic 2 ft x 2 ft instructional wind tunnel. A first calibration was performed in 2009 as is reported in a previous publication [77]. For seven different velocities, the angle of attack and sideslip angle were changed independently. Calibration velocities were 3, 5.8, 9, 11, 14, 18, and 22 m/sec. The angle of attack was varied from -100° to 100° in 5° increments except for the interval $[-10^\circ -2.5^\circ]$ measured in increments of 2.5° , $[-1^\circ -1^\circ]$ in 1° increments, and $[2.5^\circ -10^\circ]$ in 2.5° increments. The side slip angle was varied from -45° to 45° in 5° increments except for intervals $[-10^\circ -2.5^\circ]$ in increments of 2.5° , $[-1^\circ -1^\circ]$ in 1° increments, and $[2.5^\circ -10^\circ]$ in 2.5° increments. The angle of attack and sideslip angles were varied over these ranges or until the sensors saturated. For the highest velocity of 22 m/s the angle of attack was varied from -20° to 25° and the sideslip angle was varied from -15° to 15° . Saturation of the sensors did not occur anywhere in the test range until the flow reached velocities of 18 m/s. The calibration accommodated the region in which

the airframe operated, which is the moderate velocity, high angle of attack region. For each measurement after the flow angle was changed, once the flow reached a steady state, ten seconds of data were taken. This data was then used to construct various calibrations curves to effectively measure angles of attack from -75° to 75° and sideslip angles between -45° and 45° .

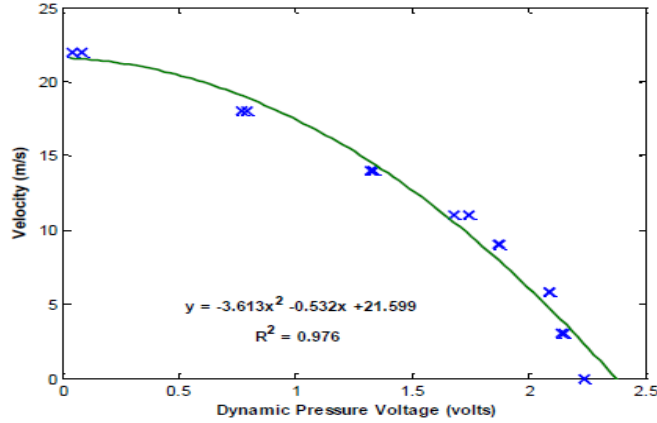
Appendix A.2.1 Airspeed Calibration

Airspeed was calibrated by using the measurement of the dynamic pressure for each airspeed at an angle of attack of 0° and sideslip angle of 0° . This data yields the expected quadratic equation found in Figure A.3 and shown in Equation (A.1). Note that since dynamic pressure $q = \frac{1}{2}\rho V_{air}^2$, the data fits this curve well with some deviation as expected from pitot tubes measuring very low speeds.

$$V_i = a_q(q)^2 + m_q(q) + b_q \quad (A.1)$$

Appendix A.2.2 Normalization by dynamic pressure

The angle of attack and sideslip angles are calculated using the pressure difference between the two tubes corresponding to the angle of attack or sideslip angle and then are normalized by the dynamic pressure as measured by the Pitot tube. These ratios, as shown in Equation (A.2), can then be related to the angle of attack and sideslip angle using linear curve fits shown in Equations (A.3) and (A.4). These are the ratios of the current voltage reading subtracted by the sensor's nominal voltage at a flow velocity of zero.



A.3 Airspeed calibration curve

$$\frac{\Delta\alpha}{\Delta q} = \frac{\alpha_i - \alpha_0}{q_i - q_0} \quad \frac{\Delta\beta}{\Delta q} = \frac{\beta_i - \beta_0}{q_i - q_0} \quad (\text{A.2})$$

$$\alpha_i = m_{\alpha 1} \frac{\Delta\alpha}{\Delta q} + b_{\alpha 1} \quad \text{For } -25^\circ < \alpha < 25^\circ \quad (\text{A.3})$$

$$\beta_i = m_{\beta 1} \frac{\Delta\beta}{\Delta q} + b_{\beta 1} \quad \text{For } -25^\circ < \beta < 25^\circ \quad (\text{A.4})$$

Figure A.3 and Figure A.4 show plots of these ratios as the angle of attack and sideslip angle are changed for various velocities. For both graphs there is a large range where the relationship between the ratios and angle of attack or sideslip angle is linear. There are also regions where the angle of attack is no longer independent of velocity and the normalization breaks down. For angle of attack, the plot is linear for angles of attack between -30° and 30° . For angles of attack with a magnitude higher than 30° , the various curves are no longer independent of velocity as shown in Figure A.5 for angles of attack between 30° and 100° . These errant regions are caused by cancellation errors occurring as the velocity approaches zero as this causes $\frac{\Delta\alpha}{\Delta q}$ to go towards infinity. This occurs when the pressure at the stagnation and static ports of the Pitot tube becomes the same, which occurs for angles near 45° . In Figure A.4, the sideslip angle is linear for angles between -25° and 25° and outside of this range the sideslip angle becomes nonlinear and by 30° it can no longer be normalized by velocity as the curves diverge from each other.

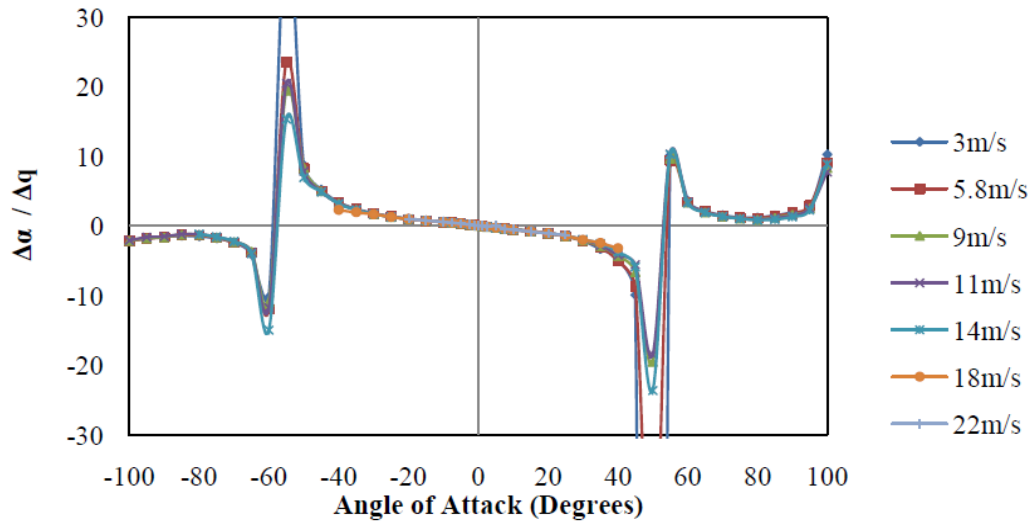


Figure A.3 Alpha/q differential pressure voltage ratio vs. angle of attack

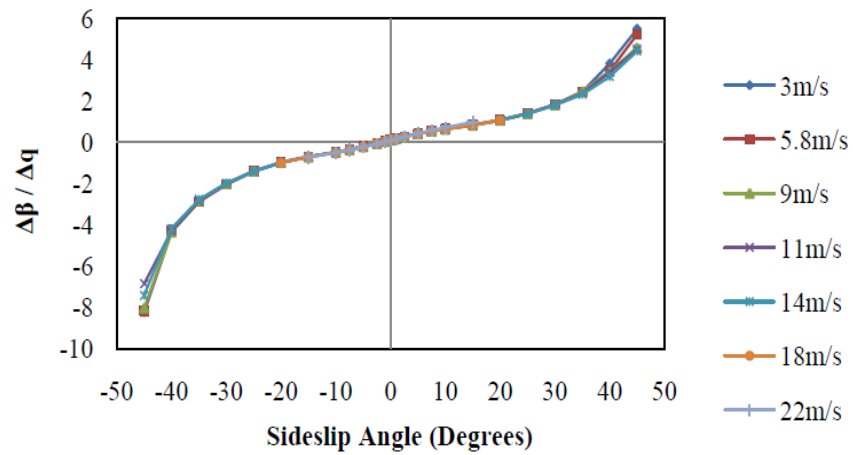


Figure A.4 Sideslip angle calibration: reverse normalization by dynamic pressure

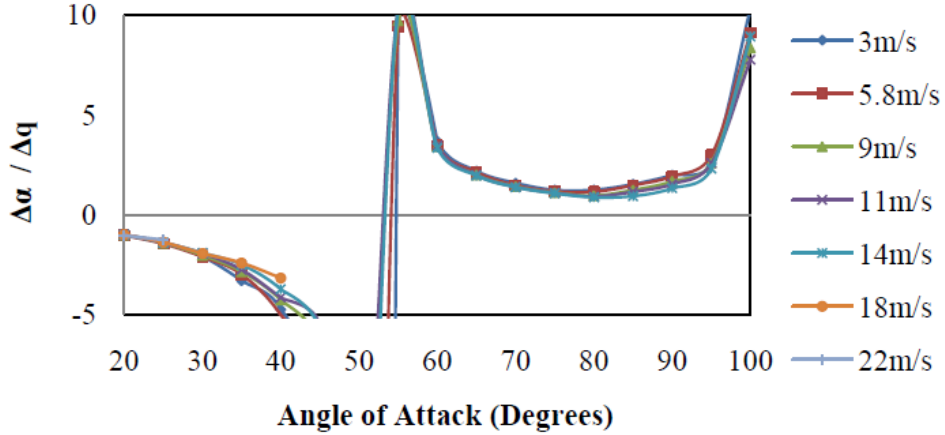


Figure A.5 Forward $\Delta\alpha / \Delta q$ normalization failure at large flow angles

The previous 'forward normalization' of the measured differential pressures by the dynamic pressure causes cancellation errors to occur when the airspeed approaches zero or when the angle of attack is near 45° . By changing the reference dynamic pressure to be where the dynamic pressure is normalized by the differential pressure the cancellation errors are then moved to when the angle of attack or sideslip angle approach zero. The equations for these new ratios are shown below in Equation (A.5). For the angle of attack, this method yields two linear equations as shown in Equations (A.6) and (A.7). For the sideslip angle, this method yields two quadratic Equations (A.8) and (A.9).

$$\frac{\Delta q}{\Delta\alpha} = \frac{q_i - q_0}{\alpha_i - \alpha_0}; \quad \frac{\Delta q}{\Delta\beta} = \frac{q_i - q_0}{\beta - \beta_0}; \quad (\text{A.5})$$

$$\alpha_i = m_{\alpha 2} \frac{\Delta q}{\Delta\alpha} + b_{\alpha 2} \quad \text{For } 25^\circ < \alpha < 70^\circ \quad (\text{A.6})$$

$$\alpha_i = m_{\alpha 3} \frac{\Delta q}{\Delta\alpha} + b_{\alpha 3} \quad \text{For } -70^\circ < \alpha < -25^\circ \quad (\text{A.7})$$

$$\beta_i = a_{\beta 1} \left(\frac{\Delta q}{\Delta\beta} \right)^2 + m_{\beta 2} \frac{\Delta q}{\Delta\beta} + b_{\beta 2} \quad \text{For } 20^\circ < \beta < 45^\circ \quad (\text{A.8})$$

$$\beta_i = a_{\beta 2} \left(\frac{\Delta q}{\Delta\beta} \right)^2 + m_{\beta 3} \frac{\Delta q}{\Delta\beta} + b_{\beta 3} \quad \text{For } -45^\circ < \beta < -20^\circ \quad (\text{A.9})$$

Figure A.6 shows as the angle of attack approaches zero degrees the plot does indeed approach infinity as expected. There are two linear regions for angles of attack with a magnitude between 25° and 75° . Outside of these regions, the angle of attack measurement is dependent on velocity and cannot be normalized

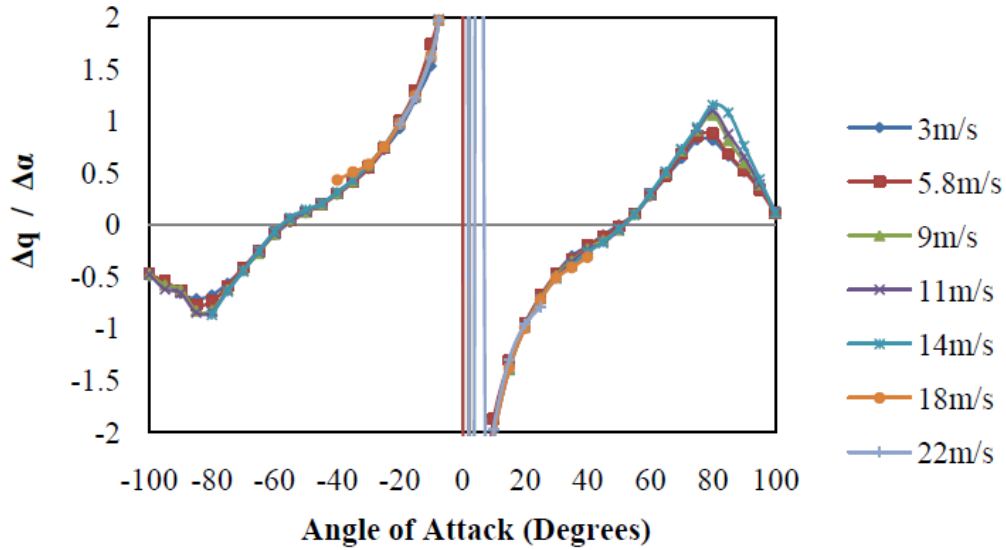


Figure A.6 Reverse $\Delta q/\Delta\alpha$ normalization for large angles of attack

Figure A.7 shows as the sideslip angle approaches zero degrees cancellation errors occur.. Normalization by the differential pressure yields two quadratic curves for sideslip angles with a magnitude between 20° and 45°. For sideslip angles with a magnitude less than 20° the sideslip angle is dependent on velocity.

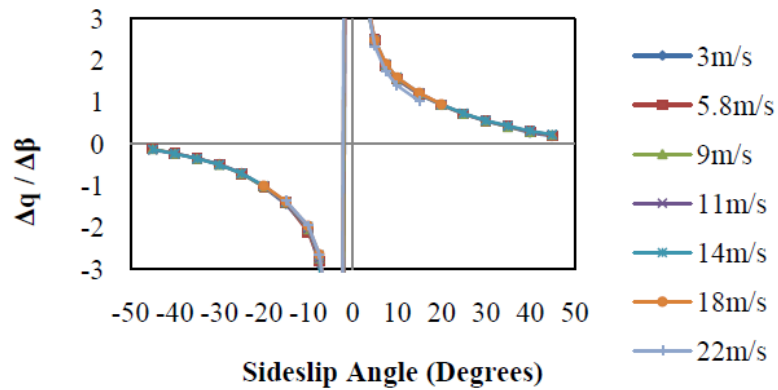


Figure A.7 $\Delta q/\Delta\beta$ differential pressure voltage ratio vs. angle of attack

In spring 2012, the probe was refurbished and recalibrated. The new sensor configuration allowed the calibration process to be improved. More details are provided in the following sub-section.

5.3.i.a 2nd generation calibration

The multiple curve calibration method was refined and extended in range to enable flow angles up to 80 degrees. In the previous system, a filter that tracked flow angle history was used to choose between calibration curves in real time. With the new sensor configuration, the direction of the probe can be obtained by the direction of the pressure difference between prongs. With the new algorithm, the pitot probe measurement of dynamic pressure is first normalized by the α prong pressure difference, giving a reverse-normalization variable. By taking into account the magnitude and direction of the reverse-normalization variable, the appropriate calibration curve can be determined uniquely. The map shown in Figure A.8 presents ranges of reverse-norm values and the appropriate calibration curve that was chosen.

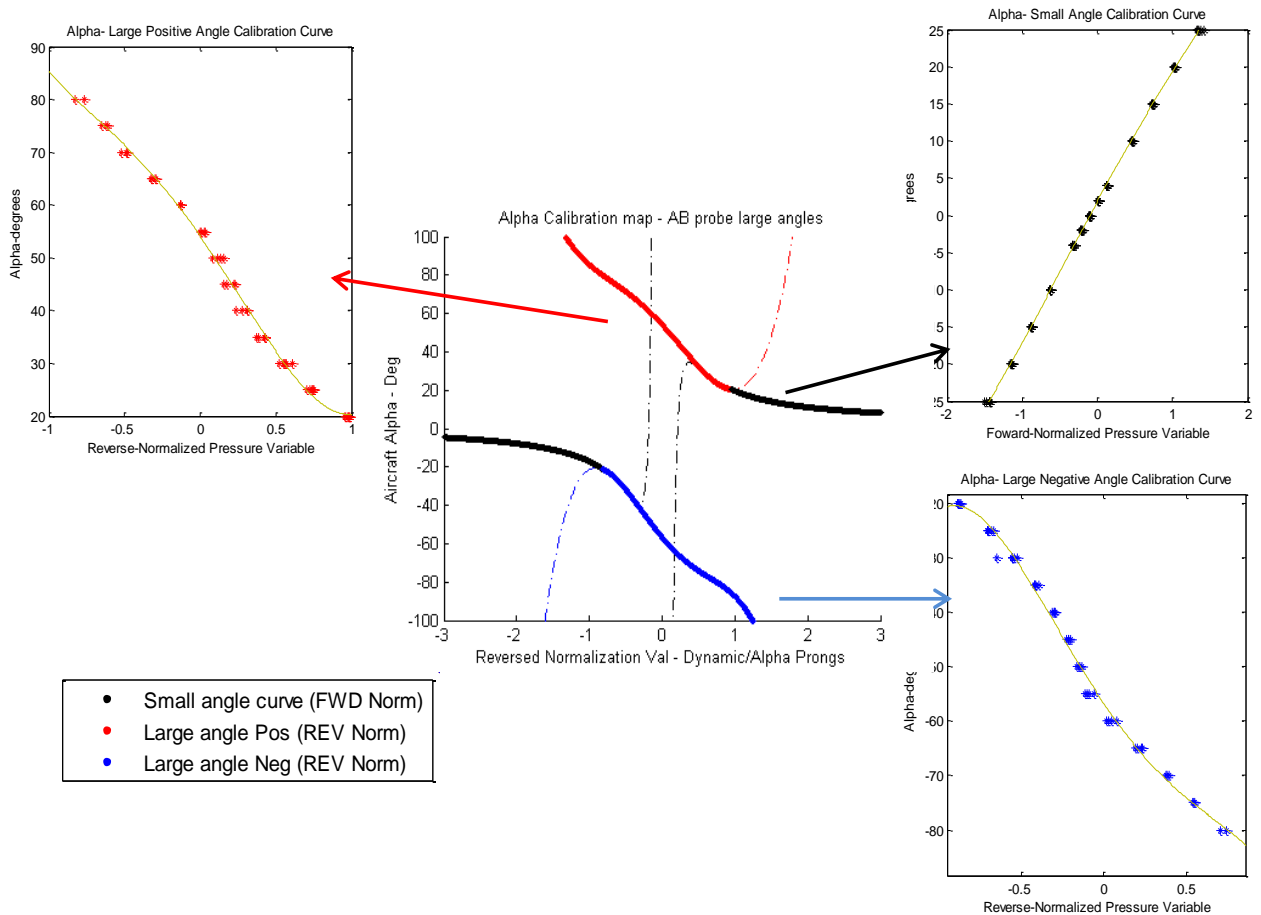


Figure A.8 Sample expanded range curve selection map for α

5.4 Appendix A.3 Wing pressure instrumentation and stall detection results

The instrumented wing concept from [77] has been expanded in this work to offer better coverage and measurement accuracy in flight regimes where aerodynamic feedback can be most valuable. Using a different type of smaller pressure sensor allows for pressure sensors to be located near pressure ports, allowing improved response times and greater flexibility in locating pressure measurement points, such as within the ailerons. The pressure sensors were assembled and embedded along the pressure ports to avoid long pressure lines and long response times. The ports were fabricated from aluminum tubing and rubber hosing depending on where the port needed to be embedded. These are shown in A.9. The aircraft currently has one instrumented chord on either wing and more ports are being added as flight testing continues.

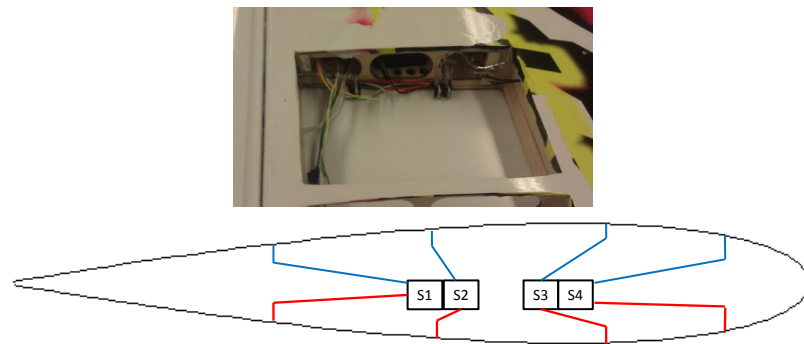


Figure A.9 Wing ports - sensor placement and pressure line routing schematic

As with the previous system, the embedded pressure ports offer an autopilot the ability to estimate the lift being generated by each wing. With the new configuration however, the pressure sensors are connected to give differential pressure between ports located at the top and bottom wing surfaces instead of between individual ports and the leading edge. This allows a direct and straightforward estimate of lift that is more suited to flight at very low airspeeds. This avoids normalization difficulties associated with small dynamic pressure and

allows a wing lift estimate to be made with fewer measurements, reducing the effects of sensor noise. Using differential pressure measurements, a coarse discretization and area integration scheme, lift estimates from pressure sensor measurements in unsteady flow conditions can be calculated. Adapted for the Funtana wings, the proposed discretization scheme is shown in Figure A.10 where total lift can be estimated as in Equation (4.22). The mid-span ports on either wing have been embedded and port locations are being finalized based on ongoing flight test results.

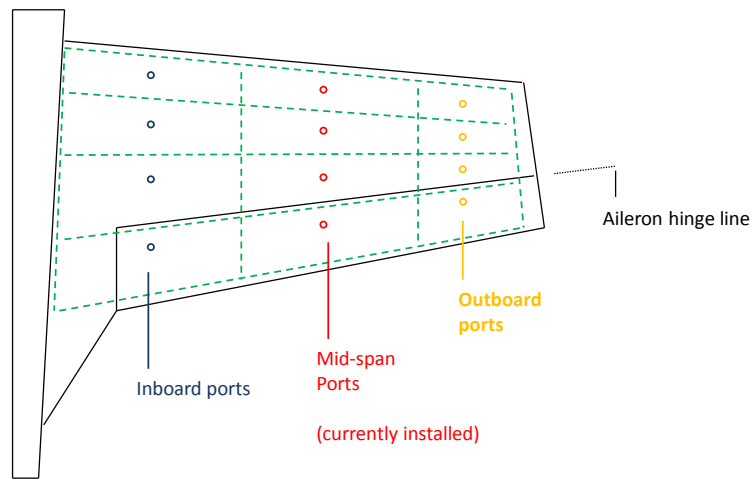


Figure A.10: Proposed wing discretization for pressure based lift estimation
 With the instrumentation expanded to both wings, the new pressure port network offers a variety of capabilities that were not possible when only one chord on one wing was instrumented. Being able to estimate lift generated by either wing at high angles of attack allows for the aerodynamic roll moments generated by the wings due to external disturbances or non-linear aerodynamics to be estimated.

Appendix A.3.1 First generation Stall Detection

The addition of wing pressure sensing capability allows for the detection of a deep wing stall or when boundary layer separation has occurred across the top

of the wing and lift generation is severely reduced. Such a detection algorithm represents the ability to observe a fundamental property of the vehicles aerodynamic state under extraordinary flight conditions. It plays an important role in characterizing the aerodynamic state of the vehicle.

The first generation stall detection algorithm operates on the principle that if the static pressure measurements along the top of the wing converge to the same, low value, this indicates that the main flow has separated from the top of the airfoil leaving pockets of re-circulating air above the wing. This traditional notion of stall is readily observed with wind tunnel experiments. The coefficient of pressure (C_p) data shown in Figure A.11 was taken in the UM wind tunnel over a generic NACA 2412 airfoil at a Reynolds number of 110,000. The ‘loss of suction’ trend over the top of the airfoil after stall is shown at angles of attack at and beyond 15 degrees. This type of behavior is typical for airfoils operating under similar Reynolds numbers.

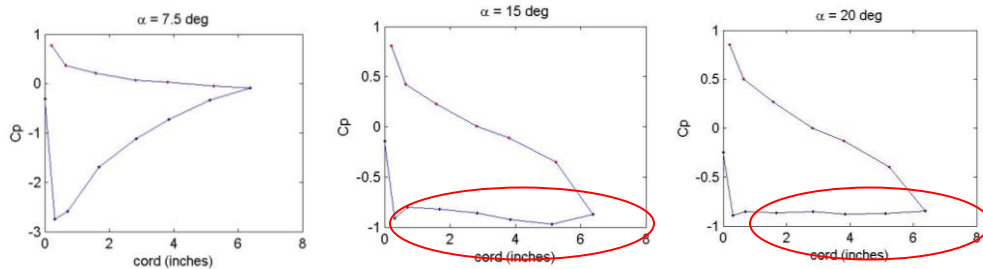


Figure A.11: Windtunnel data : C_p trends at stall

The wind tunnel test conditions correspond to the flight regime in which the Funtana’s operates during a transition. The stall characterization concept is based on straightforward aerodynamic fundamentals and is valid for different airfoils. Translated into a form that fits within the framework of our sensor package, this means detecting sensor reading profiles where the maximum and minimum values fall within a certain range. The algorithm is presented in Equations (A.10) through (A.12). First, wing pressure port sensor readings are

normalized by the measured dynamic pressure in order to construct a wing C_p profile. The profile must show that the pressure distribution along the top of the wing chord is small with respect to dynamic pressure. Additionally, the C_p variation between the different wing ports has to be small. During a transition to hover, the dynamic pressure experienced by the aircraft becomes small due to the very low airspeeds. This creates C_p calculation problems when airspeed becomes too low to be used for the normalization process.

In order to overcome these problems at very low speeds, the stall detector is coupled with a Loss-of-Lift detector that considers pressure readings that are not normalized by the dynamic pressure. Once the actual pressure difference between the stagnation point of the wing and its top surface becomes negligible, it becomes suitable to consider the wing to no longer be an aerodynamic lifting surface. Since mild wing stall can occur without a total loss of wing lift, using both detection algorithms allows the aerodynamic data system to estimate the severity of a stall during flight.

$$\text{Profile} = [P_1, P_2, P_3, P_4, \dots P_n] \quad (\text{A.10})$$

$$C_{p_{\min}} = \min_{i=1..n} \left(\frac{P_i}{q} \right) \quad C_{p_{\text{diffs}}} = \sum_{i=1}^{n-1} \frac{|P_{i+1} - P_i|}{q} \quad P_{\text{diffs}} = \sum_{i=1}^{n-1} |P_{i+1} - P_i| \quad (\text{A.11})$$

$$\text{Stall State} = \begin{cases} \text{Total Lift Loss} & q < q_{\text{thresh}} \text{ and } P_{\text{diffs}} < P_{\text{diffs}_{\min}} \\ \text{Stall} & C_{p_{\min}} > -1 \text{ and } C_{p_{\text{diffs}}} < 0.4 \\ \text{No Stall Detected} & \text{Otherwise} \end{cases} \quad (\text{A.12})$$

While stall detection and quantification is useful, it can only provide information once stall has occurred and cannot offer a means to avoid stall. With the 2nd generation pressure measurement scheme, the stall detection algorithm was further developed to provide in flight stall-prediction.

5.4.i.a Second Generation Stall Prediction Algorithm

With the differential pressure being monitored at more locations, the relative differences between pressure measurements from the leading edge and trailing edge can be compared with against each other, allowing a degree of stall prediction capability. The pressure port configuration at each wing chord is shown in Figure A.12

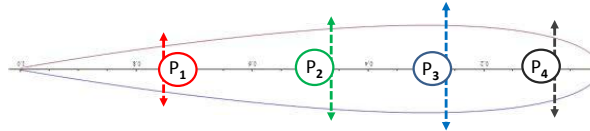


Figure A.12 Chord-wise pressure port locations and differential sensor connections

To develop a stall prediction algorithm based on our instrumentation scheme, the pressure port data leading up all recorded stalls flown by the aircraft were isolated and compiled. A number of pressure measurement based variables were formulated based on what is expected from flow separation, and their evolution is tracked during the period before a stall was detected. A sample pressure distribution plot that is characteristic of attached flow and the corresponding pressure measurements is shown in Figure A.13. These variables are calculated using Equations (A.13) and (A.14).

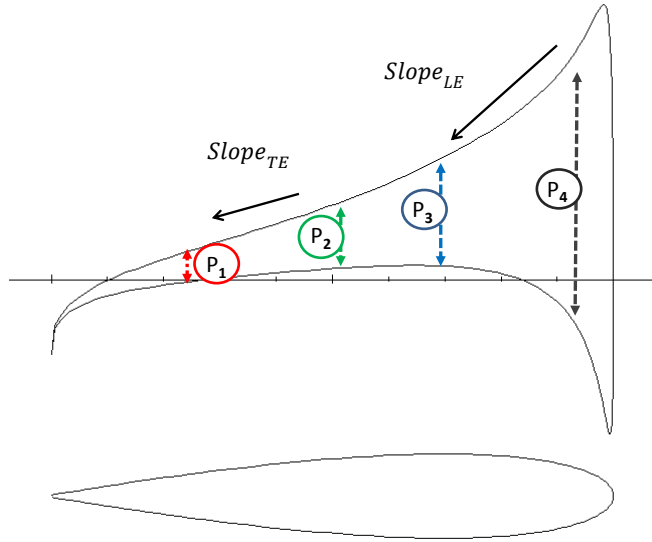


Figure A.13: Pressure measurement overview and stall detection variables

$$P_{\text{Profile}} = [P_1, P_2, P_3, P_4]$$

$$P_{\text{band}} = \max(P_{\text{Profile}}) - \min(P_{\text{Profile}}) \quad (\text{A.13})$$

$$\text{Slope}_{LE} = P_4 - P_3 \quad \text{Slope}_{TE} = P_2 - P_1 \quad (\text{A.14})$$

Flight test results of both stall detection algorithms are presented in Appendix C.

Appendix B: Instrumentation details

This appendix describes the process of instrumenting the tail surfaces of the Funtana, a COTS aerobatic fixed-wing airframe primarily constructed from balsa and plywood with monokote covering. Embedded instrumentation was installed directly into the tail surfaces, requiring modification to the airframe. In order to ensure the consistent and accurate placement of the pressure ports, a set of templates were designed. The templates depicted in Figure B.1 were used to locate access panels and pressure ports on the actual tail surfaces. The pieces are split so they can be cut from smaller sheets of wood. These were then joined with wood glue and laid on the actual surfaces so that pressure port locations and access panel locations could be marked.

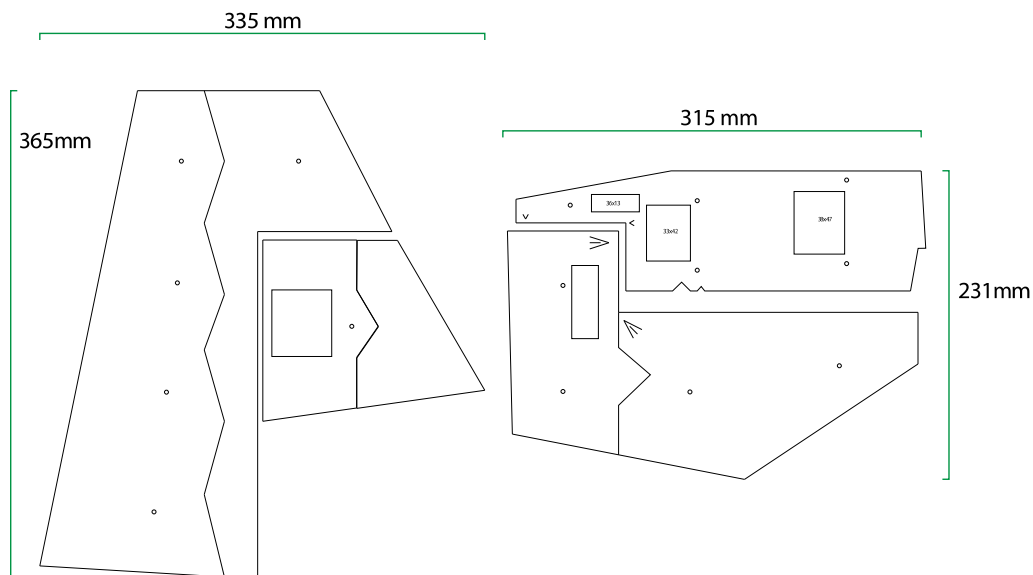


Figure B.2: Tail surface access panel and pressure port location templates

Once outlines of the access panels were drawn with a permanent marker, the balsa skin was cut with a sharp blade. In order to ensure the correct curvature and fit, the sheets of balsa that were cut were used as the panels.

Holes in the balsa skin were drilled to accommodate lengths of tygon tubing. Once these tubes are installed, they are cut flush to the surface so that the port diameters are consistent. At port locations where there is no balsa skin and only covering film, additional skin was built to fit the existing structure. This is depicted in Figure B.2 which shows the vertical surfaces during a preliminary sensor power-up test. It shows the access panels, supporting balsa structure, and tygon tubing. The sensors are calibrated through the excess lengths of tubing before they are cut flush.

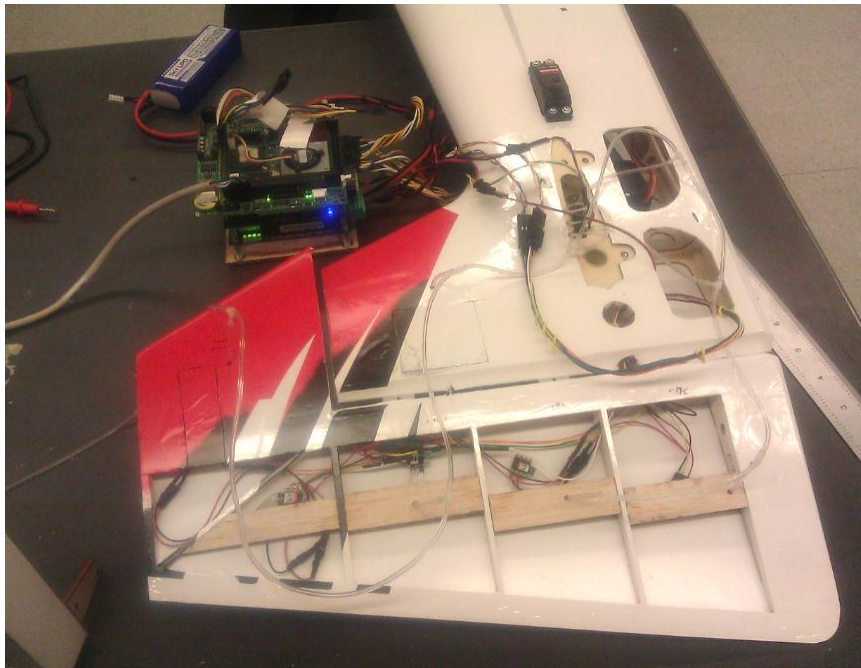


Figure B.2 Vertical tail and rudder

Appendix C: Flight test results

Appendix C.1 First generation flight test results

The first aerodynamic sensing system was comprised of a single instrumented chord and the extended range air data probe. This is depicted in Figure C.1. The expanded range air data probe provided real time alpha/beta measurements which augmented the pitch angle data from the IMU. The single instrumented chord allowed for stall detection on the right wing.

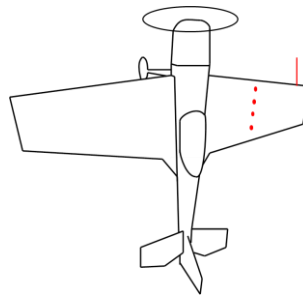


Figure C.1 First generation instrumentation

The system was first tested through remotely piloted flights before it was used in a guidance law for autonomous cruise to hover transitions. Both sets of flight test results are described in the following sub-sections.

Appendix C.1.1 Remotely piloted flight data

The Funtana was flown remotely in both level flight and vertical hover to collect pressure and inertial data during steady flight and transitions between modes. Approximately ten transitions were flown over the course of two separate flights. The pilot attempted to execute transitions on a straight and level flight path into the prevailing wind over a distance of approximately 15 meters indicated by the GPS data. The pilot held the aircraft in a hover using the ground as a reference

frame before transitioning back into the forward flight mode. The system was also flown at level flight through a series of race track patterns. Figure C.2 shows the reported IMU roll angle, wing pressure port readings in inches of water and the variation between inertial pitch and measured angle of attack in a turn and followed by straight and level flight.

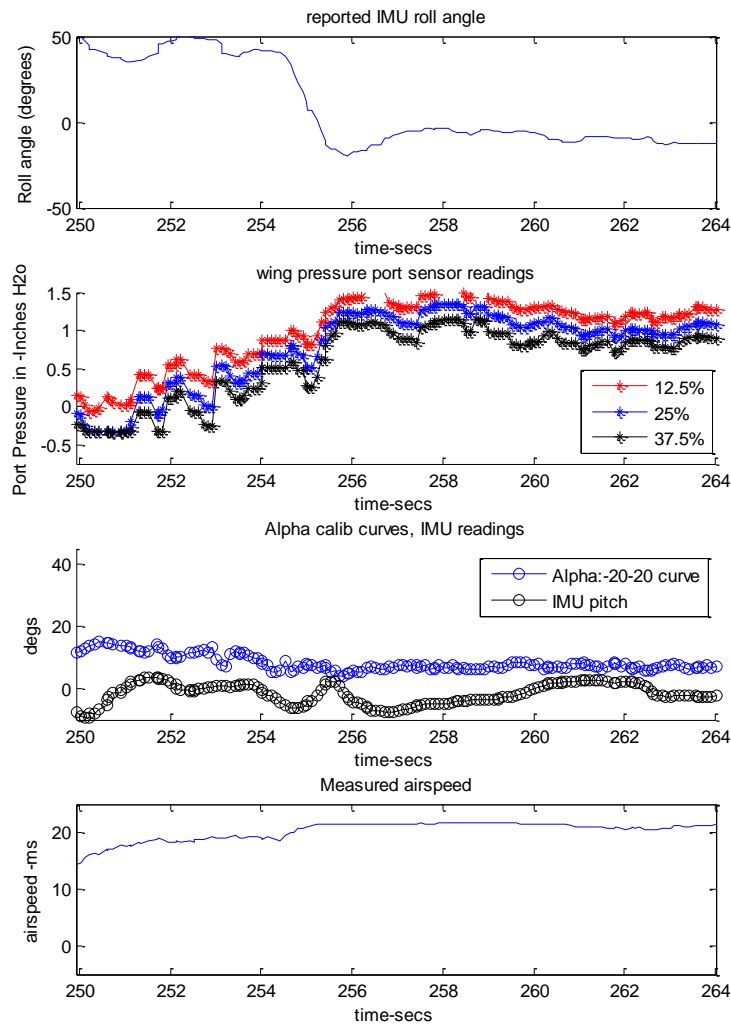


Figure C.2 Sample aerodynamic data : forward flight

5.4.i.b First Generation Stall Detection

During flight tests, a combination of both the C_p based stall detector and the pressure difference based loss-of-lift detector was successful in indicating conditions during a transition when the aircraft entered a stall condition and when

wing lift became no longer available. Presented along with Figure C.3 is a comparison of both algorithms working through out a transition. The results show stall occurring during the earlier part of the transition and progressing to a total loss of wing lift as airspeed decreases further.

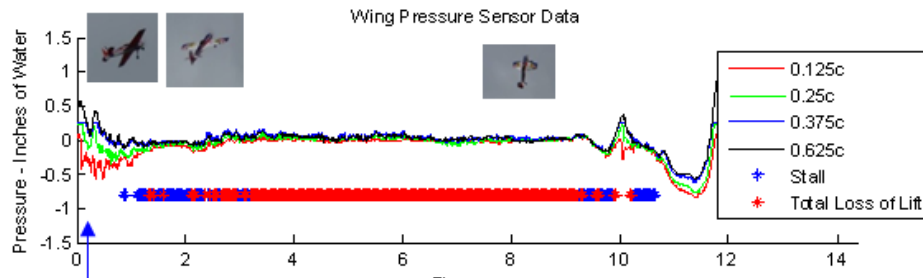


Figure C.3 Stall detection variables - remotely piloted transition

5.4.i.c Air Data Probe Transition Data

The plots in Figure C.4 shows a time history of measured IMU pitch angle, wing pressure sensor data and measured airspeed as the Funtana is transitioned from forward flight into a vertical attitude, and hovered at near zero airspeed. The data shows that additional aerodynamic data is sufficiently accurate to be used within an alternative guidance/control strategy over the course of a transition.

At high angles of attack and very low airspeeds, the pressure readings over the wings drop to a nominal level and remain within a certain range despite ongoing changes in the aircraft pitch and roll angles. At this point in the transition it can be argued that the wings begin to function more like control vanes directing propeller wash. It is a logical point during which a forward flight controller will be ineffective. Figure C.5 shows the full sequence of representative readings for a pressure port: transition to hover, hover, and exit from hover and Figure C.6 presents a closer view of the pressure distribution during a remotely piloted transition and hover sequence.

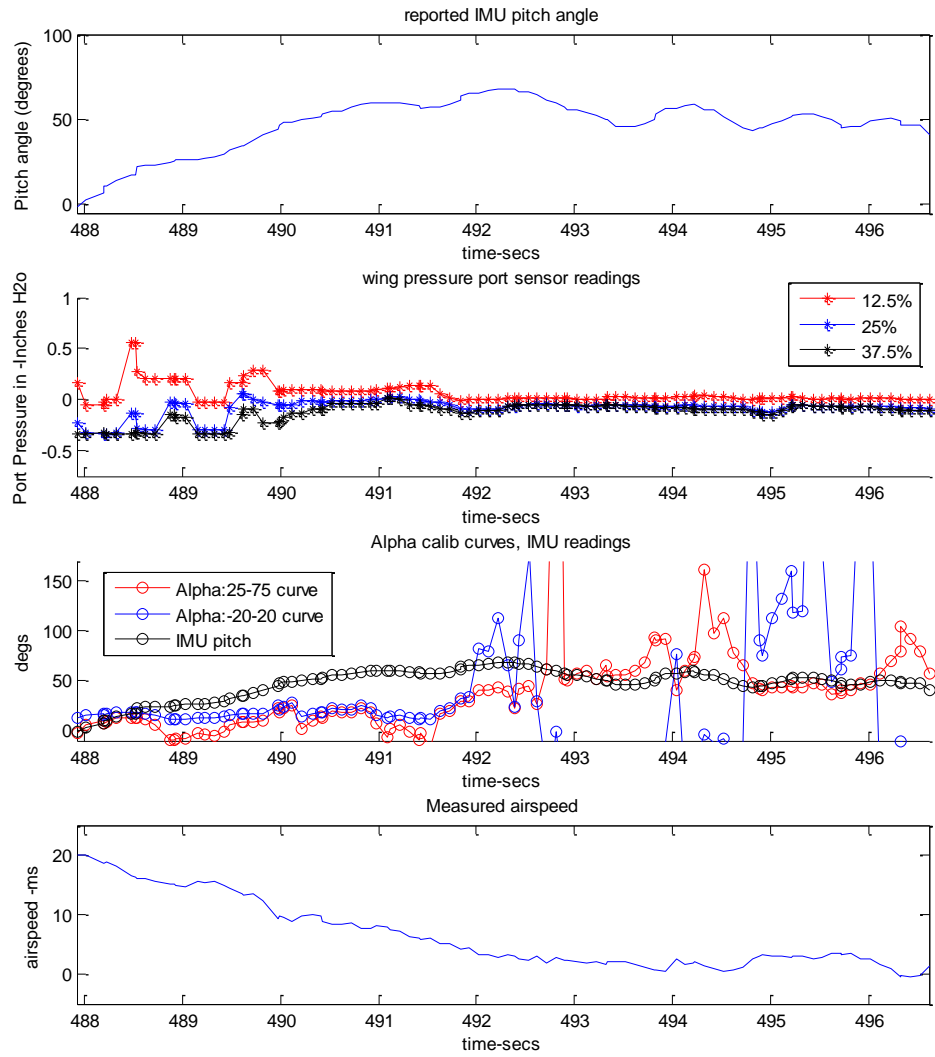


Figure C.4 Remotely piloted transition data : Pitch and pressure port readings

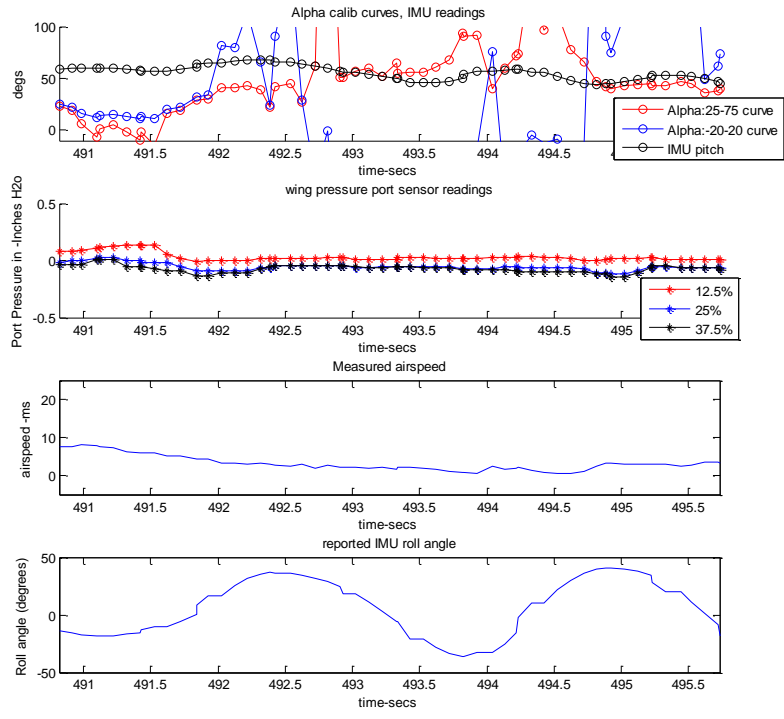


Figure C.5 Data from multiple transition maneuvers

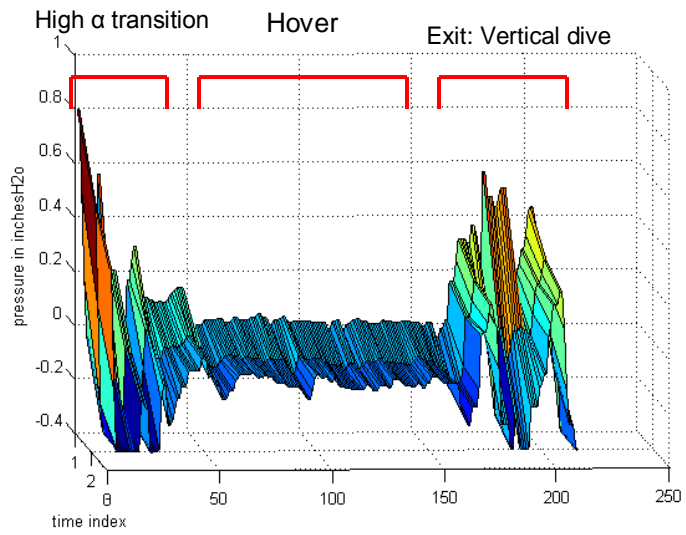


Figure C.6 Pressure data from a complete sequence.

Appendix C.1.2 Autonomous Cruise to Hover Transitions

The first generation aerodynamic sensing scheme was integrated into a cruise to hover transition autopilot and flight tested. Outdoor autonomous transitions were

previously performed outdoors by Johnson et al [51] using an adaptive neural network controller to successfully control the aircraft solely on inertial measurements in both orientations. The autopilot used by Johnson et al to transition the aircraft through high angle of attack flight and stall was open loop with respect to the aerodynamics. Only inertial pitch angle references were used during transitions and no measurements of the flow conditions were taken. Johnson et al found that linearly changing reference pitch and airspeed resulted in significant altitude change during a transition. They noted that future work will require an ‘airspeed bleed’ scheme.

It was thought that with additional flow measurements, a simple autopilot could be implemented during such a phase when the aerodynamic forces were unsteady.

5.4.i.d Stall-Aware Transition Guidance Law

A key feature of the airspeed bleeding process is encountering stall. A transition guidance law was proposed that inserts an additional “Trans LP” phase where airspeed is bled until the aircraft has flown into a stall before switching to “Trans HP” which is a phase comparable to the transition strategy previously implemented. The transition guidance used for first generation autonomy is shown in Figure C.7 .

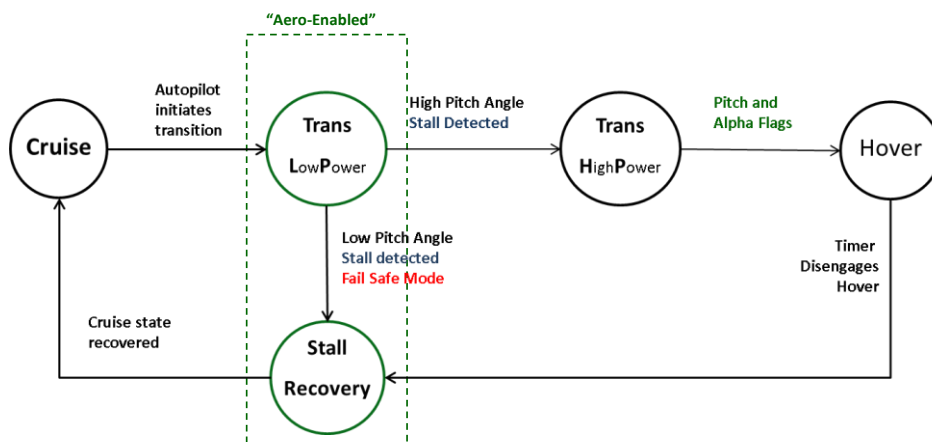


Figure C.7: Aerodynamic data driven transition guidance law

An additional stall recovery phase was added in case the autopilot failed to detect stall until the nose of the aircraft had already pitched downwards from level flight. In this phase, the autopilot aborts the transition and returns to a cruise state.

5.4.i.e Autonomous Transition Results

The aerodynamic-sensing enabled guidance scheme was combined with a decoupled lateral/longitudinal autopilot for tests. Stall detection data and expanded angle of attack data is used to trigger mode changes. Airspeed data is used to schedule gains. During a typical test flight, the aircraft is first taxied and taken off remotely by a RC pilot. Once the aircraft is lined up for a straight flight pass, the autopilot is given control of the aircraft. The autopilot begins in the cruise mode where the wings are leveled using the inertial frame. The pitch reference is set based on an altitude hold loop which uses the initial GPS altitude as a reference. The heading at initialization is also used as the heading reference for cruise and subsequent modes until the autopilot is deactivated. Once the aircraft has reached a stable cruise and the rotation rates decrease below a set threshold, the autopilot self-initiates the Trans LP airspeed bleed phase. The motor is powered off and the autopilot attempts to maintain a the cruise inertial pitch angle at the time of mode switch while the airspeed decreases. This causes the autopilot to increase elevator deflection to maintain a level pitch angle until stall is detected by the onboard computer using the stall detector describe. Unless the aircraft has entered a nose-down dive with an inertial pitch angle of below -10° , Trans HP is initiated. This phase executes the remainder of the transition in a way similar to that used by other researchers. The throttle is increased to maximum and the reference inertial pitch angle is set to vertical. The autopilot recognizes a hover state once a near vertical pitch angle and a sufficiently high angle of attack is measured. For the first generation, there is no dedicated hover controller and the aircraft recovers after a 2 second delay. In the recovery phase, the autopilot points the nose downward while increasing throttle until stall is no longer detected and switches to a cruise state. Data from a single transition is shown in Figure C.8 Angle of attack is compared against inertial

pitch angle and wing pressure port data is presented along with stall detection results. The GPS track and airspeed are also presented.

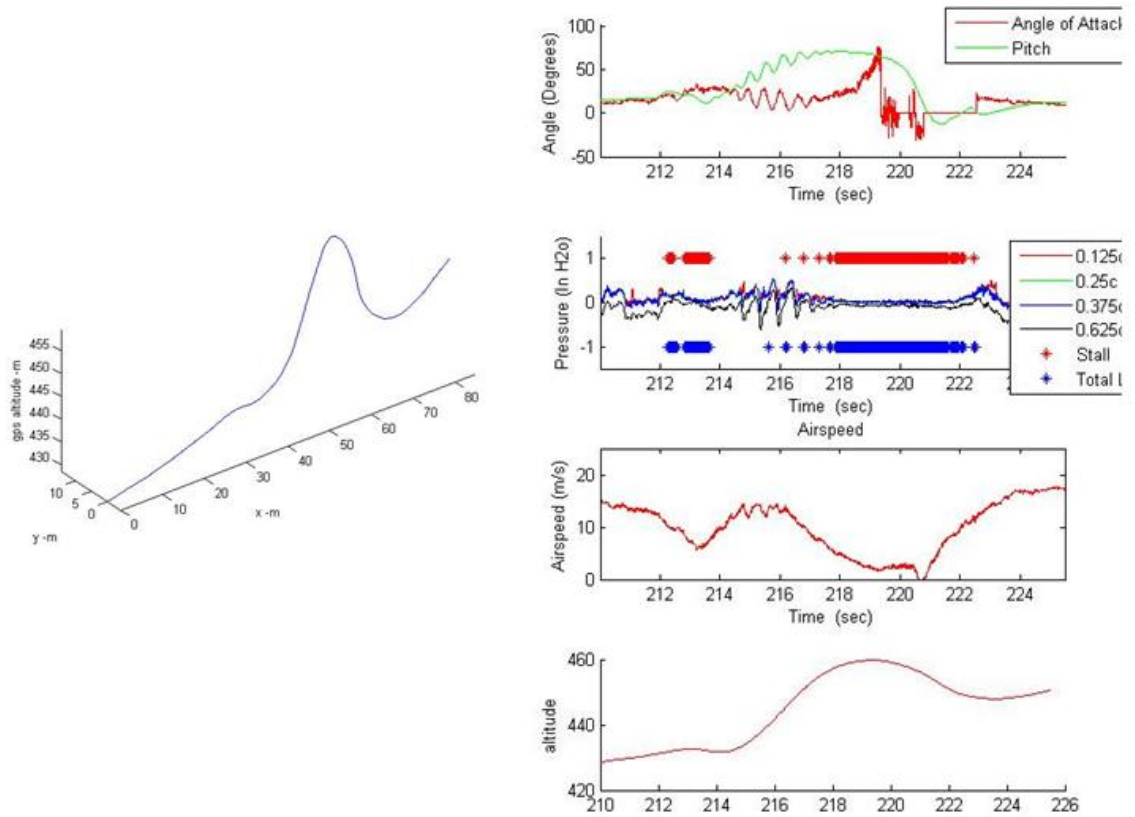


Figure C.8: Sample autonomous cruise to hover transition data

Flight testing shows that the controller provided reliable stall detection and mode switch triggering. It performed repeatable and consistent transition maneuvers consecutively despite the unsteady aerodynamics involved. From the data the autopilot consistently recognized stall and switched modes to Trans HP. However, the high power phase encountered problems with large oscillations in pitch resulting in an extended vertical climb and excursions in altitude. This trend result was repeated consistently throughout different flights. The plots in Figure C.9 show this trend occurring over a sequence of four consecutive transitions. Average altitude increase across a transition maneuver was approximately 25m

after factoring in a constant climb rate during cruise. The large oscillations in pitch during the high power transition phase prevented smooth rotation into a hover orientation at low airspeed. Despite this, the ability to consistently bleed airspeed and fly into a stall meant vertical excursions were comparable to those achieved with more advanced controllers suggesting that the strategy could be tuned to afford improved vertical accuracy during cruise-to-hover transitions with simple control strategies.

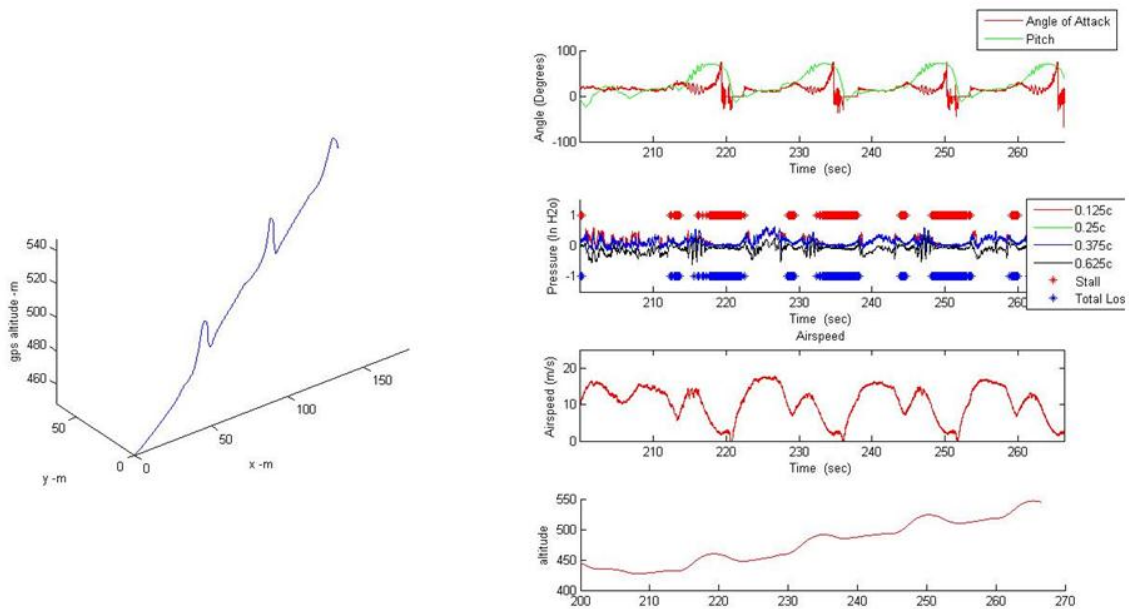


Figure C.9: Flight data from four consecutive autonomous transitions

While the airspeed bleed phase appears to function well, the Trans HP phase can benefit from a number of changes. With no feedback on motor RPM or thrust, the throttle ramp was set to maximum during Trans HP, causing an excessive thrust for the weight of the aircraft. It can be noted in the data that when the aircraft is pitched upwards, the airspeed actually approaches that of the entry cruise airspeed and the wings are seen to have recovered from stall. While the performance of Trans HP might be improved through tuning the open loop parameters in this application, it is believed that implementing simple feedback control strategies based on additional sensing can offer the most benefits for this type of maneuver.

Appendix C.2 Second Generation Funtana Flight Data

The aerodynamic data system was expanded to include a multi-hole probe for prop-wash estimation, an additional instrumented chord and an updated pressure port configuration. The second generation configuration is capable of measuring more aspects of the aircrafts aerodynamic state and can support the development of more sophisticated aerodynamic feedback control strategies. It has been flight tested through a series of remotely piloted aerobatic maneuvers. In addition to cruise-hover transitions, high angle of attack passes with wing rock and snap rolls were executed to assess the new instrumentation during high angle of attack maneuvers. The wings-level transitions and forward-stalls allow data from the prop-wash probe to be evaluated. Asymmetric stall conditions present in rock and roll maneuvers might be better characterized by examining both left and right wing pressure datasets. The higher performance maneuvers involved substantial aircraft rotations in addition to largely separated flow conditions. Where applicable, data from the aerodynamic instrumentation is presented along with inertial measurements taken by the IMU.

Appendix C.2.1 2nd Generation Stall Prediction Performance

The presented stall detection system was used in a mode switching capacity as shown in Figure C.8 when the aircraft entered a stall condition for transition-to-hover. At stall, the aerodynamic lift generated by the wings begins to decrease with increasing angles of attack due to the domination of separated flow across the wing surfaces. As described earlier, the wing is considered to have entered a 'full stall' when the pressure distribution has flat lined along the instrumented chord line. This was a straightforward process since in a full stall the pressure distribution is simply a flat line which needs little work to detect. However, notification can only be reliably given after the aircraft has transitioned between an attached flow condition and fully separated flow condition with no advance warning of the significant changes in handling characteristics.

Appendix C.2.1.a Stall prediction scheme

Developing the concept further, a methodology for indicating the onset of flow separation across the top of the wing could benefit an onboard controller by providing advance indication of imminent changes in flight condition. This second generation stall prediction algorithm is presented in Appendix B where different combinations of the pressure measurements are tracked.

Through flight testing, it was found that the departure from attached flow conditions can indeed be reliably detected by monitoring the $Slope_{LE}$ variable, which is the difference between the first two measurement points near the leading edge. When the value of this variable changes sign or approaches zero, it is analogous to a loss of the suction peak characteristic of attached flow. This signals that stall conditions are imminent. On the Funtana platform, this can happen at low airspeeds when slowly decelerating, or at high speeds during aggressive maneuvering. In either case, stall detection is preceded by such a sign change of the $Slope_{LE}$ variable. Approximately 40 cruise-stall maneuvers were recorded over a series of three flights. Due to space constraints, only the first four detected stalls are shown but the behavior of the $Slope_{LE}$ variable is consistent across all datasets. The evolution of these variables when flying into the first four stalls is shown in Figure C.10 where each plot depicts a different remotely piloted stall from different airspeeds.

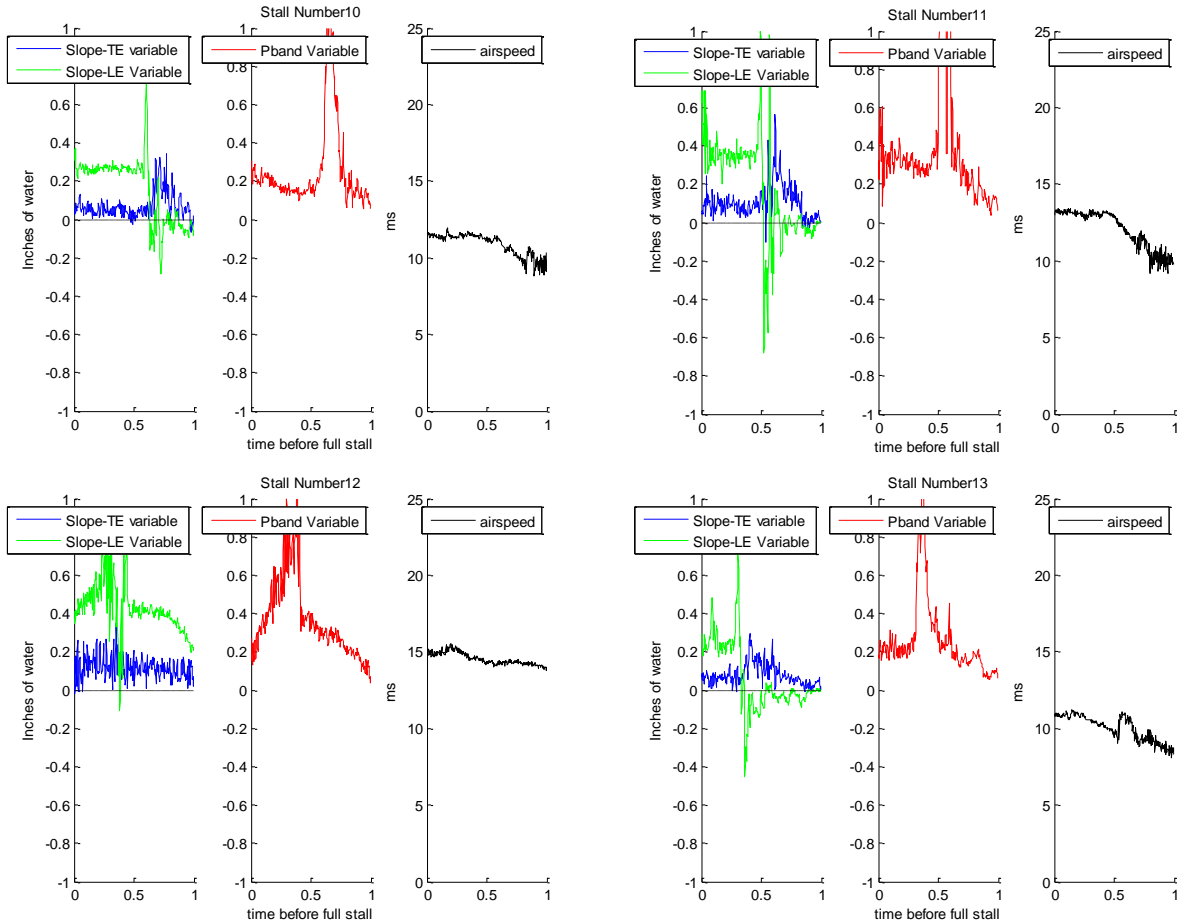


Figure C.10 Stall detection variable history - sample set of stall maneuvers

Appendix C.2.2 Differential lift measurements – onset of un-commanded wing rock

The left/right wing ports allow an initial test of flow measurement-based predictions of aerodynamic forces and resulting vehicle motion. Instances of un-commanded wing rock with no aileron input or throttle were initiated during which the differential lift measurements between left and right wings were compared against the roll rate histories measured by the IMU. During these maneuvers, the aircraft was flown at high angle of attack near 45 degrees with throttle held constant and aileron held at its neutral trim condition. This makes the differential lift generated by left vs. right wing the primary source of aircraft roll moment. The onset of wing rock is shown in Figure C.11 and Figure C.12, where estimated aerodynamic moments are compared against measured roll rates from the IMU.

It can be noted that in these situations, the lift-differential histories precede reported aircraft roll rates. This suggests that aerodynamic data can provide an advance indication of disturbances due to aerodynamic forces before inertial instrumentation can.

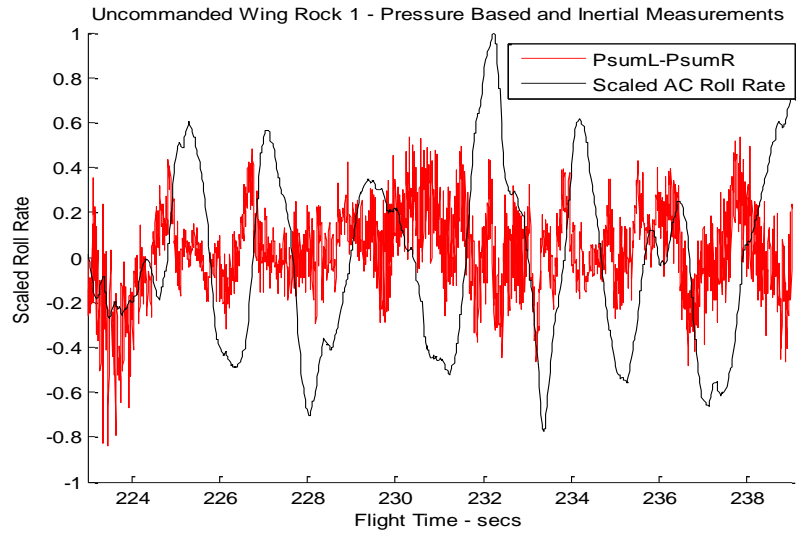


Figure C.11 Uncommanded wing rock onset - maneuver 1

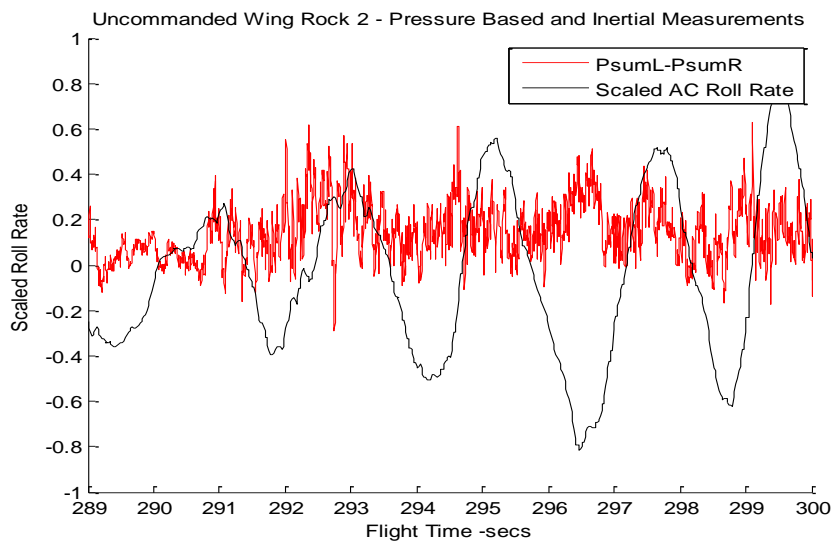


Figure C.12 Uncommanded wing rock onset - maneuver 2

A preliminary characterization of this phase difference is summarized in Table 4.1. The periods of the aircraft roll rate signal over steady wing rock cycles were manually tabulated and compared against the differential aerodynamic lift signal for phase. This was done for data from two different flights. The 12 periods from flight A were consecutive, but the 15 periods from flight B were from two different passes. For both flights, the average airspeed during the maneuver was 7ms at an average angle of attack of approximately 45 degrees. While preliminary, the data indicates a degree of repeatability that warrants further testing.

Table C.0.1 Averaged wing rock phase information for two flights

Flight A - 12 periods

Average α 45 deg	Average	Stdev
Average period (s)	2.14	0.19
Average Aero-Advance (s)	0.53	0.08
% phase advance	24	0.03

FlightB 9+6 periods

Average α 45 deg	Average	Stdev
Average period (s)	2.24	0.14
Average Aero-Advance (s)	0.48	0.15
% phase advance	21	0.06

Aerodynamic-based predictions of aircraft roll rates can be helpful in controlling phenomena such as wing rock. Wing rock has been studied extensively and has been likened to a limit cycle oscillation driven by a form of aerodynamic hysteresis [98]. In a wind tunnel implementation of a fuzzy logic delta-wing stabilizing controller based on roll-rate feedback, Anavatti et al [99] found that actuation lag could cause a controller to be unsuccessful in reducing wing rock amplitude, requiring a manual phase shift to allow the actuation to occur at the appropriate time during the next cycle. Measuring the aerodynamic roll moments might afford additional lead time for future autopilots encountering wing rock. The aerodynamic forcing can potentially be used to tune a simple spring-mass-damper to model the aircraft in the roll axis. While promising, more flight testing must be done to refine these results and to define flight parameters during which the use of differential lift measurements is useful to a controller. Data filtering can also be used to smooth noise in the raw aerodynamic measurements to minimize the possibility of defining wing rock from transient noise in the data.

Appendix C.2.3 Prop-wash Probe: Cruise to Hover

At high angles of attack when weight is primarily balanced by propeller thrust rather than lift, the difference in flow conditions between the wings and the tail section is most dramatic. The plots in Figure C.13 show the ability of our prop wash probe to track the evolution of the prop-wash on the tail section during a remotely piloted transition and recovery maneuver. The flow field behind the prop is turbulent with intense velocity fluctuations, and a simple 3 point moving average filter was used for prop wash flow angle measurements. From the data, it can be seen that the longitudinal prop-wash velocity component tracks the indicated airspeed when entering the maneuver. Half way through the transition at an airspeed of approximately 10m/s, the two flow velocities begin to differ dramatically. The previous generation autopilot that largely scheduled gains based on indicated airspeed during the deceleration phase was not able to account for this effect. During the transition and high angle of attack (>50degrees) flight, it was also noticed that the flow angles measured were large but within the limits of the calibration range.

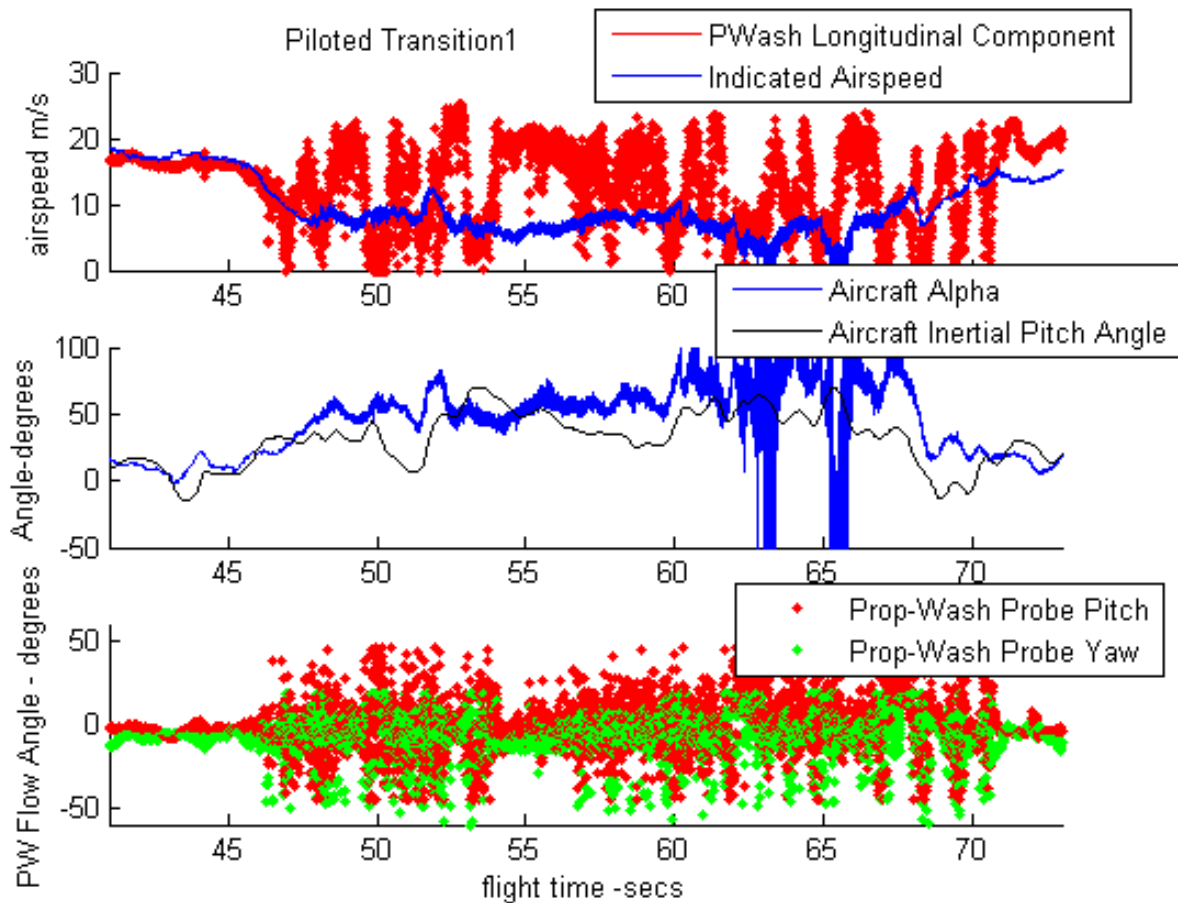


Figure C.13 Prop-Wash measurement during piloted transition at high α

It is hypothesized that accounting for the local flow incident on the tail surfaces will enable the transition autopilot described in an earlier section to improve its performance during the high power transition phase. Subject to the intense velocity fluctuations in the prop-wash, the relationship between control surface deflection and resulting pitch moment can be more accurately linearized about the incident flow even though the aircraft itself is flying through stall. The use of prop-wash estimates over the tail to apply more appropriately scaled linear control gains for the tail surfaces is being investigated in ongoing work.

Appendix C.3 Flight test conclusions and ongoing work

The preceding two sections have presented an aerodynamic feedback scheme for use on small UAS operating in unsteady flow conditions. A first-generation aerodynamic sensing scheme has demonstrated its ability to support a simple linear controller to detect stall during autonomous transition-to-hover maneuvers. Upgrades to the sensing package, including new embedded flow sensors and a prop wash probe, have been made to extend its capabilities. The new instrumentation functions as expected in flight. By combining simple aerodynamic principles, readily available materials and pressure transducers systems, a sensing and flight data scheme can be implemented that offer possibilities for small UAS flight control based on aerodynamic feedback. The control possibilities represented by the current package are currently being investigated through a series of windtunnel based tests. Remotely piloted and autonomous flight testing is expected to continue in the near-term, with the short-term goal of using the new aerodynamic data to improve accuracy and robustness in a suite of transition and hover flight control laws.

Appendix D: Air data probe design

The air data probes used for this research were designed to provide high-angle flow measurements while being low cost and easily manufactured. This appendix will describe the process used to develop the expanded range air-data probe referenced in Appendix A and the prop-wash probe described in Chapter 4. It will document the development process by providing schematics of early designs as well as providing a brief commentary.

Expanded Range Air-Data Probe

The air data probe design used in flight tests was first conceived as a low cost alternative to a five-hole probe on a RC trainer aircraft that was serving a role as a small UAS test platform. The first device assembled was constructed from two lengths of 1/16" diameter aluminum tubing fastened to the edges of a square piece of perforated board and connected to a differential pressure sensor through tygon tubes. The perforated board was strapped to the end of a long screwdriver so it could be conveniently held in a free-stream. This configuration featured two pressure ports that were perpendicular to each other on the end of aluminum prongs as shown in Figure D.1.

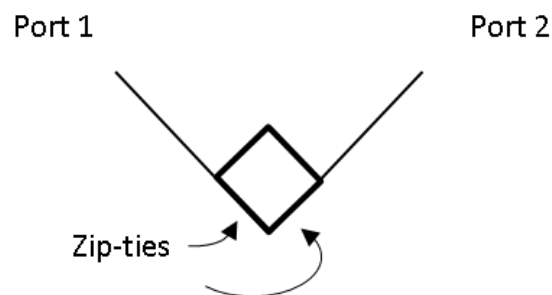


Figure D.1 Instrumented screwdriver pressure port geometry.

The geometry resulted in a pressure differential that varied when the probe was rotated relative to the incoming free stream. When the probe was centered in the flow stream with both prongs were each oriented at 45° to the incoming flow, the combination of static and total pressure at each prong resulted in a negligible pressure differential. When the left prong was aligned with the incident free stream, the prongs acted like the total and static ports on a conventional pitot-static probe and resulted in a pressure differential across the ports equivalent to 1 dynamic pressure, or $\frac{1}{2}\rho V_{ac}^2$. At a given airspeed, the differential pressure across the two ports was noted to vary smoothly with changing flow angle, showing that the concept was worth pursuing further.

To provide a dynamic pressure measurement, a low cost pitot probe was augmented with two pairs of aluminum prongs in the vertical and horizontal plane. As with the first prototype, each pair is oriented at 45° relative to the pitot probe. To avoid interfering with the pitot-static measurements, this first probe has the directional prongs behind the static ports of the probe as portrayed in Figure D2. The probe calibration normalized the pressure differential across the direction-prongs by the dynamic pressure and returned flow angles between of -25° to 25° .

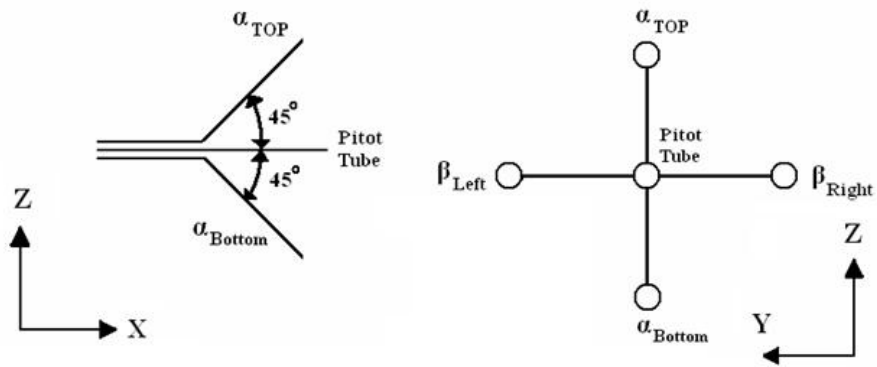


Figure D.2 First generation, small angle air data probe geometry.

When the Funtana high-angle-of-attack platform was conceived, large flow angles close to 90° at low airspeeds were sought. It was reasoned that extending the direction prongs till they were in line with the total port and spreading the pressure ports apart will minimize flow interference from other parts of the probe. This current generation of probe has been calibrated to accommodate flow angles of up to 80° is shown in Figure D3.

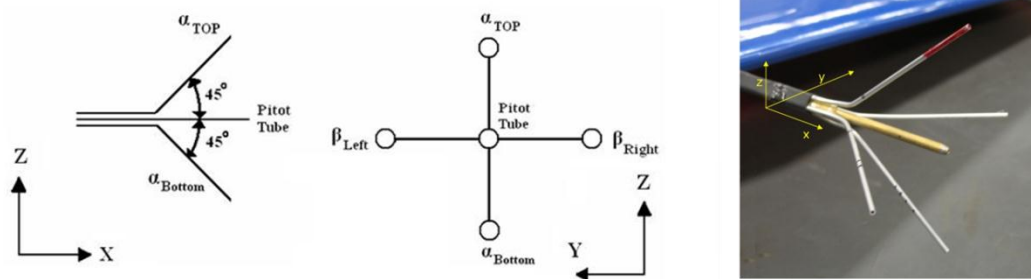


Figure D.3 Current expanded air data probe geometry and design.

Propeller-wash probe development

The requirements of the prop-wash probe motivated the next variant of multi-hole probe that did not require a separately manufactured pitot probe. Due to its location, a conventional pitot probe configuration would have proven inconvenient. Further, the probe may be required to provide negative velocity measurements in the event of an unpowered tail-slide. As such, a design constructed entirely out of aluminum tubing was developed. In order to provide longitudinal velocity measurements, a pair of fore and aft facing prongs was used to provide a measurement of dynamic pressure. The first geometry that was manufactured involved an arrangement of 5 tubes perpendicular to each other as shown in Figure D4.



Figure D.4 First gen prop-wash probe geometry

The total port was split between two sensors and also used to provide a measurement of probe pitch angle. The first calibration run showed that the ‘dual application’ total port and the ‘fore-aft’ measurement of dynamic pressure was successful. While the measurements could be normalized, the symmetric geometry resulted in a curve that had a minimum point at about -5° pitch as shown in Figure D5.

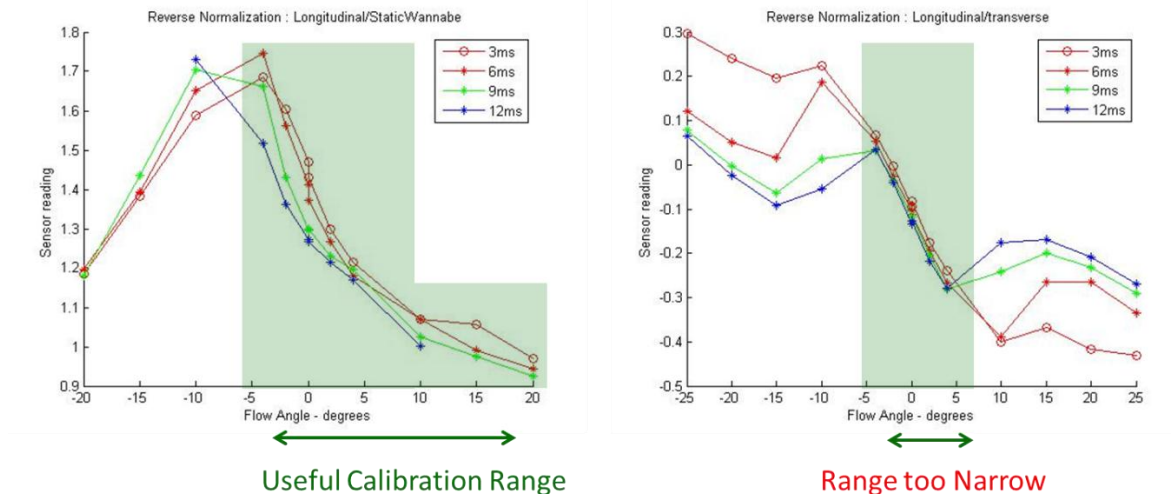


Figure D.5 First gen prop-wash probe calibration ranges

This meant that normalized sensor readings were not unique. Two different probe pitch angles would result in the same sensor measurement. For example, a normalized pitch measurement of 0.7 could indicate either -15° or 0° . The probe yaw direction readings were also seen to quickly become airspeed-dependent at flow angles larger than 5° .

As a quick solution, the direction prongs were simply oriented at 45° to the flow, creating a degree of asymmetry and allowing for useable calibration curves. The final geometry is shown in Figure D6.

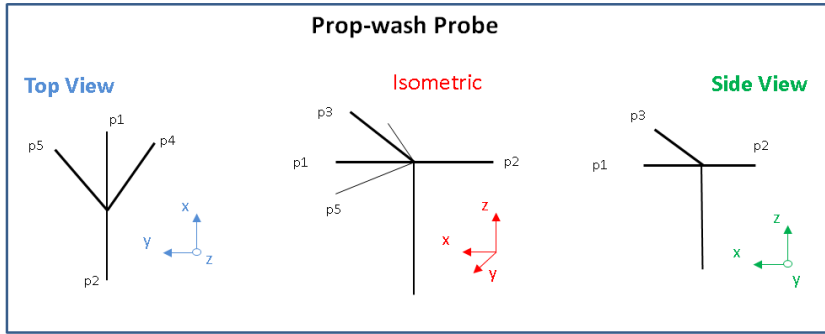


Figure D.6 Final prop-wash probe geometry

The final geometry was fixed using a laser cut “probe jig” with length markings engraved on the sides to ensure each prong was cut to the correct length during manufacturing, and to aid in realigning the prongs at 45° in case of damage.

References

- ¹ L. Pearson, "Developing the Flying Bomb," *Naval Aviation in World War I*, Published by The Chief of Naval Operations, 1969. pp. 70-73
- ² S. Zaloga, "V-1 Flying Bomb 1942-52", Osprey Publishing, 1st ed. 2005
- ³ F. Johnsen, "B-17 Flying Fortress: The Symbol of Second World War Air Power", McGraw-Hill, 1st ed. 2000
- ⁴ B. Yenne, "Attack of the Drones", MBI Publishing Company, 1st ed. 2004
- ⁵ B. Harvey, " Soviet and Russian Lunar Exploration " Springer Praxis Books, 1st ed. 2007
- ⁶ W. Shyy, Y. Lian, J. Tang, D. Viieru, and H. Liu, *Aerodynamics of Low Reynolds Number Flyers*, Cambridge University Press, 2007.
- ⁷ M. Shields and K. Mohseni, "Limitations of Using the Linearized Equations of Motion for MAV Control," *Proc. AIAA Guidance Navigation and Control Conference*, 8-11 August 2011, Portland, Oregon (AIAA 2011-6221).
- ⁸ M. Abdulrahim, S. Watkins, R. Segal, M. Marino, J. Sheridan, "Dynamic Sensitivity to Atmospheric Turbulence of Unmanned Air Vehicles with Varying configuration," *Journal of Aircraft* Vol. 47 No.6 pp. 1873-1883, 2010.
- ⁹ D. Galway, J. Etele, G. Fusina, "Modelling of Urban Wind Field Effects on Unmanned Rotorcraft Flight," *Journal of Aircraft* Vol 48 No.5 pp 1613-1620, 2011
- ¹⁰ F. White, *Viscous Fluid Flow* 3, McGraw-Hill, 3rd ed. 2005
- ¹¹ J. Anderson, *Introduction to Flight*, McGraw-Hill, 3rd ed. 1989
- ¹² F. Vignola, J. Michalsky and T. Stoffel, "Solar and Infrared Radiation Measurements", CRC Press, 1st ed. 2012
- ¹³ J. Stocking, W. Eberhardt, Y. Shakhshed, B. Calhoun, J. Paulus, and M. Appleby, "A Capacitance-based Whisker-like Artificial Sensor for Fluid Motion Sensing" *IEEE Sensors* 2010, pp. 2224-2229, 1 Nov 2010
- ¹⁴ M. Marana under direction of A.Flatau, "Development of a Bio-inspired Magnetorestrictive flow and tactile sensor" MS thesis, Department of Aerospace Engineering, University of Maryland, College Park, Maryland 2012.

- ¹⁵ W. Lauterbon and A. Vogel. "Modern Optical Techniques in Fluid Mechanics" Annual Review of Fluid Mechanics 1984. Vol 16:pp223-244
- ¹⁶ J. Fraden, " Handbook of Modern Sensors", Springer, 4th ed. 2010
- ¹⁷ A. Hilairw and F. Carta, " Analysis of unswept and swept wing chordwise pressure data from an oscillating NACA 0012 airfoil experiment. NASA CR-3567, 1983
- ¹⁸ J. Usherwood, T.Hedrick and A. Biewener, "The Aerodynamics of Avian take-off from Direct Pressure Measurements in Canada Geese" *Journal of Experimental Biology* 2003; 206 pp. 4051-4056.
- ¹⁹ H.Takahashi, Y.Aoyama, K.Ohsawa, H. Tanaka, E. Iwase, K. Matsumoto, I.Shimoyama, "Differential pressure measurement using a free flying insect-like ornithopter with a MEMs sensor" *Bioinspiration and Biomimetics*, vol. 5 no. 3, 036005, 2010.
- ²⁰ R. Wood, "The First Takeoff of a Biologically Inspired Robotic Insect" *IEEE Transactions On Robotics*, Vol.24, No.2, April 2008.
- ²¹ D.Mueller, H.A. Bruck, S.K. Gupta, "Measurement of Thrust and Lift Forces Associated With Drag of Compliant Flapping Wing for Micro Air Vehicles Using a New Test Stand Design", *J. Experimental Mechanics*. vol. 50, pp. 725 – 735, 2010
- ²² K. De Clercq, R. de Kat, B. Remes, B. van Oudheusden, and H. Bijl, "Flow Visualization and Force Measurements on a Hovering Flapping-Wing MAV 'DeIFly II'," *Proc. 39th AIAA Fluid Dynamics Conference*, 22-25 June 2009, San Antonio, Texas. (AIAA-2009-4035)
- ²³ D. Dawson, " Repeatability Manufacture of Wings for Flapping Wing Micro Air Vehicles Using Microelectromechanical Systems (MEMS) Fabrication Techniques" *Masters thesis*, Dept. of Aeronautics and Astronautic, Air Force Institute of Technology, Wright-Patterson AFB, Ohio. March 2011
- ²⁴ D. Li, S. Guo, N. Matteo, D. Yang, "Design, Experiment and Aerodynamic Calculation of a Flapping Wing Rotor Micro Aerial Vehicle", *Proc. 52nd AIAA Structures, Structural Dynamics and Materials Conference*, 4-7 April 2011, Denver Colorado (AIAA 2011-1988)
- ²⁵ J. Grauer and J. Hubbard Jr. "Development of a Sensor Suite for a Flapping-Wing UAV Platform," *Proc. 46th AIAA Aerospace Sciences Meeting*, January 2008. (AIAA 2008-224)
- ²⁶ Z. Jackowski directed by R. Tedrake, *Design and Construction of an Autonomous Ornithopter*, MS Thesis, Dept. of Mechanical Engineering, Massachusetts Institute of Technology, June 2009.
- ²⁷ J. Lee, D. Lee and J. Han, "Ornithopter Attitude Estimation: Ground Test" *World Automation Congress*, pp. 1-6 19-23 September 2010

- ²⁸ R. Krashanitsa, D. Silin, S. Shkarayev, "Flight Dynamics of Flapping-Wing Air Vehicle" *Proc, 49th AIAA Aerospace Sciences Meeting*, January 2009 Reno, Nevada. (AIAA 2008-6698)
- ²⁹ Festo (2011, Mar,) Festo. [Online]. http://www.festo.com/cms/en_corp/11369.htm (Retrieved 8th October, 2012)
- ³⁰ S.Ansari, R.Zbibowski, and K.Knowles, "Non-linear Unsteady Aerodynamic Model for Insect-like Flapping wings in the Hover. Part 1" *Proceedings of the Institution of Mechanical Engineers, Part G: Journal of Aerospace Engineering*, vol. 220, no. 2, pp. 61-83, 2006
- ³¹ D.J.Willis, J.Peraire and J.K.White, "FastAero - a Precorrected FFT - Fast Multipole Tree Steady and Unsteady Potential Flow Solver," presented at the *SMA Symposium, Singapore 2005*.
- ³² W.Shyy, H. Aono, S. Chimakurthi, P. Trizilia, C. Kang, C. Cesnik, and H. Liu, Recent Progress in Flapping Wing Aerodynamics and Aeroelasticity," *Progress in Aerospace Sciences*, Vol. 46, No.7 2010, pp 284 -327.
- ³³ A. Gogulapati, P. Friedmann, E. Kheng, and W. Shyy, "Approximate Aeroelastic Modeling of Flapping Wings in Hover," *AIAA Journal*, Vol. 51 No.3, 2013, pp. 567-583.
- ³⁴ C. Kang, H. Aono, C. Cesnik, and W. Shyy, "Effects of Flexibility on the Aerodynamic Performance of Flapping Wings," *Journal of Fluid Mechanics*, Vol. 689, Dec 2011, pp 32-74.
- ³⁵ S. Walker, A. Thomas, G. Taylow, "Deformable Wing Kinematics in the Desert Locust: How and Why do Camber, Twist and Topography Vary Through the Stroke?" *J R Soc Interface* 2008; 6 (38): 735-747
- ³⁶ C. Soms and M. Luttges, "Dragonfly Flight: Novel Uses of Unsteady Separated Flows," *Science*, Vol 228, No. 4705, 1985
- ³⁷ M. Dickinson, F. Lehmann, and S. Sane., "Wing Rotation and the Aerodynamic Basis of Insect Flight," *Science*, Vol. 284, No. 5422, 1999.
- ³⁸ D. Read, J. Hover, M. Triantafyllou, "Forces on Oscillation Foils for Propulsion and Maneuvering," *J. Fluid Struct.*, vol. 17, pp. 163 -- 193, 2003.
- ³⁹ Y. Baik, J. Rausch, L. Bernal, and M. Ol, "Experimental Investigation of Pitching and lunging Airfoils at Reynolds Number between 1×10^4 and 6×10^4 ," *Proc. 39th AIAA Fluid Dynamics Conference, San Antonio, Texas, June 22-25, 2009*, 2009, pp. AIAA-2009-4030.
- ⁴⁰ C. Berg and C. Ellington, " The Vortex Wake of a 'Hovering' Model Hawkmoth," *Philosophical Transactions: Biological Sciences*, Vol. 352. No. 1351, 1997, pp 317-328.

- ⁴¹ W. Maybury and F. Lehmann, "The Fluid Dynamics of Flight Control by Kinematic Phase Lag Variation Between Two Robotic Insect Wings," *Journal of Experimental Biology*, Vol. 207, No. 26, 2003, pp. 4704-4726.
- ⁴² K.Massey, A. Flick, and G. Jadhav, "Force Measurements and Flow Visualization for a Flexible Flapping Wing Mechanism" *Proc. 47th AIAA Aerospace Sciences Meeting*, 5-8 January 2009, Orlando, Florida. (AIAA 2009-877)
- ⁴³ T. Hubel and C. Tropea, "Experimental Investigation of a Flapping Wing Model," *Experimental Fluids*, Vol. 46, No.5, 2009, pp. 945-961.
- ⁴⁴ B. Singh, I. Chopra, M. Ramasamy and J. Leishman, "Insect-Based Flapping Wings for Micro Hovering Air Vehicles: Experimental Investigation," AHS International Specialists' Meeting on Unmanned Rotorcraft: Design, Control and Testing, January 2005. Phoenix, Arizona.
- ⁴⁵ P. Wu, "Deformation and Performance Measurements of MAV Flapping Wings," *Proc. SEM Annual Conference* June 1-4, 2009 Albuquerque, New Mexico
- ⁴⁶ J. Usherwood, T.Hedrick, C. McGowan and A. Biewener, "Dynamic Pressure Maps for Wings and Tails of Pigeons in Slow, Flapping Flight and Their Energetic Implications" *Journal of Experimental Biology* 2005; 208, pp. 355-369.
- ⁴⁷ H.Takashi, K. Matsumoto, and I.Shimoyama, "Differential Pressure Distribution Measurement for the Development of Insect-sized wings" , *Measurement Science and Technology* v.24, no. 5 055304 , 2013
- ⁴⁸ J. Usherwood, "The Aerodynamic Forces and Pressure Distribution of a Revolving Pigeon Wing," *Experimental Fluids*, Vol. 46 No.5, 2009, pp. 991-1003.
- ⁴⁹ J. Usherwood and C. Ellington, "The Aerodynamics of Revolving Wings I, Model Hawkmoth Wings," *Journal of Experimental Biology*, Vol. 205 No.11, 2002, pp. 1547-1564.
- ⁵⁰ Unmanned Aircraft Systems Roadmap 2005-2030, Office of the Secretary of Defence, 2005. [Online] URL: https://www.fas.org/irp/program/collect/uav_roadmap2005.pdf [Retrieved 20th August 2013]
- ⁵¹ E. Johnson, A. Wu, J. Neidhoefer, S.Kannan and M. Turbe. "Flight-Test Results of Autonomous Airplane Transitions Between Steady-Level and Hovering Flight," *AIAA Journal of Guidance, Control, and Dynamics*, Vol. 31, No. 2, March–April 2008
- ⁵² A. Wickenheiser, and E. Garcia, "Longitudinal Dynamics of a Perching Aircraft". *Journal of Aircraft*, Vol. 43, No.5, pp. 1386-1392.
- ⁵³ R. Cory and R. Tedrake. "Experiments in Fixed-Wing UAV Perching". *Proc. AIAA Guidance Navigation and Control Conference*, August 2008, Honolulu, Hawaii.
- ⁵⁴ H. Taniguchi, "Analysis of Deepstall Landing for UAV," *26th International Council of the Aeronautical Sciences*, 2008.

- ⁵⁵ W. Hoburg and R. Tedrake, "System Identification of Post Stall Aerodynamics for UAV Perching," *Proc. AIAA Unmanned...Unlimited Conference*, 6-9 April 2009, Seattle, Washington (AIAA 2009-1930)
- ⁵⁶ A. Desbiens and R. Cutkosky, "Landing and Perching on Vertical Surfaces with Microspines for Small Unmanned Air Vehicles," *Journal of Intelligent Robotic Systems*, Vol. 57, 2010, pp 313-327.
- ⁵⁷ R. Choe and N Hovakimyan, "Perching Maneuver for an MAV Augmented with a L-1 Adaptive Controller," *Proc. AIAA Guidance Navigation and Control Conference*, 8-11 August 2011, Portland, Oregon (AIAA 2011-6455)
- ⁵⁸ A. Paranjape, S. Chung, H. Hilton and A. Chakravathy. "Dynamics and Performance of Tailless Micro Aerial Vehicle with Flexible Articulated Wings". *AIAA Journal of Aircraft*, Vol. 50 No.5 May 2012 and *Proc.AIAA Atmospheric Flight Mechanics Conference*, Toronto, Ontario 2-5 August 2010.
- ⁵⁹ A. Paranjape, J. Kim, N. Gandhi and S. Chung, "Experimental Demonstration of Perching by an Articulated Wing MAV," *Proc. AIAA Guidance, Navigation and Control Conference* 8-11 August 2011, Portland, Oregon (AIAA 2011-6403)
- ⁶⁰ B. Johnson and R. Lind, "Characterizing Wing Rock with Variations in Size and Configuration of Vertical Tail" *AIAA Journal of aircraft*, Vol. 47, No. 2, March–April 2010, pp 567 – 577.
- ⁶¹ J. Chambers, "High-Angle-of-Attack Aerodynamics: Lessons Learned," *Proc, AIAA 4th Applied Aerodynamics Conference*, 9-11 June 1986, San Diego, California (A86-495780)
- ⁶² J. Chambers and S. Grafton, " Aerodynamic Characteristics of Airplanes at High Angles of Attack". NASA Technical Memorandum 74097, Langley Research Center, Hampton, Virginia, 1977
- ⁶³ L. Nguyen, "Simulator Study of Stall/Post-Stall Characteristics of a Fighter Airplane with Relaxed Longitudinal Static Stability," NASA TP1536, December 1979.
- ⁶⁴ J. Simon, "Dynamic Derivative Data for High Angle of Attack Simulation," *Proc. AIAA Guidance Navigation, and Control Conference*, 10-12 August 1992, Hilton Head Island, South Carolina (AIAA-92-4355-CP)
- ⁶⁵ J. Bauer, R. Clarke, J. Burken, "Flight Test of the X-29A at High Angle of Attack: Flight Dynamics and Control" NASA Technical Paper 3537, Dryden Flight Research Center, Edwards AFB, California 1995
- ⁶⁶ S. Herwitz, K. Allmendinger, R. Slye, S. Dunagan, B. Lobitz, L. Johnson, and J. Brass, "Nighttime UAV Vineyard Mission: Challenges of See-and-Avoid in the NAS," *Proc. AIAA 3rd Unmanned...Unlimited Conference, Workshop and Exhibit*, 20-23 September 2004 Chicago, Illinois(AIAA 2004-6417)
- ⁶⁷ R. Beard, D. Kingston, M. Quigley, D. Snyder, R. Christiansen, W. Johnson, T. McLain and M. Goodrich, "Autonomous Vehicle Technologies for Small Fixed Wing

UAVs," *AIAA Journal of Aerospace Computing, Information, and Communication*, Vol. 2, January 2005 pp. 92 – 108.

- ⁶⁸ R. Hirokawa, D. Kubo, S. Suzuki, J. Meguro and T. Suzuki, "A Small UAV for Immediate Hazard Map Generation," *Proc. AIAA Infotech@Aerospace Conference and Exhibit*, 7-10 May 2007, Rohnert Park, California. (AIAA 2007-2725)
- ⁶⁹ F. Hsiao, Y. Ding, C. Chuang, C. Lin and Y. Huang, "The Design of a Small UAV system as a Testbed of Formation Flight," *Proc. Infotech@Aerospace 2011*, 29-31 March 2011, St. Louis, Missouri (AIAA 2011-1422)
- ⁷⁰ R. Eubank, E. Atkins and D. Macy, "Autonomous Guidance and Control of the Flying Fish Ocean Surveillance Platform," *Proc. Infotech@Aerospace Conference and AIAA Unmanned...Unlimited Conference*, 6-9 April 2009, Seattle, Washington. (AIAA 2009-2021)
- ⁷¹ N. Rasmussen, B. Morse, and C. Taylor, "A Fixed-Wing, Mini-UAV System for Aerial Search Operations," *Proc. AIAA Guidance Navigation and Control Conference and Exhibit*, 20-23 August 2007, Hilton Head, South Carolina. (AIAA 2007-6819)
- ⁷² P. Xie, A. Flores-Abad, G. Martinez and O. Ma, "Development of a Small UAV with Autopilot Capability," *Proc. AIAA Atmospheric Flight Mechanics Conference*, 8-11 August 2011, Portland, Oregon (AIAA 2011-6449)
- ⁷³ J. Kaloust "Enhanced Stall and Recovery Control System (ESARCS) : A Nonlinear Model-Based Flight Control System For Uninhabited Airborne Vehicles (UAV)," *Proc. AIAA 1st Technical Conference and Workshop on Unmanned Aerospace Vehicles*, 20-23 May 2002, Portsmouth, Virginia, (AIAA 2002-3489).
- ⁷⁴ W. Green and P. Oh, "A MAV That Flies Like an Airplane and Hovers Like a Helicopter". *Proc. 2005 IEEE/ASME International Conference on Advanced Intelligent Mechatronics*. 24-28 July Monterey, California.
- ⁷⁵ A. Frank, M. Valenti, D. Leveine, J. How. " Hover Transitions and Level Flight Control Design for a Single-Propeller Indoor Airplane", *Proc. AIAA Guidance Navigation and Control conference and Exhibit*, August 2007, Hilton Head, South Carolina.
- ⁷⁶ E. Johnson and S. Kannan, " Adaptive Flight Control for an Autonomous Unmanned Helicopter", *Proc. AIAA Guidance, Navigation, and Control Conference*, 5-8 August 2002, Monterey, California . (AIAA 2002-4439)
- ⁷⁷ D. Yeo, J. Henderson, and E Atkins, "An Aerodynamic Data System for Small Hovering Fixed-Wing UAS," *Proc. AIAA Guidance, Navigation, and Control Conference*, 10-13 August 2009, Chicago, Illinois. (AIAA 2009-5756)
- ⁷⁸ D. Yeo, E. Atkins, L. Bernal and W. Shyy, "Aerodynamic Sensing for a Fixed Wing UAS Operating at High Angles of Attack," *Proc. AIAA Atmospheric Flight Mechanics Conference*, 13-16 August 2012, Minneapolis Minnesota.(AIAA 2012-4416)

- ⁷⁹ M. Patel, Z. Sowle, T. Corke and C. He, "Autonomous Sensing and Control of Wing Stall Using a smart Plasma Slat", *Proc. 44th AIAA Aerospace Sciences Meeting*, 9-12 January 2006, Reno Nevada, (AIAA 2006-1207)
- ⁸⁰ P. Bowles and T. Corke. "Stall Detection on a Leading-edge Plasma Actuated Pitching Airfoil Utilizing Onboard Measurement", *Proc. 47th Aerospace Sciences Meeting*, 5-8 January 2009, Orlando, Florida. (AIAA 2009-93)
- ⁸¹ C. Cox, A. Gopalarathnam, C. Hall. "Flight Test of Stable Automated Cruise Flap for an Adaptive Wing Aircraft". *Journal of Aircraft*, Vol. 47, No. 4, 2012 pp 1178-1188.
- ⁸² W. Barnwell directed by N. Chokani and C. Hall. "UAV Flight Control Using Distributed Actuation and Sensing". Masters Thesis, North Carolina State University 2003.
- ⁸³ S. Lion directed by C. Hall. "Control Authorities of a distributed Actuation and Sensing Array on a Blended-Wing-Body Uninhabited Aerial Vehicle". Masters Thesis, North Carolina State University 2007.
- ⁸⁴ Air Force Office of Scientific Research (AFOSR) Multidisciplinary University Research Initiative (MURI) AFOSR Grant FA9550-05-1-0411, [online] <http://www.avocet.gatech.edu> [Retrieved 20th August 2013]
- ⁸⁵ E. Morelli and R. DeLoach, "Wind Tunnel Database Development Using Modern Experiment Design and Multivariate Orthogonal Functions," *Proc. 41st Aerospace Sciences Meeting and Exhibit*, 6-9 January 2003, Reno, Nevada. (AIAA 2003-653)
- ⁸⁶ R. Guiler and W. Huebsch, "Wind Tunnel Analysis of a Morphing Swept Wing Tailless Aircraft," *Proc. AIAA Applied Aerodynamics Conference*, 6-9 June 2005, Toronto, Ontario, Canada. (AIAA 2005-4981)
- ⁸⁷ P. Marmier and N. Wereley, "Morphing Wings of a Small Scale UAV Using Inflatable Actuators for Sweep Control," *Proc. 44th AIAA Structures, Structural Dynamics and Materials Conference*, 7-10 April 2003, Norfolk, Virginia (AIAA 2003-1802)
- ⁸⁸ D. Landman, C. Britcher, and W. Bennet, "A Power-On Full-Scale Wind Tunnel Test of a UAV," *Proc. 17th Applied Aerodynamics Conference, Norfolk Virginia* (AIAA-99-3166)
- ⁸⁹ M. Ol, C. Zeune, T. White and T. Kudla, "Wind Tunnel Evaluation of Powered Static Aerodynamics of an Aerobatic UAV," *Proc. 51st Aerospace Sciences Meeting*, 7-10 January 2013, Grapevine, Texas (AIAA 2013-0241)
- ⁹⁰ T. Apker, "Measurements of Time-Resolved Flapping Wing Vehicle Forces in Hover," *Proc. AIAA Atmospheric Flight Mechanics Conference*, 10-13 August 2009, Chicago IL. (AIAA 2009-5847)
- ⁹¹ D. Yeo, E. Atkins, W. Shyy, "Aerodynamic Sensing as Feedback for Ornithopter Flight Control," *Proc. 49th AIAA Aerospace Sciences Meeting*, January 2011, Orlando, Florida. (AIAA 2011-552)

- ⁹² Y. Hong and A. Altman, "Streamwise Vorticity in Simple Mechanical Flapping Wings", *Journal of Aircraft*, Vo. 44, No. 5, pp. 1588 – 1597, 2007.
- ⁹³ D. Yeo E. Atkins, L. Bernal and W. Shyy, "Experimental Investigation of the Pressure, Forces and Torque Characteristics of a Rigid Flapping Wing", *Proc. 50th AIAA Aerospace Sciences Meeting*, January 2012, Nashville, Tennessee. (AIAA 2012-0849)
- ⁹⁴ N. McClamroch, *Steady Aircraft Flight and Performance*, Princeton University Press, 2011.
- ⁹⁵ S. Mallipudi, M.Selig, and L. Long, "Use of a Four-Hole Cobra Pressure Probe to Determine the Unsteady Wake Characteristics of Rotating Objects," *Proc. 24th AIAA Aerodynamic Measurement Technology and Ground Testing Conference*, 24 June – 1 July 2004, Portland, Oregon. (AIAA 2004-2299).
- ⁹⁶ H. Glauert, " *The Elements of Aerofoil and Airscrew Theory*, " Cambridge University Press, June 1983. p.199
- ⁹⁷ C. Ostowari and H. Wentz, "Modified Calibration Technique of a Five-Hole Probe for High Flow Angles," *Experiments in Fluids*, Vol. 1, No. 3, Sept. 1983, pp. 166–168.
- ⁹⁸ A.Arena and R. Nelson, , "Experimental Investigations on Limit Cycle Wing Rock of Slender Wings" *AIAA Journal of aircraft*, Vol. 31, No. 5, September-October 1004, pp. 1148-1162.
- ⁹⁹ A. Anavatti, J. Choi and P. Wong, "Design and Implementation of Fuzzy Logic Controller for Wing Rock" , *International Journal of Control, Automation and Systems*, Vol. 2, No.4, December 2004. Pp. 494-500.
- ¹⁰⁰ L. DeVries and D. Paley, "Multi-vehicle Control in a Strong Flowfield with Application to Hurricane Sampling", *Proc. AIAA Guidance Navigation and Control Conference*, 8-11 August 2011, Portland, Oregon. (AIAA 2011-6478)